Synthesis, Functionalisation, and Biomedical Application of Phospholipid–Functionalised Gold Nanorods for Cancer Therapy

Lucien Roach

Department of Physics and Astronomy

University of Leeds

A thesis submitted for the degree of

Doctor of Philosophy

30th September 2019

Acknowledgements

I would like to thank my supervisors, Prof. Stephen Evans, Dr. Kevin Critchley and Dr. Louise Coletta for offering me the opportunity of this PhD project and the support, encouragement and guidance which they have offered throughout my degree.

I also wish to acknowledge the work of all the PhD students and researchers who have contributed to this work, particularly Dr. Sunjie Ye, Dr. Mary Booth, and Dr. Nicola Ingram, without whom large parts of this thesis would not have been completed. I would also like to thank Samuel Moorcroft, Damien Batchelor and Daniel Paterson, for their contributions towards various experiments in this thesis, their work and help has aided me considerably.

I want to express gratitude to the whole of the Molecular and Nanoscale Physics group at Leeds, in particular those in the Nanoparticle Research Group, who have offered me advice and encouragement throughout my degree. Also the support staff in the department, especially those in the Mechanical and Electronics Workshops, whose work has been integral to assembly of many of the experimental rigs used in this thesis.

I also wish to extend thanks towards Prof. Mina Okochi and Masayoshi Tanaka, for the opportunity to work with them twice at the Tokyo Institute of Technology during the course of my PhD. The members of the Okochi Group who were welcoming and offered me warm hospitality throughout my time with them.

Finally, I want to thank my parents and sister, who have offered me nothing but support throughout.

Abstract

Cancer is the most common cause of death in the UK. Due to its aging population, the rate of cancer diagnoses is expected to rise dramatically in the coming decades. Currently cancer treatments have harsh side effects that cannot be well tolerated by the elderly, hence there is a need to develop new methods of cancer therapy which offer substantially better patient experiences. One such route is the use of near infrared–absorbent gold nanorods (AuNRs), which offer suitable optical and thermal properties to enable their use in techniques such as photothermal therapy and photoacoustic imaging. In this thesis we will explore the use of AuNRs in these roles as cancer theranostic agents.

This is addressed in three core areas; firstly the seedless production of AuNRs using binary surfactants. It is demonstrated how the morphology and optical properties of such particles can be manipulated through the inclusion of a co–surfactant. As well as yielding improvements in the monodispersity, shape yield and scalability of the protocol. Secondly, the surface functionalisation of AuNRs with phospholipids, we demonstrate the effective removal of CTAB, a toxic surfactant used in the synthesis, this is demonstrated through the use of ^{1}H nuclear magnetic spectroscopy, surface enhanced Raman spectroscopy and pH–dependent zeta potential measurements, this is present alongside stability studies of AuNRs of different coating, demonstrating the improved stability of AuNRs prepared with phospholipids. Finally, the application of phospholipid–coated AuNRs in cancer therapy is explored. We show that these particles are non–toxic *in vitro* and *in vivo*. We also explore their efficacy as photothermal conversion agents, measuring the achievable temperature rises under CW illumination, as well as imaging them using multispectral optoacoustic tomography of the particles in phantoms. *In vivo* measurements of the effects of heating these AuNRs under CW and nanosecond lasers on human carcinoma cell lines were also investigated. Finally the biodistribution of these particles was explored, when passively targeted or functionalised with cancer specific adhirons though ICP–MS analysis of *ex vivo* murine samples.

Abbreviations

AAS	Atomic absorbance spectroscopy
ANSI	American National Standards Institute
AuNR	Gold nanorod
AuNP	Gold nanoparticle
AuNS	Gold nanosphere
AuNSh	Gold nanoshell
BSI	British Standards Institute
BSA	Bovine Serum Albumin
CEA	Carcinoembryonic antigen
CTAB	Cetyltrimethylammonium bromide
CW	Continuous wave
D_2O	Deuterated water/Deuterium oxide
DIC	Differental interference contrast (microscopy)
DMEM	Dulbecco's modified eagle (cell cuture) medium
DOPC	1,2–dioleoyl–*sn*–glycero–3–phosphocholine
DOPG	1,2–dioleoyl–*sn*–glycero–3–phospho–*rac*–(1–glycerol)
DPBS	Dulbecco's phosphate buffered saline
DSPE-mPEG	1,2–distearoyl–*sn*–glycero–3–phosphoethanolamine–N–[methoxy–(ethylene glycol)$_{45}$]
DSPE-mPEG-Mal	1,2–distearoyl–*sn*–glycero–3–phosphoethanolamine–N–[maleimide–(ethylene glycol)$_{45}$]
EDTA	Ethylenediaminetetraacetic acid
Hb	Haemoglobin
HbO_2	Oxyhaemoglobin
ICP–MS	Inductively coupled plasma – mass spectrometry
IPA	Isopropanol
LSPR	Longitudinal surface plasmon resonance
NaOL	Sodium oleate
NMR	Nuclear magnetic resonance
MALDI–TOF MS	Matrix assisted laser desorption/ionisation – time of flight – mass spectrometry
MOPS	(3-(*N*-morpholino)propanesulfonic acid)
MPE	Maximum permissible exposure
MPS	Mononuclear phagocyte system
PAI	Photoacoustic imaging
PL148	Plasmalyte–148
PP	'Pseudo plasma' (buffer)
PPTT	Plasmonic photothermal therapy
PSS	Poly(styrene sulfonate)
QCM–D	Quartz crystal microgravimetry – with dissipation monitoring
RPMI 1640	Roswell Park Memorial Institute (RPMI) 1640 (cell culture medium)
SDS	Sodium dodecyl sulphate
SERS	Surface enhanced Raman spectroscopy
SNR	Signal–to–noise ratio
SPS	Single particle spectroscopy
TEM	Transmission electron microscopy
TCEP	Tris(2–carboxyethyl)phosphine
TSPR	Transverse surface plasmon resonance

Contents

List of Figures

Attribution of Work

Not all experimental work in this thesis was completed by myself. The following people should be acknowledged as contributors who performed experimental work during the course of this project. I wish to express my gratitude for their contributing work.

Chapter 3

The electron microscopy in this section was partially performed by myself, however Sunjie Ye performed the majority of the electron microscopy in this section. Mr Samuel C T Moorcroft also contributed some electron microscopy images. All other experimental work was performed completed by myself.

Chapter 4

The Raman spectra in this chapter were collected by Mr Damien Batchelor. The NMR spectra in this chapter were collected by Mr Daniel Paterson. The mouse plasma used in stability testing was collected by myself. All analysis and other experimental work was performed by myself.

Chapter 5

The majority of the work in this section was performed in collaboration with Leeds Institute of Medical Research at the University of Leeds. The *in vitro* cytotoxicity assays, immunofluorescence assays, flow cytometry and haemolysis experiments were performed by Dr Mary Booth. All work involving the handling of live animals was performed by Dr Nicola Ingram. All other experimental work was performed by myself.

Chapter 1

Introduction and Theoretical Background

1.1 Introduction

Gold nanoparticles (AuNPs) offer a set of exciting set of material properties which has led to them finding application in a large number of fields. AuNPs have highly tunable surface chemistry (whilst being relatively nonreactive), that can strongly absorb and scatter light at visible and near–infrared (NIR) wavelengths, and generate strongly localised electric fields. They can be synthesised relatively easily in a wide range of sizes and shapes. This has meant they have proved very versatile; finding a wide range of applications, such as catalysis, biosensing, and SERS probes [39]. A particularly popular application is their use as photothermal conversion agents in the therapy and imaging of cancer. This is the application that this thesis will explore.

Cancer is the most common cause of death in the UK, causing 28.1% of all deaths in 2017 [93]. Because of the aging population now found in Western countries, it is expected that number of new cancer diagnoses per year will increase by over 80% in the next 20 years [350]. Current treatment methods, such as radiotherapy and chemotherapeutic drugs, present significant problems such as causing harmful damage to healthy tissue, and presenting high levels of toxicity, respectively. Elderly patients show much lower tolerances to current methods for the treatment of cancers such as chemotherapy [373]. Hence there is a need to develop new treatment modalities, which are significantly less detrimental to patient experience over the course of treatment and can be more readily used in elderly patients. This is an extremely active area of research interest with many new methods being proposed, such as therapeutic microbubbles [227], targeted drug delivery [354] and viral therapies [179].

Gold nanoparticles with their unique combination of optical, photothermal and chemical properties offer one such route to potentially achieve this. This is discussed more thoroughly in this chapter. In brief, gold nanorods (AuNRs) can be synthesised such that they strongly absorb light in the near–infrared, at these wavelengths penetration of light into human tissue is significantly increased. AuNPs very efficiently convert absorbed light into heat, hence these particles when deployed *in vivo* can be used to remotely heat surrounding tissue upon illumination with NIR light, without the need for invasive surgery. It is possible to generate temperatures high enough to induce the death of cells via this route, and thus it is hoped that

by generating locally high concentrations of such particles within tumours, that this heating can be used to thermally treat tumours with minimal damage to surrounding healthy tissue. A large number of challenges are still left to be addressed before implementation of this technique will be realisable, these are discussed later in this chapter, alongside the theoretical underpinnings that enable this technique to be considered.

Chapter 2, presents a summary of the experimental techniques and materials used in this thesis. Further details of the theory and reasoning for the methods used are also given where it was felt that it was required.

This thesis contains three experimental results chapters, the first of which, **Chapter 3**, describes progress made in the synthesis of AuNRs using binary surfactants and how this produces more monodisperse AuNRs with high yield and can simultaneously be used to control the morphology and optical properties of synthesised AuNRs. The effects of controlling other parameters in the synthesis have also been investigated. Attempts have been made to understand the formation process of AuNRs during the synthesis and specific role that the two surfactants play.

In the second results chapter, **Chapter 4**, we functionalise our nanorods with phospholipids, and demonstrate the removal of hexadecyltrimethylammonium bromide from the surface of the AuNRs, via surface enhanced Raman spectroscopy, nuclear magnetic resonance spectroscopy and pH–dependent zeta potential measurements. We also investigate the colloidal stability of these particles in various physiological media and demonstrate their suitability for use in *in vitro* and *in vivo* experiments.

In the final results chapter, **Chapter 5** we look to the biomedical applications of these particles. We demonstrate that the phospholipid coatings show improved biocompatibility compared to commonly used polymer coatings, as well as investigating their uptake into cells. We demonstrate their suitability for use as photothermal conversion agents by measuring the heat generation under NIR illumination. The particles were then used in a pre–clinical photoacoustic imaging system. *In vivo* experiments were performed in mice, to demonstrate their *in vivo* biocompatibility and biodistribution. Finally, an initial attempt at targeting the AuNRs to a tumours were made.

In the rest of this introduction, a discussion of the theoretical background to this project is given, with a focus on the optical and thermal properties of AuNPs, alongside the applications they have found in medicine. Also discussed are the methods to synthesise AuNPs (in particular gold nanorods), and the methods used to manipulate their surface chemistry.

1.2 Optical Properties of Gold Nanoparticles

1.2.1 Electrons in Metals

It is impossible to discuss the interaction of light with such particles without first discussing the electronic structure of metals. Conduction electrons within metals are ‘quasi-free’, able to move freely relative to the positively charged lattice resulting in properties such as their high electronic and thermal conductivities and high reflectivity in the visible region. This behaviour is approximated by the Drude model [80], which is an application of Lorentz’ dipole oscillator model to bulk metals [213]. Under this model conduction electrons are considered to be free oscillators with no restoring force provided by the surrounding nuclei, and hence because of this, there is no natural resonance frequency, ω_0, as seen in dielectric materials.

This model does not account for all the optical effects seen in gold, such as intraband transitions (which explain why many metals are have colour). However the model provides a good approximation of the major electronic–optical effects in metals. The high density of free carriers in Au ($N_{\mathrm{Au}} = 5.9 \cdot 10^{28}$ m^{-3}), means even at the nanoscale electronic energy levels are effectively continuous relative to thermal excitations $k_B T$ at room temperature [217]. Hence quantum effects which are important in nanoscale structures made from materials, with low free carrier densities, such as semiconductors can be ignored and Drude's model can be used as an accurate description of the electronic properties of nanoscale gold.

Under this model the electronic response of Au to a driving oscillating electric field of frequency, ω, can is described as:

$$\epsilon(\omega) = 1 - \frac{\omega_p^2 \tau}{(\omega^2 \tau + i\omega)} \tag{1.1}$$

$$= 1 - \frac{\omega_p^2 \tau}{1 + \omega^2 \tau} + i \frac{\omega_p^2 \tau}{\omega(1 + \omega^2 \tau^2)} \tag{1.2}$$

where τ is the characteristic scattering time of an electron and ω_p is the plasma frequency, defined as:

$$\omega_p = \left(\frac{Ne^2}{\epsilon_0 m^*} \right)^{1/2} \tag{1.3}$$

N is the free electron density of the metal, e is the charge of the electron and m^* is the effective mass of the electron within the medium. τ as a parameter contains all the scattering processes which damp any charge oscillations in the plasma, these include electron–electron, electron–phonon, electron–defect, and electron–surface scattering all of which have their own characteristic timescales. This model makes a number of important predictions, firstly it can be seen from eq. (1.2) that for $\omega < \omega_p$ the real part of the ϵ_r is ~ 1 and rapidly decays to 0 above ω_p. Hence metals display high reflectivity below ω_p, before becoming rapidly transparent above it. We can also calculate the absorption coefficient from this expression for the dielectric based on the following relation (assuming $\epsilon'' \gg \epsilon'$):

$$\alpha = \frac{2\omega k(\omega)}{c} = \frac{2\omega}{c} \sqrt{\frac{\epsilon''(\omega)}{2}} = \sqrt{\frac{2\omega_p^2 \tau \omega}{c^2}} \tag{1.4}$$

The absorption coefficient for metals is thus very high ($5 - 7 \times 10^7$ m^{-1}) preventing the penetration of light into the interior of the metal. Electric field strength decreases in strength from the surface exponentially ($E(x) = E_0 \exp\{-2x/\alpha\}$), hence a characteristic lengthscale known as the skin depth can be defined as follows:

$$\delta = \frac{2}{\alpha} = \sqrt{\frac{2c^2}{\omega_p^2 \tau \omega}} \tag{1.5}$$

Hence the excitation of electrons within bulk metals is restricted to immediate vicinity of the metal surface, whilst electrons within the bulk of the metal are effectively screened from external AC electric fields above ω_p. The frequency dependence of the skin depth is plotted in fig 1.1. This effect is fundamental to the existance of surface plasmon resonances (SPR) in gold, the driving of an evanescent wave at a metallic surface. However, the ability to excite electrons at a metallic surface produces significantly more interesting optical effects when the metal object is restricted in size to dimensions less than or similar to the skin depth.

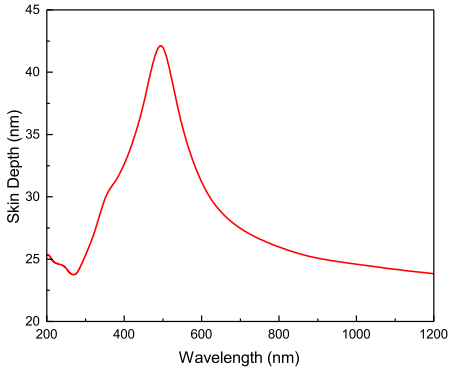

Figure 1.1: Skin depth of Au in the visible and NIR part of the spectrum. Calculated using permittivity values for Au from ref [156].

In these circumstances, incident light fields are able to drive collective oscillation of all electrons within such an object.

1.2.2 Intraband Transitions

There are limits to the Drude model which become important when considering the optical properties of AuNPs. The Drude model does not account for the band structures of metals, and the most important effect that emerges from this, intraband transitions. It can be from the density of states of Au (fig. 1.2 (a) that the Fermi energy, E_F of bulk Au falls within the $6s$ conduction band, with a large population of electrons in the $5d$ valence band, ~ 2 eV below E_F, an energy that corresponds to a wavelength of ~ 600 nm. Hence photons below this can excite electrons from the $5d$ band into the unoccupied energy levels within the $6s$–p band. The effect of this is very apparent in the dielectric function of gold when compared directly to the Drude model (fig. 1.2 (b)).

There is a noticeable difference between the empirically derived values and the Drude model below 600 nm, as the unaccounted for absorbance driven by intraband transitions becomes an increasingly important process. Incidentally this absorbance below 600 nm explains why Au has it characteristic yellow hue, instead of acting as a mirror at all wavelengths of light above the plasma frequency. This absorbance becomes an important consideration in optical properties of AuNPs, as intraband transitions will create electron–hole pairs simultaneously with any plasmonic excitation, significantly increasing the $e - e$ scattering rate, ultimately damping the plasmon. The impact of damping from scattering processes is normally considered through the plasmonic quality factor, $Q_{\mathrm{SPR}} = \varepsilon'/\varepsilon''$, which is plotted in fig. 1.2 (c) as function of excitation wavelength for both the Drude model and empirically derived permittivity values. The significance of the damping can readily be seen in the rapid drop off of the quality factor below 600 nm. As will be show in section 1.2.3, the expected plasmon band of small nanospheres falls within this range, leading to significant damping of the plasmon. Hence to truly realise the plasmonic potential of gold nanoparticles, we must attempt to use AuNPs with resonances >600 nm, where Q_{SPR} is maximised.

This highlights the need to use empirically-derived permittivities in the calculations of the optical properties of Au due to limitations of the Drude model below the band edge wavelength. The model is incapable of explaining the observed damping of plasmons in Au below 600 nm and fails to predict the

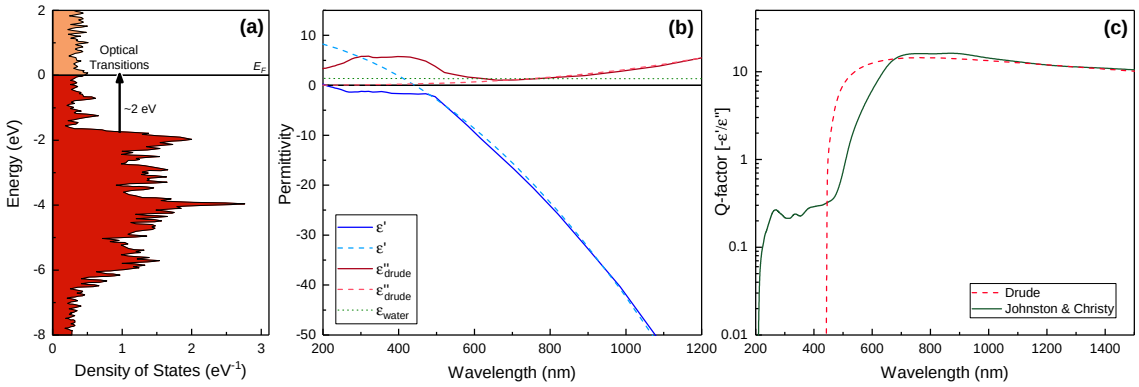

Figure 1.2: Intraband transitions in Au. **(a)** Density of states of bulk Au [46]. **(b)** Experimental permittivity values for Au and water compared with the calculated Drude permittivity (ω_p = 2.18 PHz and $1/\tau$ = 18.0 THz). **(c)** Plasmonic Q–factor as calculated from experimental data and the Drude model. Permittivity data for Au and water taken from refs [156] and [117] respectively.

absorbance of Au below ω_p. Regardless, the Drude model serves as a good starting point from which to understand the origins of plasmonic behaviour in metals, and accurately describes the electronic behaviour of Au in the NIR, above its band edge wavelength.

1.2.3 Localised Surface Plasmon Resonances – Mie Theory[1]

Whilst named after the effect seen at continuous metal surfaces known as SPR, and emerging from the same physics; localised surface plasmon resonances (LSPR) should be considered distinct phenomena. LSPRs are the collective oscillation of all the free carriers within a metal nano–object. They emerge as a result of the spatial confinement of an electronic plasma to length scales at or around the skin depth, and the resultant behaviours of such systems are substantially different from those seen in SPR experiments.

Classical solutions already exist for the interaction of a electric plane wave and a metallic sphere using Maxwell's equations. First formulated in 1908, Mie theory was the first rigorous mathematical treatment of the interaction between metallic particles and light [228]. In its original formulation the solutions are given as an expansion of multipolar contributions to the electric field generated by the electronic response of the particle (fig. 1.3). Without derivation, solutions to this problem are typically given in the form of two scattering functions, for perpendicular polarisations, calculated in the far-field ($d \gg \lambda$):

$$\begin{aligned} S_1(\vartheta) &= \sum_{m=1}^{\infty} \frac{2m+1}{m(m+1)} [a_m \pi_m(\cos\vartheta) + b_m \tau_m(\cos\vartheta)] \\ S_2(\vartheta) &= \sum_{m=1}^{\infty} \frac{2m+1}{m(m+1)} [b_m \pi_m(\cos\vartheta) + a_m \tau_m(\cos\vartheta)] \end{aligned} \tag{1.6}$$

where π_m and τ_m are angle-dependent functions defined by:

$$\pi_m(\cos\vartheta) = \frac{1}{\sin\vartheta} P_n^1(\cos\vartheta) \qquad \tau_m(\cos\vartheta) = \frac{d}{d\vartheta} P_n^1(\cos\vartheta) \tag{1.7}$$

P_n^1 are the Legendre polynomials of the first degree. a_m and b_m are scattering coefficients to be determined

[1] The equations in this section are largely adapted from Bohren and Huffman [36].

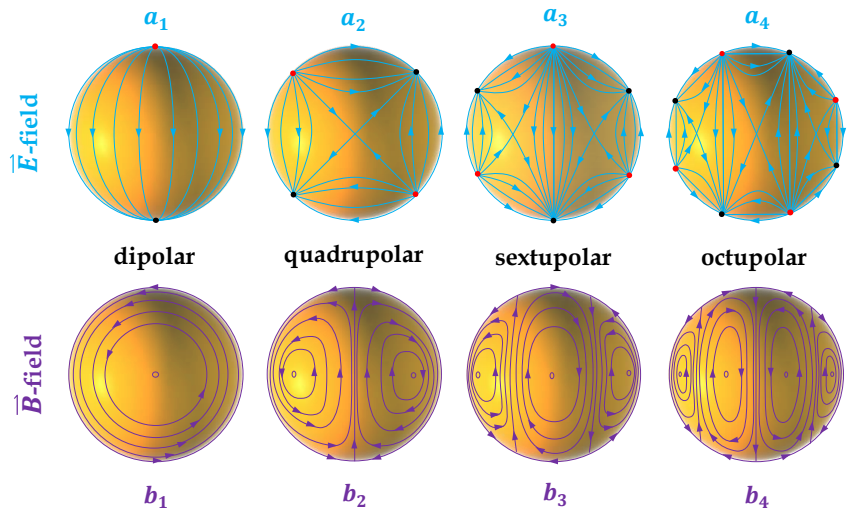

Figure 1.3: Multipolar contributions: Electric and magnetic field lines generated at the surface of a metal spheroid when interacting by light polarised in the vertical axis. Figure adapted from [228].

which dictate the contribution of each multipolar contribution. These require the most computation in Mie theory calculations; the absorption and scattering cross sections can be expressed in terms of these coefficients:

$$\begin{aligned} \sigma_{\text{abs}} &= \frac{2\pi}{k^2} \sum_{m=1}^{\infty} (2m+1)\,\text{Im}\{a_m + b_m\} \\ \sigma_{\text{scat}} &= \frac{2\pi}{k^2} \sum_{m=1}^{\infty} (2m+1)\left(|a_m|^2 + |b_m|^2\right) \\ \sigma_{\text{ext}} &= \sigma_{\text{abs}} + \sigma_{\text{scat}} \end{aligned} \tag{1.8}$$

1.2.4 The Quasistatic Approximation

For particles with diameters in the range 10 – 60 nm only the dipolar contributions ($m = 1$) need to be considered to accurately calculate their optical properties. For particles larger than this, quadrupole and higher order multipole contributions can no longer be considered negligible. Whereas small particles less than 10 nm in diameter exist at scales below the typical electronic mean free path in metals leading electron–surface scattering becoming the dominant electronic interaction which will damp any plasmon resonance.

This is known as the dipolar or quasistatic approximation. Under which only the $m = 1$ terms in the above sum are considered. Examination of the known boundary conditions allows it to be shown that the only non–trivial solutions are $a_1 = -E_0$ and $b_1 = E_0 4\pi\varepsilon_0 a^3(\varepsilon - \varepsilon_m)/(\varepsilon + 2\varepsilon_m)$. b_1 can be identified as containing the sphere polarisability:

$$\alpha = 4\pi a^3 \frac{\varepsilon - \varepsilon_m}{\varepsilon + 2\varepsilon_m} \tag{1.9}$$

where a is the radius of the particle, ε ($= \varepsilon_1 + i\varepsilon_2$) is the permittivity of the particle and ε_m is the permittivity of the surrounding medium. Combining this with eq. (1.8) yields the following relations:

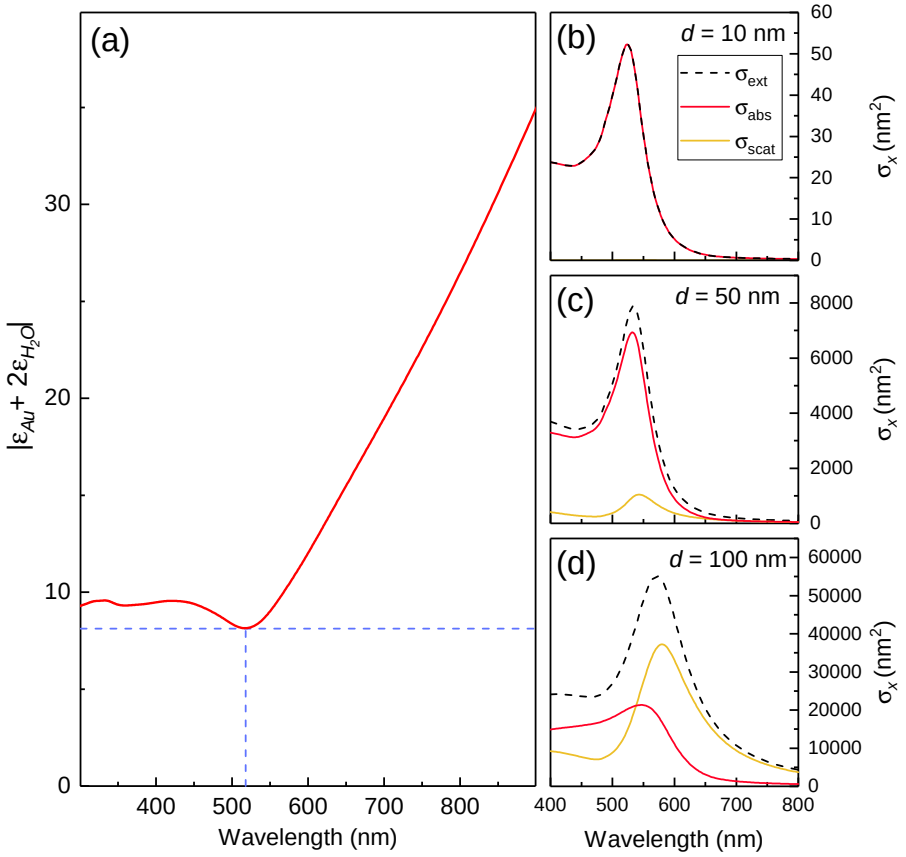

Figure 1.4: **(a)** Plot of the Frölich condition for Au in an aqueous environment showing a global minima at 518 nm. **(b)-(d)** Generated spectra in the quasistatic approximation for 10, 50, and 100 nm AuNPs respectively. Permittivity values for gold and water taken from refs [156] and [117] respectively.

$$\left.\begin{aligned}\sigma_{\text{abs}} &= 3k\,\text{Im}\{\alpha\}\\ \sigma_{\text{scat}} &= \tfrac{k^4}{2\pi}|\alpha|^2\end{aligned}\right\} \quad \sigma_{\text{ext}} = \sigma_{\text{abs}} + \sigma_{\text{scat}} \tag{1.10}$$

where k is the wave vector given by $\text{k} = 2\pi\varepsilon_m/\lambda$. From eq. (1.9) it can be seen that both σ_{abs} and σ_{scat} are at a maximum when $|\varepsilon + 2\varepsilon_m|$ is minimised, this is known as the Fröhlich condition [99]. It can be calculated from experimentally obtained permittivity values for gold that the expected absorbance peak will be found at a wavelength of ~520 nm (fig. 1.4 (a)) [156].

These relations provide a good approximation for particles with diameters in the range 10–60 nm and closely match experimentally obtained spectra. It can be see that absorbance scales with a^3, and scattering scales with a^6, with scattering becoming the dominant extinction mode for particles with $a > 50$ nm. The rapid increase in scattering cross–section with particle radius has important implications for applications such as darkfield microscopy which are unable to resolve particles below some critical diameter. From these relations and experimentally obtained permittivity values, spectra can be calculated showing the single predicted resonance predicted from the Frölich condition with some redshifting of the resonance with particle diameter (fig. 1.4 (b)–(d)).

In the quasistatic limit, it is also possible to calculate the local electric field as a result of the induced

dipole [17]. This can be expressed outside of the particle as follows:

$$\vec{E}_{ind} = 3\frac{\hat{r}(\hat{r}\cdot\vec{p}) - \vec{p}}{4\pi\varepsilon_0\varepsilon_m}\frac{1}{r^3} \tag{1.11}$$

where $\hat{r}$ is radial unit vector, $\vec{p}$ is the dipole moment given by $\vec{p} = \alpha\vec{E}_0$, and r is the distance from the centre of the particle. It can be seen that field decays with the third power of the radius and increases linearly with the incident field. The maximum induced field will thus be at the particle surface, aligned with the axis of excitation and equal to $|E_{ind}|_{max} = 2p/4\pi\varepsilon_0\varepsilon_m a^3$. For a 50 nm AuNP this field maximum is approximately 14× greater than E_0 [234]. This field enhancement seen at the surface of nanoparticles makes them particularly appealing as probes for surface enhanced Raman spectroscopy (SERS), where the SERS enhancement scales with the fourth power of this enhancement, enabling the detection of molecular species bound to nanoparticles resonant at the incident laser wavelength with high sensitivity [171]. This is discussed further in section 1.2.8, and can be improved substantially by tuning the nanoparticle morphology.

1.2.5 Gans' Solution

Often incorrectly referred to as a theory, in 1912 Gans provided a solution of Mie theory for ellipsoids in the quasistatic approximation [101]. The significance of this solution comes from its prediction of the optical properties of elongated particles 80 years in advance of their first synthesis [94]. In summary Gans' solution re–expresses the Mie relations in terms of an anisotropic polarisability, α_j, where $j = x, y, z$. Which is defined as:

$$\alpha_j = \frac{4\pi}{3}a_x a_{yz}^2\frac{\varepsilon_1 - \varepsilon_m}{\varepsilon_m + L_j(\varepsilon_1 - \varepsilon_m)} \tag{1.12}$$

where a_x and a_{yz} are lengths of the major and minor axes of the ellipsoid respectively. ε_1 is the real part of the permittivity of the medium and ε_m is the permittivity of the surrounding medium. L_j is the shape factor associated with each axis of the ellipsoid defined by:

$$\begin{aligned} L_x &= \frac{1-e^2}{2e^3}\left(\ln\left(\frac{1+e}{1-e}\right) - 1\right) \\ L_y = L_z &= \frac{1-L_x}{2} \end{aligned} \tag{1.13}$$

where e is the eccentricity of the ellipsoid defined by the particle dimensions:

$$e = \sqrt{1 - \left(\frac{a_{yz}}{a_x}\right)^2} \tag{1.14}$$

an important feature of these factors is that they are only dependent on the aspect ratio of the particle, rather than the individual dimensions themselves, although this is only true for particles small enough for the dipolar moment to dominate. It is also notable that as the aspect ratio of the particle tends to unity (i.e. $L_x = L_y = L_z = \frac{1}{3}$), eq. (1.12) returns the sphere polarisability. Using the above relations, eq. (1.10) can be

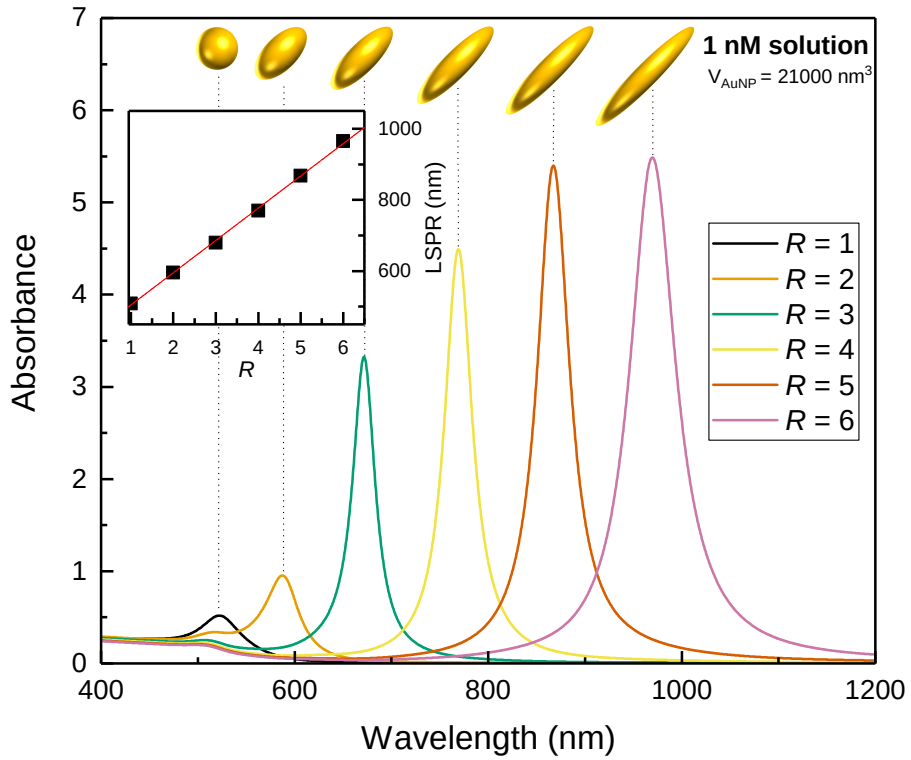

Figure 1.5: Gans' solution predicted absorption spectra for ellipsoids at a range of aspect ratios. The particle volume has been held constant at 21000 nm^3. Inset is a plot of the peak absorbance as a function of aspect, demonstrating the linear dependence of the LM on the aspect ratio of the particle. Values for the permittivity of bulk gold were taken from Johnston and Christy [156].

redefined as:

$$\left.\begin{aligned}\sigma_{\text{abs}} &= k\,\text{Im}\left\{\tfrac{1}{3}\alpha_x + \tfrac{1}{3}\alpha_y + \tfrac{1}{3}\alpha_z\right\}\\ \sigma_{\text{scat}} &= \tfrac{k^4}{6\pi}\left(\tfrac{1}{3}|\alpha_x|^2 + \tfrac{1}{3}|\alpha_y|^2 + \tfrac{1}{3}|\alpha_z|^2\right)\end{aligned}\right\} \quad \sigma_{\text{ext}} = \sigma_{\text{abs}} + \sigma_{\text{scat}} \tag{1.15}$$

Spectra generated using these relations tend to display several common characteristics, firstly there exists two modes of excitation for these particles, a smaller doubly degenerate transverse mode (TM), at 520 nm or lower, associated with excitation by light with a polarisation orientated along the minor axes of the ellipsoid. This mode decreases in intensity and is slightly blue shifted with increasing particle aspect ratio. A second much larger longitudinal mode (LM) associated with excitation by light with its polarisation orientated along the major axis of the particle. This mode dramatically increases in intensity and red shifts with increasing aspect ratio. Typically for the size of particle for which Gans' solution is valid (d_{eff} <60 nm), scattering is negligible and can be ignored. Example spectra generated by this theory are given in fig. 1.5.

Gans' solution can be used as an effective estimate of the optical properties of small AuNRs. However in comparison with the observed spectra the LM peak is always significantly blue–shifted due to differences in morphology between an ellipsoid and an actual AuNR. Also Gans' solution fails to account for effects such as surface–electron scattering, which acts as a damping term at resonance leading to broadening of this peak. The relative ease of these calculations, compared with computational simulations still makes them a relatively attractive option as a crude but effective estimation of the optical properties of AuNRs.

Further extensions to Mie Theory

There are a number of other notable extensions to Mie theory allowing calculations to be made for particles, notably Aden and Kerker's solution for concentric spherical shells which can accurately model the optical properties of gold nanoshells and can be extended further to include coated ellipsoids [3], and Lind and Greenberg's solution for infinite cylinders, applicable to metal nanowires [205].

1.2.6 Computational Simulation of Gold Nanoparticles

Beyond the few morphologies given above, there are no other simple solutions to Mie theory, instead the problem must solved computationally. This offers the ability to predict the optical response of any given particle morphology in an arbitrarily complex environment. Several common methods appear in the literature, detailed as follows:

Direct Dipole Approximation - DDA

The discrete dipole approximation, these calculations represent an arbitrary–shaped particle as a cubic lattice of N point dipoles each with a local polarisability, α_i, leading to a set of $3N$ coupled linear equations [76, 77, 281]. These equations are then typically solved numerically using the conjugate gradient method [79]. DDA is currently the most popular simulation technique for metal nanoparticles, and offers simple parameterisation and only requires that the particle volume be discretised [239]. However the simulations typically require large amounts of computation time and are limited by the fact the accuracy suffers with increasing refractive index, requiring finer meshing increasing N to often computationally prohibitive levels for Au in the NIR. Freely distributed codes such as DDSCAT and OpenDDA make these simulations relatively straightforward to implement.

Finite–Difference Time–Domain – FDTD

Finite–difference time–domain, these calculations provide numerical solutions to wave equations using the Yee algorithm [397]. The entire space over which solutions are sought is modeled as a 3D–grid over which Maxwell's equations are discretised based on finite steps in time and space. The electric and magnetic field over each finite volume are calculated and solved at a given instant in time and then stepped until steady-state behaviour is achieved. This method is very processor and memory intensive, but given a fine enough mesh and that the wavelength is much larger than the physical dimensions of the particle, can accurately provide solutions to Maxwell's equations over all space. These simulations are fairly easy to implement, but require large amounts of computation time. It also requires that the permittivity be expressed as the sum over multiple Lorentzians, which can make inclusion of experimentally determined values of $\varepsilon(\omega)$ more difficult [239]. The most commonly utilised software distribution for these calculations in the literature is Lumerical.

Boundary Element Modelling – BEM

Boundary element modelling, which models the physical situation as a series of 2D elements situated on the interface of materials and at the boundaries of region of interest; a set of differential equations can then be solved for each element by minimising an error function [150, 336]. It can accurately calculate the optical response of plasmonic nanostructures, and generally over a shorter timescale than other methods, since

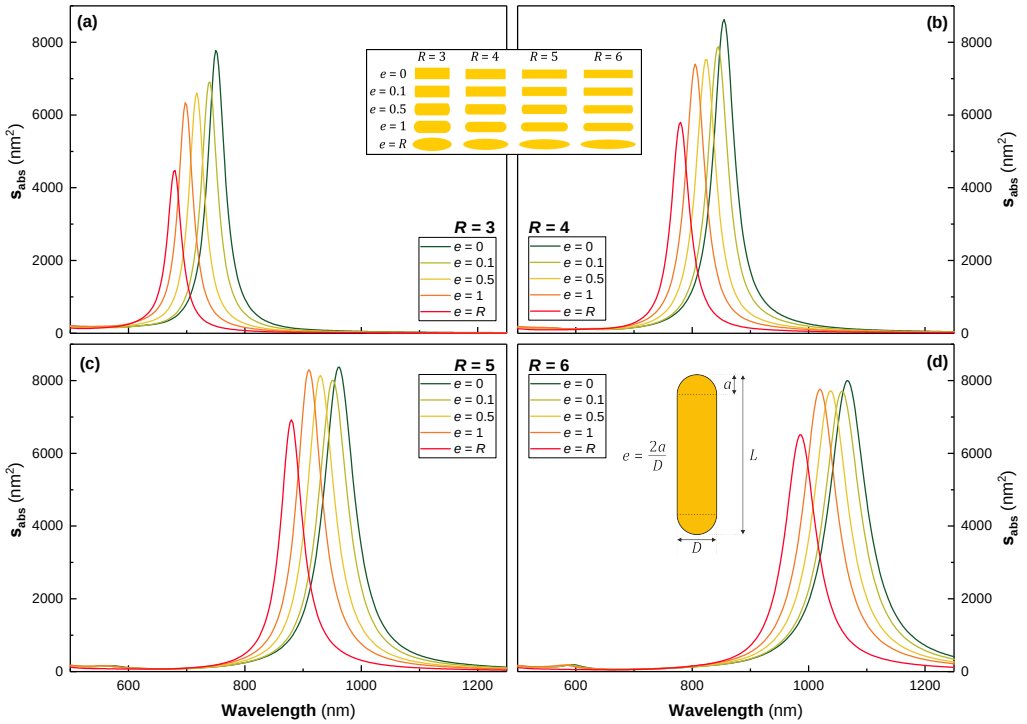

Figure 1.6: FEM simulated spectra of AuNRs varying aspect ratio, R, and end–cap eccentricity, e. Spectra have been calculated for values of e between 0 and R (i.e. a cylinder and an ellipsoid) for AuNRs with aspect ratios of **(a)** 3, **(b)** 4, **(c)** 5, and **(d)** 6. Inset are diagrams showing the crossection through the major axis of each AuNR and a diagram showing the values with with e were calculated. Permittivity data for Au taken from refs [156] and ε_{H_2O} was assumed to be 1.77.

solutions only have to found for the interfaces in the system. This comes at the cost of losing information on the volumetric distribution of calculated quantities, such as the electric field. Beyond this, BEM techniques are limited to solving linear differential equations, any non–linear couplings are thus not calculable via this technique. BEM is better suited to dealing with simple morphologies with low surface–to–volume ratios, as increasing surface area results in increasing number of elements per particle. The computational requirements of these simulation scale with the square of the number of elements (compared with FEM which increases linearly with the number of elements), hence higher surface area particle morphologies increase computation time significantly. MNPBEM is a commonly used MATLAB plugin for the purposes of these simulations.

Finite Element Modelling – FEM

Finite element modelling, is a volume–discretisation technique, using a (typically irregular) mesh. Solutions to differential equations throughout the volume can then be solved using variational methods from the calculus of variations to solve each finite element. Typically solutions are coupled to neighbouring elements and thus several runs must be completed to minimise the associated error. Typically the associated error is minimised through the use of algorithms such as the Runge–Kutta method. Solutions for simple problems may require a large amount of memory and computation time compared with BEM, but additional information is garnered on the variation of individual parameters over the entire volume. For more complex geometries with a high surface–to–volume ratio typically are solved faster in this formalism. Common FEM simulation packages used for these calculations are COMSOL and ANSYS. These packages offer the additional benefit of being bundled as multiphysics packages allowing the simulations of other physical phenomena to be considered alongside plasmonic resonances such as heating or fluid dynamics.

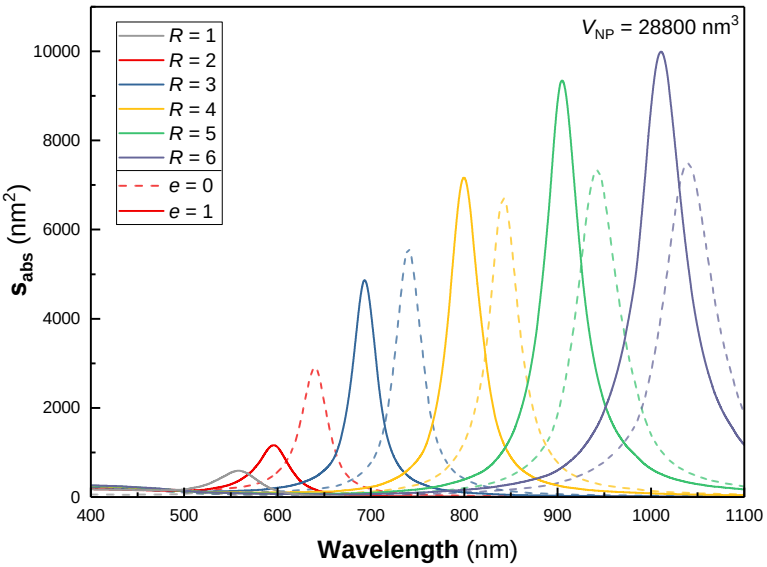

Figure 1.7: Simulated absorbance crosssections of AuNRs calculated using the method published by Yu *et al* [401]. Spectra have been calculated for cylinders ($e = 0$, dashed lines) and hemispherically–capped AuNRs ($e = 1$, solid lines) for aspect ratios between 1 and 6. Permittivity data for Au taken from refs [156] and ε_{H_2O} was assumed to be 1.77. The parameter sets used to calculate these spectra are those given in ref. [401].

Example FEM simulated spectra calculated using COMSOL are shown in fig. 1.6.

1.2.7 Extensions to Computational Simulation

A more recent approach has been to create simple numerical model which can generalise the results of the above methods to all similar nanoparticle shapes. Yu *et al* have shown it is possible to calculate the optical response on certain metal NPs from a set of four parameters which can be extracted from computational simulations, after which all NP of similar form can be calculated with minimal computational resources [401]. The method is limited to the quasistatic limit, and hence can only be applied to simple with a single electrostatic dipolar mode per symmetry axis.

These four parameters are ε_j, the resonant permittivity, which describes the effects of geometry as an effective permittivity. It can be extracted from fitting of the peak strength and postion of mode j from several simulated absorption spectra. Secondly, V_1, the electrostatic mode volume, and particle polarisability expansion coefficients, a_{12} and a_{14}, which can be calculated from the simulations of the induced electric field. Sets of these parameters have to be calculated for each excitation modes of a given particle. These numbers are independent of particle size (under the quasistatic limit), composition and environment, and hence once calculated can be used to calculate the optical properties of particles of the same shape, but of different characteristic dimensions (with in the limits of the quasistatic approximation).

These variables appear in a modified particle polarisability of form:

$$\alpha(\omega) = \frac{1}{3\varepsilon_m^{3/2}} V_1 \left(\frac{\varepsilon_m}{\varepsilon - \varepsilon_m} - \frac{1}{\varepsilon_1 - 1} - A_1(s) \right)^{-1} \tag{1.16}$$

where s is the shape factor defined by $\sqrt{\varepsilon_m} L/\lambda$, and $A_j(s)$ is function which describes retardation effects due to the finite size of the particle relative to the wavelength of light defined by $A_j = a_{j2}s^2 + \frac{4\pi^2 i V}{2L^3} s^3 + a_{j4}s^4 + ...$

This polarisability can be inserted into the relations for σ_{abs}, σ_{scat}, and σ_{ext} given in eq. (1.15) to give the optical response of a given particle.

Once the four requisite parameters described above have been calculated, they can be inserted into eq. (1.16). and subsequently eq. (1.15), enabling calculation of spectra in fractions of a second. However, the calculated results are only as good as the simulations used to calculate the particle properties. It is also not suited for any study which requires even relatively minor morphological changes to be made to the particle geometry (such as end–cap modification of AuNRs) as a large number of simulations need to be performed in order to arrive at each parameter set. Example spectra calculated using this method for cylindrical and hemispherically–capped AuNRs are given in fig. 1.7 (using the parameter sets given in [401]).

1.2.8 Other Plasmonic Effects

Local Field Enhancement

As discussed in section 1.2.4, a metal NP excited close to its plasmonic resonance will induce a local field in the surrounding enviroment. The near–field generated on the particle surface is greatly enhanced compared to the excitation field, E_0. This is true for all plasmonic nanostructures and has found a variety of applications. The induced field can be greatly enhanced by fine tuning of the particle morphology to maximise the plasmonic Q–factor, in the case of AuNPs by tuning the particle resonance above 700 nm (fig. 1.2(c)). Presented in fig. 1.8(a) is the calculated field enhancement surrounding a (16 × 60) nm AuNR, excited at resonance (λ_{LSPR} = 803 nm), it can be seen that an enhancement factor in excess of 70× is expected. By comparison a 60 nm AuNS excited at resonance (λ_{LSPR} = 536 nm) has an expected enhancement factor of 14 [234]. It can also be seen that the field becomes localised to areas of high curvature, in the case of the AuNR above, this falls close to the intersection between the body of the AuNR and tip (fig. 1.8(b)&(c)).

These high field intensities close to the particle surface greatly enhance electronic transitions of optical emitters and absorbers, leading to enhanced signal from electronic processes such as Raman scattering [144]. The actual enhancements of the Raman signal is proportional to the fourth power of the electric field enhancement and is given by the local field enhancement factor, ${}^{\mathrm{em}}G_{\mathrm{SERS}}$, defined by [171]:

$$ {}^{\mathrm{em}}G_{\mathrm{SERS}} = \left|\frac{E}{E_0}\right|^4 \tag{1.17} $$

Figure 1.8(b)&(c) gives ${}^{\mathrm{em}}G_{\mathrm{SERS}}$ as calculated along various axes and contours within the model, with a maximum value of ${}^{\mathrm{em}}G_{\mathrm{SERS}}$ of $2{\times}10^7$ being predicted by the model. These significant enhancements in Raman signal intensity have wide use in applications requiring high sensitivity such as the detection of explosives, pollutants and biomolecules [34]. Raman spectroscopy thus also provides a robust method to with which to characterise the surface coatings of plasmonically active NPs.

Plasmonic Coupling (and Aggregation)

When multiple particles are considered in close proximity this induced field becomes important as it will interact with surrounding particles. Calculations become more involved, as a universal plane electric field can no longer be considered to be the only excitation source. Hence neighbouring particles will experience plasmonic coupling. Under such conditions The field felt by an individual nanoparticle can be considered to

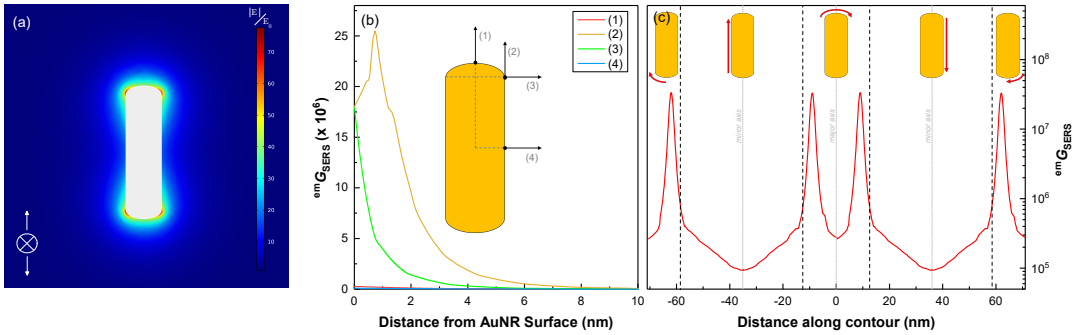

Figure 1.8: Local electric field during excitation of the LSPR of a AuNR. **(a)** FEM simulated map of the ratio of amplitudes of the local field and excitation field ($|E|/|E_0|$) around a (16 × 60) nm AuNR ($\lambda_{\mathrm{LSPR}} = \lambda_0$ = 803 nm). The excitation wave was polarised along the major axis of the AuNR and traveling into the plane of the image. **(b)** Plots of the local field enhancement factor, ${}^{\mathrm{em}}G_{\mathrm{SERS}}$ along lines located *(1)* along the major axis of the AuNR, *(2)* parallel to the particle surface originating from the intersection of the half–ellipsoid and cylindrical sections of the AuNR, *(3)* perpendicular to the particle surface from the same point, and *(4)* along the minor axis of the AuNR. For clarity, each of this vectors have been marked on the inset diagram. **(c)** ${}^{\mathrm{em}}G_{\mathrm{SERS}}$ along the surface contour shown in (a). The points along the contour which intersect with the major and minor axis have been marked on the figure, as well the intersections between the half-ellipsoidal caps and cylindrical sections of the AuNR. Diagrams above each section of the curve indicates which the section of the contour corresponds with that section of the curve. The electrical response of the AuNR was rotationally symmetric about the long axis of the AuNR, hence the contours perpendicular to this axis have not been plotted as they can be determined from (c).

be $\vec{E} = \vec{E}_0 + \sum_i E_{i,nf}$, where $\vec{E}_0$ is the excitation field and $E_{i,nf}$ is the near field response of an individual nanoparticle. These calculations are complicated as the near–field response of each particle is altered by the presence of the others.

The net result of this are well–documented, in the simplest case, the spectral response of two NSs will become increasingly red–shifted as the interparticle distance is reduced and the peak is seen to broaden. The resulting colour change is significant enough that it has been widely exploited as a method of colourimetric biosensing (e.g. see refs [10, 116, 233, 317]). In the case of anisotropic NPs, consideration of the relative orientation of each particle must be given. Figure 1.9(a)&(b) shows FEM simulated extinction crosssections of pairs of AuNRs as a function of interparticle distance. Showing how longitudinal alignment leads to red–shifting of the plasmon and transverse alignment leads to blueshifting (it should be noted that transverse alignment is significantly more energetically preferable) and that the magnitude of this shift is inversely dependent on the interparticle distance.

In order to preserve the optical properties of a colloidal suspension of plasmonic NPs, the stability of the particles must thus be maintained. Hence a great detail of consideration is given to functionalising particles with suitable ligands to prevent aggregation and thus plasmonic coupling. This is particularly problematic in the cases of large clusters of particles where the observed broadening can lead to complete suppression of any observable plasmonic behaviour.

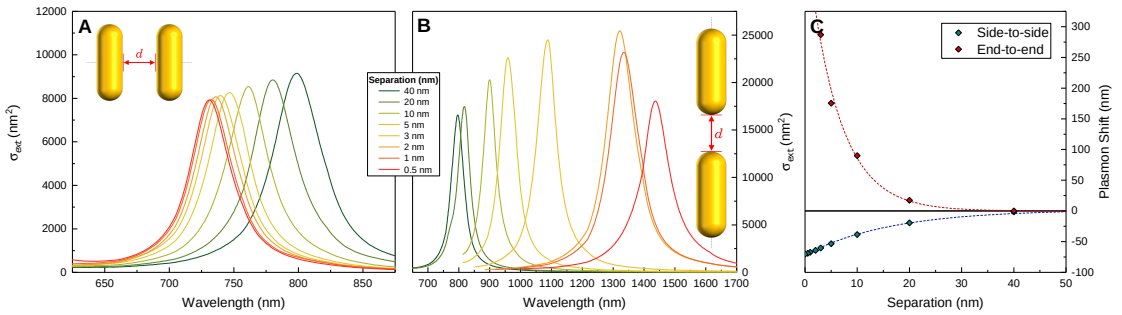

Figure 1.9: FEM simulated extinction cross–sections for pairs of coupled AuNRs organised in **(a)** side-to-side and **(b)** end-to-end configurations at a range of particle separations. **(c)** Plot of the observed plasmon shift in both cases as a function of interparticle distance.

1.3 Photothermal Properties of Gold Nanoparticles

1.3.1 Heat Generation by Gold Nanoparticles

As in any physical system with a resonance condition, some form of damping must be present in the system to prevent catastrophic failure of the system. In this case, the complete disassociation of the electrons from the metallic lattice of the AuNP. Hence damping in plasmonic NPs occurs through electron thermalisation, which can happen through two primary means, photoluminescence or resistive heating. Gold does not have a band gap and hence presents quantum yields $\ll 1\%$, thus thermalisation must occur predominantly through resistive heating of the particle. Thus, to a good approximation all light absorbed by a NP is converted into heat [149]. Resistive heating occurs through electron scattering, primarily electron–phonon (*e–ph*, >85%), but also through electron-electron (*e–e*, <15%). Hence, *e–ph* scattering is the main means by which excited electrons in the AuNP exchange heat with the lattice, this process has a typical timescale of, $\tau_{ph} \sim 1$ ps, and thermal equilibrium between the electrons and lattice will be achieved in 10–50 ps [84]. For excitations longer than these timescales it can be assumed given the high thermal diffusivity of gold ($\alpha_{\mathrm{Au}} = 1.27 \times 10^{-4}$ m$^2 \cdot$ s^{-1}) that the heat distribution through the particle will be uniform. The particle surface and surrounding medium (presumed to be water in this case) will equilibrate over a time scale of several 100 ps though phonon-phonon scattering (*ph–ph*). Typically for CW or pulse widths larger than several nanoseconds these processes effectively happen simultaneously and a steady state of heat flow out of the NP occurs throughout the entire pulse. On the assumption all absorbed light is converted into heat, the power of heat generation by a NP, Q_{abs}, is given by:

$$\begin{aligned} Q_{abs} &= \sigma_{\mathrm{abs}} I \\ &= \sigma_{\mathrm{abs}} c \varepsilon_0 |\vec{E}|^2 \end{aligned} \tag{1.18}$$

where I is the intensity of the incident light field and $\vec{E}$ is the electric field inside the nanoparticle.

In the case of steady-state heating (i.e. for pulses > 1 ns), the temperature distribution around a spherical particle is given by the solution to the classical heat equation with an additional source term, $Q(\vec{r}, t)$:

$$\frac{1}{\alpha} \partial_t T(\vec{r}, t) = \nabla^2 T(\vec{r}, t) + Q(\vec{r}, t) \tag{1.19}$$

where α is thermal diffusivity of the medium. For a particle of effective radius, r_0, under illumination, this

equation has a solution of form:

$$T(r) - T_0 = \begin{cases} \frac{Q_{\text{abs}}}{4\pi\kappa}\frac{1}{r_0} & |\vec{r}| \leq r_0 \\ \frac{Q_{\text{abs}}}{4\pi\kappa}\frac{1}{r_0}\text{erfc}\left(\frac{|\vec{r}|-r_0}{\sqrt{4\alpha t}}\right) & |\vec{r}| > r_0 \end{cases} \tag{1.20}$$

where κ is thermal conductivity of the surrounding medium and $\text{erfc}(x)$ is the complementary error function [256, 388]. This solution has been computed for a AuNR under continuous wave illumination in fig. 1.10. The resulting temperature rise for a single AuNR is <1 mK, at a beam power of 1 W·cm^2. This superficially seems very low, but NPs are very rarely seen in isolation (i.e. the typical NP concentration in a AuNR synthesis is ~10^{11} ml^{-1}), much more substantial temperatures are achieved in colloidal solutions.

Accounting for multiple particles in close proximity makes the heat equation significantly more complex, because heat can now flow between particles, reducing the heat flow out of neighbouring particles, in turn increasing the temperature of the particle and the medium. The heat source term, $Q(\vec{r}, t)$, in the heat equation is replaced by a sum over all particles $\Sigma_i Q_i(\vec{r}, t)$. The accumulative effect of several particles can yield significant increases in temperature [113], this has been calculated theoretically for arrays of AuNSs [288] and demonstrated experimentally though changes in the melt rates of frozen colloids a a function of AuNS concentration [290].

1.3.2 Illumination Modes

The choice of light source used to heat the particles significantly affects the temperatures and mechanism of action on surrounding tissue. With two options being most commonly used in the literature, continuous wave (CW) lasers and nanosecond–pulsed lasers.

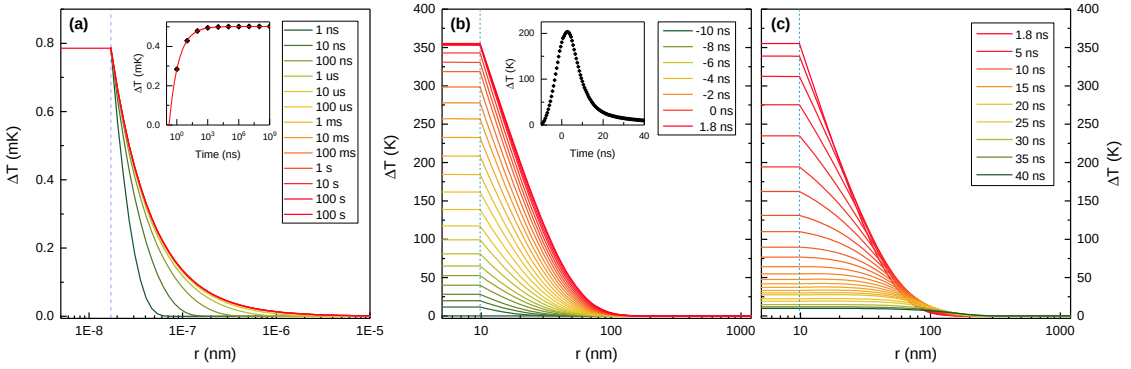

Figure 1.10: (a) Calculated temperature profiles for a single randomly–orientated AuNR under 1 W·cm^{-2} continuous wave illumination at resonance (LSPR = 800 nm) calculated as the solution of the heat diffusion equation. The particle 'radius' (dashed line) is given at the effective spherical radius, 17.1 nm. Inset is the temperature at a point 10 nm from the particle surface, showing a steady state temperature distribution is achieved after ~1 µs. **(b) & (c)** FEM simulated temperature profiles in the lateral plane of a AuNR excited by a single Gaussian nanosecond laser pulse (τ_p = 7 ns, fluence = 13 mJ·cm^{-2}) on resonance (LSPR = 800 nm). Times are given relative to the centre of the pulse (i.e. t = 0 is during the peak intensity of the laser pulse). The curves during the heating of the particle are given in **(b)** and the subsequent cooling is shown in **(c)**. Inset in **(b)** is the temperature of a point 10 nm from the particle surface demonstrating the transient nature of the heating.

Continuous Wave Illumination

Continuous wave sources are commonly used due to them being cheaper than pulsed sources, with suitable high intensity single wavelength diode lasers being available for around 5–6× less than the cheapest suitable nanosecond sources. However these are not useful in all medical applications and typically require greater exposure times or total fluences to achieve suitable levels of cell death. From the calculated thermal profile in fig. 1.10(a), it can be seen that the temperature distribution for a single NP effectively achieves equilibrium heating after ~1 μs. At this point, the thermal gradient has a characteristic length of ~1 μm. Whilst this increase may seem small initially, the mean inter–particle distance for a typical colloidal AuNR solution (~ 10^{11} ml^{-1}) is 0.13 μm[1], hence these thermal gradients overlap. Illumination of a solution with a continuous wave light source should hence be considered a bulk heating effect, with local temperature variations due to plasmonic excitation are typically less than ~1 mK based on these calculations.

Similarly whilst 1 mK superficially seems like a tiny temperature increase, the high number of particles in solution means that cumulatively they can increase the bulk temperature of a solution significantly. For an infinite bulk solution of AuNRs at a concentration of 10^{11} ml^{-1}, under 1 $W{\cdot}cm^{-2}$ illumination, we would expect an increase in the bulk temperature of ~2.4 $°C{\cdot}s^{-1}$, however the finite volume of any solution means that heat losses to the surrounding environment will diminish the rate of localised heating with increasing temperature.[2]. Heating colloidal solutions with continuous wave sources can generate bulk temperature increases of several 10°C over several minutes of illumination.

Nanosecond–Pulsed Illumination

The other laser sources typically used in medical applications of AuNPs are nanosecond pulsed sources. These are normally Nd:YAG laser pumped optical parametric oscillators, which usually offer ~100 mJ pulses, 2 – 20 ns in duration, at repetition rates between 10 and 30 Hz (there is a lot of variability between lasers). These can usually deliver similar laser average powers to continuous wave lasers, but have very small duty cycles (~10^{-5}%). Significant heat diffusion cannot occur over the timescale of a single pulse. Hence such lasers achieve temperatures increases that are restricted in both time and space. Often reaching temperatures that are several times higher than the boiling point of water in a volume highly localised to the excited nanoparticle. The transient temperature increases caused by such lasers are capable of instantaneously denaturing proteins and cavitating nanobubbles in the surrounding medium, providing strong mechanical agitation alongside the extreme heat profiles provided, hence these lasers are generally significantly more effective at inducing cell death than CW lasers at the same average power.

Figure 1.10(b)&(c) show FEM–simulated temperature profiles around an AuNR under a typical Nd:YAG OPO laser pulse. Comparison with the solution for CW heating (fig. 1.10(a)) shows how radically different these heating regimes are. With a maximum temperature increase of ~350°C expected for a 7 ns, 13 $mJ{\cdot}cm^{-2}$ Gaussian pulse. These simulations do not account for phase change of the surrounding medium, and hence the insulating effects steam would have on the particle; it is expected in reality the particle would increase in temperature further than calculated here in the case of nanobubble generation.

[1] Defined by the Wigner–Seitz radius: $\langle r \rangle = (3/(4\pi n))^{1/3}$.

[2] $\partial_t T = Pmc$ where P is the power of heat generation, m is the mass of the heated volume and c is the specific heat capacity

1.3.3 Thermal Reshaping

A major issue faced by nanoparticles when heated in this manner is that of thermal stability. Gold nanoparticles have been observed to thermally reshape under both continuous wave and nanosecond pulsed lasers [121]. This is often erroneously attributed to melting point depression, the reduction in the melting point of nanoparticles with decreasing radius (as expressed by the Gibbs–Thompson equation). This is only really an effect seen for particularly small nanoparticles (i.e. $r \ll 10$ nm) [271], the majority of nanorods in the literature are of a size that would be expected to have melting points very close to bulk Au.

Instead this phenomenon is almost entirely driven by surface migration of atoms at elevated temperatures. [276, 287, 341, 371]. With surface atoms located at high energy, high curvature sites at the tips of AuNRs preferentially moving towards to more energetically preferable sites along the edge of the AuNR. The net result of this for AuNRs is reduction in aspect ratio. The effects can be observed at temperatures as low as 50°C [247], and more rapidly change shape with increasing temperature above this [162]. The threshold for thermal reshaping is sensitive to both surface coating [127, 162] and NP size, with smaller particles being expected to reshape less readily than larger particles [51, 162, 174].

This phenomenon is extremely problematic for applications that are dependent on the optical properties of AuNPs. These properties are shape–dependent and, for instance, any reduction in the aspect ratio of AuNRs will result in a blue–shift of the LSPR peak. Given how spectrally narrow most laser sources are, this will likely result in the absorbance peak no longer overlapping the excitation source, resulting in little, or no, plasmonic activity. Hence, this represents a major concern facing the application of AuNRs as photothermal conversion agents. Hence, an area of active research interest is to find strategies to prevent this, including the use of stabilising surface capping agents such as silica [31, 53, 59, 60, 157, 216, 382], or optimisation of the particle morphology [51, 173].

1.3.4 Photoacoustic Pulse Generation

Another interesting phenomenon that emerges from the intense heating generated by AuNPs under illumination is that of sound generation. This is the result of the photoacoustic effect, first recognised by Alexander Graham Bell in 1880, in which he observed that a selenium disc exposed to a modulated beam of light produced an audible sound at the frequency of modulation [32]. This effects stems from the thermal expansion due to heating driven by optical absorption by the material, resulting in an oscillating thermal expansion at the frequency of modulation. The strength of this effect is thus proportional to the absorbance of the material at particular wavelength and can be used to distinguish between materials [33]. The advent of much more intense light sources in the form of lasers in the 1960s led to the development of photoacoustic spectroscopy enabling detection of parts–per–trillion concentrations of analytes based on their absorbance spectra [295].

In the case of AuNPs, the combination of their extremely large absorbance cross–sections, high photothermal conversion efficiency and very small size means that they are effectively point sources from which acoustic pulses can be generated.

Before consideration of the photoacoustic response of AuNPs, the **stress confinement time** should be discussed, τ_s, which characterises the time for a sound wave to cross the heated region. Any sudden increase in stress which occurs below this timescale, will result in a localised buildup of stress. This will then be

dissipated as acoustic pulse equal in width to τ_s. It is expressed as $\tau_s = l/v_s$, where l is the characteristic length of the heated region and v_s is the speed of sound in a medium. When a nanoparticle is illuminated it will produce heat and the particle and its surroundings will expand linearly with ΔT, with coefficient of proportionality, β, this also creates stress in the material which is dissipated as a pressure wave. If the heating occurs in less than τ_s, localised stress will build up in the heated region. The greater the heating the more severe the stress gradient within the heated region. For pulsed excitations, with $\tau_p \ll \tau_s$, this will be dissipated as a broadband acoustic pulse which will propagate in all directions at velocity, v_s. For such a pulse generated by plasmonic exciting a AuNP, the majority of the signal will be generated in the medium, since heat diffuses out of the particle within ~50 ps [271], and the stress relaxation time for water/biological media will typically be ~ 1 µs; hence the nanoparticles act as the heat source for pulse generation[1].

We will consider heating a distribution of particles throughout a volume. The photoacoustic wave equation dictating the pressure generated by heating of a localised region is [63]:

$$\left(\nabla^2 - \frac{1}{v_s^2}\partial_t^2\right) p(\vec{r}, t) = -\frac{\beta}{C_p}\partial_t Q(\vec{r}, t) \tag{1.21}$$

where $p(\vec{r}, t)$ is the pressure field, and C_p is the specific heat capacity at constant pressure. $Q(\vec{r}, t)$ is the heating function describing the cumulative effect of a spatial distribution of absorbers. For a single AuNR it is given by eq. (1.18), but is normally given as $Q(\vec{r}, t) = \alpha(\vec{r})F(\vec{r})$, for a distribution of absorbers under pulsed illumination (where $\alpha(\vec{r})$ is the absorption distribution and $F(\vec{r})$ is the local laser fluence). The photoacoustic wave equation has a general solution of form:

$$p(\vec{r}, t) = \frac{\beta}{4\pi C_p}\int \frac{1}{\vec{r} - \vec{r}'}\partial_t Q(\vec{r}', t)\Big|_{t=t'-|\vec{r}-\vec{r}'|/v_s} d\vec{r}' \tag{1.22}$$

From this we can take that the maximum pressure will be achieved by minimising $|\vec{r} - \vec{r}'|$, hence reducing displacements due to thermal expansion, by restricting the excitation pulse width to significantly below the stress confinement time. The maximum pressure is linearly proportional to the energy of the pulse, where the peak pressure can be calculated as:

$$p_0 = \Gamma(T)Q(\vec{r}', t) \tag{1.23}$$

$$= \Gamma(T)\alpha(\vec{r})F(\vec{r}) \tag{1.24}$$

where Γ is the Grüneisen parameter. Hence it can be seen that the photoacoustic response of a system is linearly proportional to laser fluence and the absorbance cross-section of the absorber. Combining this with the expressions for σ_{abs} in eq. (1.15), it can be seen for a distribution of AuNRs the photoacoustic response should be linearly proportional to the concentration of Au. Hence the primary means of maximizing the photoacoustic response, is to optimise the monodispersity of the sample to yield the highest possible absorbance at the illumination wavelength.

The twin requirements of high pulse fluence and pulse widths $\ll \tau_s$, have led to led to Nd:YAG pumped OPO lasers becoming particularly popular for this application, offering pulse widths of a few nanoseconds, over a very broad range of wavelengths with extremely high pulse energies of several hundred mJ available.

[1] A pulse is actually generated by the nanoparticle, but is typically < 1% of the total signal.

(peak powers of 0.1–1 MW). There has been work however attempting to use diode lasers as cheaper alternative light sources, they suffer from the key disadvantage of having significantly much lower peak powers/pulse energies[1], but are considerably less costly, being typically 10% the cost of Nd:YAG OPOs, are very compact and offer variable pulse widths and repetition rates. The ability to vary the repetition rate is key since it offers the opportunity to sample acoustic pulses at many times the rate offered by a Nd:YAG pumped OPO (10–30 Hz), allowing significantly better averaging to be performed, increasing the signal–to–noise ratio substantially. These systems have been successfully implemented by Beard's group at UCL for *in vitro* tests [14, 15, 16, 192, 193].

1.4 Applications of Gold Nanoparticles in Cancer Nanomedicine

The optical and thermal properties discussed above have been utilised as agents for both the treatment and imaging of cancer. Discussed here are the relevance of those properties and the some of the most prolific methods utilising them in the literature.

1.4.1 The Near–Infrared Biological Window

The primary interest in AuNRs over other particle morphologies and materials is their strong absorbance peaks which are tunable throughout the near infrared (NIR). They fall into what is known as the first NIR window in biological tissue, a range of wavelengths at which light sees increased penetration into tissue. The first NIR window falls on a wavelength range[2] between 650 and 850 nm, a second window between 950 and 1400 nm has also attracted increasing attention in recent years [323]. As shown in fig. 1.11 between 650 and 900 nm haemoglobin (Hb), oxyhaemoglobin (HbO_2), and water and have their lowest absorbance in the UV-vis-NIR region [376]. At such wavelengths the penetration depths of light at increased from 1 – 1.5 mm at blue/green wavelength to 1–2 cm at 800 nm [344]. Hence AuNPs can be made such that they absorb strongly at wavelengths which can penetrate *in vivo* and can thus be used as *in vivo* photothermal conversion agents in theranostic applications.

1.4.2 Plasmonic Photothermal Therapy

Using NIR–absorbent particles thus offers a potential method to remotely heat localised regions within the body without significant damage to surrounding tissue along the light path. As discussed above, plasmonic nanoparticles irradiated at their resonance wavelength will rapidly heat up, diffusing heat into the surrounding environment. Living cells cannot withstand temperatures beyond a few degrees beyond homeostasis, hence remotely heating them using plasmonic nanoheaters irradiated with NIR light offers a non–invasive, collateral–free and potentially non-toxic route to destroy tumours within the body.

The increasingly severe effects of increasing temperature on human tissue are shown in fig. 1.12. Prolonged exposure to elevated temperatures of around 42–43°C will induce cell necrosis, this is already widely exploited in current hyperthermia treatments [215]. Hence, the temperature range between 42 and 48°C is often referred to as the 'clinically relevant' regime. Above this the thermal damage is severe and

[1] The highest available peak power nanosecond–pulsed diode was 650W/100μJ at the time of writing

[2] Other limits to this range are given in the literature, 850 nm has been given as the upper limit as it is the point at which the detrimental effects of water absorption begin to be see in photoacoustics.

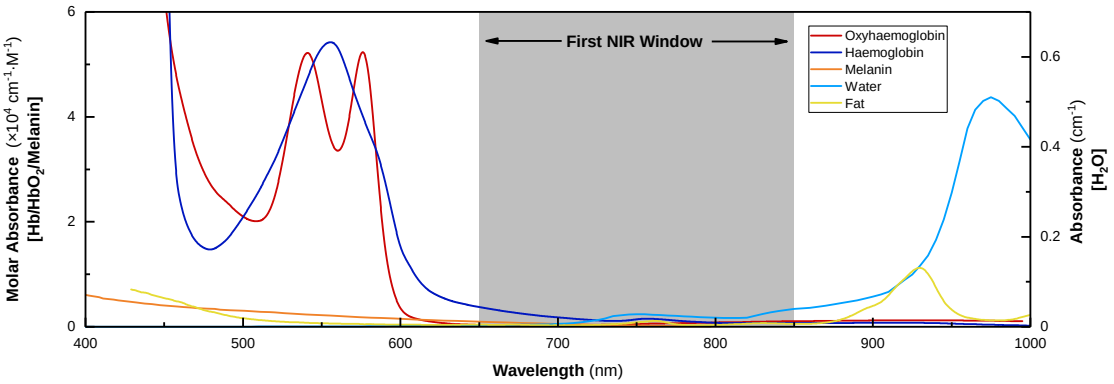

Figure 1.11: Optical absorbance of key *in vivo* chromophores. There is clear reduction in absorbance for all components between 650 and 850 nm known as the first NIR biological window in tissue. Hb/HbO_2 values taken from ref. [340], H_2O values taken from ref. [270], Fat values were taken from ref. [353], and Melanin values were taken from refs. [65] and [305].

instantaneous, prolonged heating at such temperatures is not clinically safe without good control of the local distribution of the heat generation [149, 357].

Hence the use of thermal conversion agents have become a widely investigated method to deliver heat in a highly localised manner, either through tumour–specific targeting or direct intratumoural injection, with AuNPs being identified to as a one potential candidate. Alternatives include organic fluorophores such as indocyanine green [56, 57, 58], which whilst NIR–absorbent, are significantly less efficient at generating heat. Typically fluorophores have an absorption cross section six orders of magnitude smaller than a typical AuNP. They also cannot be targeted to the tumour site efficiently (given the much larger size of targeting ligands) and hence require significantly higher doses of photothermal agent for safe levels of radiation to be maintained due to the reduced heating efficiency and lack of specificity [1].

In looking to optimise the effectiveness of photothermal heat generation an inspection of eq. (1.18), points to the immediate dependence on absorption cross–section, and hence its morphological dependence. Currently AuNRs offer the highest known σ_{abs}–to–volume ratio of all AuNPs[1], typically with σ_{abs} an order of magnitude higher than AuNSs or AuNShs at equivalent volumes of Au per particle, and come with a smaller effective radius [145]. This smaller effective radius increases the allowed high penetration of tissue and small blood vessels and hence improves the efficacy of AuNP accumulation at specific target sites [83], although these suggested benefits are still under investigation.

The first attempts at utilising the photothermal effects of AuNPs to destroy cancer cells came in 2003, when Hirsch *et al* used gold nanoshells (AuNShs) to selectively kill cells *in vitro* upon illumination with NIR light. With the first *in vivo* murine model following in the next year, when O'Neal *et al* used multiple treatments of intravenously injected PEGylated AuNShs followed by illumination with a 850 mW diode laser, to completely destroy tumours containing CT26.WT cells; after 90 days all treated mice were still alive [261]. A number of reports on the use of AuNShs *in vivo* has followed these reports [54, 197, 212, 225, 369]. This has ultimately culminated in the first human trials utilising AuNShs (branded as AuroShell) for photothermal treatment of prostate neoplasms, delivered via intratumoural injection [190].

The first *in vitro* photothermal experiments using AuNRs came later in 2006 [141, 338]. Despite the better theoretical optical properties of nanorods, the synthetic protocols and surface functionalisation strategies

[1] There are some simulations that suggest nanobipyramids might be better, although the improvement is marginal at best

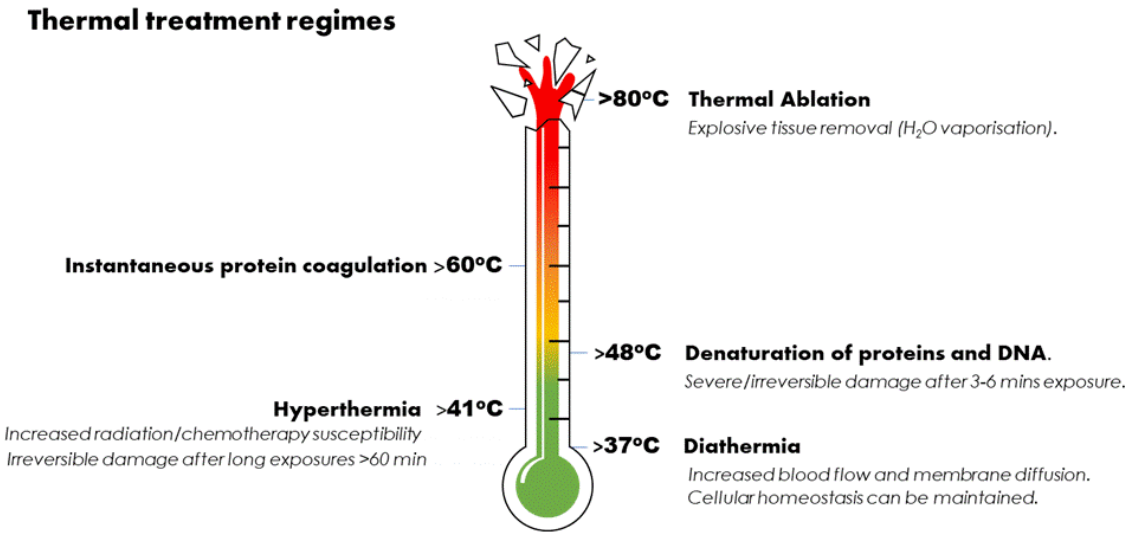

Figure 1.12: The effects of different temperatures on cells within the body. Adapted from: [149].

required to make them in bulk and use them in biological contexts only emerged in the mid–2000s (discussed in section 1.5 and section 1.6). In the first photothermal studies Huang *et al* achieved selective killing of HSC and HOC cells at intensities below 15 W·cm^{-2} using EGFR–targeted AuNRs with a LM of 800 nm [141]. There have been a large number of studies since demonstrating that heat generation from AuNRs can induce death in Human cell lines since (i.e. [11, 138, 251, 380]). AuNRs have also been heavily studied *in vivo*, with most treated mice showing improved mortality (i.e. [111, 203]) or reduced tumour volumes [55, 61, 198] after the combined administration of AuNRs and NIR exposure.

This is not to say that the technique is not without difficulties, a number of issues remain. The largest is that of actually delivering the particles to the tumour site. The easiest solution to this is intratumoural injection, but this cannot always be implemented depending on the location of the tumour. Instead many studies using intravenously administered AuNPs rely on what is known as the enhanced permeability and retention effect (EPR). This is the effect whereby intravenously administered small molecules are be disproportionately taken up by tumours, which would be a panacea for drug delivery researchers. However the EPR effect remains controversial, with open questions about its veracity, having often proved unreliable in murine models [249], and further questions about how translatable any observed EPR effect in murine model is to humans [68, 249]. The other strategy left open is that of targeting, but the results of these strategies in the literature are also fairly inconsistent. A recent review article by Willhelm *et al* found that the average delivery of non–targeted particles to tumour sites was 0.6% of the injected dose (%ID), by comparison particles functionalised with a targeting ligand achieved just 0.7% [379]. There was a large degree of variability in the reviewed papers with both non–targeted and targeted particles having a %ID in the literature of ~10.5%. As it stands there is no intravenous delivery strategy that results in consistent and significant uptake of the injected nanoparticles.

Beyond delivery other issues exist, such as maintaining colloidal stability *in vivo* and preventing intracellular aggregation after endocytosis [2, 314, 406], which can potentially destroy the useful optical properties of AuNPs. Alternatively there are the competing priorities of preventing the immune system too rapidly collecting administered particles whilst simultaneously preventing particles remaining in the

body indefinitely [11]. These are all issues that also affect the next technique to be discussed, photoacoustic imaging.

1.4.3 Photoacoustic Imaging

As discussed above, the photoacoustic effect only really found use in spectroscopy for most of the 20^{th} century [295]. In 1981, Bowen was the first to suggest the potential of photoacoustics in biomedical imaging [38]. The technique was developed during the early to mid 1990s (e.g. [187, 264]) predominantly using NIR–absorbent dyes as the contrast agent.

Using the photoacoustic effect to generate images relies on pulse generation as described in section 1.3.4. Fluorophores heated under a nanosecond pulsed laser will effectively act as a point source for acoustic pulse generation. The generated pulse will travel with a group velocity equal to the speed of sound in the surrounding medium v_s. Hence the position of the pulse can be calculated using time–of–flight measurements from multiple transducers allowing the source to be located in space with a theoretical maximum precision equal to $v_s\tau_p$, where τ_p is the pulse width, for a 1 µs wide pulse the highest resolution achievable is thus ~1 mm. Imaging a complex distribution of pulse sources requires use of specialist time–of–flight imaging algorithms able to convert the complex signals recorded by an array of transducers into a 2D dimensional slice. It is thus possible to map the biodistribution of an administered dose of NIR absorbent–chromophore within an animal due to the increased penetration of light.

It is possible to extend this further using a technique known as multispectral optoacoustic tomography. By choosing a series of wavelengths at the major turning points in the spectra of water, Hb, HbO_2 and the chromophore of choice, it is possible to map the distribution of all four components simultaneously. Deconvolution algorithms can be used to 'spectrally unmix' each pixel of the obtained image. This process is optimised by choosing a chromophore with a large, narrow absorbance peak between 800 and 850 nm, where all other components are at minimum absorbance. Hence AuNRs are well suited to this role, with their tunable absorbance peaks and high photothermal conversion efficiency.

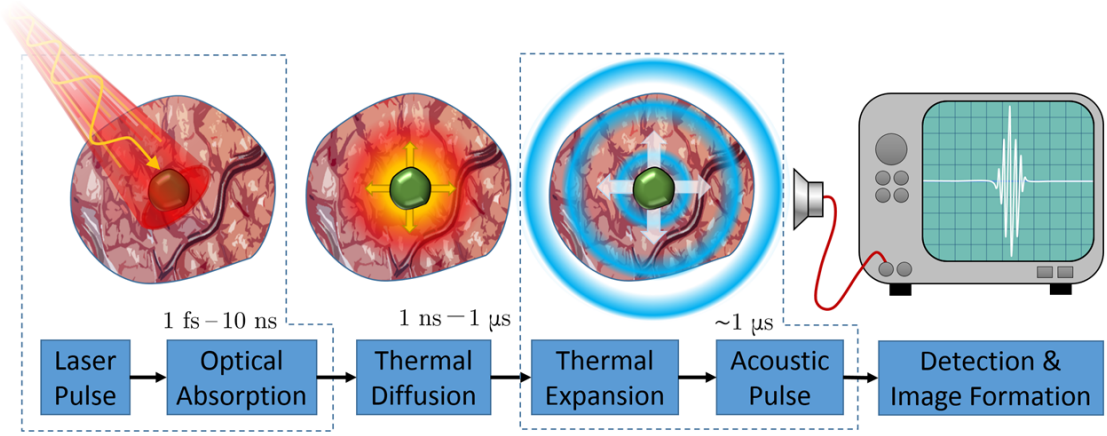

Figure 1.13: Schematic showing the key processes and the involved timescales used in *in–vivo* photoacoustic imaging. An optical pulse < 10 ns illuminates a target leading to heating of the target and the surrounding medium. This leads to localised thermal expansion and ultimately at high enough intensities is dissipated as an acoustic pulse. Such pulses can be located in space through time–of–flight measurements allowing the formation of an image of the target absorber within the medium.

The first studies using AuNPs as photoacoustic contrast agents were in 2001, which demonstrated the efficacy of AuNSs as photoacoustic contrast agents in phantoms [161, 265]. In particular, it was shown that AuNS' ability to cavitate nanobubbles in the surrounding medium significantly increases the amplitude of the generated PA signal. In 2004 the first NIR–absorbent particles were used for PAI, where non–targeted AuNShs were used to image a rat brain *in vivo* [369].

Some early work demonstrated that AuNRs could generate strong PA pulses in biosensing systems, showing their potential for use in photoacoustics [199, 200]. The first *in vivo* use of AuNRs for PAI did not occur until 2007, allowing whole body imaging of a mouse [83]. Since these early studies, there have been a large number of improvements in utilising AuNPs in photoacoustics, including three dimensional mapping [169], and the observation of both passive [284] and targeted [55, 327] uptake of AuNRs into tumours. A wide range of other AuNP morphologies have found application in PA imaging [201], including other NIR–absorbent morphologies such as nanocages [389], nanoprisms [26] and nanotubes [393].

Photoacoustic imaging utilising AuNRs suffers many of the same limitations as photothermal therapies, its efficacy is significantly reduced by any effect that will change the optical properties of the photothermal contrast agent, such as thermal reshaping or aggregation (plasmonic coupling). The lasers required to generate the required pulse intensities are typically Nd:YAG–pumped OPOs, the intense fluence of these lasers has been regularly observed to result in the reshaping of AuNRs (and hence the loss of their optical properties) [121, 127, 162, 337]. This is also a problem faced by photothermal therapy if a nanosecond pulsed laser is used. Hence a number of strategies have been devised to cope with this such as coating the AuNRs in a silica shell which does not so easily thermally reshape [31, 59], or optimising the nanorod morphology to minimise thermal reshaping [51, 174]. In relation to prevention of aggregation, silica coating offer a potential solution to this if made thick enough to prevent plasmonic coupling [62]. Alternatively targeting AuNPs to extracellular sites, in an attempt to prevent endocytotic uptake and ultimately intracellular aggregation [348].

1.4.4 Other Medical Applications of Gold Nanoparticles

PPTT-Assisted Chemotherapy

There are several potential methods to extend to PPTT which could significantly increase its effectiveness, firstly, AuNPs offer a potential delivery vehicle through which to deliver chemotherapeutic drugs to a tumour site. Delivery of these drugs would be hugely beneficial; current chemotherapeutic drugs are very effective at killing cancer cells, but they are also toxic resulting in significant collateral damage to healthy cells and a severe depreciation of the quality of life of patients. A large proportion of these suffer from solubility problems, with around 40% of currently available drugs and 90% of upcoming drugs showing poor water–solubility, preventing delivery to the tumour site [159]. Hence there is now a concerted effort to devise *in vivo* delivery mechanisms to overcome these problems such as targeted AuNPs. These have the potential to allow a significant reduction in required dosage and increased efficacy due to the proximity of drug release to tumour sites. Beyond this chemotherapeutic drugs when used alongside thermal therapy become significantly more effective, due to the increased vascular permeability (encouraging local drug delivery) and increased cellular pore size (allowing large-molecule drug absorption) brought about by localised heating of tissue. For example, Yavus *et al* have developed a drug delivery based on gold nanocages coated in a smart polymer,

which when irradiated in the NIR contracts to allow the release of drug molecules contained inside [392]. *In vitro* tests showed a 40% decline in cell viability after drug release showing the potential effectiveness of this alongside PPTT in ensuring cell death.

Biosensing

The strong optical properties of gold nanoparticles makes them potentially useful as colourimetric biosensors. The proposed methods tend to fall under two schemes of based either on specific binding or induced aggregation in the presence of a molecule of interest. The former are generally simple lateral flow assays in which AuNPs functionalised with an antibody will bind to another antibody–functionalised strip in the presence of an analyte (i.e. ref. [168]). Alternatively, deliberately induced aggregation in the presence of an analyte of interest can be used [10]. If the analyte present several binding sites multiple AuNPs can be bound to it leading to rapid aggregation in the presence of enough analyte. These changes can be easily detected through UV-vis spectroscopy, enabling rapid quantification of the analyte concentration.

The other significant form of biosensing is that of single particle SERS, especially in the case of AuNP dimers, or particle–on–a mirror configurations [158, 322]. Which enable huge enhancement of the Raman signal from single molecules. For example enabling sensitive monitoring of trace levels of hormones such as dopamine in urine and correspondingly allowing dosage of medication to be made directly in response to actual physiological levels of biomarkers.

1.5 Chemical Synthesis of Gold Nanoparticles

The discussion here is limited to the liquid–phase synthesis of gold nanoparticles using chemical reducing agents, a number of other methods exist but are not well suited to the bulk production of nanoparticles for the applications discussed here.

1.5.1 A Brief History of Gold Nanoparticle Synthesis

The earliest reported nanoparticle synthesis in the scientific literature remains that of Faraday in 1857 [87]. In the course of preparing gold films, Faraday inadvertently synthesised a red colloidal suspension through the reduction of $NaAuCl_4$ by white phosphorus. Faraday correctly identified the origin of this colour emerging from the optical properties of suspended particles. However the study of gold colloidal suspensions languished for most of the next century, with only a few notable exceptions, such as the work of Zsigmondy, who created liquid–suspensions of gold nanospheres through the reduction of gold salts by tin chlorides and studied their optical properties through darkfield microscopy [412]. Also the work of Turkevich in 1951, further developed by Frens in the early 1970s [97, 98, 349], which developed the most commonly used method the synthesis of AuNSs currently used today. This was the single step reduction of $HAuCl_4$ by sodium citrate at elevated temperature, leading to the production of relatively monodisperse citrate capped AuNSs 10–20 nm in diameter.

From the late–1980s there was an increased interest in the synthesis of AuNPs, with a number of important synthetic protocols emerging. Including the development of the polyol process in 1989 [89, 90], where by metal salts are reduced in a α–diol such as 1,2-ethanediol (ethylene glycol) at high temperature

(210°C). It is a widely used process due to the relatively facile synthesis and ease–of–scalability, it has also notably been adapted for the synthesis of metal nanowires ([332, 333, 334]). The early 1990s saw the publication of the Brust–Schiffrin method, an important method for the organic phase synthesis of monodisperse alkanethiol–capped AuNPs with diameters less than 10 nm [42]. It was also in this period that the first NIR–absorbent gold nanoparticles were synthesised in the liquid–phase with in the form of gold nanoshells, initially on Au_2S cores in 1994 [409], but rapidly followed by the use of silica cores in 1998 [260].

The earliest liquid–phase syntheses of AuNRs appeared during this period via photochemical [86] and electrochemical [400] methods. Both protocols used a shape directing agent called cetyltrimethylammonium bromide (CTAB) to yield AuNRs in solution. The real surge in interest in the synthesis of AuNRs appeared after the publication by Jana *et al* of a protocol, which seeded the reaction with pre-synthesised AuNPs and used a weak reducing in tandem CTAB to yield AuNRs in solution [148]. This protocol suffered from high polydispersity and poor shape yield, requiring a large number of rounds of shape separation by centrifugation in order to produce AuNRs in high yield. Following this an number of additional improvements were made to the synthesis, through the inclusion of silver nitrate [253] and the optimisation of the reaction pH [12]. More recently trends have focused on the inclusion of aromatic additives, such as salicylate [307, 395], dopamine [209], hydroquinone [355] or resveratrol [367], or through the inclusion of co-surfactants such as BDAC [253] and oleic acid [396]. Other strategies have involved controlling micellular structure through inclusion of Hofmeister salts [269] or the use of alternative surfactants such as dodecylethyldimethylammonium bromide [16, 253, 359] and gemini surfactants [385]. A discussion of the formation processes of AuNRs and the effects of these is given in section 1.5.2 and the following sections.

1.5.2 Control of Colloidal Synthesis

The typical starting point from which to consider the product of any chemical process is that of kinetic and thermodynamic products. Often in a chemical reaction there exist competing pathways to the formation of multiple products, the composition of which are determined by the reaction conditions. Typically these are grouped into either 'thermodynamic' products, that is the product which exists at the global Gibbs free energy minimum, ΔG^0; or 'kinetic' products, which exist at a higher Gibbs free energy, $\Delta G^{0\prime}$, but have a lower energetic barrier, E_a' to formation.

In the archetypal case (fig. 1.14), there exists a higher energetic barrier to the formation of the thermodynamic product, such that $E_a > E_a'$, and hence control over the reaction temperature and reduction potential, allows for direct control of the composition of the resulting populations of the thermodynamic and kinetic products. Under such conditions the lower activation energy of the kinetic product leads to higher rate of product formation, and simultaneously the thermodynamic product forms at a lower rate due to the kinetic barrier to formation. The ratio of the rates of formation, k_x, is determined by the difference in the activation energy, E_a, of the two products and the available thermal energy, given by:

$$\frac{k_C}{k_D} = \exp\left(-\frac{\Delta E_a}{RT}\right) \tag{1.25}$$

However, if this reaction is reversible (i.e. A + B $\rightleftharpoons$ C), the thermodynamic product (A + B $\rightleftharpoons$ D) will form at a lower rate due to its higher activation energy, but simultaneously is more stable than the kinetic

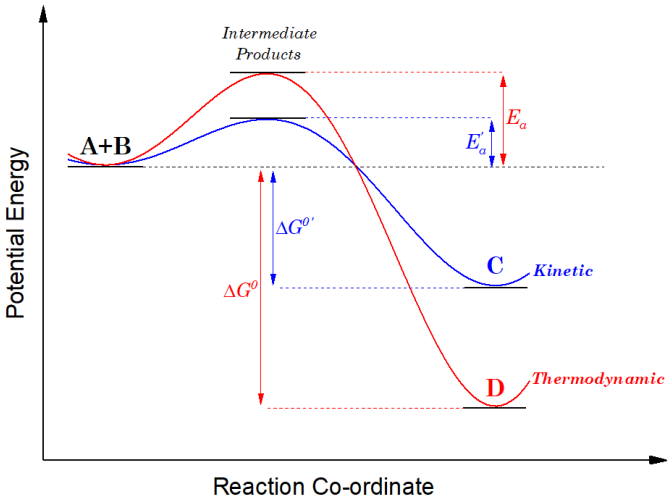

Figure 1.14: Typical representation of the energy profiles involves in kinetic vs. thermodynamic processes. In the example reaction two possible products can emerge as a result of the reaction i.e. A + B $\rightleftharpoons$ C $\vee$ D,. Firstly, the thermodynamic product, D, which has the lowest chemical potential, but there exists a large activation energy, E_a, providing a kinetic barrier to its formation. Alternatively, the kinetic product, C, which has a lower activation energy, E_a', but whose final product, C, sits at a higher potential energy than D. The lower activation energy of C leads to it forming at much faster rate than D. It can be seen for hot reactions, such that $k_BT \gtrsim E_a + \Delta G^{0\prime}$ that the thermodynamic product will dominate, whereas below this the kinetic product will be preferable. It is possible for a product to be both kinetically and thermodynamically preferable.

product as result of its lower Gibbs free energy. Hence if the reaction is allowed to continue for an increasing amount of time we expect to see thermodynamic products make up a increasingly larger fraction of the products. Ultimately reaching a stable ratio of product concentrations, known as the equilibrium ratio, K_{eq}, determined by the difference in Gibbs free energies, and the the available thermal energy, given by:

$$K_{eq} = \exp\left(-\frac{\Delta G^{0\prime} - \Delta G^0}{RT}\right) \tag{1.26}$$

A number of factors can be utilised to control the resultant product from such reactions. For instance, the concentration of kinetic products can maximised, by reducing the reaction temperature to the minimum required for kinetic product formation, restricting the reaction time and controlling the reduction potential. Conversely, long and high temperature reactions will maximise the number of thermodynamic products that are formed.

It is worth noting that it is possible for a single product to be both kinetically and thermodynamically favourable, in which case no control over the reaction can be achieved. Simultaneously if a kinetic product is irreversibly formed (i.e. A + B $\longrightarrow$ C), then no thermodynamic control can be exerted once this product has formed.

Kinetic vs. Thermodynamic Considerations in Nanoparticle Synthesis

These considerations have important implications to the synthesis of AuNPs, however unlike the above system nanosynthesis typically involves the complex interplay of kinetic and thermodynamic processes. Factors ranging from the minimization of surface energy, energies of individual crystal facets (and the respective binding affinities of ligands to them), ligand–ligand packing density, and interactions between the

nanoparticle, ligand and surrounding solvents all must be considered in understanding the formation of a nanocrystal.

Foremost, the thermodynamic shape is usually that which minimises the surface energy, (i.e. that which minimises the surface–to–volume ratio). For a liquid droplet the solution is simple, it is a sphere; but in the case of solids there exist cohesive interactions between atoms, requiring a consideration of both the surface free energy, γ_i, and strain energy [368]. Atoms at the surface with the highest number of neighbors have the lowest surface free energies, hence it follows that specific surface facets are energetically preferable to form and in the case of fcc–metals, $\gamma_{(111)} < \gamma_{(100)} < \gamma_{(110)} < \gamma_{HI}$ (HI = higher index) [370]. These energies can be modified through use of facet–specific capping agents enabling direct morphological control to be achieved. Generally speaking, for such materials, the shapes that predominantly present {111} and {100} facets are typically global thermodynamic structures [220], such solutions are called Wulff constructions. For Au these comprise of monocrystalline icosahedra, octahedra, truncated octahedra, cubes, truncated cubes and cubooctahedra; or penta–twinned decahedra [29]. Hence in general it can be said that anisotropic AuNP morphologies are kinetic products [220], and thus a great degree of thought must be put into controlling the reaction conditions to yield them.

The simplest methods for controlling the growth kinetics of such reactions include temperature and pH, the effect of each on the reduction potential, E_h, of a reaction is readily expressed in the Nernst Equation [244, 245, 246]:

$$E_h = E_0 - \frac{RT}{F}\frac{h}{n}\mathrm{pH} \tag{1.27}$$

where E_0 is the reference potential, R is the universal gas constant, T is temperature, F is the Faraday constant, h is the number of protons transfered, and n is the number of electrons transfered in the reaction. It can be seen that E_h increases linearly with T, and decreases linearly with pH. Under standard reaction conditions (T = 25 °C), RT/F = 59.16 mV; we expect a linear decrease in E_h with pH, with a gradient of -59.16 h/n mV.

More generally when discussing particle synthesis, it is typical to frame it in terms of monomer generation, with the initial barrier to achieving particle formation being that of nucleation itself. This emerges from a consideration of the Gibbs free energy; for a sphere this is given by $\Delta G = 4\pi r^2\sigma - {}^4/_3\pi r^3 G_v$, where G_v is the energy per unit volume and σ is the surface energy per unit area. It can be seen that a critical radius exists at $r^* = 2\sigma/G_v$ below which we expect dissolution of any forming nucleus and above which particle growth is preferable. For many materials this means that supersaturation of monomers in solution must be achieved before large enough nuclei can form that are stable (i.e. for calcite, r^* = 1–3 nm [132]). However, in the case of most metal salts, the critical radius is effectively non-existent at common synthesis temperatures and dissolution of small clusters need not be considered, with even metal dimers remaining stable in solution [241]. Hence formation of most metal nanoparticles can occur stably even at relatively low concentrations of metal salts.

The classic example of a thermodynamically controlled nanoparticle synthesis is that of the Turkevich synthesis [97, 98, 349]. This is the simplest possible case, a two component system containing a metal salt ($HAuCl_4$) and a reducing agent (sodium citrate). The whole reaction is heated close to boiling, run over a long period of time providing enough energy to clear any kinetic barriers to complete reduction of the metal

salt resulting in a homogeneous population of thermodynamic products (in this case amorphous spheres). The main challenge which emerges under these conditions is that continuous nucleation will occur, leading to nuclei forming at different time points, and hence having varied growth times, resulting in a polydisperse population. The entire reaction is thus performed under very rapid stirring to encourage collisions between freshly–formed monomer units and already–formed particles, leading to more homogeneous particle growth. The size of the particle can be controlled between 10 and 150 nm through variation of the Au:citrate ratio, additional of additional surfactants and control of the reaction pH [311].

The alternative is a kinetically controlled nanoparticle synthesis. That is a reaction performed as rapidly as possible to deplete free monomers units in solution, preventing further particle growth. A good example of this is the Creighton method for the preparation of gold seeds [64]. In this system a $HAuCl_4$ solution under vigorous stirring is rapidly reduced by a strong reducing agent in the form of $NaBH_4$. The result of this reaction, if performed properly[1] is to yield very small monocrystalline particles (<4 nm), instead of the more thermodynamically stable penta–twinned morphologies which present only {111} facets. Another example of this is the so-called "hot injection" technique used in quantum dot synthesis, in which one precursor is injected at lower temperature relative to the main reaction vessel, resulting in an initial burst of nucleation followed by a slower growth phase as the temperature drops [274]. The net result of this is to achieve growth directly onto the initially kinetically favoured product.

The final consideration is that of shape–directing capping agents, ligands can be added to a growth system which will bind to specific facets which high affinity. Examples of commonly used capping agents selected for this role include citrate, which preferentially binds to {111} facets or poly(vinyl pyrrolidone) which preferentially binds to {100} [404]. The net result of including either capping agents allows generation of structures that present majority {111} or {100} facets (in the case of Au, decahedra or cubooctahedra respectively). Hence, control over what is considered the kinetic product of a reaction can be tuned through the inclusion of additional additives in the growth solution.

Separation of Nucleation and Growth

As alluded to above, a large number of nanoparticle syntheses require the synthesis of seed particles, that is an initial particle from which to grow the rest of the particle. These are typically prepared under completely different reaction conditions to the final product. Seeding fits under a broader strategy deemed separation of nucleation and growth which applies equally as a description to seeded and so–called 'seedless' synthetic protocols. The discussion here will be limited to gold nanorods, but seed synthesis protocols have much wider use in the synthesis of other particle morphologies such as plates, bipyramids and decahedra.

The synthesis of seeds is typically achieved via the Creighton method, albeit normally assisted by the inclusion either CTAB or citrate. In short a mixture of $HAuCl_4$ and either citrate or CTAB is prepared. The $HAuCl_4$ is then rapidly reduced by $NaBH_4$ under vigorous stirring. In these cases the choice to do these syntheses rapidly is due to the desire to keep particles small and monodisperse, rather than to achieve kinetic or thermodynamic control of the morphology.

CTAB has a high affinity for the {100} facets of Au compared with citrate and will considerably lower their surface potential upon binding, leading to preferential formation of these facets alongside {111} facets

[1] Using just $NaBH_4$ is typically unreliable, and so CTAB is usually adding to stabilise the {100} facets not seen on penta-twinned seeds

and hence produce monocrystalline seed particles. Such particles can be used in the synthesis of particles such as monocrystalline AuNRs and nanoplates. As stated above, the decahedral seed morphology is the thermodynamic product and hence populations of monocrystalline seeds synthesised using CTAB, can be converted to penta–twinned decahedra through thermal annealing post–synthesis [303]

Whereas citrate has higher affinity to {111} facets [272], and particle formation in its presence will lead to morphologies which maximise these facets, in the case of gold this is penta–twinned decahedra. Such particles have five twinned defect planes dividing monocrystalline regions which only present outward {111} facets. Such particles are crucial to the formation of particles such as bipyramids, penta–twinned nanorods and decahedra, all of which present fivefold symmetry.

The synthesis of penta–twinned AuNRs would not be possible if the seeds were produced in the same growth solution the rest of the growth was performed because this second step is done in the presence of CTAB (which has a higher affinity for Au than citrate). Hence separation of nucleation and particle growth is a requirement of such syntheses. By comparison the CTAB–directed seeds can be produced in the same growth solution, this is the basis of the so–called seedless and one–pot recipes. A small volume of $NaBH_4$ is added to the CTAB containing growth solution, to nucleate a limited number of particles relative to the total amount of available gold. Under such a procedure the nucleation and growth are effectively separated, due to the seeds being generated by a different reducing agent to that which drives the growth. It should be noted that seedless protocol tend to generate small nanorods than those grown from seeds.

Inducing Anisotropy – Synthesis of Gold Nanorods

The actual growth process of AuNRs is still not fully understood, but fairly robust models have been established which appear to explain the main observed processes. The actual growth processes of monocrystalline AuNRs and penta–twinned AuNRs are different in the processes that drive anisotropic growth, but share certain common features

Seeds are typically added to a solution containing a growth mixture of $HAuCl_4$, CTAB, and ascorbic acid (AA). Mixing $HAuCl_4$ with CTAB in solution leads to rapid formation of $AuBr_4^-$ through a halide-exchange reaction ($4\,CTAB + AuCl_4^- \longrightarrow CTA{-}AuBr_4 + 4\,Cl^- + 3CTA^+$). $AuBr_4^-$ is more stable than $AuCl_4^-$ and hence less easily reduced which appears to be key to controlling the growth kinetics during the synthesis. $AuBr_4^-$ readily forms a complex with CTA^+ ions in solutions resulting in the mixture becoming a distinct orange colour[1]. Addition of AA, a mild reducing agent, then results the reduction of Au^{3+} to Au^{1+} via the following two–step reaction[2] [164]:

$$(1)\quad CTA{-}AuBr_4^- + C_6H_8O_6 \longrightarrow AuBr_3^- + C_6H_7O_6^- + H^+ + Br^-$$
$$(2)\quad CTA{-}AuBr_3^- + C_6H_7O_6^- \longrightarrow AuBr_2^- + C_6H_6O_6 + H^+ + Br^-$$

This is visible during the course of the reaction due to the disappearance of broad absorbance band at 395 nm, leading the solution to turn from a semi-transparent orange to near completely clear [316]. Under the pH and temperature conditions of a typical growth solution, reduction of $AuCl_2^-$ cannot occur without presence of a surface potential to catalyze the reaction. Hence at this point the reaction is normally initiated by addition

[1] CTA-$AuBr_4^-$ has a characteristic broad absorbance band at 395 nm
[2] Ascorbic acid and dehydroascorbic acid can fulfill the role of reducing agent in either step.

of seed particles (or in the case of seedless syntheses addition of a much stronger reducing agent such as $NaBH_4$ which can nucleate seeds *in situ*).

There is a debate around the specific role that ascorbic acid plays in the synthesis beyond this. Some have suggested that growth of the AuNRs occurs primarily through a autocatalytic disproportionation reaction of form:

$$3\,AuCl_2^- \xrightarrow{Au^0\,surface} AuCl_4^- + 2\,Au^0 + 2\,Cl^-$$

in which the ascorbic acid primarily performs the role as a scavenger, reducing the $AuCl_4^-$ produced from this reaction to $AuCl_2^-$, allowing all ionic Au in solution to be reduced on to the surface of the forming AuNR [82]. However, this does not seem to be the case, if the synthesis is performed in the presence of weaker reducing agents such as salicylic acid [307] or oleic acid [189, 292, 396], without AA, no growth onto the AuNRs is observed. Both of these molecules are capable of reducing Au^{3+} to Au^{1+}, and are hence capable of performing the Au^{3+} scavenging role suggested in the above scheme. Instead the ascorbic acid is suggested to play a direct role in reducing Au^{1+} onto the particle surface in the following autocatalytic reaction:

$$CTA{-}AuBr_2^- + C_6H_8O_6 \xrightarrow{Au^0\,surface} Au^0 + C_6H_7O_6^- + CTA^+ + H^+ + 2\,Br^-$$

Also counter to proposed disproportionation reaction, other studies have suggested that in the presence of CTAB, the reverse comproportionation reaction is actually more preferable (i.e. $Au^{3+} + 2\,Au^0 \longrightarrow 3\,Au^{1+}$) [275, 294]. This process is essentially oxidative etching of the nanoparticle surface, and probably does occur during synthesis, but is largely outpaced by the much faster parallel reduction of Au driven by the large excess of AA in solution [390]. It is possible to use other mild reducing agents to drive this growth (i.e. refs [81, 91]), although AA is by far the most commonly used reducing agent.

Regardless of the exact mechanism, the presence of AA leads to reduction of the $AuBr^-$ in solution onto the surface of a seed particle. In order to achieve anisotropic growth with both penta–twinned seeded AuNRs and monocrystalline seeds, a shape directing agent in the form of CTAB[1] is required (and in the case of monocrystalline seeds the presence of Ag ions) to direct anisotropic growth.

The precise role of CTAB was similarly misunderstood for along time, with a number of the early papers attributing its role to that of a soft template in which nascent AuNRs could form. Hence there was a large emphasis placed on the requirement for the formation of 'needle'– or 'rod'–like micelles (e.g. [148, 238, 254]). It is now widely accepted that the actual growth mechanism occurs through preferential adsorption onto {110} facets located the edge of the AuNRs (and {100 facets in single crystalline AuNRs} [25]. Although this preferential binding on its own is not enough to ensure uniaxial growth. Hydrophobic interactions between surfactant molecules are important too, studies looking at the impact of the hydrocarbon chain length attached to the $N^+[CH_3]_3$ headgroup have found shorter chains ($H_{21}C_{10}$–TAB) only create AuNSs. Whilst longer chains allow the synthesis of rods of increasing aspect ratio up to C_{16} (CTAB), after which the aspect ratio decreased alongside the rod yield decreased[2] [103] .This appears to result from the optimised bilayer packing density providing better suited growth rates on each facet. The counterion is also crucial, replacement with iodide results in binding to the surface becoming too stable inhibiting particle

[1] Alternative shape directing agents to CTAB have been used in the literature, such as dodecylethyldimethylammonium bromide [16], gemini surfactants [385], and hydrogen peroxide [361] (the latter is yet to be replicated in literature and reported very low shape yield). CTAB is by far the most commonly used shape–directing agent in synthesising AuNRs.

[2] This seems to result from the effect decreased solubility of C_{18}TAB rather than and inability to pack on the AuNR surface.

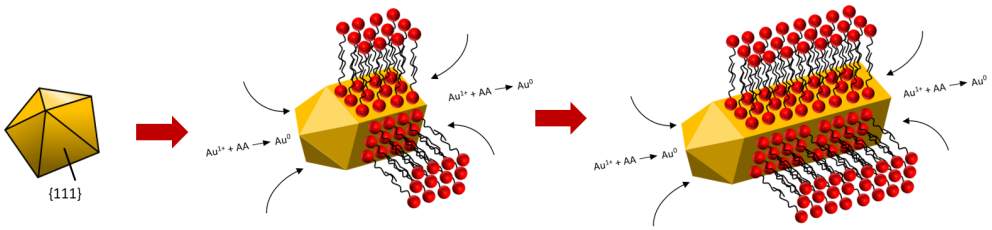

Figure 1.15: Schematic: Formation of penta–twinned AuNRs.

growth, whereas replacement with chloride results in too weaker binding of CTAB to the particle surface [211].

The specific role of CTAB in the synthesis of penta–twinned AuNRs vs. that of monocrystalline AuNRs is worth considering. In the penta–twinned case the initial seed has no {110} facets present hence initial particle growth is required to create {110} facets along the plane of symmetry in the seed. CTAB molecule can then bind to this nascent surface stabilising it and slowing the rate at which Au can be reduced on to it. This process is shown in fig. 1.15, whereby CTAB is able to consistently bind to the forming {110} facets whilst reduction continues at the {111} facets at the tips. CTAB also plays another important role in this process, by supplying bromide ions, which help further encourage uniaxial growth by oxidatively etching the {111} facets. This oxidative etching dually prevents the binding of CTAB at the tips (encouraging uniaxial growth), and offers kinetic inhibition slowing the rate at which Au is deposited at the tips [25, 381]. The resultant AuNRs are thus pentagonal in cross–section and can be hypothetically grown indefinitely to produce very high aspect ratio AuNRs.

By comparison, monocrystalline AuNRs are grown from seeds that are typically cuboctahedral, these present {100} and {111} facets in all directions, meaning there is no preferential direction of growth. Hence additional components must be added to growth solution in order to induce anisotropic growth, in the form of silver ions [362]. This is true for seedless growths also.

The Role of Silver in the Growth of Monocrystalline AuNRs

The advantages of adding silver ions to the growth solution was realised fairly quickly after the 2001 Jana publication [147], although there was little elucidation the role played by silver in the synthesis (i.e. at this point it was still being used in conjunction with citrate–capped seeds). The most commonly excepted model is that $AgNO_3$ is deposited on to the AuNRs through a process known as underpotential deposition (UPD). UPD is an electrochemical technique whereby a monolayer of a metal is deposited on another metal at a redox potential more positive than the Nernst potential [28]. Above this potential a metal will no longer be readily deposited onto itself, but can be deposited on by a metal higher in the reactivity series. The net result of this in this system is that silver will be reduced onto the nanorod surface, but no other metals ions in solution can will be reduced on top of this, hence a silver monolayer forms. Hence the reduction potential must be finely tuned to achieve this, too higher pH and no UPD will occur. UPD is sensitive to the surface free energy of individual facets, and hence the reduction potential can be set such that silver is only deposited on the {110} facets along the sides of the AuNR [362].

The importance of this is twofold, firstly, the deposition of Ag early in the growth appears to be key to providing the initial symmetry breaking. Attempting the synthesis of monocrystalline AuNRs without Ag (in

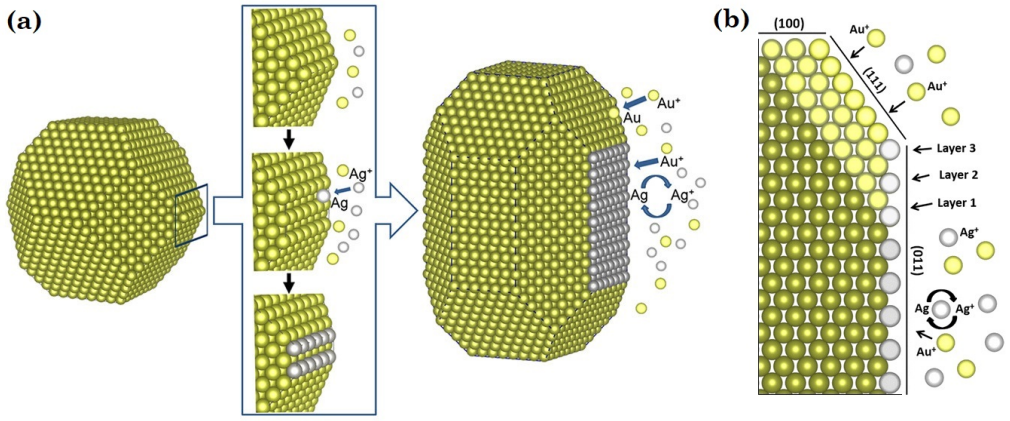

Figure 1.16: Schematic: The role of silver in stabilising a nascent truncating {110} surface during AuNR synthesis and subsequent stabilisation of that surface by UPD. Figure taken from [362].

both seeded and seedless reactions) will result in the formation of no AuNRs. Instead only spherical particles will grow from the seeds. The seeds are effectively isotropic, with no preferential growth direction, as these seeds grow at the start of the reaction {110} truncations will intermittently appear along the intersections of facets, before further reduction of Au destroys them. However in the presence of Ag will disproportionately reduce on to these embryonic {110} surfaces, resulting in them being stabilised. It is speculated that strong internal mechanical forces encourage the formation of 'paired' {110} truncations in a single plane [362]. The growth of these facets then leads to preferential growth along a single axis. This mechanism is shown in fig. 1.16(a).

Secondly, the presence of Ag plays an important role in regulating anisotropic, beyond this initial symmetry breaking role. The epitaxial layer of Ag on the {110} facets serves an important role in slowing Au reduction along the sides of the AuNR. Silver on these surfaces can be redissolved into solution via a galvanic replacement reaction[1], hence the capping is not permanent. Instead what is occurs is a continuous parallel process of UPD and galvanic replacement, the net result of which is that growth in these directions is inhibited, rather than completely prevented. Thus the AuNRs growth in both length and diameter during the synthesis. The mechanism which drives the growth of the {110} facets is shown in fig. 1.16(b), whereby disproportionate growth at the {111} and {100} facets at the tips leads to progressive expansion of the {110} facets along the major axis of the AuNR [362].

Experimental evidence seems to support this model, energy dispersive X–ray spectroscopy suggests that silver is located only on the surface of the AuNR and not in the bulk interior [143]. Attempts at overgrowing monocrystalline AuNRs without the the presence of Ag also results in isotropic growth of the particles ultimately resulting in their conversion to spheres, demonstrating the important role Ag plays in controlling anisotropic growth beyond the initial symmetry breaking [307]. X–ray photoelectron spectroscopy has also been used to demonstrate that alternative explanations for the role of Ag, such as surface passivation by AgBr species is unlikely to be true, as the observed concentrations of Br^- were independent of the [Au]:[Ag] ratio of a given set of AuNRs [405].

It has also been observed that commonly reported problems resulting for iodide impurities in CTAB can be mitigated by increasing the concentration of Ag ions during the growth [152]

[1] Probably via $Ag + AuCl_2^- \longrightarrow AgCl + Au + Cl^-$, rather than $3\,Ag + AuCl_4^- \longrightarrow AgCl_3 + Au + Cl^-$, due to the large excess of reducing agent present.

Other Additives

The roles of additional additives in monocrystalline AuNR syntheses is still not fully understood, but seems to stem from manipulating the packing density of CTAB monomers on the surface of the forming AuNR. The most obvious example of this is the inclusion of oleate in the synthesis, a negatively charged surfactant that will intercalate into the bilayer, adding additional screening between CTAB headgroups and encouraging higher packing on the AuNR surface [396]. The inclusion of aromatic additives seems to similarly result in intercalation into the bilayer, and providing a similar screening effect [395]. The same dynamics have been demonstrated by varying the concentrations of Hofmeister salts in the growth solution which will similarly provide screening of the positively–charged CTAB headgroups enabling tight packing of the CTAB monomers [269]. This higher packing density will help lower the access of Au ions to AuNR surface along the sides of the AuNRs slowing lateral growth, encouraging the formation of anisotropic particles and hence resulting higher shape yields. These additives also result in higher monodispersity in the synthesised AuNRs which probably results from the impact of the effect of increased surfactant packing on the growth kinetics.

1.6 Surface Functionalisation of Gold Nanorods

The surface coating of AuNPs are highly important to their applications, as they imbue particles with a wide range of properties such as hydro–phobicity/–philicity, surface charge, steric stability, specific targeting and biocompatibility. Hence an active area of research is the development of novel surface coatings with which to prepare AuNPs for the wide variety of applications in which they are now used. This section will focus primarily on the functionalisation of AuNRs, but the majority of techniques can be more widely applied to all AuNPs.

Thiol Displacement

These are a general strategy by which any simple thiol containing molecule can be bound onto the surface of a particle. Thiols have a particularly high affinity for binding with the noble metals, as such in theory can easily displace more weakly bound molecules such as CTAB. Typically the molecules used for this are alkanethiols [48] or PEG–thiols [310, 407], these can be decorated by large number of functional groups to provide additional desired properties. The efficiency of ligand transfer is can be very low in some of these protocols, and hence additional strategies have been developed recently to optimise this exchange [310].

Passivation

These are a set of protocols grouped together because they do not actually remove CTAB from the surface of the AuNRs. Instead they passivate the CTAB bilayer by coating it with a layer of silica or organic materials which prevents release of free CTAB from the particle surface.

The first of these is silica coating. A layer of silica can be grown directly on the CTAB bilayer coating the AuNR surface [112]. This has been shown to be an effective strategy for increasing the biocompatibility of CTAB–capped AuNRs [140]. It also has a number of other advantages in that it can prevent thermal reshaping [31, 53, 59, 60, 157, 216, 382] and plasmonic coupling [62].

Other passivation strategies include coating the CTAB layer with polymers. This is normally achieved based on simple charge interactions with a negatively charged polymer, which will readily bind to the positively charged AuNR surface. Popular materials for this include poly(styrene sulphonate) [109, 196] and poly(acrylic acid) [129, 130]. Such protocols can easily allow thick coatings to be created through building up multiple alternating layers of negatively and positively charged polymers [109].

Both the polymeric and silica coating strategies offer the opportunity for drug–loading enabling the inclusion of small molecules in the passivating layer, for slow or thermally–triggered released [109, 328].

Direct Exchange

Because of the manner in which CTAB actively exchanges with with molecules in solution, it is possible to directly exchange the CTAB bilayer with other molecules if a sufficiently large excess is placed in the bulk solution. Hence CTAB–coated particles can be resuspended in a strong solution of the desired molecule and additional agitation provided to encourage exchange (by heating or sonicating). These techniques have been reported for a number of molecules including phospholipids [222, 266, 304, 339, 398], oleic acid [204, 364] and bovine serum albumin [342]

Conjugation of Targeting Ligands

Finally, in a wide number of applications additional functionalisation with targeting ligands (or other molecules, such as fluorophores) is desirable, hence conjugation of these molecules to the surface is desirable. A wide number of routes to conjugate such molecules to surface ligands are available such as 'click chemistry' [37, 40], NHS–EDC linker chemistry [30, 286], biotin – streptavidin coupling [277] and thiol – maleimide coupling [365].

1.7 Gold Nanoparticles and Biology

1.7.1 *In Vitro* Toxicology

Nanotoxicology, study of the toxic effects of nanoparticles, has grown substantially in the last 20 years with from 1,100 publications in 1998 to over 75,000 last year. A large amount of concern has been expressed about the potential toxic effects of nanomaterials. These are not limited to manufactured nanoparticles, but include the wide array of nanoparticles generated as a result of combustion and industrial processes as well naturally occurring particles from events such as volcanic eruptions. Here we discuss very briefly the current questions surrounding the human toxicology of AuNPs, with specific emphasis on AuNRs.

A lot of the results in the literature are contradictory, as is attested by a recent major review by Krug which laments the current state of nanotoxicology [186]. In particular the problems arising from the large number of studies that are now being contributed by non–toxicologists, highlighting the large number of studies that lack careful analysis of the dose–response relationship of nanoparticles without identifying a safe, intermediate or lethal dose of nanoparticles. A number of studies reporting toxic effects were based on exposure of cells to very high *in vitro* concentrations of AuNPs unrepresentative of the exposures expected during actual treatments [186]. Hence an important aspect of taking this research forward in a sensible direction will that of collaboration between material scientists and biomedical researchers.

In a similar vein, the toxicological properties of gold nanoparticles remain improperly understood, as the large number of inconclusive reviews can attest (e.g. [47, 96, 166]). Whilst gold in bulk remains one of the least reactive elements, when reduced to the nanoscale this can no longer be taken for granted. The high surface area of AuNPs makes them significantly more reactive than the bulk state and their plasmonic activity makes it possible catalyse chemical reactions. Toxicology studies on AuNPs present a particular problem due to significant range of sizes, morphologies, and surface functionalisations which have to be considered, making broad general statements about to toxicity of AuNPs difficult to conclusively argue. In the case of 'bare' AuNPs (i.e. citrate–capped), the primary concern is largely that of oxidative stress, resulting from the generation of reactive oxygen species at the surface of the particle [185, 218]. This is an inherent property of all AuNPs and means they will always present a low level toxicity, although this is a relatively minor effect with citrate–capped AuNRs presenting an $IC_{50} > 150$ $\mu g \cdot ml^{-1}$ [356]. However different surface coatings and morphologies radically change this how AuNPs will interact with biological systems.

In the case of AuNRs the most commonly used methods for synthesis require the use of CTAB. This is extremely problematic, CTAB is highly cytotoxic, presenting an IC_{50} of ~ 4 μM [232, 296], whereas the typical background concentrations of CTAB required to maintain colloidal stability are typically >100 μM [13, 296]. Hence CTAB coated particles are completely unsuited for use in biological application. Free CTAB is a positively charged surfactant and will disrupt cellular membranes and simultaneously quench the enzyme ATPsynthase preventing metabolisation of energy by cells [309]. Hence, there is a large amount of work seeking to detoxify CTAB–capped AuNPs, such as AuNRs, by replacing or passivating CTAB on the surface of such NPs. These strategies are discussed in section 1.6, but generally speaking the most common strategies are PEGylation and silica–coating resulting in IC_{50} values around or higher than that seen for citrate capped particles [134, 297] with charged polyelectrolyte coated AuNRs showing IC_{50} values around ~ 150 $\mu g \cdot ml^{-1}$ [196], although these numbers vary considerably in the literature and are cell–line dependent. These IC_{50} values are well above the local concentrations likely to achievable *in vivo* when administered intravenously, and inform the suitable dose for *in vivo* experiments.

1.7.2 *In Vivo* Toxicology

The fate of nanoparticles after *in vivo* administration is also an open question. The broad mechanisms by which particles are cleared are relatively well understood, smaller particles (< 5 nm) are at least partially captured by the kidneys and disposed via the urinary tract [73]. However this clearance is not based only simplistic size filtration, and is charge dependent, preferentially allowing the passage of positively–charged particles [41]. Larger particles are typically collected by the mononuclear phagocyte system (MPS), and then accumulate in the liver and spleen, before being eliminated via the digestive tract. Accumulation in the liver is the most commonly observed result in the administration of nanoparticles [352]

The rate at which the MPS can collect particles is highly dependent on the surface charge, with charged particles being collected and more rapidly delivered to the liver [352]. This has been attributed to increased interaction between the particle surface and charged biomolecules in the blood identifying these cells to macrophages for clearance. This rate seems to also be size–dependent, where larger particles are much more rapidly collected by the MPS than smaller ones [326].

The clearance of particles from the liver to the digestive tract is also problematic. With a number of papers reporting very slow clearance from the liver for a variety of surface functionalisations, with typically <20% reduction in Au concentration of the liver for citrate (6 months later [300]), silica (3 days [363]) and PEG (3 months) [282] and 15 months [11]) capped AuNRs [5]. This persistence in the liver could be very problematic, since the long term impact of these on organ function remains unclear, with potential side–effects including drug– or nanoparticle–related toxicity [352].

PEGylation is the most commonly strategy to increase blood circulation time. PEGylated particles display low surface charge and non-specific binding and are hence are much more slowly uptaken by the MPS [251]. Once cleared to the liver or spleen, the particles tend to accumulate there, only very slowly clearing thereafter, with particles still being detectable months after administration. Although the benefits of this increased blood circulation are open to question, with some papers suggesting that there is very little evidence to demonstrate increased blood circulation time necessarily leads to with increased tumour uptake [352].

1.7.3 Interactions of Particles with Physiological Media – Formation of Protein Corona

Nanoparticles in media containing charged biomolecules, such as proteins, peptides and lipids, will rapidly undergo the formation of what are known as protein corona. That is non–specific binding of such molecules to the particle surface, which radically alters the surface functionalisation of such particles. The nature of the formed corona is dependent not only particle properties such as size, curvature, surface charge and functionalisation, but also on factors such as exposure time (corona biomolecule populations change dynamically) and temperature [78]. These have been observed for a wide range of surface functionalisations [13, 313], and seem to be largely unavoidable, with even PEGylated particles so far showing the formation of coronae [352]. Zwitterionic coatings have, to a limited extent, been shown to display some resistance to non–specific binding [126].

These are potentially a major problem, as the unknown surface chemistry of these corona make prediction of NP behaviour difficult to predict. It also has the potential to completely undermine targeting strategies, given that corona can often be as much as 100 nm thick [178], obscuring any small surface bound targeting ligand. Hence there is a need for an understanding of the nature of such corona, the effects it has on NP interactions *in vivo* and *in vitro* and potential methods for mitigating the effects of them or utilising them as part of a therapeutic strategy. There are a large number of studies attempting to characterise and understand the nature of corona on nanoparticles using techniques such as differential centrifugal sedimentation [69, 70], isothermal titration calorimetry [24], liquid chromatography – mass spectroscopy [343], as well as molecular spectroscopy techniques (i.e. FTIR, Raman or NMR).

1.7.4 Uptake of Nanoparticles by Cells

Humans have been exposed to naturally occurring nanomaterials throughout their evolutionary history and as such have evolved defenses to deal with the potential negative health consequences. This is as true at a cellular level, as it is at the level of the whole organism. Cells interact with NPs primarily through endocytosis, a process in which foreign material is brought into the interior of cell contained within a

vesicle [181]. The rate at which this occurs is dependent on both the cell type and the characteristics of the nanoparticle itself (i.e. size, shape, surface charge, protein corona...) [4, 408]. Charged particles are typically endocytosised at a higher rate than non–charged particles, due charge interactions between the phospholipid headgroups in cellular membrane and the particle surface [243]. Particle size also plays an important role with smaller NPs (<50 nm) being taken up by cells much more rapidly than larger ones [188].

Endocytosis is a potential problem when using plasmonic NPs, as multiple particles are typically enclosed in each endosome. The small volume combined with the a relatively high concentration of NPs makes aggregation inevitable. In the case of plasmonic AuNPs this means that plasmonic coupling will occur and the desired optical properties will be lost, this is a widely recognized problem [8, 115, 280]. Some solutions have been demonstrated such as thick silica–coating which prevents coupling between particles, even during aggregation [62] or the functionalisation of particles with cell penetrating peptides which avoid endocytotic uptake [242].

Chapter 2

Methods and Materials

2.1 Synthesis of AuNRs

All glassware used in the synthesis were cleaned by sonication in a 10% Decon90 solution for 10 minutes, followed by through rinsing using Milli-Q water and further sonication in Milli-Q. The glassware was then by soaking in freshly prepared *aqua regia* for 30 minutes. *Aqua regia* is a 1:3 mixture of concentrated HNO_3 and HCl, a mixture of a strong oxidiser and source of Cl^- ions which will readily dissolve gold, removing any potential nucleation sites for the reduction of gold during the synthesis reaction. All glassware was then throughly rinsed with Milli-Q water and dried overnight in an oven at 70°C. All glassware was cooled to room temperature before use.

Small Batch Syntheses

To prepare 10 mL of AuNR colloidal solution the following steps were performed. Solutions of CTAB and NaOL (200 mM) were prepared in advance of the synthesis and heated to 70°C until all solute was dissolved. These were then added in the desired ratio and topped up to 5 mL with Milli–Q (total surfactant concentration between 20 mM and 180 mM). This was followed by adding sequentially 5 mL $HAuCl_4$ (1 mM), 240 μL $AgNO_3$ (4 mM), 50 μL HCl (11.8 M), and 75 μL ascorbic acid (85.8 mM). To this 7.5 μL freshly prepared, ice–cold $NaBH_4$ (10 mM) was rapidly injected into the mixture. The mixture was then kept at 30°C for 4 hours. The AuNRs were then isolated by centrifugation at 9000 *g* for 30 minutes. The supernatant was discarded and the precipitate resuspended in Milli–Q. AuNR solutions were stored in the dark at room temperature.

Large Batch Syntheses

For the production of larger batch sizes of ~0.5 L, some modification to this recipe is required. The initial CTAB–NaOL surfactant mix was prepared by heating 250 ml Milli–Q water to 70°C in a water bath, under constant stirring. The desired quantity of powdered CTAB and NaOL were then added directly to the heated water and stirred until completely dissolved. The stirred solution was then cooled to 30°C. 250 ml $HAuCl_4$ (1 mM), 12 ml $AgNO_3$ (4 mM), 2.5 ml HCl (11.8 M), 3.75 ml ascorbic acid (85.8 mM) were added in sequence under constant stirring, the mixture was allowed to stir for ~5 minutes between addition of each solution. Finally, the stirring of the solution was increased to 1200 rpm and 0.375 ml ice–cold freshly–prepared

$NaBH_4$ (10 mM) was rapidly injected. Stirring was immediately ceased and the solution kept at 30°C for 4 hours. The resulting AuNRs were cleaned by centrifugation at 9000*g* for 30 min as above.

2.2 Surface Modification of AuNRs

2.2.1 Preparation of PSS–Functionalised AuNRs

1 ml of as–synthesised 75 μg·mL^{-1} AuNR solution was washed twice by centrifugation and was then placed under magnetic stirring. To this was added dropwise a solution containing 10 mg·mL^{-1} PSS and 5 mM NaCl. The mixture was left stirring for 24 hours, followed by cleaning by centrifugation (9000*g*, 30 min) and the pellet was redispersed in a 1 mg·mL^{-1} PSS solution. This cleaning process was repeated twice more, before redispersal in Milli–Q grade water. This process was scaled up as required.

2.2.2 Preparation of Phospholipid SUV Solutions

Upon receipt from Avanti and Lipoid, phospholipids were dissolved in a 2:1 chloroform–methanol mixture by volume to a known concentration of 10–20 mg·mL^{-1} using the method originally described by Folch *et al.* [92]. Stock lipid–solvent solutions were stored at -20°C. In order to prepare SUV solutions, the solvent was evaporated using a rotary evaporator (40 mbar, 100 rpm and 30°C), until the lipids formed a visible film on the inside surface of the flask and no solvent was apparent. Residual solvent was removed by dessicating the lipid film overnight. The films were then hydrated using to a desired concentration and then bath–sonicated for a further 24–hours in a refridgerated sonicating bath. The peak size of the vesicles were then measured using a Malvern Zetasizer Nano ZSP and used if the size peak of the vesicles was $\lesssim$ 50 nm.

2.2.3 Preparation of Phospholipid–Functionalised AuNRs

1 mL of as–synthesised 75 μg·mL^{-1} AuNR solution was washed twice by centrifugation and was resuspended in 300 μl 10 mg·mL^{-1} phospholipid SUV solution. The mixture was placed in a refrigerated sonicating bath for 24 hours. The AuNRs were cleaned by centrifugation (2000*g*, 15 min) and redispersal in 300 μL 10 mg·mL^{-1} phospholipid SUV solution. This process was repeated threefold (i.e three rounds of redispersal, sonication, centrifugation, and removal of the supernatant). After the third round, the pellet was redispersed in Milli–Q grade water. To reduce the background concentration of free lipid the AuNRs were cleaned further by centrifugation. This process was scaled up as required.

2.2.4 Conjugation of Targetting Affimer

A portion of the lipids can be replaced with DSPE-mPEG-Maleimide enabling conjugation of thiolated molecules to the surface. For the purposes of targetting our AuNRs, a CEA–specific affimer was selected. After preparation of the phospholipid–functionalised particles (with for instance 5% mol. DSPE-mPEG-Mal). A solution containing 23 mM TCEP, 0.2 M MOPS and 1 mM EDTA (pH 8.2) was prepared and added to a stock of the affirmer (55 μM) at a ratio of 1:2 TCEP solution to adhiron suspension (210× molar excess of TCEP). The solution was kept at room temperature for 90 minutes. AuNRs were centrifuged at 3000*g* for

10 minutes, the supernatant discarded and the pellet resuspended in the prepared affimer–TCEP mixture, such there was a 3.3× molar excess of adhiron per maleimide site. The number of maleimide sites availible was calculated based on assuming that each lipid headgroup occupied a 1 nm^2 space on the surface on the AuNR and the molar composition of lipids on the surface was the same as that in the SUV solution. Post–conjugation particles were cleaned by centrifugation and sterile–filtered.

2.3 Characterisation

Lower manification TEM images were obtained using a Tecnai G2 Spirit TWIN/BioTWIN with an acceleration voltage of 120 kV. A field emission gun TEM microscope (Philips CM200 FEGTEM; 200kV) equipped with a Gatan GIF200 imaging filter running Digital-Micrograph software was used to take higher magnification TEM images and selected area of diffraction. TEM samples were prepared by drying ~5 µL of 10× concentrated nanoparticle dispersion (in Milli–Q) on an amorphous carbon–coated 400–mesh copper grid (Electron Microscopy Services, CF400–Cu). Sizes of AuNRs were measured manually using ImageJ.

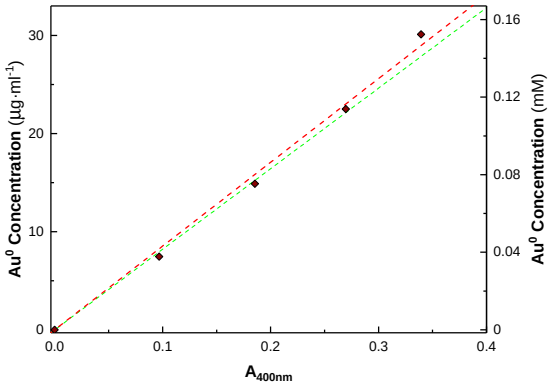

Figure 2.1: Measured Au^0 concentrations as a function of A_{400nm}. The red line is a linear fit, whereas the green line is the published value of ~0.416 mM.

Concentrations were determined by using either a Varian 240fs atomic absorbance spectrometer (AAS) or from by measurements of the absorbance of AuNP solutions at 400 nm. The latter method was prefered, due to the increased convenience, and seems to provide similar levels of accuracy to AAS itself. It relies on using the change in absorbance in the section of the AuNP spectrum dominated by interband transitions (see section 1.2.2), rather than the higher wavelengths dominated by plasmonics which are sensitive to other factors other than cocentration, such as polydispersity. This technique is only viable for small particles, around or below the skin depth, where absorbance is the still the dominant optical effect. In fig. 2.1 a comparison of A_{400nm} and the AAS determined C[Au^0] values is shown, demonstrating the strong linear correlation between the two measurements for a set of four samples. The measured gradient is in close agreement with the values published in the literature [167, 308, 315]. This was used in conjunction with the TEM determined geometries to ascertain the particle concentrations in solution.

UV–vis spectroscopy

UV–vis spectra were taken with a Agilent Cary 5000 UV–vis-NIR using quartz crystal cuvettes (path length = 1 cm). Samples were typically diluted by a factor of 10 before spectra acquisition. Where spectra are

presented unnormalised, they have been multiplied through by the dilution factor to account for this spectra are multiplied through by a factor of 10 to account for this (in accordance with the Beer–Lambert law).

For kinetic spectra, AuNR growth solutions were prepared in a 20 mL vial, after addition of the $NaBH_4$, the solution was mixed quickly and 700 µl was pipetted into a cuvette and spectra capture immediately started. During the first 5 hours of a synthesis kinetic spectra were taken at 2 minute intervals at the 1800 nm·min^{-1}, this was then followed by 10 minute intervals at 900 nm·min^{-1} for the following 24 hours. Solutions were heated to 30°C throughout. Samples monitored during the kinetic spectra were undiluted, instead a quartz cuvette with a path length of 0.1 cm was used in order to prevent the LSPR peak exceeding the detection threshold of the instrument. Spectra from these measurements are multiplied through by a factor of 10 in order to retrieve the true extinction value (again in accordance with the Beer–Lambert law).

2.4 Optical Microscopy

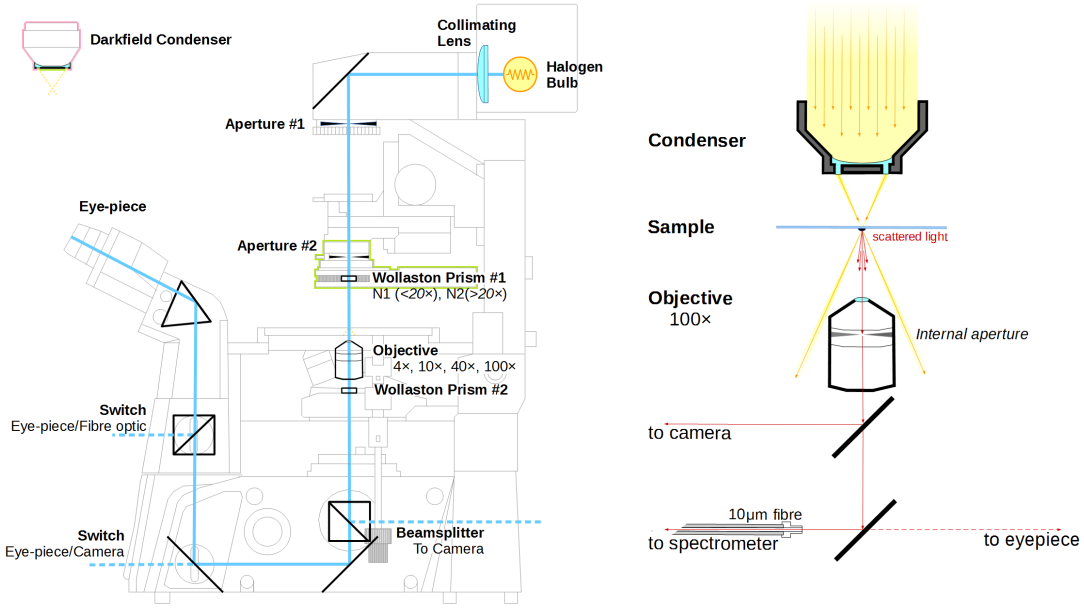

Figure 2.2: Left: Simplified diagram of key optical components in the DIC–darkfield microscope. The assembly shown above is for use as a DIC microscope. The condenser turret assembly (highlighted in green) containing aperture #2 and Wollaston prism #1 can be replaced with a darkfield condenser (highlighted in pink) to allow the system to be used as a darkfield microscope. **Right:** Diagram demonstrating the principle behind transmission darkfield microscopy. Collimated light travels through a condenser lens and with a central patch stop, creating a hollow cone of illumination which is focussed onto the sample. Directly scattered light is collected by the objective. For high numerical aperture objectives, an internal iris is used to further eliminate indirectly scattered light. The image then directed to a digital camera, and the eye–piece or a ⊘10 µm multimode optical fibre centred on the image. This fibre carries scattered light to a high sensitivity spectrometer allowing measurement of the scattered light spectrum from a sample.

2.4.1 Darkfield Microscopy and Single Particle Spectroscopy

Darkfield microscopy images only the light scattered by the sample to produce an image. It is particularly useful for imaging plasmonic metal nanostructures due to their high scattering cross sections. The first use of such techniques to image plasmonic nanoparticles was by Zsigmondy *et al.* in 1902 [321], who pioneered the development of optical darkfield techniques in the study of colloids [402, 403]. The core components of

such systems include a collimiated bright light source with a broad emission spectrum, which is focused through a darkfield condenser (consisting of a condensing lens and annulus shaped aperture) onto the sample. This produces an inverted hollow cone with the sample at the apex. The angle of incidence of this cone is such that only light scattered by the sample is collected by the objective, whilst transmitted light is discarded. For higher numerical aperture objectives, some of this light may also be collected and an internal iris must be used to shutter it from reaching the camera/eye–piece.

Individual scatter spectra can be collected by using a fibre optic to sample the emitted light across a circular spot. The fibre will a combined spectrum resulting from the background and any particles within this region. We can thus express the measured spectrum from the sampled area as:

$$I_{meas}(\lambda) = I_{bulb}(\lambda) \cdot \left[S_{NP}(\lambda) + S_{bkgd}(\lambda)\right] \tag{2.1}$$

where $I_{meas}(\lambda)$, and $I_{bulb}(\lambda)$ are the measured and illumination spectra, and $S_{NP}(\lambda)$, and $S_{bkgd}(\lambda)$ are the scattering functions of the nanoparticle and surrounding substrate. The angular dependence of the scattering functions are ignored, as the numerical aperture of the condenser is fixed at ~0.875, resulting in a angle of incidence of 61°. This fortunately means the unpolarised light focussed on the sample closely excites the LSPR and TSPR of particles roughly correct proportions for a random orientation in space. Hence from eq. (2.1), measured signals must be corrected by dividing through by the normalised spectrum of the illumination source and then subtracting the corrected background spectrum. The background spectrum is taken to be equal that of a region of the substrate free from particles.

Experimental Set–up

Darkfield microscopy images were taken on a Nikon Ti–S microscope using a TI–DF dry darkfield condenser and a CFI Plan Fluor 100× oil–coupled objective. Images were captured using an Olympus UC90 camera and spectra collected via Ocean Optics QE–Pro fibre–coupled to the microscope with a 1000 μm fibre optic (Ocean Optics, QP1000–2–VIS–BX). The fibre optic collected light from a 10 μm spot. In order to obtain a scatter spectrum, background spectra were collected from regions without particles. A particle was then moved into the central focus and a spectrum collected. The background spectrum was then subtracted from this and then divided through by the normalized illumination spectrum, to correct for the non–uniform power spectrum density of the bulb. Particles with a LSPR outside of the human visual spectrum (>750 nm) were beyond the spectral range of the camera. The following steps during sample preparation were found to minimize background scatter during spectra collection. Samples were prepared on (24 × 50) mm coverslips (Menzel Gläser, CS2450100). To minimize background scatter these cleaned by washing sequentially in 10% Decon90 solution, acetone, isopropanol and finally Milli–Q water. These were then placed in piranha solution heated to 80°C for 30 minutes, rinsed using Milli–Q water and then stored under ethanol until use. After drying, the coverslip was placed in a spin–coater and 100 μl of AuNR solution diluted to ~5 fM was placed onto the centre of it. The coverslip was spun at 1000 rpm for 1 minute ensuring all particles which adhered to the surface were well separated during imaging and spectra collection.

2.5 Measurements of Colloidal Stability

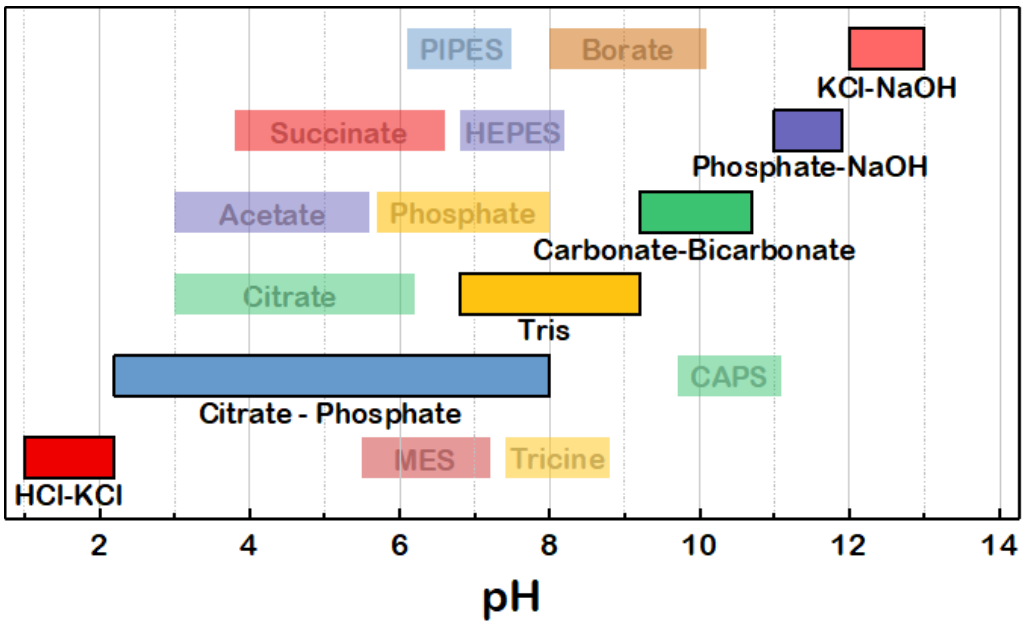

Figure 2.3: Comparison of the effective buffering ranges of commonly used buffers. Buffers used in this thesis for ζ–potential measurments are outlined with bold text.

Buffer	pH	Solution #1 (100 mM)		Solution #2 (100mM)	
HCl – KCl	**1**	HCl	39.7 ml	KCl	10.3 ml
	2		14.9 ml		35.1 ml
Phosphate–Citrate	**3**	$C_6H_8O_7$	39.8 ml	Na_2HPO_4	10.2 ml
	4		30.7 ml		19.3 ml
	5		24.3 ml		25.7 ml
	6		17.9 ml		32.1 ml
	7		6.5 ml		43.6 ml
	8		3.5 ml		46.5 ml
Tris	**9**	HCl	4.5 ml	$C_4H_{11}NO_3$	45.5 ml
Carbonate–Bicarbonate	**10**	$NaHCO_3$	22.5 ml	Na_2CO_3	27.5 ml
Hydroxide–Phosphate	**11**	NaH_2PO_4	7.2 ml	NaOH	42.8 ml
KCl – Hydroxide	**12**	KCl	9.7 ml	NaOH	40.3 ml
	13		13.8 ml		36.2 ml

Table 2.1: Recipes used for preparing 50 ml 100 mM buffer between pH 1 and pH 13. Small adjustments to in the pH were acheived by adding dropwise 100 mM NaOH or 100 mM HCl

2.5.1 Zeta Potential Measurements

In order to monitor the surface charge of nanoparticles, measurements were taken of the ζ–potential of solutions using a Malvern Zetasizer Nano ZSP. ζ–potential is measured by monitoring the response of particles in solution to an applied DC voltage. Specifically the electrophoretic mobility is directly measured and then related to the ζ–potential through the Henry equation [124]:

$$U_E = \frac{2\varepsilon\zeta f(ka)}{3\eta} \tag{2.2}$$

where U_E is the electrophoretic mobility, ε is the dielectric constant of the dispersant, ζ is the zeta potential,

η is the dispersant viscosity and $f(ka)$ is Henry's function [1], k is the debye length and a is the paticle radius. For the measurements here $f(ka)$ is taken to be 1 under the Debye–Hückel approximation (a < 100 nm and $c_{electrolyte}$ << 10 M) [74].

The Malvern Zetasizer uses laser doppler velocimetry to measure the particle velocity distribution. Briefly, a monochromatic light beam illuminating the sample is modulated by an oscillating mirror, the intensity of the light scattered by the particles in solution is recorded and then analysed by a digital signal processor to extract the characteristic frequencies in the scattered light. the frequency of the fluctuating scatter intensity signal is directly proportional to the electrophoretic mobility and measurement of the Doppler shifts of the incident light gives an a direct measure of the direction of motion.

Colloidal solutions are often quoted to display stability, if $|\zeta|$ > 30 mV, based on the qualititative definitions outlined by Riddick in his 1968 book [291], although this threshold is somewhat arbitrarily selected. Optimisation of the ζ–potential of solution through proper surface modification and buffer pH is key to maintaining the long–term stability of charged stabilised samples.

Stability characteristics	**ζ–potential (mV)**
Extreme to very good stability	-100 < ζ ≤ -60
Reasonable stability	-60 < ζ ≤ -40
Moderate stability	-40 < ζ ≤ -15
Threshold of light dispersion	-15 < ζ ≤ -10
Threshold of agglomeration	-10 < ζ ≤ -5
Strong agglomeration and precipitation	-5 < ζ ≤ 5

Table 2.2: Stability of colloidal solutions from their ζ-potential. Taken from ref. [291]

Two key parameters to consider during these measurement are the ζ–potential are pH and electrolyte–concentration, which will radically change the measured ζ–potential. Hence because of the low buffering capacity of DI water, the pH is very poorly defined, meaning all measured values of ζ in this medium are pratically meaningless. Beyond this, the poor conductivity of DI water leads to electrode polarisation, making it impossible to reliably produce a uniform electric field with in the typical folded capilliary cuvettes used for ζ–potential measurements. Hence all measurements must be performed in buffer at known pH and ion concentration. Hence the following buffers were used to control the pH during ζ–potential measurements:

ζ–potential measurements are taken in disposable folded capilliary cells purchased directly from Malvern. In a standard measurement the folded capillary is filled throughout with the colloidal dispersion, however a number of issues arise from this technique when applied to highly conductive colloidal samples. For instance, Joule heating and electrode polarization, which can be minimised by reducing measurement time and voltage. But more concerningly electrode blackening and sample degradation, due the denaturation of many organic materials, including surface–stabilising ligands, in response to the high electric field in close proximity to electrodes. The only route to avoid this is to avoid direct contact of the colloid with the electrode. Either through the use of a semi–permeable membrane or through a diffusion–limited barrier methodology [18, 19, 236, 237, 347].

All work here was performed using the diffusion barrier method. The folded capillary was loaded with buffer at known pH and concentration (typically 10–100 mM). A small volume (~50 µl) of colloidal solution

[1] Henry's function: $f(ka) = 1 + \frac{1}{16}(ka)^2 - \frac{5}{48}(ka)^3 - \frac{1}{8}\left[\frac{1}{12}(1-ka) - \left(1 - \frac{1}{12}(ka)^2\right)e^{ka}E_1(ka)\right]$ from refs [124] and [335]. $E_1(ka)$ is the exponential integral.

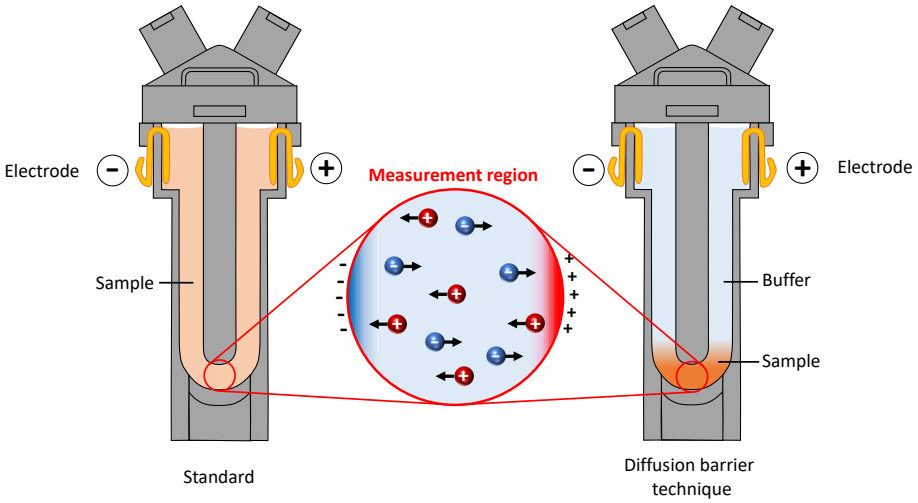

Figure 2.4: Different configurations for ζ–potential measurement. The "standard" measurement with colloid in close proximity to the electrodes and the difusion–limited measured with the colloidal solution isolated at the bottom of the folded capillary.

suspended in the buffer was injected into the base of the cuvette using a 200 µl gel–loading tip. This creates a high concentration of colloid in the measurement region of the cuvette with minimal osmotic pressure (i.e diffusion–limited). Further to prevent material from reaching the electrode, the measurement voltage in reduced with increasing buffer concentration[1]. Measuring via this technique is in full compliance with the current standard for measuring the colloidal stability of biological nanomaterials (ASTM E2865-12(2018) [21]).

2.5.2 Surface Enhanced Raman Spectrscopy

Quartz slides were sonicated with acetone, 1% Decon 90 and rinsed with Milli–Q prior to piranha etching using 30% Hydrogen Peroxide and Sulfuric Acid (>95%) at 3:7 (v/v) ratio. Slides were cleaned for 20 m and rinsed and stored in Milli–Q and dried with nitrogen gas prior to use.

Concentrated AuNR sample was dried onto the quartz slide using hydrophobic chambers. A Raman confocal microscope system (inVia Raman, Renishaw) was used with a 785 nm laser line, 1800 mm^{-1} grating and a near infrared enhanced CCD array detection. Before each experiment, the system was calibrated by collecting spectra of a silicon sample using a 10× objective and peak calibrated to 520.5 cm^{-1}. For AuNR measurements, a 40× objective was used and focused on the dried surface. For each sample, a Raman spectra map was acquired over a 200 × 200 µm area with 25 measurement points with a spot size of ~10 µm and laser power of 10 %, to prevent sample degradation. Raw spectra were background corrected using the f_baseline_corr MATLAB function with a smoothing width of 30 and bandwidth of 350 for 75 iterations [175]. After background subtraction, each spectra was summed and normalised to the maximum peak value.

2.5.3 NMR

All NMR spectra were taken on a Bruker Avance500 instrument at 500 MHz at 295 K using a 5 mm broadband solution probe. For CTAB, Oleate, DOPC and DSPE–mPEG-2000 an acquisition time of 3.6

[1]The measurement voltage was approximately set using the following relationship: $V_{meas} = 18 + 162 \cdot \exp\{-0.02 \cdot C\}$, where V_{meas} is the measurement voltage in mV and C is the buffer concentration in mM.

s and 16 scans were used. For AuNR spectra an acquisition time of 3.6 s and 128 scans were used. All spectra were taken using D_2O as the solvent. Spectra were corrected according to the expected position of the chemical shift resulting from residual HDO.

Preparation of solutions for NMR

Solutions of 10 mM CTAB and sodium oleate were prepared by hydration of the powder in D_2O. Phospholipid solutions were prepared by first drying the lipid stock (in $CHCl_3$ – CH_3OH (1:1)) under a nitrogen stream for 30 minutes. Residual solvent was removed by overnight dessication. The lipids were rehydrated using D_2O and tip–sonicated for 30 minutes. The solutions were then repeatedly passed through a 50 nm track–etched membrane to further reduced the size of formed vesicles. Without extrusion only poor quality NMR spectra were recovered for phospholipid solutions. AuNR solutions were cleaned by centrifugation and resuspending the pellet in D_2O, this was repeated threefold to remove as much residual H_2O as possible.

2.5.4 Stability in Biorelevant Media

In order to test the long–term stability of AuNRs, AuNRs were resuspended in various biorelevant media at 75 μg·ml−1 including a number of buffers, media, serum and mouse plasma. The resuspended AuNRs were placed in a 96–well plate and the longitudinal surface plasmon monitored at various timepoints across a 2–week period using a well plate reader. The solutions were stored at room temperature during this period. The following buffers were prepared as biorelevant surrogates for blood plasma, due to their similar ionic compositions in addition to DPBS.

Compound	**Plasma-lyte 148**		**Pseudo-plasma Buffer**	
	Conc. (mM)	*Mass in 100 ml (mg)*	*Conc. (mM)*	*Mass in 100 ml (mg)*
Sodium Chloride	90.00	526.0	89.70	523.8
Potassium Chloride	5.00	37.0	4.25	31.7
Sodium Lactate	1.50	30.0	2.00	22.4
Trisodium Phosphate	–	–	1.15	18.9
Calcium Chloride	–	–	1.15	12.8
Magnesium Chloride	–	–	0.88	8.4
Sodium Persuphate	–	–	1.00	23.8
Sodium Acetate	27.00	368.0	–	–
Sodium Gluconate	23.00	502.0	–	–
Sodium Bicarbonate	–	–	20.00	168.0
Sodium Carbonate	–	–	11.90	126.1

Table 2.3: Recipes used in buffers prepared for measuring the stability of various nanoparticle functionalisations.

2.6 Photothermal Experiments

A bespoke system was assembled to allow the automated photothermal heating of cells a tunable laser source in a controlled environment. The rig allowed a well–plate to be precisely moved above the laser source

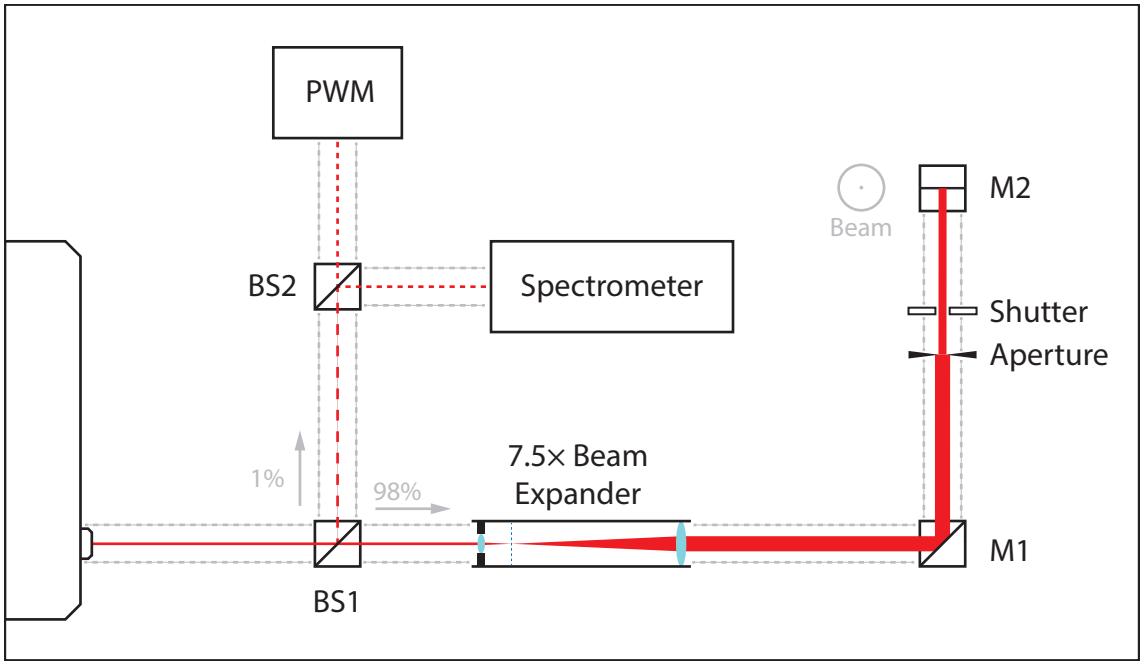

Figure 2.5: Optical Schematic showing the components used to shape and monitor the beam used in photothermal heating experiments.

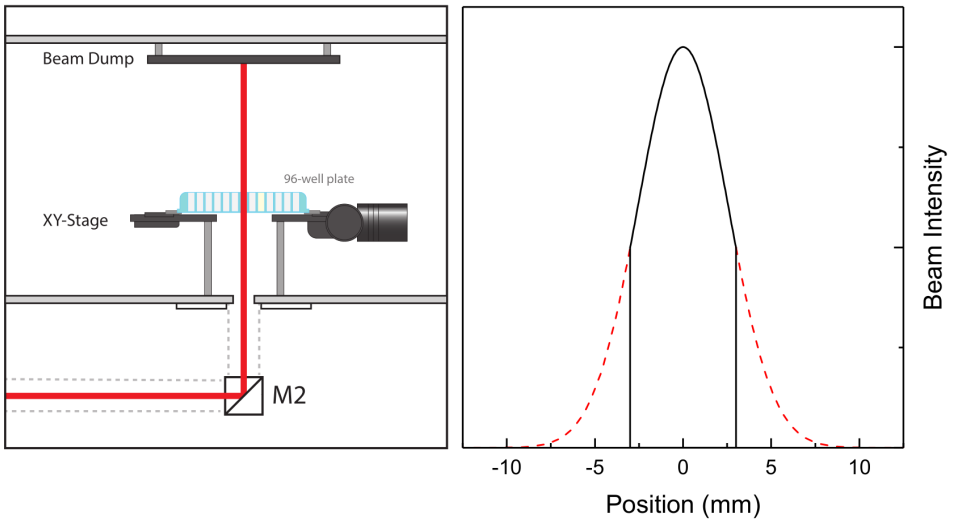

Figure 2.6: Optical Schematic showing relative positives of the XY–stage, well–plate, and beam dump relative to the final mirror in the optics path. **Right:** Beam intensity profile after passing through the aperture. Red dashed lines indicate the lost beam intensity at the periphery of the beam.

within an environment maintained at 37°C. Additionally the resultant temperature change could be monitored through an 8–channel thermocouple logger.

A Coherent Mira 900–F was selected as the light–source. This is a tunable femtosecond–pulsed Ti:Sapphire laser, however it was utilised as a CW source. The Mira 900–F provides a 0.8 mm diameter horizontally polarised Gaussian beam, tunable between 700 and 980 nm, at up to 2.2 W in CW mode. ~1% of this beam was sampled using a polarised beam splitter and the power measured using a Thorlabs PM100D power meter fitted with a S120C sensor–head, and the wavelength monitored using a fibre–coupled Ocean Optics Flame spectrometer.

The main beam was expanded 7.5 times to achieve a FWHM of 6 mm (the diameter of a well on a 96–well plate). The low intensity region outside the FWHM were removed by passings the beam through a 6

mm aperture, the effect of this on the beam profile is shown in fig. 2.6. The beam was then passed through an interlocked bespoke shutter (which simultaneously acted as a beam dump when closed), allow remote control when the sample was exposed to the beam. Finally the beam was reflected vertically by a 45° prism mirror into the main chamber (fig. 2.6).

The main chamber contained a Prior H128 motorised XY–stage, fitted with a mount for standard well plates, allowing them to be moved directly above the beam. Directly above this was a beam dump terminating the path of the beam. The chamber could be maintained at a setpoint temperature, typically 37°C, using an IncuKit cabinet incubator heater. Finally, an 8–channel Pico Technology data logger could be mounted to the stage allowing direct monitoring of the temperature inside well using thermocouples. The entire chamber and beam path were self contained and interlocked to prevent exposure to the beam. After the beam had passed through all components beam intensities upto 2.7 $W \cdot cm^{-2}$ could be acheived across a 6 mm diameter circle, dependent on wavelength.

The spectrometer, thermocouple datalogger, XY–stage and shutter were all connected to a PC via USB. A python script was written to allow a sequence of wells and exposure times to be directly input through a graphical user interface and allow experiments to proceed without the need for constant monitoring.

2.7 Tissue Culture

All tissue culture was performed under sterile conditions in a class II A1 biosafety cabinet. All consumables were either purchased sterile or autoclaved at 131°C for 30 mins. Cells were incubated at 37°C in 5% CO_2 and passaged at a 1:10 ratio upon reaching ~70% confluency. Cells were disgarded as the passage number approached 100. The following cell lines were used during the course of this thesis:

2.7.1 Cell Viability Assays

The cytotoxity of AuNPs to the various cell lines were assessed using the CCK-8 cell viability assay. In brief, CCK-8 consists of a water soluble tetrazolium salt, WST–8 which is reduced by dehydrogenase inside living cells leading to the formation of WST-8 formazan an orange dye which a strong absorbance peak at 450 nm. The absorbance at this wavelength is linearly proportional to the number of viable cells and hence can be used to ascertain the relative viabilities of cells under different conditions.

Cells were seeded in 96 well plates at a density of 5000 cells per well in 100 µl media. The plates were then incubated at 37°C in 5% CO_2 for 24 hours. Post–incubation the media was exchanged with media containing a known concentration of AuNRs and the plate incubated for the required exposure time. Following this the media was replaced with media containing 10% CCK-8 solution and incubated for a further 4 hours. The absorbance at 450 nm was then measured using a a microplate reader (Mithras LB 940).

Cell line	Tissue	Disease	Morphology	Origin	Culture Medium
SW620	Colon, *derived from metastatic lymph node*	Colorectal adenocarcinoma *Duke's type C*	epithelial	Male, 51, Caucasian	RPMI 1640 + *10% FBS*
HEK293	Embryonic kidney	–	epithelial	Female, Fetus, *ethnicity unknown*	RPMI 1640 + *10% FBS*
HCT116	Colon	Colorectal carcinoma	epithelial	Male, *Adult*, Caucasian	RPMI 1640 + *10% FBS*
LS174T	Colon	Colorectal adenocarcinoma *Duke's type B*	epithelial	Female, 58, Caucasian	DMEM + *10% FBS*

Cell viabilities were then expressed as a fraction of the untreated control viability. The measurement was background corrected through subtraction of the absorbance of wells treated with AuNRs and media, but containing no cells. All absorbances were calculated from the average of at least six wells and the experiment performed in triplicate on different cell passages. The expression for the cell viability, θ, is as follows:

$$\theta_{viability} = \frac{A^{(sample)}_{450\text{ nm}} - A^{(bkgd)}_{450\text{ nm}}}{A^{(control)}_{450\text{ nm}} - A^{(bkgd)}_{450\text{ nm}}} \tag{2.3}$$

2.7.2 Photothermal Assays

Cell viability was assessed using the CCK-8 cell viability assay as above. Cells were seeded in 96 well plates at a density of 5000 cells per well in 100 µl media. The plates were then incubated at 37°C in 5% CO_2 for 24 hours. Post–incubation the media was exchanged with media containing a known concentration of AuNRs and the plate incubated for the required exposure time. Cells kept at 37°C were then illuminated using a continuous wave tunable laser at a known light intensity and wavelength, before a further incubation of 24 hours. Following this the media was replaced with media containing 10% CCK-8 solution and incubated for a further 4 hours. The absorbance at 450 nm was then measured using a a microplate reader (Mithras LB 940). Cell viabilities then calculated as a fraction of the untreated control viability (eq. 2.3, as above). All absorbances were calculated from the average of at least three wells and the experiment performed in triplicate on different cell passages.

2.7.3 Preparation of Cells for Optical Microscopy

Cells were seeded on to a 20 × 20 mm glass coverslip in a six-well plate at density of $2 \cdot 10^5$ cells per well and incubated at 37°C in 5% CO_2 for 48 hours. The media was then exchanged with media containing known concentrations of AuNRs. The cells were then incubated for the desired exposure time. Following this the cells were washed twofold with DPBS, before being placed in a 4% paraformaldehyde solution in DPBS for 10 minutes, fixing the cells. The cells were then rinsed with DPBS a further two times before removing excess fluid and adhering the coverslips to clean glass slides using an aqueous mounting medium.

2.7.4 Preparation of Cell Sections for Electron Microscopy

The method followed here is adapted from J.H. Luft 1961. '*Improvements in epoxy resign embedding methods*' [214].

SW620 and LS174T were seeded in 6-well plates at densities of $6 \cdot 10^5$ and $6.9 \cdot 10^5$ cells per well respectively. Cells were incubated at 37°C in 5% CO_2 for 24 hours before the media was exchanged with media containing 15 µg·ml^{-1} AuNRs. After a set amount of time had occured, cells were washed three times with 150 mM PBS, before being trypsinised and washed once more with PBS. The cells were fixed using 2.5% glutaraldehyde in 150 mM PBS for 2.5 hours. The cells were then centrifuged again and washed twice in 150 mM PBS. The supernatant was disgarded and replaced by 1% osmium tetroxide in 150 mM PBS overnight. The cells were then washed twice in in 150 mM PBS. The pellet was then dehydrated by washing in an ascending alcohol (in water) series at 20%, 40%, 60%, 80%, 100% (twice) for 20 min per step. The pellet was then washed in propylene oxide twice for 20 min to remove residual alcohol, before resuspension in 50% propylene oxide – 50% araldite mixture and being left overnight. Araldyte mixture is comprised of

52.9% Araldite CY212, 45.1% DDSA, 1.9% DMP 30. The pellet was then transferred to 25% propylene oxide – 75% araldite mixture and left for 6 hours. Finally the pellet was transfered to 100% araldite mixture and left in an oven overnight to cure at 60°C.

Sections were then prepared by taking ~90 nm sections using a ultramicrotome (Reichert-Jung Ultracut E) fitted with a 45° glass knife. Sections were collected in an aqueous bath, and prepared on 300 mesh copper grids and then post-section stained with uranyl acetate.

2.7.5 Protein Expression

The CEA–expression of the following cell–lines was measured by immunofluorescence and flow cytometry; LS174T, HEK293, SW620, SW480, LoVo, HCT116, and DLD–1. The primary antibody used was CEA/CD66e (mouse) and the secondary was anti–Alexa488.

Immunofluorescence Measurements on Fixed Cells

Cells were plated on coverslips in 6–well plates at densities of 10^5 cells per well and incubated for 72 h. Cells were then fixed with ice–cold methanol or 4% PFA, cell were then washed threefold with DPBS. 100 μL 1% BSA in DPBS was then added to each well for 1 h at room temp to block non–specific binding. This was replaced by the primary antibody at the appropriate concentration in 1% BSA in PBS and incubated for a further 1 h. The cells were washed threefold with DPBS. The secondary antibody (with fluorophore) at the appropriate concentration in PBS was added to each well and incubated for 1 h in the dark. The cells were washed threefold in DPBS and mounted using 20 μL of Prolong Gold Antifade Mountant. This was allowed to set in the dark overnight at room temperature.

Flow Cytometry for the Titration of Antibodies

Cells were washed in DPBS and 1 mM sterile–filtered EDTA added, a minimal amount was left on the cell monolayer for 10 m at room temperature. Cells were then trypsinised until individual cells were suspended in solution. The trypsin was then inactivated by the addition of media and then the cells then spun down into a pellet at 400*g*, before being resuspended in FACS buffer (5% FBS + 0.05% NaN_3 in PBS). 10^7 cells were placed into FACS tubes and increasingly dilute concentrations of antibodies (1:200 – 1:1600) added to each tube (100 μL). The cells were then incubated for 30 m in the dark on ice. 2 mL FACS buffer was added and the cells spun down to a pellet before the addition of 50 μL of the secondary antibody (1:300). Cells were then incubated for 30 m in the dark on ice. 2 mL FACs buffers was then added and the cells pelleted. The buffer was removed and 5 μL of 10 μg·mL PBS added before reading on a flow cytometer.

2.8 Murine Models

All mice used were BALB/c nude mice (originally obtained from Charles River Laboratories, Kent) and maintained in house. All mice were maintained under high health status and are specific pathogen free (SPF) status. Mice were housed in individually vented cages (IVCs) with access to food and water *ad libitum*. All procedures were approved by the UK Home Office and carried out according to the Animals (Scientific

Procedures) Act 1986 and under the project licence of Dr Louise Coletta (70/7965) with the technical work carried out by Dr Nicola Ingram under PIL IDD6965FF.

2.8.1 Administration of Gold Nanomaterials *in vivo*

BALB/c mice were injected substaneously with 1×10^9 of LS174T cells in 100 μL 289 mOsm·L^{-1} DPBS (culture protocols given in section 2.7). Tumour volumes were measured by calliper until a desired tumour volume of ~200 mm^3 was reached. Gold nanomaterials were concentrated to 200 μg·mL^{-1} suspended in 289 mOsm·L^{-1} DPBS. 200 μL of this preparation was then administered to the mice via tail vein injection. Mice were then monitored to determine if any adverse effects on the health of the animals. Mice were sacrificed at predetermined time–points and tissue harvested for *ex vivo* analysis.

2.8.2 Tissue collection and *ex vivo* Biodistribution Analysis

Organs were extracted immediately post–sacrifice. Individual organs were measured for their mass and then placed in cryo–vials. These were then flash–frozen in liquid nitrogen before transfer to a freezer at -80°C.

Preparation of the samples for elemental analysis requires digestion in *aqua regia* to liberate metal ions into solution. Hence water must be removed from the samples prior to digestion, this was acheived by placing samples in a lyophyliser for at least three days. Each organs was then measured for its mass again and transferred to an acid–resistant 15 mL centrifuge tube. Larger samples were homogenised prior to digestion. 1 mL *aqua regia* was then placed in each tube and left overnight to digest. Occasionally samples were agitated by vortexing if required. After digestion an additional 10 mL Milli–Q grade water was added to each tube and the samples centrifuged at 4000 *g* for 30 minutes and the supernatant collected, this was repeated twice, ensuring the removal any non-digested particulate matter.

In order to demonstrate the efficacy of the extraction process, a liver from a mouse untreated with AuNPs was dissected into five and doped with a known quantities of Au prior to lyophilisation. The samples were then processed by the same digestion process described above.

2.8.3 Blood Collection and Haemolysis Assays

Blood was collected post–sacrifice by terminal cardiac puncture into an EDTA-coated paediatric blood collection tube (Greiner). Tubes were centrifuged at 500 g for 5 min at 4°C. The plasma and red blood cells and were then separated.

Haemolysis Assays

Red blood cells were then gently resuspended in 150 mM NaCl. The red blood cells were washed a further two times with 150 mM NaCl. Finally the red blood cells were resuspended in PBS. This was then diluted 1:50 with PBS. 10 μl of particles at 2000 μg·mL^{-1} and 400 μg·mL^{-1} were added to 190 μL of diluted red blood cells in a 96–well plate in triplicate alongside a positive control (1% (v/v) Triton x-100) and negative control (PBS). The final concentrations of AuNRs were 100 μg·mL^{-1} and 20 μg·mL^{-1}. The cells were incubated at 37°C for one hour at 100 rpm on an orbital shaker. The plate was then centrifuged at 500 g

for 5 minutes to pellet the intact red blood cells. 100 µl of the supernatant was placed in a fresh 96 well plate and the absorbance at 420 nm was read [1]. The lysed fraction, θ_{lysed}, was then expressed as:

$$\theta_{lysed} = \frac{A^{(sample)}_{420\text{ nm}} - A^{(negative)}_{420\text{ nm}}}{A^{(positive)}_{420\text{ nm}} - A^{(negative)}_{420\text{ nm}}} \tag{2.4}$$

where $A^{(sample)}_{420\text{ nm}}$, $A^{(negative)}_{420\text{ nm}}$, and $A^{(positive)}_{420\text{ nm}}$ are the absorbances at 420 nm for the sample, negative control, and positive control respectively.

CTAB AuNRs for this assay, were cleaned twice by centrifugation after synthesis, reducing the background CTAB concentration to approximately 40 µM. The particles were then centrifuged a third time and ~96% of the supernatant removed, concentrating the sample to 2000 $\mu g \cdot mL^{-1}$. Cleaning the particles further than this this resulted in loss of colloidal stability, hence it was decided that this represented the best case lowest acheivable cytotoxicity without comprising the properties of the CTAB–functionalised AuNRs.

2.9 Photoacoustic Imaging

All photoacoustic (PA) measurements were taken in a real–time preclinical multi spectral optoacoustic tomography (MSOT) scanner (MSOT inVision 128, iThera Medical Germany). All photoacoustic spectra were calculated from 'raw' PA intensity maps, any other images are multispectral projections, based on the provided absorbance spectra of the administered particles.

2.9.1 Phantoms & Photoacoustic Spectra

For assessment of the spectral response of AuNRs, solutions were placed in an agar phantom (fig. 2.7). The solutions were contained within 4 mm plastic straws and capped with glue. Agar phantoms were prepared according to published protocols [66]. 0.75 g Agar was added to 50 mL of Milli–Q grade water and brought to boil. To this was added 1.5 mL Intralipid and a drop of Germall Plus. The mixture was then poured into moulds and allowed to set. The Intralipid served to give similar attentuation due scattering as observed in human tissue and the Germall Plus prolonged the life span of the phantoms by preventing mould growth. A multispectral reconstruction of the AuNR solution distribibution is given in (fig. 2.7).

Photoacoustic spectra could then be measured by sweeping the illumination wavelength and recorded the PA intensity through a single plane inside the phantom. A second sample containing only H_2O was also inserted in the agar phantom, allowing the spectrum of the supernatant to be recorded. The PA signal was recorded by placing measuring the average intensity of the top 5% most intense pixels. The PA response of the H_2O control was subtracted from the PA response of the AuNR solution, to give the PA reponse of the AuNRs.

2.9.2 *In Vivo* Imaging

All mice were prepared with subcutaneous tumours and administered according to the protocol given in section 2.8.1. During imaging mice with anesthetized with isofluorane and placed in supine position inside

[1] Normally 540 nm is used for haemoglobin, the transverse band of the AuNRs interfered too much at this wavelength, 420 nm (Soret band) was used instead.

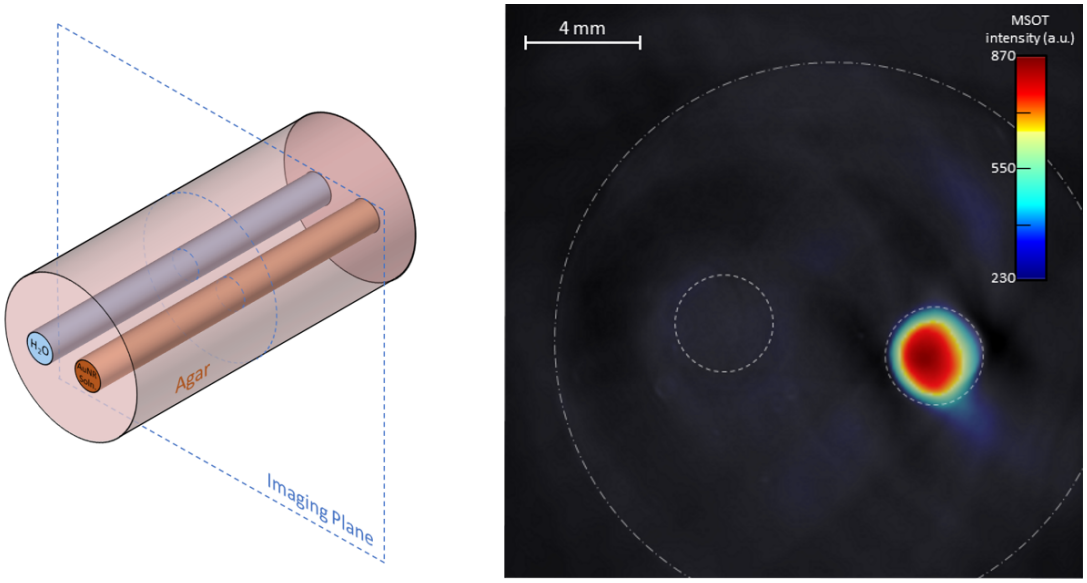

Figure 2.7: Left: Diagram of agar phantom, showing the relative positions of the sample and water control. Not shown are the plastic straws used to contain the samples when submerged in the water bath. **Right**: MSOT image of phantom containing H_2O (left circle) and 37 $\mu g \cdot mL^{-1}$ AuNR solution (λ_{LSPR} = 811 nm), right circle). The MSOT signal was reconstructed using a linear regression algorithm which calculated the spatial distribution of the AuNR solution based on an extinction spectrum measured using a UV-vis spectrometer. The background signal is the response seen at 680 nm.

the imaging chamber. Imaging was taken during AuNP administration, although only the 24 h time point is presented here. Transverse slices through the mouse were taken at 1 mm intervals throughout the abdomen of the mouse. Laser excitation wavelengths of 715, 730, 760, 800, 830, 850, and 900 nm were selected corresponding to the absorption maxima and minima in the spectra of the PSS–AuNRs, oxyhaemoglobin and haemoglobin. Each frame was construction from an averages of 10 pulses per transverse slice. Images were reconstucted and individual spectral components were decovoluted using a using a linear regression model. No background correction was performed after the initial scan due to the mouse being repositioned between scans.

2.10 Finite Element Simulation of Gold Nanoparticles

For the purposes of the simulations in this work finite element analysis was utilised via the COMSOL Multiphysics package. COMSOL was used since it offers a user-friendly interface with no requirement for significant prior knowledge of the underlying modelling technique to generate accurate solutions to the physical problem (only a knowledge of the relevant physics to be solved). Secondly, as a multiphysics package it offers the ability to solve complex problems that involve multiple physical phenomena, such as the thermal response of a nanoparticle to an incident light field.

2.10.1 Absorption and Scattering Cross Sections

For the simulation of the optical response of AuNPs, COMSOL's radio frequency module was used. This is a module designed for solving general physics problems involving electromagnetic waves. To reduce computation time simulations were performed in the frequency domain under the assumption that all electronic responses would show a sinusoidal time dependence. For excitation of a simple plasmonic

nanostructure by an electro-magnetic plane wave of the form $\vec{\boldsymbol{E}}_{\mathbf{b}}(\vec{\boldsymbol{r}},t) = \vec{\boldsymbol{E}}_{\mathbf{0}}\exp\{i\vec{\boldsymbol{k}}\cdot\vec{\boldsymbol{r}} - i\omega t\}$, this is a reasonable assumption.

Each AuNP was simulated in a centrally located position embedded within an ambient medium, typically water, with a width several times larger than the length of the largest wavelength of light used. Values for the refractive index of gold were taken from Johnston and Christy [156], and the values for the medium were taken from the COMSOL Multiphysics Material Library. The surrounding medium was encased by a perfectly matched layer, a region which perfectly absorbs incident radiation without reflection or scattering. This is used to prevent the external boundaries of the model creating radiation patterns which overlap with the calculated solution of interest.

To further improve accuracy all calculations were computed in the scattered field formulation, the benefits of this are two fold. Firstly, the incident field is usually significantly larger than the scattered field (the quantity of interest), leading to it being inaccurately resolved in the full–field formulation. By solving only for the scattered field this problem it is thus possibe to significantly boost the accuracy of solutions. Secondly, it allows for a global plane–wave excitation to be used without any need to account for the damping inside the PML, which is otherwise required in the full–field approximation.

Parameters of interest can then be found by solving the time-harmonic wave equation:

$$\vec{\nabla}\times\frac{1}{\mu_r}\left(\vec{\nabla}\times\vec{\boldsymbol{E}}_{\mathbf{rel}}\right)-\left(\varepsilon_r - i\frac{\sigma}{\omega\varepsilon_0}\right)k_0^2\vec{\boldsymbol{E}}_{\mathbf{rel}} = 0 \tag{2.5}$$

where k_0 is the free space wavenumber, σ is the conductivity of the particle and $\vec{\boldsymbol{E}}_{\mathbf{rel}}$ is the relative field defined by $\vec{\boldsymbol{E}}_{\mathbf{rel}} = \vec{\boldsymbol{E}} - \vec{\boldsymbol{E}}_{\mathbf{b}}$, where $\vec{\boldsymbol{E}}$ is the total field at any point and $\vec{\boldsymbol{E}}_{\mathbf{b}}$ is the background field. Typically this is solved using the PARDISO direct solver included with COMSOL, which is particularly memory-intensive, but is significantly faster than other provided solvers.

$\sigma_{\text{abs}}(\lambda)$ can be obtained on the assumption that all energy dissipation from the particle occurs through resistive heating (no photoluminescence), and hence can be calculated from the volume integral of the resistive heat losses through the particle, Q_{rh}. Conversely, and $\sigma_{\text{scat}}(\lambda)$ can be calculated through a surface integral of the time averaged power flux out of the particle, or the Poynting vector, $\vec{\boldsymbol{S}}_{\mathbf{P}}$:

$$\begin{aligned}
\sigma_{\text{abs}}(\lambda) &= \frac{1}{I_0}\int_{V_{NP}} Q_{rh}(\vec{\boldsymbol{r}},\lambda)\,\mathrm{d}V \\
\sigma_{\text{scat}}(\lambda) &= \frac{1}{I_0}\int_{S_{NP}} \vec{\boldsymbol{S}}_{\mathbf{P}}(\lambda)\cdot\mathrm{d}\vec{\boldsymbol{S}} \\
\sigma_{\text{ext}}(\lambda) &= \sigma_{\text{abs}}(\lambda) + \sigma_{\text{scat}}(\lambda)
\end{aligned} \tag{2.6}$$

Considerations of the symmetry in the system allows for the averaged angular crosssection to be calculated. For a AuNR with its long axis in the z-direction, the longitudinal excitation can be driven by light polarised in the z-direction propagating in the x–y plane, (notated here as $E_{x,z}$ and $E_{x,z}$). Two methods to then excite the transverse mode; firstly light both polarised and propagating in the x–y plane ($E_{x,y}$ and $E_{y,x}$) can excite it across the waist of the particle, and secondly, light propagating in the z direction ($E_{z,x}$ and $E_{z,y}$) will similarly excite the transverse mode but with a different particle orientation relative to the plane wave.

Due to the symmetries of rods, all three cases are doubly degenerate and only need to be simulated in a single case to calculate the averaged crosssection i.e only using $E_{x,z}$, $E_{x,y}$ and $E_{z,x}$ (fig. 2.8 (a)).

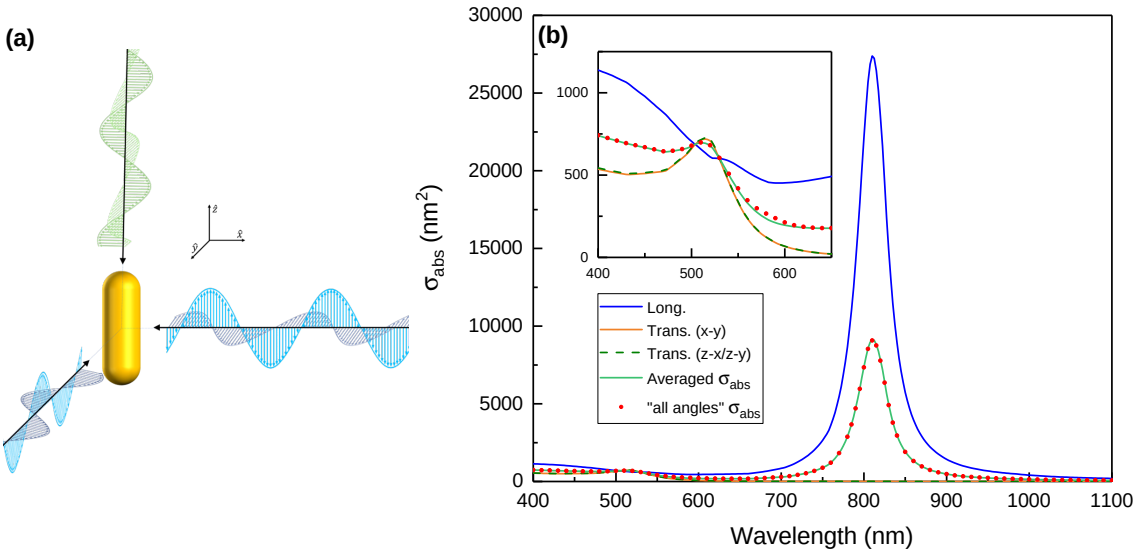

Figure 2.8: **(a)** Different plasmonic excitations of AuNRs. Longitudinal excitations in blue, Transverse excitations in the $x-y$ plane in purple and transverse excitations perpendicular to the $z$axis in green. **(b)** COMSOL simulated absorbance crosssections for a (60×16)nm AuNR, with a tip eccentricity of 0.5, alongside the averaged crosssection and crosssection for a aingle simulation calculated to reflect the averaged angular crosssection. Good correlation can be seen between this model and the average from the three individual excitations. **Inset:** Closeup of the crosssections around the transverse excitation.

Further consideration allows the averaged angular crosssection to calculated in a single simulation, exciting the particle with light propagating the x direction with the polarisation axis at 45 from the y-axis ($E_{x,yz}$) allows excitation of both the longitudinal and transverse axis across the side of the AuNR. Furthermore in addition to this a rotation of the AuNR about the y-axis of $\sin^{-1}(\frac{1}{\sqrt{3}})$ ~35.26° allows excitation of the transverse mode from the end of the AuNR in the correct proportion to produce a value equal to the average angular excitation. Fig. 2.8 (b) shows the all three calculated crosssections, the averaged crosssection and the crosssection from the arrangement just described, showing near perfect agreement

The end–caps of AuNRs were paramerised as hemispheres of an ellipsoid, with an eccentricity defined by, $e = 2a/D$, where a is the semi–minor axis of the ellipsoid and D is the diameter of the AuNR [384]. Eccentricities were considered between the two theoretical extremes, a cylinder ($e = 0$) and a prolate ellipsoid ($e = R$).

2.10.2 Particle–on–a–substrate

In order to simulate the expected scatter spectra for AuNRs at a glass–air interface, such as is the case with the darkfield–single particle scatter spectroscopy system, a different approach was required. Simulations were still performed using the RF module in the frequency domain. Due to the presence of the interface the background field can no longer be assumed to be the same as the excitation field. Hence a travelling–wave incident at 61° from normal to the surface (average angle of incident for the darkfield condenser) was used with port conditions above and below the interface. All side boundaries were set up with Floquet boundary counditions, effectively extending the geometry infinitely in the plane of the interface.

The simulation was initially run without the AuNP present, allowing the background field to be calculated. A second RF frequency interface was then set up to introduce the AuNP and solve for the scattered field. This particle was typically a single hemispherically–capped AuNR in contact with the glass surface. As

above an angle of polarisation and incidence was selected such a single simulation provided the averaged excitation expected from darkfield excitation. The effect of surface coating was not considered, real–world spectra are expected to be red–shifted relative to those simulated due to the presence of CTAB on the surface of the AuNRs.

2.10.3 Heat Generation

The results of section 2.10.1 can be used to calculate the expected heat generation from pulsed light sources. This is conditional on the region being simulated being large enough to contain the generated temperature gradient within the simulated timescale. The Heat Transfer in Solids module in the time domain was used as second-simulation step. This simulation is restricted to using a single wavelength, this is not a significant issue, since most lasers used for photothermal heating have spectral bandwidths significantly narrower than the typical longitudinal SPR peak. A single wavelength simulation at the LSPR and expected peak intensity of a nanosecond pulse of was run to determine $\sigma_{\text{abs}}(\lambda_{\text{LSPR}})$. From this simulation the corresponding heat generation function, $Q(\lambda, \vec{r}, t)$ inside the domains constituting the AuNP was obtained. This can then be multiplied by a normalised Gaussian pulse of form:

$$f(t) = \frac{2}{w}\sqrt{\frac{\ln 2}{\pi}}\exp\left\{-4\ln 2\frac{(t-t_0)^2}{w^2}\right\} \tag{2.7}$$

where w is the pulse width and t_0 is the pulse centre. Providing a heating pulse which is Gaussian in time and the correct peak intensity. Temperature distributions can then be recovered from point probes along a single axis. At the time of writing there are no boundary condition availible which allow heat to flow out of the simulated region, hence the upper time limit over which these temperature distributions will be physical is given by the thermal diffusion time, $\tau_{\text{th}} = L^2/\alpha$, where L is the shortest distance between the particle and the boundary of the simulation and α is the thermal diffusivity (1.43×10^{-7} m^2s^{-1} for water). However for nanosecond pulses in sufficiently large volumes the bulk temperature rise is sufficiently low relative to the localised heating in the vicinity of the AuNP that is not a major concern.

2.11 Materials

Milli–Q water (18 MΩ·cm) was used in the preparation of all solutions. All chemicals were used without further purification.

2.11.1 Synthesis

Reagent Name	Product No.	Supplier
L–(+)–ascorbic acid	A15613	Alfa Aesar
Hydrochloric acid (12.1 M)	UN1789	Fisher Scientific
Silver nitrate	11414	Fisher Scientific
Sodium borohydride	10599010	Fisher Scientific
Gold (III) chloride trihydrate	520918	Sigma–Aldrich
Hexadecylammonium bromide	H6269	Sigma–Aldrich
Sodium oleate	O0057	TCI

2.11.2 Phospholipids

Reagent Name	Product No.	Supplier
DOPC *1,2-dioleoyl-sn-glycero-3-phosphocholine*	556600	Lipoid
DSPC-PEG_{2000} *1,2-distearoyl-sn-glycero-3-phosphoethanolamine-N-[methoxy(polyethylene glycol)-2000]*	588200	Lipoid
DOPG *1,2-dioleoyl-sn-glycero-3-phospho-(1'-rac-glycerol)*	564300	Lipoid
DSPC-PEG_{2000}-Maleimide *1,2-distearoyl-sn-glycero-3-phosphoethanolamine-N-[maleimide(polyethylene glycol)-2000]*	880126	Avanti

2.11.3 Tissue Culture

Reagent Name	Product No.	Supplier
DMEM + GlutaMAX media	31966	Gibco Life Sciences
Dulbecco's phosphate–buffered saline	14190-144	Gibco Life Sciences
Foetal bovine serum	A3160401	Gibco Life Sciences
RPMI 1640 + GlutaMAX media	11875-093	Gibco Life Sciences
TrypLE express	12604054	Gibco Life Sciences
CCK-8 cytotoxicity assay reagent	96992	Sigma–Aldrich
Paraformaldehyde	158127	Sigma–Aldrich
Poly–L–lysine	P4707	Sigma–Aldrich
Trypan blue	T8154	Sigma–Aldrich

Consumable	Product No.	Supplier
0.22 μm–pore syringe filters	SLGP033RS	Millipore
T75 culture flasks	3290	Corning
96 well plates, clear	3599	Corning
12 well plates, clear	3513	Corning
6 well plates, clear	3516	Corning

2.11.4 Preparation of Tissue Samples for Electron Microscopy

Reagent Name	Product No.	Supplier
DDSA – dodecenyl succinic anhydride	R1053	Agar Scientific
DMP-30 – 2,4,6-tris(dimethylaminolmethyl)phenol	R1042	Agar Scientific
Osmium tetroxide	R1016	Agar Scientific
Propylene oxide	R1080	Agar Scientific
Uranyl acetate	R1260A	Agar Scientific
Glutaraldehyde	G-5882	Sigma

2.11.5 Surface Coating, Conjugation and Targetting Experiments

Chemical Name	Product No.	Supplier
MOPS	327661000	Acros
Poly(sodium-p-styrenesulfonate) M.W. 70000	222271000	Acros
CEA protein	30-AC25	Fitzgerald
Tris(hydroxymethyl)aminomethane	B2005	Melford
Ethyldiaminetetraacetic acid (EDTA)	EDS	Sigma–Aldrich
Sun Fluor 488 Thiol	SF488-TH-1	Sunlights

2.11.6 Buffer Solutions

Chemical Name	Product No.	Supplier
Tris(2-carboxyethyl)phosphine hydrochloride	C4706	Aldrich
Sodium acetate	A16230	Alfa Aesar
Trisodium citrate	45556	Alfa Aesar
Sodium lactate solution 60% w/w	S/5161/08	Fisher Scientific
Potassium chloride	P/4240/53	Fisher Scientific
Sodium bicarbonate	S6014	Fluka
Sodium chloride	71376	Fluka
Sodium phosphate dibasic	30435	Honeywell Fluka
Sodium phosphate monobasic	S9638	Honeywell Fluka
Magnesium chloride	8.14722	Merck
Gluconic acid	8.22058	Merck
Citric acid	27847	Sigma
Calcium chloride	C1016	Sigma–Aldrich
Sodium carbonate	S77795	Sigma–Aldrich
Sodium hydroxide	S5881	Sigma–Aldrich
Sodium persuphate	13457	Sigma–Aldrich
Trisodium phosphate	342483	Sigma–Aldrich

2.11.7 Other Acids, Oxidisers, Solvents... etc

Chemical Name	Product No.	Supplier
Nitric acid (15.6 M)	A15613	Fisher Scientific
Hydrogen peroxide (30%)	H/1750/17	Fisher Scientific
Ethanol	E/0650DF/17	Fisher Scientific
2–propanol	20842	VWR
Acetone	20066	VWR
Chloroform	22711	VWR
Methanol	20847	VWR
Sodium dodecyl sulphate	LS750	Sigma–Aldrich
Sulphuric acid (18.4 M)	07208	Sigma–Aldrich

Chapter 3

Synthesis and Morphological Control of Gold Nanorods

Some of the content discussed in this chapter forms the basis of the following publication:

L. Roach *et al.* 2018. ''Morphological control of the seedless synthesis of gold nanorods using binary surfactants' in *Nanotechnology* **29**:359501 [292].
The dataset associated with this paper is available from the University of Leeds: doi.org/10.5518/273.

3.0.1 Motivation

Gold nanorods (AuNRs) offer the highest absorbance cross section per unit mass of any AuNP[1]. They offer easily tunable optical properties with high photothermal conversion efficiency in the NIR. Hence AuNRs were chosen as the candidate nanomaterial for our theranostic applications. As detailed in section 1.5, two key approaches exist for the aqueous synthesis of single crystalline AuNRs, seeded and seedless methods, both present challenges. As the literature currently stands, seeded protocols currently offer the method for producing AuNRs with the highest monodispersity and shape yield, but they suffer from being a two–step process, seeds must synthesised in advance of the main growth, and used in relatively narrow time window. Seedless protocols are a single–step protocol, avoiding the seed synthesis step, but historically have suffered from high polydispersity and low shape yield. One–step protocols are desirable, in that they are simpler to perform and should be easier to translate into industrial syntheses or allowing the synthesis of AuNRs under continuous–flow.

Hence, the approach decided upon here was to pursue improvements in the seedless synthesis of AuNRs, thus making it a viable method for synthesising good quality AuNRs. Recent approaches in improving the yield of seeded AuNRs has been to include additional additives in the growth solution. Of particular interest was inclusion of oleate as a co–surfactant, which demonstrated significant improvements in the morphological control and monodispersity [396]. Here we present an investigation of the effects of including oleate in the seedless synthesis of AuNRs and have sought to further understand the underlying formation process of gold nanorods formed during this process.

[1] A possible exception to this are bipyramids, which are fairly similar in shape in that they can be approximated by an ellipse

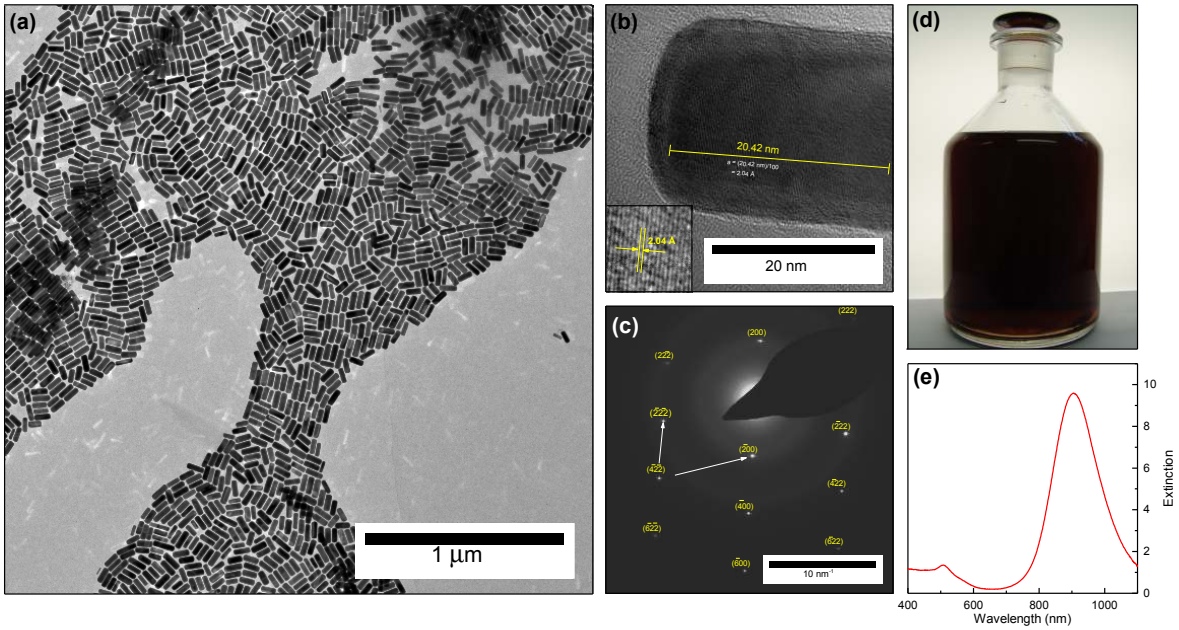

Figure 3.1: **(a)**: Wide–field TEM image of sample showing good monodispersity and high shape yield. **(b)**: High resolution TEM showing the crystalline structure of a AuNR synthesised using a 48 mM CTAB – CTAB 15 mM oleate growth solution. Annotated on the image is the measured lattice spacing of 2.04 Å (calculated from 100 lattice rows), corresponding to a (200) lattice spacing. Inset is a (4 × 4) nm region showing the visible lattice structure. **(c)**: Selected area electron diffraction image of the same AuNR. The corresponding Miller indices for each spot have been labeled on the figure. These are consistent with a monocrystalline FCC metal. **(e)**: Photo of a 500 mL as-synthesised AuNR batch synthesised using a 60 mM CTAB – 12.5 mM oleate growth solution (e) UV–vis spectrum of the same 500 mL solution.

3.1 Gold Nanorod Synthesis Protocol

The full protocol followed is detailed in sec. 2.1.

AuNRs were synthesised using a binary–surfactant seedless protocol similar to that published by Lai *et al.* [189], however the range of surfactant concentrations used to control the morphology has been expanded substantially. The particles were synthesised in a growth solution containing a mixture of cetyltrimethylammonium bromide (CTAB) and sodium oleate in the presence of a weak reducing agent, ascorbic acid (AA), and silver nitrate. Initially, $HAuCl_4$ was added, to a CTAB–oleate mixture, which was observed to turn a dark orange–yellow as CTA^+–$[AuCl_4]^-$ ion complexes were formed [308]. The unsaturated double–bond of sodium oleate is capable of the slow reduction of Au^{3+} to Au^{1+}, hence the mixture was observed to clear if left undisturbed after this point [189, 396]. To this mixture, $AgNO_3$, HCl and AA were added sequentially, any remaining yellow hue in the solution cleared following the addition of AA due to the reduction of all Au^{3+} to Au^{1+}. Finally, nucleation of the particles was initiated by the rapid injection of freshly prepared ice–cold $NaBH_4$. The solution was then left unstirred for 4 hours, at 30 °C. Particles were then cleaned by centrifugation at 9000 *g* for 30 min. The supernatant was discarded and the precipitate resuspended in Milli–Q grade water.

This protocol showed good reproducibility, with little variation in optical properties between different batches grown to the same recipe (fig. 3.3(d)) and can be scaled up substantially[1], with only a minor reduction in the quality of the end product (3.1(d)&(e). The samples synthesised by this protocol showed very high shape yields, normally in excess of 98% as shown in figure 3.1(a). For several batches it was not possible

[1]The highest volume synthesised to date is 2 L.

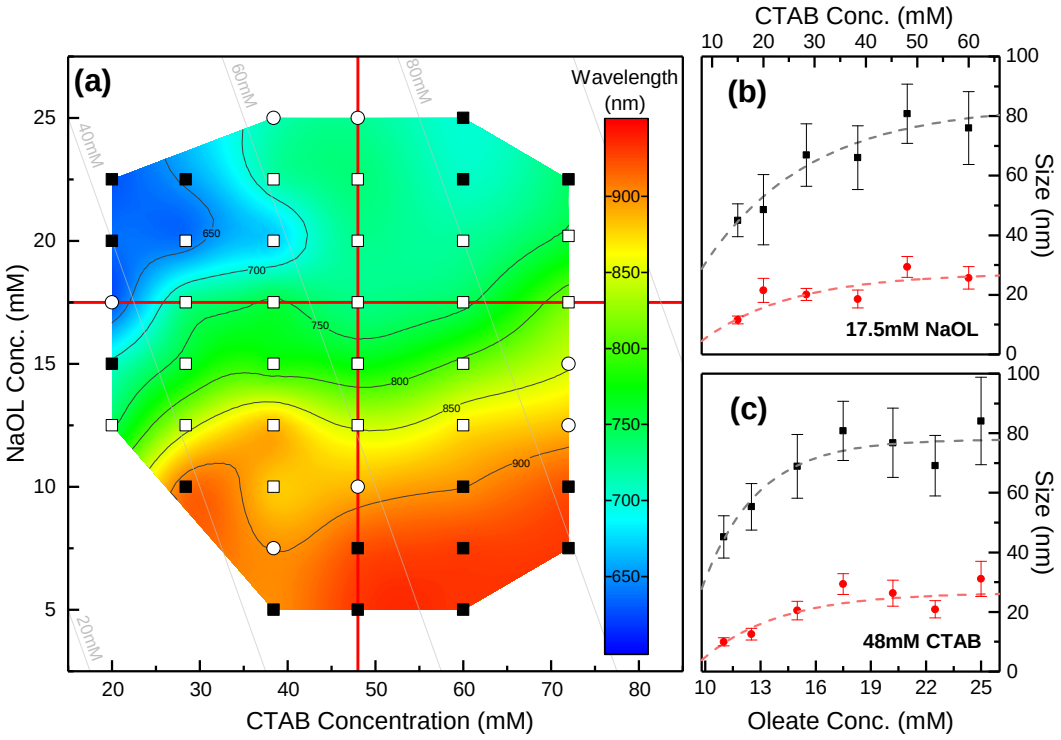

Figure 3.2: **(a)**: Effect of surfactant concentration on LSPR wavelength as function of both CTAB and oleate concentration, with all other components held constant. The shape of the each point indicative of shape yield, with: □ >98% AuNRs; ○ >90% AuNRs; ■ – low shape yield. The LSPR wavelength is interpolated between points, the colour scale for this is given in the right of the figure. **(b)**: Effect of CTAB concentration on length (black) and diameter (red) of AuNRs at a constant oleate concentration of 17.5 mM (horizontal line in **(a)**). **(c)**: Effect of oleate concentration on length (black) and diameter (red) of AuNRs at a constant CTAB concentration of 48 mM (vertical line in **(a)**). Error bars indicate the standard deviation of the AuNRs in each batch.

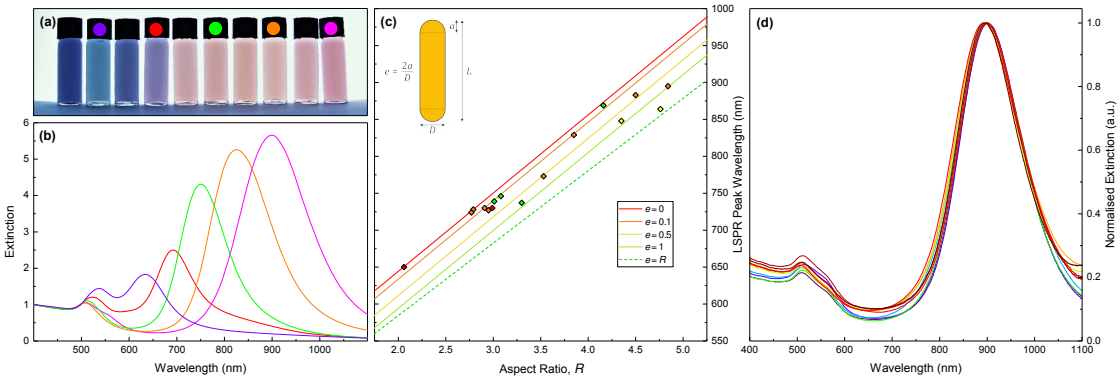

Figure 3.3: **(a)**: Photograph of particle solutions exhibiting LSPR from 520 to 900 nm, coloured circles on lid indicate the associated UV–vis spectrum shown in **(b)**. **(b)**: UV–vis spectra of solutions with resonances over same range. Spectra have been normalised to unity at 400 nm [308]. **(c)** Experimentally observed AuNR vs FEM predicted LSPRs for different end–cap geometries. Coloured lines are λ_{LSPR} by a linear fit to FEM simulated spectra for various tip eccentricities ($e = 0, 0.1, 0.5, 1, R$) as a function of aspect ratio. Experimental data collected via UV-vis and TEM measurements. Point colours represent the cap geometry most closely matched by those simulated ($0 \geq e \geq 1$). All samples fall within the theoretically expected ranges. There is some deviation from the simulations for the hemispherically–capped particles. **(d)** 11 batches grown to the same recipe, showing high reproducibility in position of the LSPR peak. All spectra were normalised to the peak absorbance of the LSPR band of each batch.

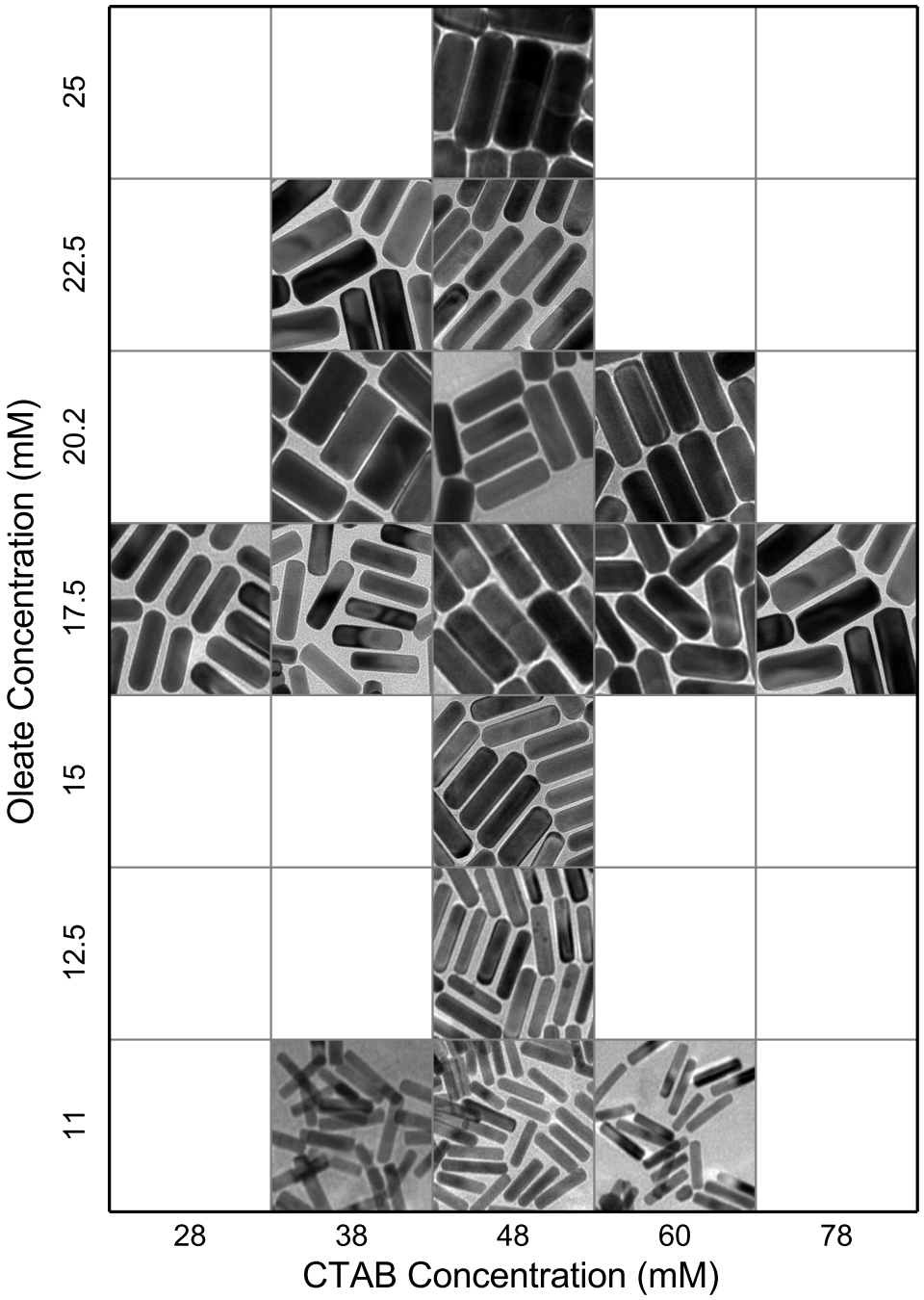

Figure 3.4: TEM of (150 × 150) nm areas of particles synthesised at different surfactant concentrations, demonstrating the change in morphology.

to locate any non–rodlike AuNPs, suggesting yields approaching 100%. Consistent with other seedless protocols the synthesised AuNRs are monocrystalline, as indicated by the strong diffraction pattern seen using SAED (figure 3.1(b)&(c)).

3.2 Morphological Control using Binary Surfactants

The effects on the morphology of synthesised AuNRs from variation of the concentrations of each surfactant in the growth solution were explored. The initial concentrations of $HAuCl_4$, $NaBH_4$, $AgNO_3$, and AA explored were decided upon based on values commonly seen in the literature, the range of surfactants

explored could probably be expanded further by synergistically varying these other parameters with the surfactant concentration. The variation of the two surfactants in tandem allows us to define a bivariate space in which the changes to the morphology can be studied.

It was found that the presence of sodium oleate in the growth solution and the reduced concentration of CTAB, increased the pH to such an extent that the growth of AuNRs became extremely rapid. This uncontrolled growth led to low rod yields and a high population of spheres. Hence the amount of HCl had to be increased from 12 μL to 50 μL compared with CTAB–only synthesis protocols, achieving a pH of ~1.5 in the growth solution. The effect of varying the amount of HCl added to the growth solution is discussed further in section 3.3.1.

Concentrations of oleate between 5 and 25 mM, and CTAB concentrations between 22 and 78 mM were added to the growth solution. Over these ranges a region of viable surfactant concentrations which produced high nanorod yields. Figure 3.2(a) plots the variation in LSPR as function of the two concentrations; it can be seen from this that a roughly ellipsoidal region centred on 45 mM CTAB – 16.5 mM oleate (with boundaries ±22 mM CTAB and ±7.5 mM oleate) exists where AuNR yields in excess of 98 % can be achieved. Shape yield drops off rapidly beyond this region, which is apparent in the UV–vis spectra through noticeable through the appearance of a third peak at ~550 nm due to the presence of spherical inclusions.

Within this region batches were synthesised with LSPR values between 620 and 900 nm (fig. 3.3). The LSPR wavelength was seen to decrease with an increase in the oleate concentrations. Conversely a small increase was observed with an increase in CTAB concentration. However this change in LSPR (and hence aspect ratio) is significantly more sensitive to changes in oleate concentration than CTAB. Analysis of this via TEM (see (fig. 3.2(b)&(c)) and fig. 3.4) showed that this reductions in aspect ratio occurred through an increase in the diameter of the synthesised AuNRs whilst yielding a proportionally smaller increase in the length, blue–shifting the LSPR. By contrast, a much greater change in the concentration of CTAB was required to have similar effects on the geometry of particles. Potentially the increased range of sizes made available here could be extended further through direct overgrowth in a two–step process [165]. Size distributions from analysis of TEM images are given in appendix A).

There is also a noticeable difference in the end–cap morphology of the AuNRs alongside the overall changes in morphology. Some batches showing end–caps varying between hemispheres whilst others have flat near–cylindrical tips (fig. 3.4). Tip geometry is known to change the optical properties of AuNRs, red–shifting the LSPR with decreasing tip eccentricity [281, 384], hence control of this represents a route for further modifying the optical properties of synthesised AuNRs. It is also expected to be of importance in the packing of AuNR assemblies, with flatter caps exhibiting higher capillary forces due to the increased available contact surface [386], making tip–to–tip arrangements more energetically favorable. Comparison with simulated spectra of AuNRs of varying tip morphology show that the measured resonances fall within the ranges expected from theoretical predictions (fig. 3.3(c)). However, there is some deviation between the simulations and the experimental data, especially for the hemispherically–capped samples, which showed generally higher resonances than expected. Hence the end–cap geometry seems to be sensitive to the changes in surfactant concentration in the growth solution and may offer a potential route to achieve control over this.

For surfactant concentrations which demonstrated a low shape yield, it was found that decreasing the pH further significantly improved the shape yield [12], although this was accompanied by a corresponding red–shift of the LSPR [374]. It seems highly probable that proper optimisation of the concentrations of

other components in the system at these surfactant concentrations would extend range of viable recipes and potentially extend the range of achievable LSPR wavelengths.

The samples synthesised by this protocol displayed good monodispersity, as indicated by the well–defined LSPR mode in the UV–vis spectra and confirmed by TEM images for a number of samples. Typically the standard deviation of a sample amounted to approximately ~15 % of both the diameter and length (appendix A). The narrow NIR absorbance peaks resulting from this low polydispersity will make them well–suited for use as photothermal agents in photoacoustic imaging [372] and plasmonic photothermal therapies [283].

3.3 Other Parameters

In addition to the effect of the surfactants on the particle morphology, the effect of the other components such as HCl, $AgNO_3$, AA and $NaBH_4$ in the growth solution were explored. The effects of each of the components are interrelated, making it difficult to categorically identify changes as the result of a single variable. However the impact of the introduction of new component, oleate, on the others was not well understood so studies were undertaken on each of these.

3.3.1 Hydrochloric Acid

The addition of sodium oleate to the growth mixture alters the reaction pH significantly which has important implications for the reaction kinetics. Solutions of sodium oleate above its CMC typically have pH values of ~pH 9. Increased concentrations of oleate will thus make the growth solution more basic and hence decrease the reduction potential increasing the formation rate of particles (see eq. (1.27)). If the pH is increased too far, this will result in the rapid formation of spherical particles.

This is already an issue in CTAB–only growth protocols where typically a concentration of 14 μM HCl is added to the growth solution to slow down the reaction kinetics, achieving a pH of ~1.5 [12]. If this HCl is not added to the reaction mostly spherical AuNPs are created. In the case of a oleate–CTAB mixture, initially an increase to 59 μM was used to reliably synthesise AuNRs.

Hence it was decided to explore the effect of changing the concentration of HCl in the growth solution. A single 48 mM CTAB, 12.5 mM oleate growth solution was prepared and aliquoted in 11 separate 10 mL aliquots, to this was added between 23 and 74 μM HCl, followed by the two reducing agents. The spectra of the synthesised AuNRs and the respective LSPR positions can be seen in fig. 3.5.

Based on the changes in the UV-vis spectra it can be seen that increases in the HCl volume above 18 μM leads to high yields of AuNRs evident from the decreased width of TSPR peak. Above this increasing the concentration leads to a redshift in the position of the LSPR, the changes in the height of the peak is broadly in line in what is expected from Gans theory, due to increasing plasmonic damping below 700 nm (see figs. 1.2 and 1.5), suggesting that the rod yield is quite high. The red–shift in this peak appears to stop once the the HCl volume is increased above 45 μL. HCl thus offers a potential method to fine–tune the LSPR resonance position of synthesised AuNRs.

A concentration of 59 μM HCl was used for all further syntheses, unless otherwise specified. It is worth noting that variations in pH will still occur for other syntheses as a result of changing the surfactant

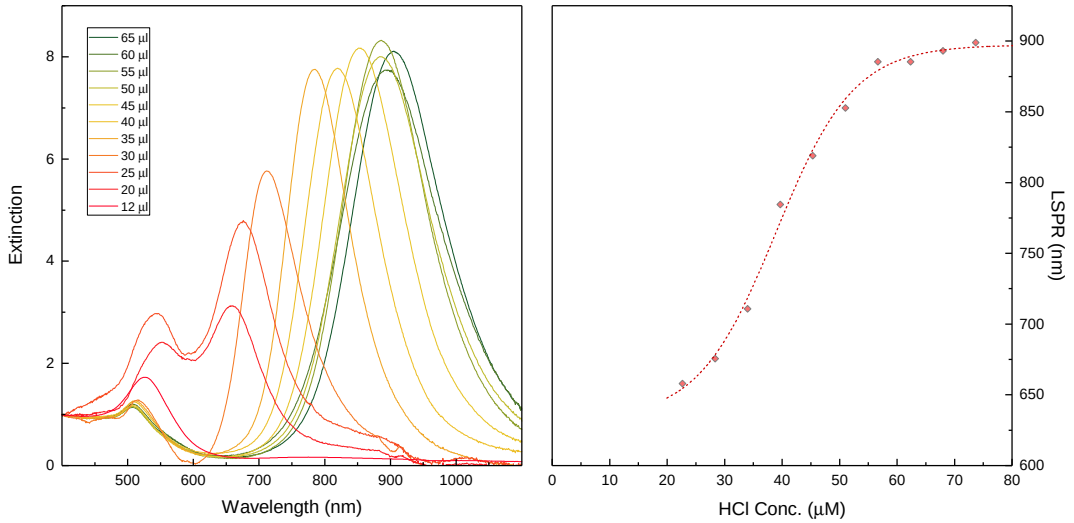

Figure 3.5: Effect of varying HCl concentration on synthesised AuNRs in a 48 mM CTAB, 12.5 mM oleate growth solution. **Left**: UV-vis spectra normalised to 400 nm. Low volumes of HCl ($\lesssim$ 25 µL) lead to high populations of AuNSs, increasing the HCl content further leads to a red–shift in the LSPR peak up to around 58.5 µM. **Right**: LSPR as a function of HCl volume, demonstrating the increase in LSPR peak position with increasing HCl concentration. This behaviour begins to plateau above $\sim$ 59 µM HCl. The data point associated with 28 µM has been omitted as no LSPR was visible (i.e. an overwhelming majority of spheres appear to have been synthesised.)

composition due to the limited buffering capacity of the growth solution, and hence further optimisation of the volume of the HCl concentration may actually improve these syntheses further.

3.3.2 Sodium Borohydride

The volume of the strong reducing agent added, $NaBH_4$, used to induce nucleation will shift the LSPR substantially. Increasing the amount of $NaBH_4$ added has been observed in other seedless protocols to decrease the aspect ratio of synthesised AuNRs (e.g. [302]). This is effectively the same as varying the number of seeds used in the seeded growth of single crystalline AuNRs. Increasing in the initial $NaBH_4$ concentration provides a greater number of nucleation sites onto which Au^0 can be reduced. Hence there are less Au ions per nucleation site, and the average particle volume will thus be lower. It has also been widely observed that monocrystalline AuNRs grow in a two–step process, initially an anisotropic growth phase leads to increasing aspect ratio, followed by a more isotropic growth phase where growth along the sides of the AuNR occurs at a similar rate to the tips, leading to increased AuNR volume, but a decreased aspect ratio [209, 367]. Hence increasing the number of AuNRs leads to the depletion of free Au ions during this initial anisotropic growth phase and the resulting AuNRs are lower volume, exhibiting a higher aspect ratio.

This behaviour can be observed in the kinetic UV–vis studies described below in section 3.5. Providing higher $NaBH_4$ concentrations leads to a lower availability of Au^{1+} per nucleation site and provides greater surface area to catalyse the reaction, leading this being depleted more rapidly and earlier completion of the reaction. Hence the growth of the nascent AuNR is terminated earlier and hence the anisotropic growth phase forms a larger fraction of the growth time cumulatively leading to the formation of smaller AuNRs with higher aspect ratio.

As shown in fig. 3.6, AuNRs synthesised in this binary CTAB–oleate system also show an increase

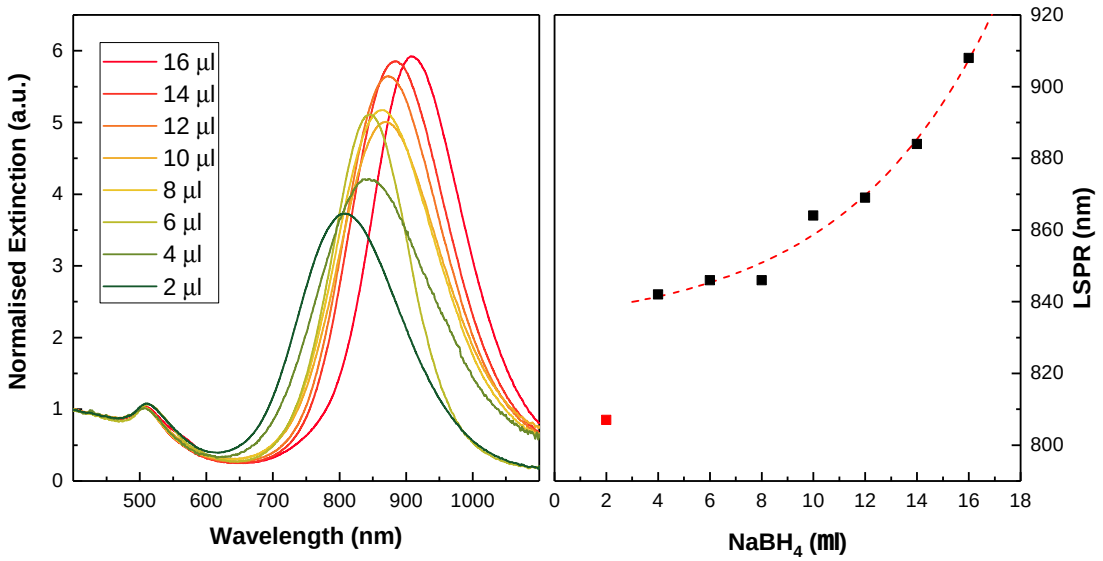

Figure 3.6: Effect of varying $NaBH_4$ concentration on synthesised AuNRs in a 48 mM CTAB, 12.5 mM oleate growth solution. **Left**: UV-vis spectra normalised to 400 nm. A general trend of increasingly red–shifted LSPR peaks can be seen with increasing $NaBH_4$ volumes. Low $NaBH_4$ volumes can be seen to lead to broader LSPR peaks (and hence more polydisperse). **Right**: LSPR as a function of $NaBH_4$ volume, demonstrating the increase in LSPR peak position with increasing $NaBH_4$ concentration. The red data point associated with 2 µL is not included in the fit.

in aspect ratio with increasing $NaBH_4$ volume. A single batch of 48 mM CTAB, 12.5 mM oleate growth solution was prepared and aliquoted in to 10 mL sub–samples; volumes of 10 mM $NaBH_4$ between 2 and 16 µL were then added to each. A clear increase in LSPR wavelength with increasing $NaBH_4$ volume can be observed, indicating higher aspect ratio AuNRs were synthesised. Given that there is expected to be an increased concentration of AuNRs and the same finite reservoir of Au ions available, it can be assumed that these AuNRs must have a lower diameter than those synthesised using smaller volumes of $NaBH_4$. The spectrum associated with 2 µL $NaBH_4$ is considerably off the general trend for other higher volumes. It is not clear whether this is the result of experimental error, or the result of a new regime of particle formation at low $NaBH_4$[1].

Whilst this demonstrates that $NaBH_4$ can be used to control the aspect ratio of synthesised AuNRs, it seems that 7.5 µL is a sensible $NaBH_4$ concentration to minimise variability between batches. This is because 7.5 µL falls in a section of the curve which is less sensitive to change in $NaBH_4$ concentration. The respective gradients at low (6 µL) and high (14 µL) $NaBH_4$ volumes are ~ 1 nm·µL^{-1} and ~ 9.7 nm·µL^{-1} respectively.

3.3.3 Silver Nitrate

The presence of silver ions in solution is essential to the formation of single crystalline AuNRs. Silver appears to play two key roles in the formation process, it is critical to the initial symmetry breaking in the formation of nascent nanorods, and beyond this is crucial to regulating the growth on the {110} facets along the sides of AuNR through a cycle of galvanic replacement and silver deposition leading to continued

[1] At some point the concentration of initial nucleation sites will become so low that the reaction will not complete within 4 hours and the LSPR wavelength measured here will no longer be representative of the 'completed' synthesis

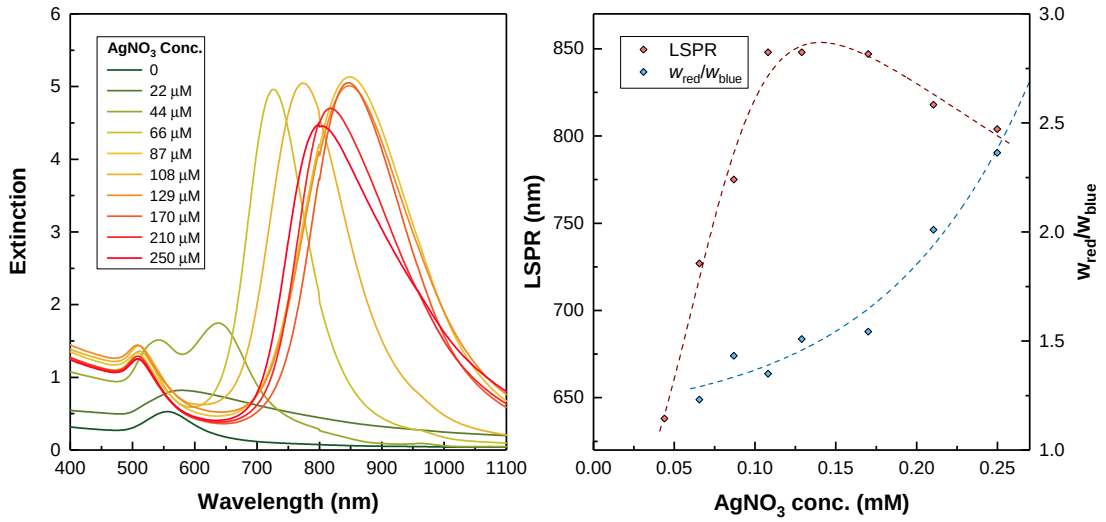

Figure 3.7: Effect of varying $AgNO_3$ concentration on synthesised AuNRs in a 48 mM CTAB, 15 mM oleate growth solution. **Left**: UV-vis spectra after inclusion of different concentrations of $AgNO_3$. A general trend of increasingly red–shifted LSPR peaks can be seen with increasing $AgNO_3$ concentrations. Low $AgNO_3$ volumes do not form AuNRs and higher ones led to increasingly polydisperse samples. **Right**: LSPR as a function of $AgNO_3$ concentrations. Also plotted is w_{red}/w_{blue} which is the ratio of the widths at half maximum above and below the LSPR peak.

anisotropic growth [348, 362]. Hence variation in the concentration of Ag in the growth solution is expected to have a strong effect on the aspect ratio of synthesised nanorods.

As is expected in the absence of $AgNO_3$, only AuNSs form, resulting from the fact that there are no Ag ions present to break the symmetry during the initial rod formation [362]. The presence of some particles of higher aspect ratio can be observed at 22 μM from the tail extending out into the NIR, but the population is still dominated by AuNSs. There then appears to be a threshold, between 22 and 44 μM, at which point nanorod formation becomes significantly more preferable. The AuNR aspect ratio can then be directly increased by increasing the amount of $AgNO_3$ added to the solution. This trend has been widely observed elsewhere in literature (e.g. [248, 253, 267, 302, 324, 394]). Interestingly though, once the Ag concentration increased up to ~108 μM, the LSPR wavelength decreases and an apparent increase in the polydispersity emerges, evident in the increasingly asymmetry in the LSPR peak.

In order to quantify this increasing asymmetry, the ratio of the widths at half maximum above and below the LSPR peak was measured for each LSPR (w_{red}/w_{blue}). This ratio is an indirect measure of the polydispersity resulting from increasing high populations of higher aspect ratio AuNRs (plotted in fig. 3.7). It was not possible to fit peaks where the LSPR and TSPR peaks overlapped significantly, hence it is only plotted for $AgNO_3$ volumes ≥66 μM. The manner in which the LSPR peak becomes increasingly weighted towards higher wavelengths is observable in the spectra of other publications, although normally uncommented upon (i.e. ref. [152]). It presumably results from the {110} stabilising role played by the $AgNO_3$, preferentially stabilising these facets making higher aspect ratio AuNRs more stable, however the limitations of this growth system seem to prevent these forming with high uniformity. It may be the case that optimisation of the growth kinetics may allow more monodisperse high aspect–ratio AuNR populations to be formed, although this has not been explored here.

Alongside the drop off in shape yield below 44 μM $AgNO_3$, there is noticeable reduction in the fraction of ionic Au that is reduced onto the particles. The reaction is also noticeably slower, taking significantly

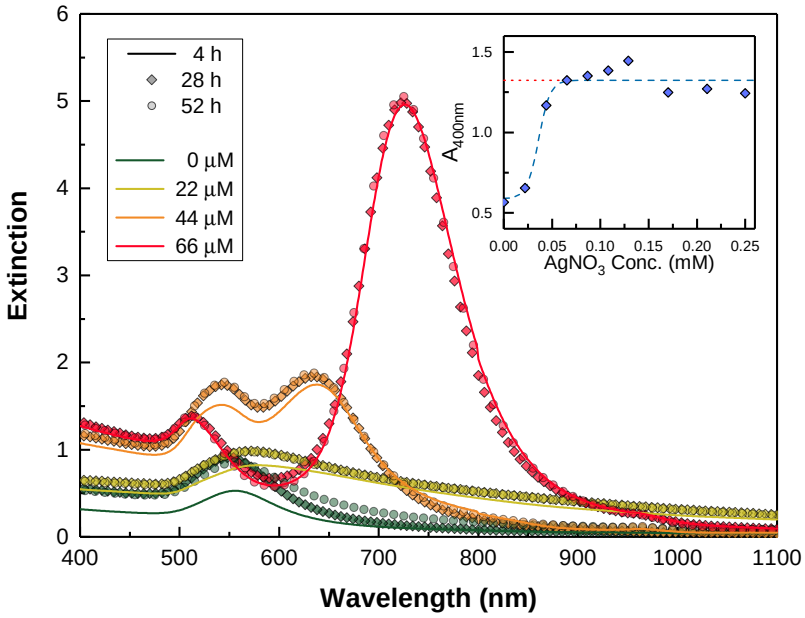

Figure 3.8: Samples at low $AgNO_3$ concentrations as recorded at 4, 28, and 52 hours after $NaBH_4$ addition. Samples above 66 µM $AgNO_3$ have been omitted as they showed no change after 4 hours. **Inset:** Absorbance at 400 nm after apparent completion of the reaction. Results are fitted with an sigmoid.

longer than 4 hours before the absorbance at 400 nm saturates[1] . This is somewhat unexpected as it has generally been reported in the literature than increased Ag concentration in the growth solution results in slower kinetics [43, 131, 308]. It can be see from fig. 3.8 that whilst there is little change 4 hours after $NaBH_4$ addition in the samples synthesised using greater than 66 µM $AgNO_3$ solution, those containing concentrations below this show continued particle growth during the following 24 hours. There were however only minor changes in the shape of spectra during this time period, suggesting an increase in the volume of the particles without any significant morphological changes.

The final values of $A_{400\,\mathrm{nm}}$ are lower, implying that Ag ions are some how acting as a limiting reagent in this synthesis at lower concentrations. This is probably not occurring through the silver acting as capping agent, as the large excess of free Au ions in solution should enable silver to be galvanically replaced on the particle surface. This has not been observed elsewhere in the literature, and remains unexplained as it currently stands.

It is apparent based on these measurements is that the $AgNO_3$ concentration is a reliable parameter to control the LSPR between ~44 µM and ~170 µM, but above this the polydispersity rapidly increases as the increasingly large population of higher aspect AuNRs form.

3.3.4 Ascorbic Acid

Ascorbic acid (AA) is the primary reduction agent during the synthesis, although the precise nature of its role is debated (see: section 1.5). Hence changes in its concentration will directly affect the kinetics of AuNR formation. There are a number of reports in the literature suggesting that increasing AA concentration leads to a decrease in aspect ratio (i.e. [198, 306]). However other reports, suggest that in fact the AA dependence of the aspect ratio falls on curve with positive gradient at low AA concentrations and negative at higher

[1] Interband transitions for Ag fall in the UV, so it should have minimal contributions to the extinction at 400 nm, hence it can be ignored as a reasonable approximation.

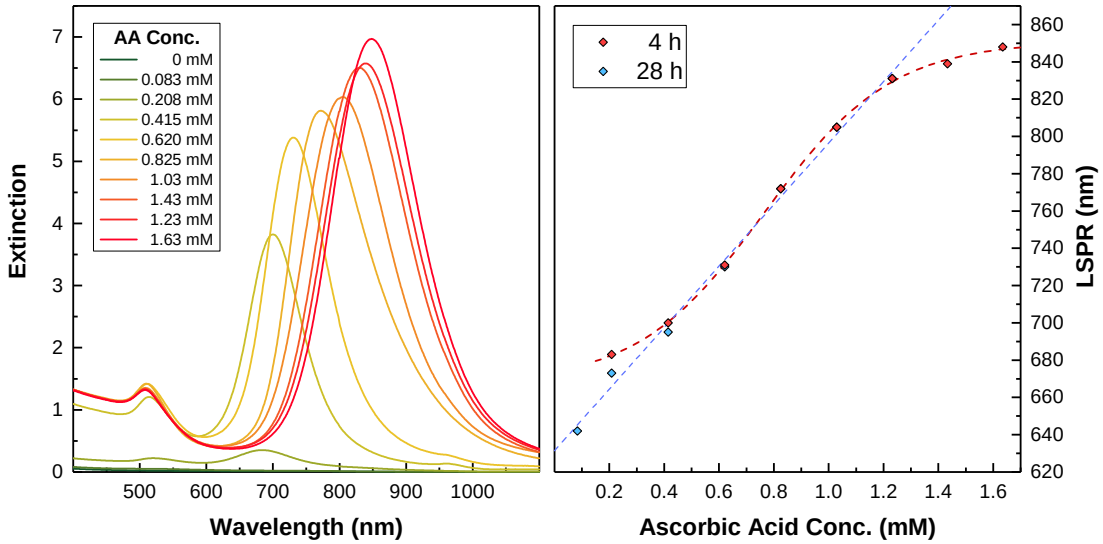

Figure 3.9: Effect of varying AA concentration on synthesised AuNRs in a 48 mM CTAB, 15 mM oleate growth solution. **Left**: UV-vis spectra of AuNRs synthesised using different concentrations of AA 4 hours after addition of $NaBH_4$. A general trend of increasingly red–shifted LSPR peaks can be seen with increasing AA concentration. LSPR peaks were not visible for the 0 and 0.083 mM samples. The 0.21 and 0.42 mM samples did not completely reduce all Au^{1+} in solution based on the the absorbance at 400 nm. All other spectra appear to have reduced the majority of Au^{1+} in solution. **Right**: LSPR as a function of AA volume. The values at 4 and 28 hours after $NaBH_4$ addition are presented as separate series they overlap above 0.62 mM. After 28 hours the additional LSPR peak visible in the 0.083 mM spectrum and shifted resonance in the 0.21 mM spectrum continue the linear trend seen at higher concentrations up to ~1.43 mM, compared with the more sigmoidal shape seen after 4 hours (see fig. 3.10 for 28 hour spectra).

concentrations [231, 399]. This relationship has been seen for other reducing agents such as hydroquinone [248]. It is not clear whether this discrepancy results from differences in the synthetic protocols or whether the same relationship is true in all and more syntheses at lower AA concentrations in studies suggesting a purely negative correlation would reveal this.

It has been also reported in the literature that large excesses of AA result in rapid uncontrolled deposition on the tips of the forming AuNR leading to the formation of 'dog–bone' or 'dumb–bell' structures [306, 399]. Although this is not immediately evident in the spectra of forming AuNRs and can only be confirmed by electron microscopy.

In the binary surfactant system used here, the presence of oleate complicates matters slightly. Oleate is a mild reducing agent, and during a synthesis can be observed to reduce Au^{3+} to Au^{1+}, evident by the clearing of the $HAuCl_4$ – surfactant mixture without the addition of AA. It is also generally present at a higher concentration than AA. The oleate–CTAB surfactant mixture alone (i.e. without the addition of Ag and HCl), is capable of nucleating AuNSs at higher temperatures (~60°C). It was not necessarily clear if oleate alone could perform the role of AA in forming AuNRs (albeit very slowly) post–introduction of $NaBH_4$ to the growth solution. Hence the reaction was performed also without the addition of any AA to the growth solution.

Following the same protocol as above, a single growth solution was split into several 10 mL samples and the concentration of AA added was varied between 0 and 1.63 mM. The resulting spectra and change in LSPR as a function of AA concentration are given in fig. 3.9. A very clear increase in the LSPR was seen with increasing AA concentration. The change in LSPR begins to plateau at around 1.43 mM. Hence the effect of AA concentration in this system appears to follow the behaviour reported in refs [231] and [399]

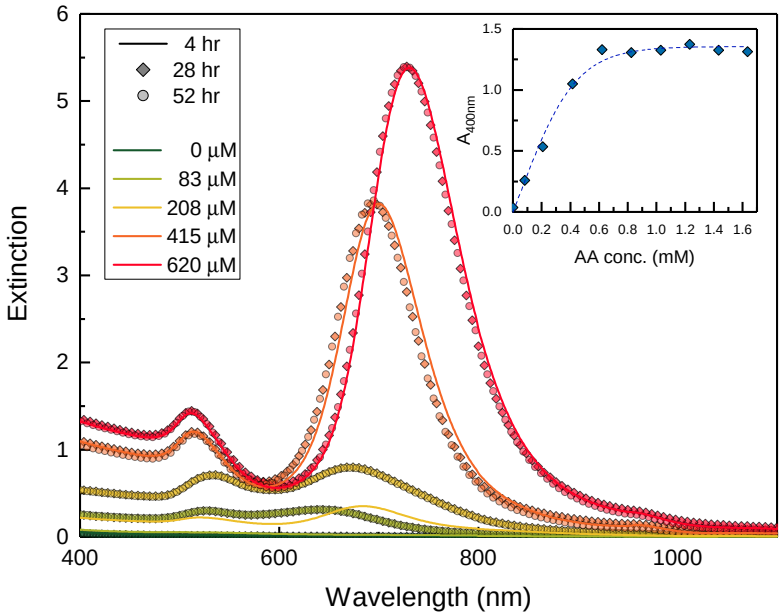

Figure 3.10: Samples at low AA concentrations as recorded at 4, 28 and 52 hours after $NaBH_4$ addition. Samples above 0.62 mM AA have been omitted as they showed no change after 4 hours. It can be seen that there is a slight change in the peak position of the 0.42 mM sample and substantial changes in the spectra of the 0.083 and 0.21 mM samples. There was no formation of AuNRs in the 0 mM sample at any time point. All samples showed no change between the 28 and 52 hour indicating the reaction had completed by 28 hours after $NaBH_4$ addition. **Inset:** Absorbance at 400 nm after apparent completion of the reaction as a function of AA concentration. Results are fitted with an exponential association.

in which the LSPR peak begins to drop at much higher AA concentrations, although to demonstrate this conclusively would require repeating this experiment with concentrations in excess of 1.7 mM.

The spectra shown in fig. 3.9 were taken four hours after addition of the $NaBH_4$, it can be seen that at concentrations of AA below 0.62 mM lead to incomplete reduction of the Au^{3+} in solution within 4 hours. Hence, the solutions were further incubated at 30°C and spectra taken at 24 hour intervals after this point. The spectra of all samples synthesised with concentrations of AA in excess of 0.62 mM showed no further change at 28 hours. However the spectra of samples containing 0.083, 0.21, and 0.42 mM AA continued to evolve over this time period, showing the reaction kinetics were considerably slower at these low AA concentrations. This is most clear in the 0.083 mM spectrum where two peaks not previously present emerged; but also in the 0.21 mM spectrum which increased considerably after this point. None of the spectra showed any change beyond 28 hours indicating the reaction had completed. The final concentration of reduced Au is also lower for these samples indicative of a regime where AA is the limiting reagent. The peaks from this 28 hour time point have been added as a separate series to fig. 3.9, and suggest that a linear change in LSPR wavelength with AA concentration is expected up to some critical value around 1.43 mM. It seems probable that the deviation from the linear trend seen above this results from depletion of the free of Au ions in solution (i.e. Au has become the limiting reagent) [82]; speculatively the addition of additional $HAuCl_4$ later in the growth may enable this trend to be extended further.

Also of note, is that the reaction does not progress at all without the presence of AA, this was also observed in the original seeded protocols utilising oleate [396]. Oleate on its own has too low a reduction potential to reduce Au^{1+} to Au^0 even with the presence of a Au surface at pH ~1.5 and T = 30°C. This would seem to imply that the role of AA in the synthesis is the direct reduction of Au^{1+} in solution to Au^0

on to the surface of the forming nanorod. Rather than acting as a scavenger of Au^{3+} after reduction on Au on the surface through a disproportionation reaction as has been suggested elsewhere [154]. Instead the conproportionation scheme suggested elsewhere seems more probable, as shown elsewhere by the inclusion of additional mild reducing agents [307].

Conversely the increase in AA will substantially speed up the reaction, and based on the spectra here appears to have little impact on the quality of the end–product. The synthesised rods show narrow symmetric peaks with high $A_{\mathrm{LSPR}} : A_{\mathrm{TSPR}}$ ratios, with no evidence of non–rodlike NPs in the spectra. This decreased synthesis time could potentially enable these sort of seedless synthesis techniques to be use to grow AuNRs via continuous flow methods which offers an easy method to substantially scale up such reactions for industrial production. However experimental confirmation of this would be required via kinetic monitoring of the UV–vis spectra of forming AuNRs at different AA concentrations allowing study of the kinetics of the reaction and electron microscopy evaluation of the morphological changes that could potentially result from this.

3.4 Darkfield Microscopy and Single Particle Spectroscopy

To investigate the change in the optical properties of the AuNRs at the single particle level, darkfield microscopy was performed on several batches of AuNRs. Single particle spectroscopy was perform on individual nanoparticles to qualitatively look at the position each AuNR's individual LSPR mode (the scattering and absorbance peaks are degenerate). In order to minimise background scattering signals piranha–cleaned glass cover slips were used at the substrates. Diluted AuNR solutions were then spun–coat onto the surface to provide well separated individual scatterers suitable for single particle spectroscopy. It was found that AuNRs with diameters below 15 nm were below the detection threshold of the single particle spectroscopy system, this is expected as the scattering section is proportional to V^2 (as approximated by Gans theory) [101].

Images showed sharp individual red spots with a consistent colour demonstrating the AuNPs were well separated on the substrate and monodisperse (fig. 3.11(d)–(f)), this colour is consistent with AuNRs resonant in the NIR [141]. Recorded single particle spectra showed distinct sharp resonance peaks for each AuNR measured, red–shifting with increasing average aspect–ratio (fig. 3.11(d)–(e)). The signal–to–noise ratio of the LSPR mode is noticeably improved for thicker AuNRs, in agreement with Gans theory [101]. The observed peaks show relatively close agreement with the optical properties expected at the morphologies given based on FEM simulations of their properties.

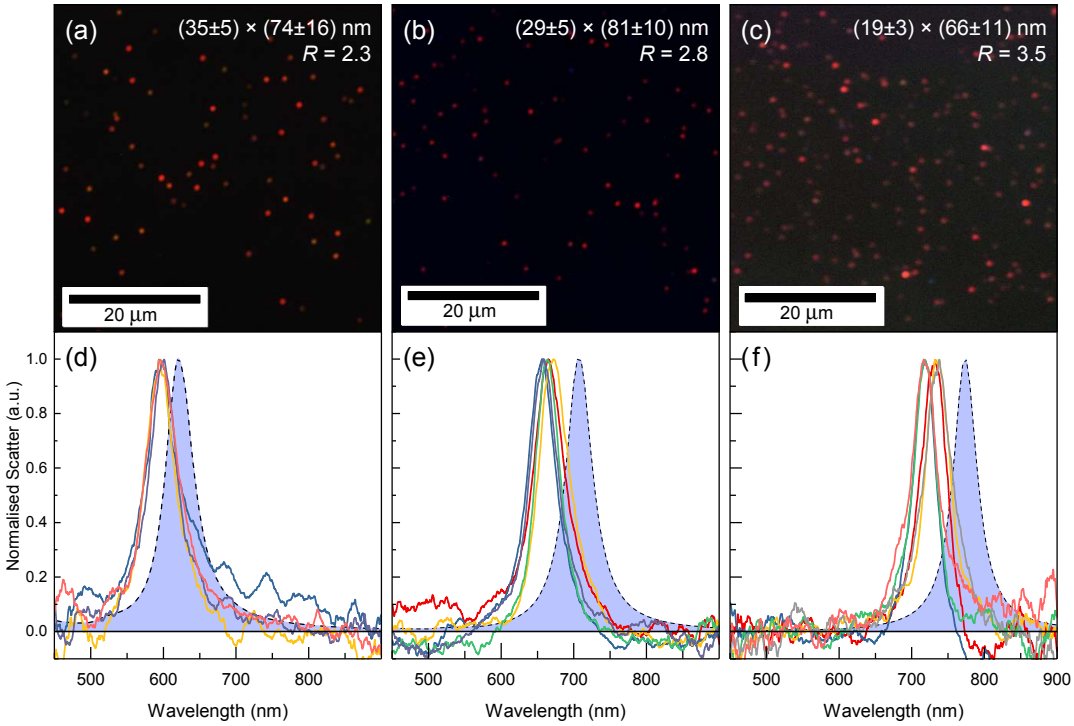

Figure 3.11: Darkfield microscopy images and single particle spectra of AuNRs.**(a)–(c)** Darkfield microscopy images of different aspect ratio (*R*) AuNRs spun–coat on a glass surface, average particle dimensions and standard deviation are inset on each figure (based on TEM measurements given in appendix A). Darkfield images are given at optimum exposure and gain settings for each sample.**(d)–(f)**: Single particle spectra obtained for each sample, showing the expected red–shift with increasing aspect ratio. The filled blue curve on each image is the FEM simulated–scatter spectra at an air/glass interface. The peak LSPR wavelength is close, but overestimated in the simulations, this likely results from end–cap geometry being presumed to be hemispherical *in–silico*. The shape of the spectra match the experiment relatively closely.

3.5 Kinetic UV–vis studies of AuNR formation[1]

To further understand the evolution of the AuNRs, their spectra during the synthesis were monitored. Spectra were taken at two minute intervals and the change in the peak wavelength, maximum extinction and FWHM of the LSPR recorded, as well as the extinction at 400 nm. From this we can make qualitative assessments of the concentration of reduced Au0 in solution, and the average aspect ratio and monodispersity of the synthesised AuNRs.

Additional kinetic spectra and their analysis are presented in appendix B.

In line with expectations, the spectra evolve in a similar fashion to those seen in silver–assisted seeded growths [82, 273, 307, 362]. The LSPR band becomes visible from the background after around 20 minutes and its position shows a rapid red–shift. This process slows and the peak position begins to blue–shift at a slower rate before settling to value in the NIR fig. 3.12. Throughout both phases there is growth in the extinction at 400 nm, indicating Au^0 is still being reduced from the solution. In the literature these shifts have largely been attributed to a rapidly anisotropic growth phase which results in a rapid increase in the forming particles aspect ratio, followed by a slower isotropic growth phase which results in a slow drop off in aspect ratio [273, 362].

[1] **n.b.** *The work presented here is ongoing and incomplete, it is intended to be supplemented with additional spectra and data.*

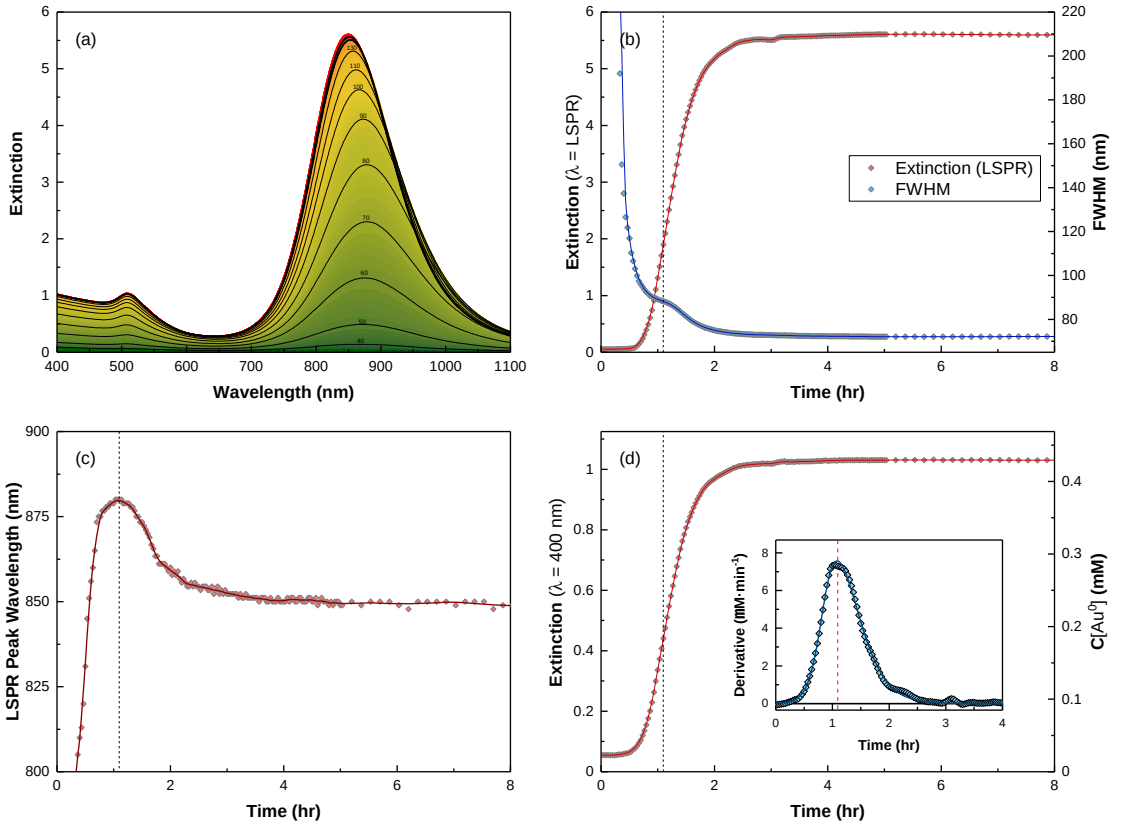

Figure 3.12: Kinetic UV-vis monitoring of AuNR synthesis. **(a)** Kinetic UV-vis spectra of a AuNR synthesis taken at 2 minute intervals using a growth solution containing 48 mM CTAB, 12.5 mM oleate. **(b)** Measured extinction at the LSPR maximum and LSPR full–width–at–half–maximum as determined by a Gaussian fit to the LSPR peak. **(c)** LSPR peak wavelength as a function of time, the stationary point of this curve at ~65 m has been marked by a dashed line in (b) and (d) also. **(d)** Extinction at 400 nm and the corresponding concentration of Au^0.

Edgar *et al.* using a CTAB–only growth solution, observed the reduction in LSPR peak wavelength occurs after Au^0 reduction has ceased. They suggest that this blue–shift cannot therefore be caused anisotropic growth and instead must be caused by reshaping of the AuNRs themselves, primarily through modification of the end–caps from sharp crystalline facets to more rounded tip geometries [82]. Changes in tip morphology can cause shifts of around 100 nm, as shown in simulations above fig. 3.3(b), so it is plausible for this be driving the change in peak LSPR wavelength. Other studies using statistical analysis of TEM images of AuNRs at different time points during synthesis, show that LSPR continues to blue–shift even after the length and diameter have stopped growing, due largely to morphological changes at the tips [273].

However, the experiments here do not show the reaction completing before the blue–shift in peak wavelength occurs. In every spectrum studied the peak LSPR wavelength was achieved at before or in tandem with the point at which the maximum Au^0 reduction rate was achieved, with extinction at 400 nm falling at ~40–50% of its maximum value at this point. Hence the AuNRs studied here are clearly still growing during this period, so it is not possible to eliminate changes in aspect ratio as the primary cause of this wavelength shift. The studies mentioned above only utilise CTAB in their growth solution, completing within 30–40 minutes [82, 273], by comparison the reactions here take more than 2 hours to complete, and are often significantly longer than this. The timescales for the processes which drive end–cap reshaping in these papers, such as cycles of oxidative etching and Au deposition, and adatom migration, occur over a

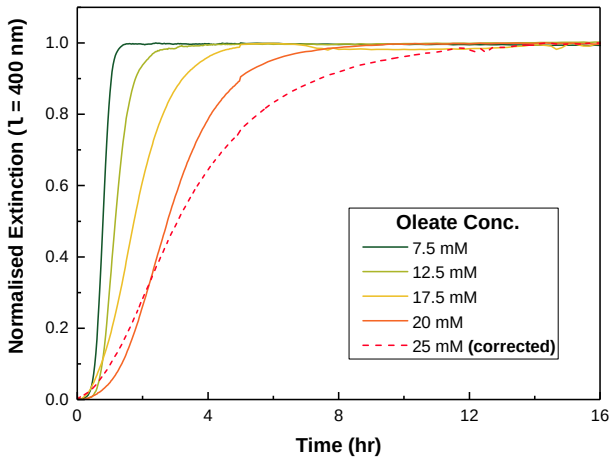

Figure 3.13: Effect of varying oleate concentration on the growth kinetics of AuNRs. Curves are normalised to the final stable value of A_{400nm}. **NOTE:** The 25 mM oleate curve is not raw data has been corrected to account for turbidity in growth solution, see appendix B for details of this.

period of an hour, hence it seems plausible that end–cap reshaping is probably occurring in tandem to the AuNR growth in our system.

The FWHM of the LSPR peak decreases throughout the reaction is occurring, suggesting the polydispersity of the AuNRs is consistently dropping. There is a noticeable point of inflection in a number of these curves that occurs around 90 minutes after $NaBH_4$ addition (A notable exception to this is appendix B, in which the reaction completed before this point). It is not clear at this point what causes this, but it seems to be largely independent of the surfactant concentrations, it is hoped further measurements will elucidate the cause.

Spectra were taken at a number of concentrations of oleate (C_{CTAB} = 48 mM), inspection of the change in the extinction at 400 nm shows a clear trend, with increasing oleate concentration leading to slower reaction rates (fig. 3.13). It seems probable that the driving force behind this is the increasing packing density of the surfactants on the AuNR as the molar fraction of oleate in the bilayer is increased reducing the accessibility of ions to the surface. However it is not possible based on these measurements alone to judge whether this is the case, this could plausibly be explained by the presence of more surfactant of any variety affecting the growth rate. It is intended that alongside completing this series; an additional series of syntheses be monitored at constant oleate concentration varying the CTAB concentration. If this results from the packing density on the surface then the reverse trend should be seen, increasing CTAB molar fraction should result in more rapid AuNR formation. Otherwise the reverse trend would indicate it results from surfactant concentration alone. Based on the trends in the LSPR peak wavelength seen in fig. 3.2 (roughly increasing LSPR with CTAB concentration, decreasing LSPR with oleate concentration), it seems probable that the former condition is true. Further clarification of this would require a study of the particle morphology at different time–points within the synthesis via electron microscopy.

The other apparent lesson learned from these experiments is that the decision to terminate the reactions after 4 hours may have erroneously led to conclusion that some of the syntheses performed at higher concentrations of oleate failed. When in fact synthesising for longer would have led to completion of the reaction.

3.6 Proposed Growth Mechanism

It is clear that the interaction between two surfactants in the system allows the synthesis of a much wider range of AuNR sizes. It is known that the addition of a negatively–charged oleate ion to the micellular CTAB structure screens electrostatic repulsion between the head groups allowing denser packing of the surfactant monomers leading to preferential formation of parallel arrangements of surfactant molecules, such as bilayers and rod–like micelles [180]. This is evident in studies of micelle formation in CTAB–oleate mixtures which show a significant reduction in the free energy of micellisation with increasing molar fractions of oleate [85, 229, 230]. For example, the 2nd CMC is reduced from 37 mM for 100% CTAB solutions [151] to ~1 mM for 90% CTAB – 10% oleate mixtures [85, 229]. Whilst the formation of these micelles has been shown to be largely irrelevant to the formation of AuNRs in the literature [104], the increasing packing implied by these results does appear to be crucial in enabling the formation of AuNRs at lower surfactant concentrations. We have synthesised AuNRs with high yield at CTAB concentrations as low as 20 mM, by contrast without the presence of oleate, concentrations of CTAB of around 100 mM were required [12, 146]. The increased packing of surfactant monomers in binary surfactant systems also appears to be crucial to accessing larger AuNRs. Broadly speaking higher molar fractions of oleate lead to lower LSPR resonance and these are generally achieved by synthesising higher diameter AuNRs.

It is proposed here that this change in packing density, alongside the role that Ag plays in driving anisotropic growth, results in the observed changes in morphology. The presence of silver is key to regulating the anisotropic growth of the AuNRs. Two competing processes lead to regulation of lateral growth, underpotential deposition of monolayers of Ag onto to the {110} facets along the edge of the AuNR preventing further Au deposition, and oxidative etching of this layer primarily by galvanic replacement [362]. This results in much slower growth in the lateral directions compared to the AuNR tips are not regulated by the presence of silver. Alongside this the presence of a CTAB bilayer at the surface also limits the rate of growth, by reducing the accessibility of Au ions to the NR surface. By incorporating oleate into this bilayer, increasing the packing density of surfactant monomers on the surface, access to the surface can be reduced further slowing the growth rate. Molecular dynamics studies suggest that CTAB is expected to pack on {100} and {110} facets at similar densities [223, 224], hence it slows growth in both the lateral and longitudinal directions to a comparable degree.

When the blocking effects of silver and the surfactants are considered in tandem, the overall effect of increasing the surfactant density on the surface of the AuNR is to decrease the growth rate to a greater relative extent than along the sides of the AuNR. Hence the overall result is a slower growth over which time relatively more growth occurs in the lateral direction[1].

Finally, the change in packing density of the surfactants may offer some explanation of the observed changes in end–cap morphology. A plausible, but untested hypothesis, is that the changes in packing density actually enable the surfactants to show increased affinity for higher index facets at the tips of the AuNRs. This may explain the range of tip morphologies seen in the TEM images of the AuNRs synthesised here. However changes in tip morphology are generally observed over the time–course of single crystalline AuNR

[1] One possible way to consider this to be the cumulative effects of two growth inhibition factors, R_{surf} and R_{Ag}, due to surfactants and Ag respectively. The ratio of cumulative effects of these on the {100} and {110} facets would thus be; $R_{surf}/(R_{\mathrm{Ag}} + R_{\mathrm{Ag}})$. Hence increasing R_{surf} would lead to this ratio tending towards unity. The net result being the relative amount of lateral growth over the course of the synthesis increases.

syntheses [82], so time–resolved electron microscopy would be required to clarify whether these result from point at which the synthesis was ceased, or they consistently form the tip geometries observed.

3.7 Conclusion

We have demonstrated that manipulation of the concentrations of CTAB and sodium oleate in the seedless synthesis of AuNRs represents a reliable method for the controlled modification of the morphology of AuNRs. The protocol has been shown to yield AuNRs of tunable dimensions with high shape yield and good monodispersity in a scalable manner. The effects of other parameters in the system have been investigated and also shown as controls on the optical properties of the synthesised AuNRs. Time–resolved UV–vis suggests the primary mechanism for affecting the synthesis is regulating the growth kinetics of the synthesised AuNRs, although this remains to be fully experimentally explored. The particles synthesised via this method will serve as a reliable method to simply produce AuNRs in large–scale with suitable optical properties for the theranostic applications we intend to pursue.

Chapter 4

Surface Modification of Gold Nanoparticles with Phospholipids

4.0.1 Motivation

The use of CTAB in the synthesis of AuNRs is problematic for their biological applications. Whilst the optical properties of AuNRs are highly desirable and requires the used of CTAB, it is highly cytotoxic (intraveneous LD_{50} = 44 mg·kg^{-1}), and particles stabilised with it present poor colloidal stability. Since no reliable alternative to the use of CTAB in the bulk liquid–phase synthesis of AuNRs has emerged, a large body of work has focused on the development of novel surface functionalisations to passivate or displace CTAB on the surface of AuNRs. These are discussed in section 1.6, and have mostly focused on thiol displacements, or coating the CTAB layer in silica or polymers. Some work, however, has been focused on the use of phospholipids to replace the CTAB bilayer. These are of particular interest as such coatings have the potential to mimic surfaces already found inside the body such as cell membranes or other theranostics moieties such as microbubbles. They also offer an easy route to improve the biocompatibility and tune the surface functionalisation of AuNRs, enabling the straight forward inclusion of targeting ligands and or fluorophores. In this chapter, we discuss the characterisation and colloidal stability of various nanoparticle surface modifications.

4.1 Functionalisation Strategies

4.1.1 Polyelectrolyte Passivation

Polyelectrolytes have become a popular method of passivating the surface of CTAB–functionalised AuNRs. Negatively–charged electrolytes such as poly(styrene sulfonate) (PSS) or poly(acrylic acid) will electrostatically self assemble on the positively charged CTAB bilayer surface. Due to the change in surface charge, the coating process must be performed in the presence of at least 1 mM buffer to screen charge interactions preventing rapid aggregation [109]. These methods were initially performed as a single–step, but further studies have shown that particles treated this way still possess a relatively high cytotoxicity largely due to the slow release of CTAB through this coating, this can be reduced much further through repeated cycles of

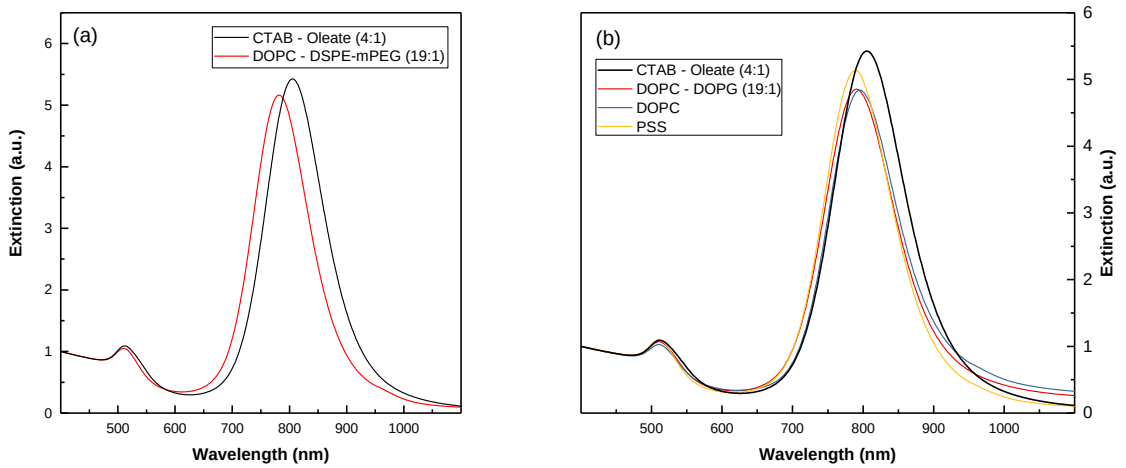

Figure 4.1: (a) UV-vis spectra of AuNRs before and after surfactant exchange with DOPC – DSPE-mPEG (19:1). **(b)** UV-vis spectra of AuNRs before and after functionalisation with DOPC, DOPC – DOPG (19:1), and PSS. Spectra have been normalised to 400 nm.

passivation [196]. These techniques also afford the ability to build–up alternating layers of negatively and positively charged polymers on the surface of the AuNR [109] and also incorporate chemotherapeutic drugs within the polyelectrolytes as a means of achieving drug delivery [139].

For the purposes of this work, particles were treated with PSS, according to three–step coating process detailed in ref. [196]. Which briefly consists of resuspending the as-synthesised concentrations of AuNRs in an equal volume of 10 mg·ml^{-1} PSS solution (+1 mM NaCl) and left stirring overnight. AuNRs were washed by centrifugation and resuspended in 1 mg·ml^{-1} PSS solution, this was repeated twice, before a final round of centrifugation followed by resuspension in Milli–Q water.

4.1.2 Surfactant Exchange

The phrase "*surfactant exchange*" is used here to refer to a group of techniques that have emerged in the literature which directly replace the CTAB bilayer on the surface of AuNRs with other surfactants, such as phospholipids or fatty acids. These techniques generally consist of redispersing a pellet of CTAB–functionalised AuNRs in a large excess of the desired surfactant in solution and then providing energy to encourage exchange between the solution and the particle surface in the form of heat or sonication. These techniques have been reported for a number of molecules including phospholipids [222, 266, 304, 339, 398] and oleic acid [204, 364]. We have elected to focus purely on phospholipids here, as oleate is too toxic to use for *in vivo* applications, having an intravenous LD_{50} of 150 mg·kg^{-1} in rats (by comparison CTAB is 44 mg·kg^{-1}). Naturally occurring phosphatidylcholines have an LD_{50} in excess of 10000 mg·kg^{-1} and are widely considered nontoxic comprising 20–25% of cell membranes [9, 377]

Phospholipids offer a number of benefits resulting from the highly tailorable properties of lipid membranes, allowing potential surface functionalisation which offer low non–specific binding, or the inclusion of specialist functionalised lipids, enabling the conjugation of targeting ligand and fluorophores, or inclusion of steric–stabilising agents such as DSPE-mPEG. Phospholipids can be purchased relatively cheaply in bulk[1] and the surfactant exchange procedure is straightforward, scalable and reproducible.

[1] For comparison, functionalisation with DOPC costs approximately £0.10 per mg of AuNRs compared with £0.05 of CTAB used to synthesise them.

The method followed here is similar to that published by Matthews *et al.* [222], although the sonication time was significantly increased. The following lipid compositions were investigated; DOPC, DOPC – DOPG (19:1), and DOPC – DSPE-mPEG (19:1). Whilst Matthews *et al.* have reported that DOPC–functionalised AuNRs were unstable [222], our results are counter to this, and a number of other studies have found that phosphatidylcholines can stably displace CTAB from the surface of AuNRs [50, 267, 304, 398]. In brief, the following protocol was used for each phospholipid functionalisation; each millilitre of 75 mg·mL^{-1} AuNR solution was centrifuged at 9000*g* for 30 m and and the precipitate resuspended in 300 µl of 10 g·L^{-1} lipid SUV solution, this mixture was then sonicated in a refrigerated sonication bath overnight. It was found after a single round of sonication that the ζ–potential of DOPC–AuNRs in 1 mM NaCl (pH 7) still presented a positive charge (+8 mV), suggesting the continued presence of CTAB (this is consistent with the observed ζ–potential results in refs [267] and [398]). An additional round of centrifugation, resuspension in DOPC SUV solution, and sonication reduced this to neutral. Thorough removal of CTAB was deemed a priority and hence a further round of phospholipid displacement was added to minimise any trace amounts of CTAB.

4.2 Nuclear Magnetic Resonance Spectroscopy

To identify the molecular species present on the surface of the AuNRs ^{1}H NMR was employed. ^{1}H NMR allows identification of molecular species by observing the relative shift in the resonance of hydrogen nuclei in a strong magnetic field. A 11.7 T magnetic field was used here producing a 500 MHz resonance for free ^{1}H. This resonance shifts due to spin–spin coupling between protons within a molecule. In particular, this shift is characterised by other atoms bound to a particular ^{1}H nucleus, and the atoms immediately neighbouring those atoms within the molecule. Hence these shifts can be used to identify the chemical environment of a proton within the molecule. These shifts are typically in the range of -4 – 14 ppm. Each molecule will generate a set of measurable characteristic chemical shifts which can be used to identify it.

NMR studies of the surface coatings of AuNPs are somewhat challenging. They pose two major challenges, firstly from the small amount of material bound to the surface of the particles, means that very high AuNP concentrations must be used in order to achieve good SNRs. Secondly, the rotational correlation time of the molecules of interest, typically on the order of ~1 ps when free in solution, are significantly increased when bound the surface of a much larger object with a rotational tumbling time on the order of ~1 µs[1]. The net result of this is a broadening (and hence reduction in amplitude) of the NMR peaks which increases with particle diameter [219], this can be particularly problematic at larger particle diameters as the resultant peaks can be difficult to resolve. The same problem occurs for molecules which self–assemble into larger structures such as micelles. Finally, the resonances associated with protons close to an Au surface are expected to undergo what is known as a 'Knight shift' [172]. An apparent chemical shift due to the hyperfine coupling between unpaired conduction electrons in the metal and nuclei in close proximity to the metal surface [172, 219, 366]. These shifts have been observed elsewhere for CTAB bound to the surface of AuNRs, for the γ–methyl protons this is normally a shift of ~0.06 ppm relative to CTAB free in solution [142, 266].

[1] Tumbling time calculated using: $\tau_R = 4\pi\eta a^3/3k_BT$. where η is the dynamic viscosity, T is the ambient temperature, and a is the hydrodynamic radius of the particle ($\eta = 10^{-3}$ Pa·s, $k_BT = 4.1 \cdot 10^{-21}$J). For an (11 × 45) nm AuNR, $a = 10.2$ nm, hence $\tau_R \sim 1$ µs [155].

Alternative methods of performing NMR on such samples have been deployed elsewhere, such as complete oxidative etching of the AuNR with KCN, followed by lyophilisation and subsequent dissolution in a deuterated solvent [310]. The resultant NMR spectra obtained by this method do not display any peak broadening, but the harsh etching conditions cause the appearance of additional peaks associated with various hydrolysis and oxidation products of reactions between the molecules functionalising the surface and the etchants. These methods have been observed to result in the complete dissolution of CTAB rendering it undetectable in the NMR spectra, which make this method completely unsuitable for use here [310].

NMR has been employed by Orendorff *et al.* to demonstrate the replacement of CTAB on the surface of their AuNRs with POPC [266]. Key to demonstrating the removal of CTAB was monitoring the chemical shifts associated with the γ–methyl protons in the trimethylammonium (3.11 ppm) and choline (3.39 ppm) groups of CTAB and POPC respectively (see fig. 4.2 for labeled molecular diagrams). The other chemical shifts associated with CTAB from the alkane chain broadly overlap with those expected from the hydrocarbon chains of a phospholipid.

The system under analysis here is more complex as the surface coatings initially comprised of a CTAB – oleate mixture and are hoped to have been replaced with a DOPC – DSPE-mPEG mixture through surfactant exchange. Hence NMR spectra must be collected for each component molecule in the surface coatings and peaks unambiguously associated with CTAB identified. Fortunately, oleate does not possess any chemical shifts in the range of 3–4 ppm and DSPE-mPEG's β and ζ chemical shifts are significantly above those expected from those in CTAB's γ–trimethylammonium group.

4.2.1 Results

CTAB and Oleate

The observed chemical shifts for the CTAB – oleate functionalised AuNRs and their identifications based on the experimentally determined chemical shifts and literature values for free CTAB and oleate are as follows:

Label	Chemical Shift (ppm)	Identification	
		CTAB	Oleate
a	0.94	1 (CH_3)	1 (CH_3)
b	1.35	2–13 (CH_2)	2–7, 12–15 (CH_2)
c	1.62	– –	16 (CH_2)
d	1.81	15 (CH_2)	– –
e	2.10	– –	8, 11 (CH_2)
f	2.18	– –	17 (CH_2)
g	3.20	γ (CH_3)	– –
h	3.39	16 CH_2	– –
i	5.41	– –	9,10 (CH)

Table 4.1: ^{1}H NMR chemical shifts from CTAB – oleate (4:1) functionalised AuNRs and their identified CTAB and oleate peaks as given in fig. 4.3(c). Peaks have been identified based on the experimentally determined chemical shifts given in fig. 4.2(a)&(b).

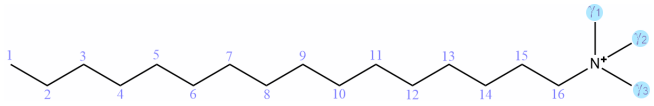

(a) CTAB

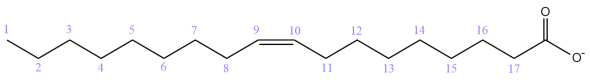

(b) Oleate

(a) CTAB chemical shifts

Chemical Shift (ppm)	Identification	*n*
0.94	1 (CH_3)	2
1.36	2–13 (CH_2)	22
1.44	14 (CH_2)	2
1.85	15 (CH_2)	2
3.24	γ (CH_3)	9
3.48	16 CH_2	2

(b) Oleate chemical shifts

Chemical Shift (ppm)	Identification	*n*
0.89	1 (CH_3)	3
1.30	2–7, 12–15 (CH_2)	20
1.56	16 (CH_2)	2
2.05	8,11 (CH_2)	4
2.17	17 (CH_2)	2
5.37	9,10 (CH)	2

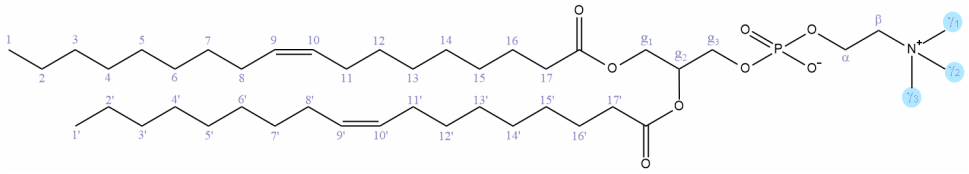

(c) DOPC

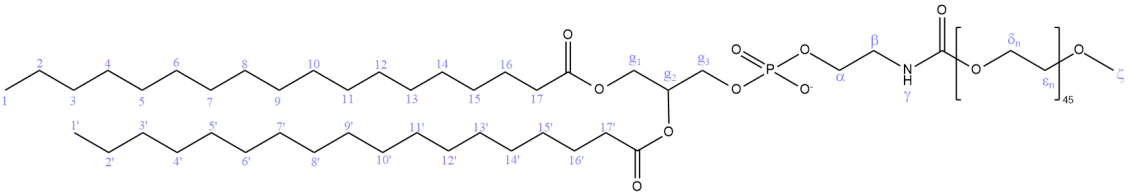

(d) DSPE-mPEG

(c) DOPC chemical shifts

Chemical Shift (ppm)	Identification	*n*
0.91	1, 1' (CH_3)	6
1.35	2–7, 12–15 (CH_2) 2'–7', 12'–15' (CH_2)	40
1.60	16, 16' (CH_2)	4
2.07	8, 11, 8', 11' (CH_2)	8
2.40	17, 17' (CH_2)	2
3.27	γ (CH_3))	9
3.70	α (CH_2)	2
4.27	g_3 (CH_2)	2
4.35	β (CH_2)	2
4.45	g_1,(CH_2)	1
5.35	g_2 (CH)	1
5.38	9, 10, 9', 10' (CH)	4

(d) DSPE-mPEG chemical shifts

Chemical Shift (ppm)	Identification	*n*
0.90	1, 1' (CH_3)	6
1.31	2–15 (CH_2) 2'–15' (CH_2)	56
1.61	16, 16' (CH_2)	4
2.35–2.40	17, 17' (CH_2)	4
3.36	ζ (CH_3)	3
3.39	β (CH_2)	2
3.57	δ_{45}, ε_{45} (CH_2)	4
3.64	ε_1 (CH_2)	2
3.72	δ_n, ε_n (CH_2)	~86
3.86–3.90	α (CH_2), γ (NH_2)	3
4.00	g_3	2
4.21	g_{1a} (CH_2)	1
4.44	g_{1b}, δ_1 (CH_2)	3
5.29	g_2 (CH)	1

Figure 4.2: ^{1}H Chemical shifts and identifications for **(a)** CTAB, **(b)** oleate, **(c)** DOPC, and **(d)** DSPE-mPEG in D_2O. The corresponding identifications for each protonated atom in each molecule are given in their respective molecular diagrams. Identifications are based on calculated chemical shifts in MestReNova and published values for CTAB [142, 183, 266], oleate [320], DOPC [330] and DSPE-mPEG [133]. *n* indicates the number of ^{1}H associated with each chemical shift on each molecule. The trimethylammonium groups in CTAB and DOPC have been highlighted.

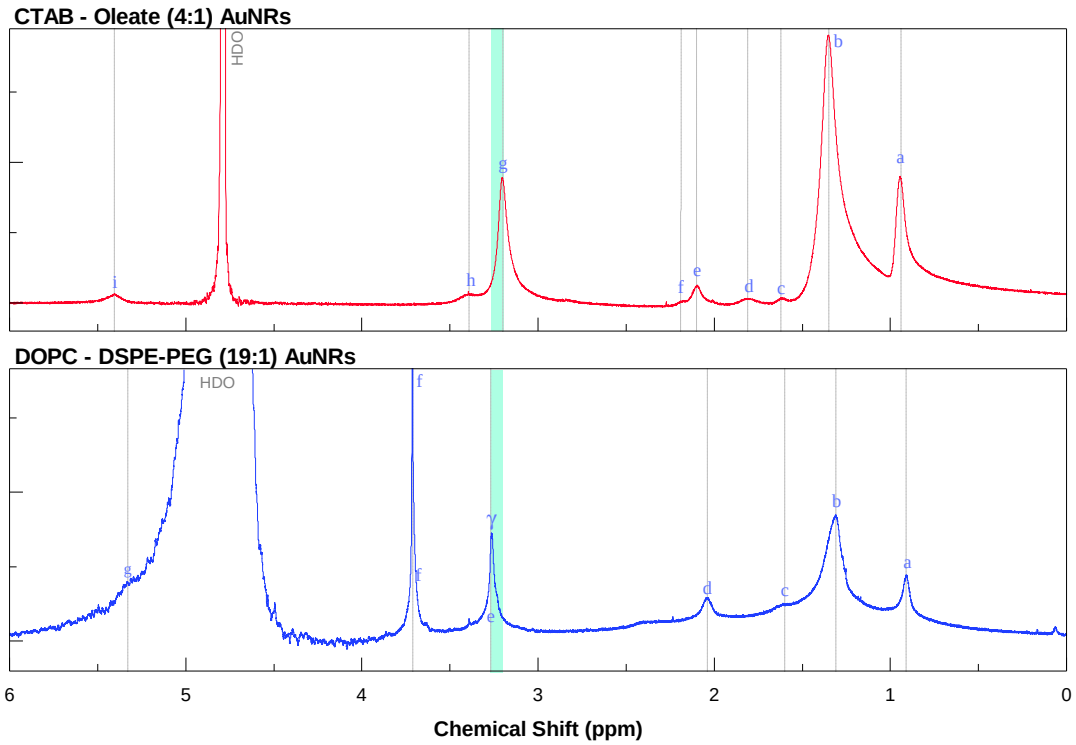

Figure 4.3: ^{1}H NMR spectra for **(top)** ~25 nM CTAB – oleate (4:1) functionalised AuNRs, and **(bottom)** ~25 nM DOPC – DSPE-mPEG (19:1) functionalised AuNRs. Chemical shifts labels are given in fig. 4.2 and tables 4.1 and 4.2. All spectra were taken in D_2O, details of sample preparation and acquisition settings for each spectrum are given in section 2.5.3. Spectra for pure CTAB, oleate, DOPC and DSPE–PEG are given in

As shown in fig. 4.3(c) the presence of both CTAB and oleate can be seen on the surface of the AuNRs based on the peaks given in fig. 4.3(a)&(b). The peaks are noticeably broader compared to the free molecular solutions as a result of the reduced mobility of the molecules when bound to the surface of an AuNR. Also, the SNR is significantly lower due to the reduced concentrations of each molecules on the surface of the AuNR compared to the 10 mM free molecular solutions. In order to achieve the SNR seen here for the colloidal scans averages over 384 spectra was required, this is an unusually large number of spectra, by comparison averaging over 16 spectra was required to get the much higher SNR seen for the free molecular solutions.

The asymmetric peaks at 0.94 and 1.36 ppm correlate well with the -CH_3 and -[CH_2]- ^{1}H nuclei of the alkyl chains. Peaks at 2.10 and 5.41 match the expected positions for ^{1}H nuclei neighbouring and within the alkene of the oleate chain. Shifts associated with the ^{1}H nuclei located in the -[CH_2]- monomers closest to the carboxylic acid head group of the oleate are also visible at 1.62 and 3.39 ppm. Similarly the protons from the equivalently positioned -[CH_2]- monomers from the CTAB can also been resolved in the spectrum at 1.62 and 3.39 ppm. These peaks suggest a mixed composition of CTAB and oleate present on the AuNR surface.

Most important for the work here is the peak observable at 3.20 ppm, associated with the γ–methyl protons in the trimethylammonium group. This is lower than observed in for the free molecular solution of CTA+. This has been observed elsewhere and is caused by a Knight shift due to the close proximity to the Au surface of the nanorod [142, 266, 331]. This peak falls in a different position to that expected for the γ–methyl protons found in the choline of DOPC, unlike other peaks which are largely degenerate with CTAB. Hence it can be used to detect the present of CTAB on the AuNR surface

The value of 3.20 ppm seen here is slightly higher than seen elsewhere (i.e. 3.12 ppm [142], 3.16 ppm [331], 3.11 ppm [266]), this may potentially result from the inclusion of the negatively charged headgroup of oleate into the CTAB bilayer on the particle, such changes in the chemical shifts have been observed in mixed micellular system [118]. Regardless this is not problematic as it is still resolvable from the observed position of the DOPC shift at 3.27 ppm.

DOPC and DSPE-mPEG

The observed chemical shifts for DOPC – DSPE-mPEG functionalised AuNRs and their identifications based on the chemical shifts experimentally determined for free DOPC and DSPE-mPEG are as follows:

Label	Chemical Shift (ppm)	Identification	
		DOPC	DSPE-mPEG
a	0.91	1,1' (CH_3)	1,1' (CH_3)
b	1.31	2–7,12–15 (CH_2) 2–7,12–15 (CH_2)	2–15 (CH_2) 2'–15' (CH_2)
c	1.60	16,16'	16,16' (CH_2)
d	2.04	8,11,8',11' (CH_2)	– –
e	3.27	γ (CH_3)	– –
f	3.71	– –	δ_n, ε_n (CH_2)
g	(5.33)	9,10,9',10'	– –

Table 4.2: ^{1}H NMR chemical shifts from DOPC – DSPE–mPEG (19:1) functionalised AuNRs and their identified DOPC and DSPE–mPEG peaks as given in fig. 4.3(f). Peaks have been identified based on the experimentally determined chemical shifts for 'free' DOPC/DSPE-mPEG given in fig. 4.2(d)&(e).

Unfortunately, in the spectra of the free lipids, a peak associated with the presence of contaminating methanol at 3.36 ppm is visible. This appears to have contaminated the system during tip sonication, as a result of residual methanol from cleaning the tip and jacketed beaker used in preparing the SUV solutions. It also overlaps the expected position of the ζ–methyl group of the DSPE-mPEG. It is not present in the spectrum of the phospholipid coated AuNRs and hence does not affect the viability of this measurement in determining the presence of CTAB.

Peaks at 0.91, 1.31 and 1.60 (weak) ppm can be attributed to the alkyl chains in both DOPC and DSPE-mPEG. Additionally peaks at 2.04 and 5.33 (weak) ppm can be attributed to the double bonds located in the chains of DOPC. The ^{1}H resonances of the -[CH_2]- monomers in the PEG chains of DSPE-mPEG are clearly visible at 3.71 ppm. There is no evidence of methanol contamination in the spectra of the phospholipid–functionalised AuNRs.

Most importantly, the chemical shift associated with the CTAB γ–methyl protons is not visible in the spectrum of the AuNRs, instead only a single peak at 3.27 ppm is visible in NMR spectra of the DOPC – DSPE-mPEG functionalised AuNRs. While complete elimination is impossible to argue from the low SNR of these measurements, they do suggest that substantial displacement of the CTAB from the surface of the AuNRs by phospholipids has occurred. However this measurement on its own is limited in its sensitivity by the low SNR and needs to be supported by additional measurements. Hence it was decided to accompany this with with additional molecular spectroscopy in the form of surface–enhanced Raman spectroscopy.

4.3 Raman Spectroscopy

Surface–enhanced Raman spectroscopy (SERS) was used as an additional technique to identify the species of molecules present on the surface of our AuNRs. Raman spectroscopy is a technique based on the measurement of inelastically scattered light from a monochromatic source off of a sample. Shifts in the frequency of scattered light are caused by interactions between the electronic distribution around the molecule and incident light. Vibrational modes in molecules which alter the polarisability of this distribution present characteristic frequencies shifts which can be used to characterise the molecular species present. Additionally, the large near–surface electric fields generated at the tips of a AuNR, when excited at their LSPR, allows enhancement of Raman scattering by as much as 10^{14}–10^{15} times [250] enabling the study of the relatively small amount of material located there with much higher sensitivity. Hence study of molecule–specific Stokes shifts enables identification of the species of molecule present on the particle surface.

The Raman system available offered illumination wavelengths at 532 and 785 nm, it was decided to maximize the field enhancement at the particle surface by utilising particles synthesised with a LSPR maximum at 800 nm. This was close to the 785 nm excitation sources and offered a resonance close to the maximum plasmonic Q–factor for Au (see fig. 1.2(c)), and hence the largest attainable field enhancement. After CTAB displacement coating this peak wavelength shifted to 790 nm offering a closer match to the excitation wavelength.

4.3.1 Raman Peak Identifications

100–350 cm^{-1} – Bromine and Poly(ethylene glycol) Deformations

The band observed at 176 cm^{-1} has been attributed to the $\nu(Au{-}Br_2^-)$ mode [177]. This peak is not present in solutions of pure CTAB and can be observed to shift in AuNP solutions when the counter–ion is exchanged with other halide ions such as chloride [195]. Bromide will form a polar covalent bond with Au atoms at the surface of the NR, enabling the weak ionic bonding of CTA^+ onto the particle surface. The presence of this peak is not unexpected, as the trimethylammonium head groups of both phosphocholine and CTA+ are both capable of binding to $AuBr^-$. This peak has been observed to remain in SERS studies of AuNRs coated by DOPC displacement of the CTAB performed by Matthews *et al.*, suggesting that phosphocholines bind to the surface through the same ionic interaction albeit at a lower density [222]. Contradicting this, more recently Santhosh *et al* published a study observing that the $\nu(Au{-}Br_2^-)$ peak vanishes over the course of displacing CTAB with DMPC [304]. However, their sensitivity to the $\nu(Au{-}Br_2^-)$ peak is far lower than observed here. Observing a $\nu(Au{-}Br^-)$ peak around half the height of the $\nu(C_4N^+)$ headgroup peak at ~ 760 cm^{-1}. By comparison, in this study and in Matthews *et al*, the $\nu(Au{-}Br^-)$ peak was significantly more intense, at $\sim 22\times$ and $\sim 60\times$ bigger respectively. This is expected due to the SERS enhanced of material in close proximity with the surface. Based on this disparity, it seems that tracking the amplitude of the $\nu(Au{-}Br^-)$ peak is not a reliable method of establishing the presence of CTAB. It is also not clear why bromine would dissociate from the particle surface during the displacement. It will form a relatively strong polar covalent bond with the Au surface, and should interact with the quaternary ammonium group of phosphocholines in the same manner as the one found on CTAB. Hence, it seems unlikely the resilient of this peak is indicative of the presence of bromine on the surface.

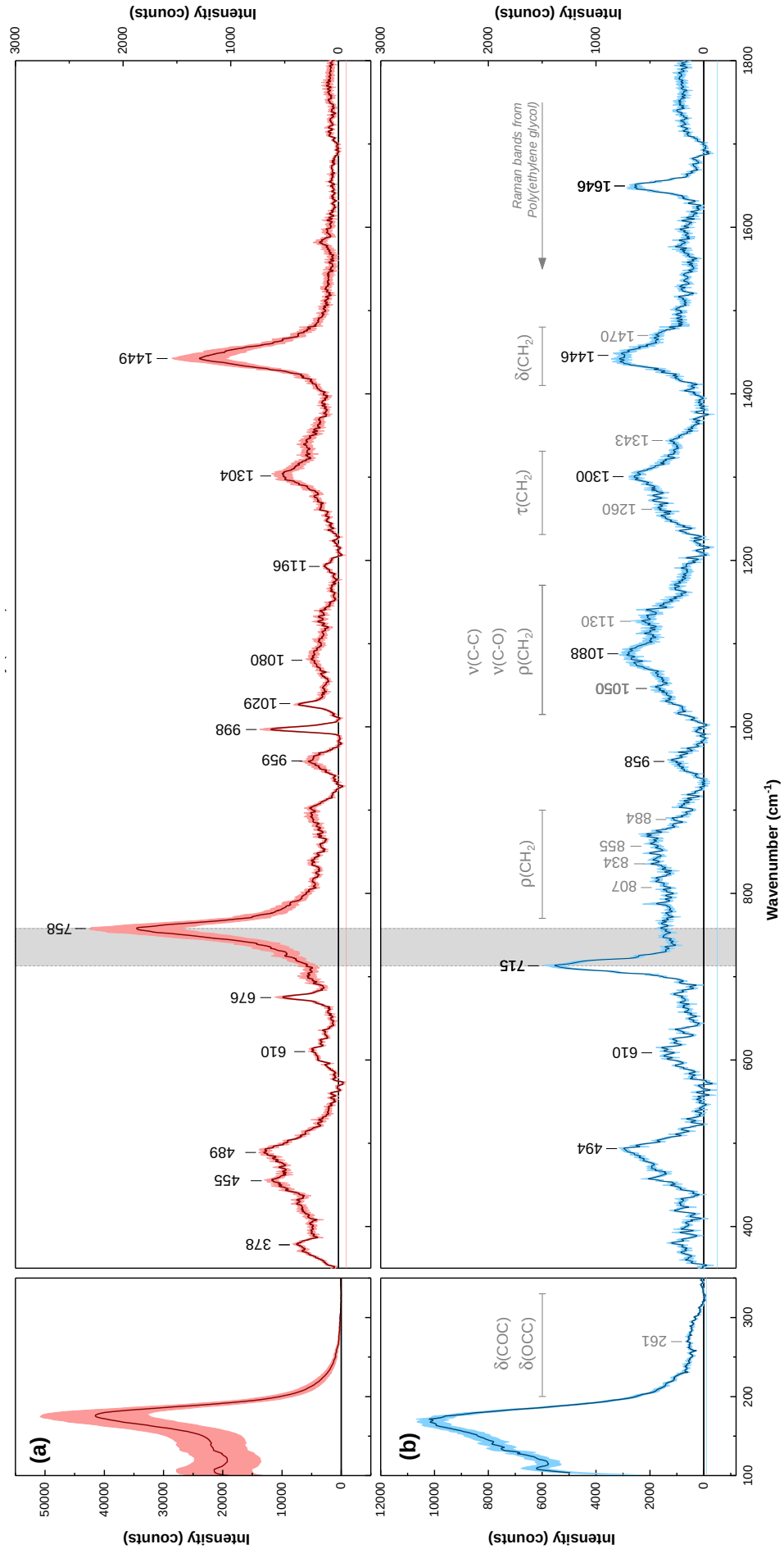

Figure 4.4: SERS spectra of AuNRs functionalised with **(a)** CTAB – oleate (3:1), and **(b)** DOPC – DSPE–mPEG (19:1). Peak positions have been annotated based on the identifications that are given in table 4.3. In **(b)** large bands are visible in the spectrum resulting from the broad overlapping peaks associated with the poly(ethylene glycol) chains of DSPE-mPEG. The regions occupied by these bands are marked in grey above the spectrum, the specific Stokes shifts contributing to these have been marked on the spectrum itself in grey.

Literature Values				Experimental
CTAB		Oleate		CTAB – oleate AuNRs
f (cm^{-1})	Identification	f (cm^{-1})	Identification	f (cm^{-1})
179	ν(Au-Br$^-$)	– –	– –	179
371	δ(C$_4$N$^+$)	– –	– –	378
455	δ(C$_4$N$^+$)	– –	– –	455
493	δ(C$_4$N$^+$)	– –	– –	489
– –	– –	602	ν(OC=O)	610
– –	– –	*630–800?*	*δ(C-O)?*	676
763	ν(C$_4$N$^+$)	– –	– –	758
964	ν(C$_4$N$^+$)	– –	– –	959
998	ν(C-C)	– –	– –	998
1029	ν(C-C)	1023	ν(C-C)	1029
1086	ν(C-C)	1096	ν(C-C)	1080
1196	*w*(C-C)	– –	– –	1196
1306	τ(C-C)	1301	τ(C-C)	1304
1449	δ(C-C)	1440	δ(C-C)	1304

Literature Values						Experimental
DOPC		DSPE		Poly(ethylene glycol)		DOPC – DSPE-mPEG AuNRs
f (cm^{-1})	Identification	f (cm^{-1})	Identification	f (cm^{-1})	Identification	f (cm^{-1})
179	ν(Au-Br$^-$)	– –	– –	– –	– –	179
– –	– –	– –	– –	261	δ(OCC)	261
483	δ(C$_4$N$^+$)	– –	– –	– –	– –	494
602	ν(OC=O)	602	ν(OC=O)	– –	– –	609
715	ν(C$_4$N$^+$)$_{gauche}$	– –	– –	– –	– –	715
(768)	ν(C$_4$N$^+$)$_{trans}$	(759)	ν(C-N)	– –	– –	(768)
				807	τ(CH$_2$)	– –
				834	τ(CH$_2$)	– –
				855	τ(CH$_2$)	– –
				884	τ(CH$_2$)	– –
960	ν(CN$^+$)	– –	– –	– –	– –	958
– –	– –	– –	– –	1052	ν(C-O), ν(C-C)	(1050)
1082	ν(O-P-O), ν(C-C)	1082	ν(O-P-O), ν(C-C)	– –	– –	1088
1128	ν(C-C)	1128	ν(C-C)	1134	ν(C-O), ν(C-C)	(1130)
– –	– –	– –	– –	1242	τ(CH$_2$)	(1260)
1305	τ(CH$_2$)	1305	τ(CH$_2$)	1292	τ(CH$_2$)	1300
1340	τ(CH$_2$)	1340	τ(CH$_2$)	1352	*w*(CH$_2$)	(1342)
1440	δ(CH$_2$)	1440	δ(CH$_2$)	1448	δ(CH$_2$)	1445
1460	δ(CH$_2$)	1460	δ(CH$_2$)	1470	δ(CH$_2$)	(1473)
1654	ν(C=C)	– –	– –	– –	– –	1646

Table 4.3: Peak wavenumbers and identifications of Raman spectra. Values found in the literature are presented alongside the values observed experimentally here. Peaks considered too weak to be confidently identified as a peak are indicated in brackets. **Left:** Raman shift peak wavenumbers for CTAB and oleate. **Right:** Raman shift peak wavenumbers for DOPC, DSPE and PEG. Gaps between the broad overlapping Raman shifts of PEG have been indicated by a horizontal line. The following symbols have been used to denote the specific vibrational modes identified: ν = stretching, δ = bending, τ = twisting and *w* = wagging modes. The wavenumbers and identifications for peaks in the Raman spectra for CTAB were identified based on values obtained from refs. [75, 95, 160, 177, 195]. Values and identifications for oleate from refs. [67, 71, 72]; Values and identifications for DOPC and DSPE from refs. [135, 182, 194, 210, 240, 268, 329]. Values and identifications for PEG from refs. [160, 176, 263, 301]. Additional information on the shifts associated with specific functional groups was taken from refs [257, 258, 325].

The presence of a monolayer of Ag is expected on the {110} facets along the sides of the AuNR [131, 405], hence relatively high amounts of $AgBr_2^-$ is expected to be present close to the particle surface [252]. These should present an additional SERS peak at 156 cm^{-1} in addition to the one from $\nu(Au-Br_2^-)$ [153], however this is not observable in either of the spectra from CTAB– or phospholipid–functionalised AuNRs. This probably results from the concentration of the excited field at the tips of the AuNR where there is expected to be minimal amounts of Ag present. The selected excitation wavelength will predominantly excite the LSPR of the particles and hence yields much higher field enhancement at the tips of the AuNR, leading to much higher sensitivity the molecules located there, as is evident from the plots of Raman enhancement in fig. 1.8(b) and (c).

A broad band centred at 261 cm^{-1} appears in the spectrum of AuNRs functionalised with DOPC – DSPE-mPEG, and is not present in the CTAB functionalised spectrum. This has been attributed to the δ(OCC) and δ(COC) modes of PEG [176]. The band comprises of the supposition of multiple peaks centred on 226, 169, and 365 cm^{-1} associated with variations on these bending modes.

350–700 cm – Trimethylammonium Asymmetric Stretching Modes and Carboxylic Acid

In the spectrum of the CTAB – oleate AuNRs, peaks can be seen at 378, 455, and 489 cm^{-1} associated with the asymmetric stretching modes of the trimethylammonium group of CTAB. Only one of these modes can be resolved in the spectrum of the DOPC – DSPE-mPEG functionalised AuNRs at 489 cm^{-1}. A peak can be seen in both spectra at 610 cm^{-1}, this can be identified as the ν(OC=O) mode of the carboxylic acid headgroups and carboxylic acid esters of the oleate and phospholipids respectively.

In addition to these, a distinct peak at 676 cm^{-1} can be seen on the CTAB – oleate functionalised AuNR spectrum. There are no functional groups in CTAB which would produce a vibrational mode at this wavenumber. For oleate, there are two potential candidates the out-of-plane $\delta(R_1HC{=}CHR_2$ mode (665–730 cm^{-1}) and the in–plane δ(C–O) mode (630–800 cm^{-1}) associated with carboxylic acid headgroup [325]. The latter seems more probable, both vibrational modes are only weakly Raman active, hence a significant field enhancement would be required to give the peak seen in the spectrum. Given that the negatively charged headgroups of oleate are expected to intercalated amongst the positively charged headgroups of CTAB, they should be in close proximity to the particle surface explaining this enhancement. However some studies of micelle–structure have suggested that the double–bond of oleate can also sit in this layer, although it is unclear that this would be true for a supported bilayer on the surface of a particle [85, 229]. This peak has been tentatively identified as the δ(C–O) mode. It is not present in the phospholipid–stabilised AuNR spectrum, whilst DOPC does contain carboxylic acid esters they will sit further from the particle surface, and hence will receive significantly less field enhancement. The removal of this peak does suggest that the oleate is removed from the particle surface during the displacement process.

700–800 cm^{-1} – Trimethylammonium Symmetric Stretching Modes

The peak observed at 763 cm^{-1}, in the spectrum of the CTAB – oleate AuNRs, has been widely recognized to be associated with the symmetric $\nu(C_4N^+)$ mode of the CTAB headgroup. The position of this peak is consistent across a range of *n*–alkyl trimethylammonium cations[1]. It has become a useful diagnostic for the

[1] i.e. for *n*–alkyl trimethylammoniums where; $n = 6$, $\nu_{CN+} \sim 760$ cm^{-1} (from FTIR [SpectraBase]), $n = 7$, $\nu_{CN+} = 762$ cm^{-1} [177], $n = 8$, $\nu_{CN+} \sim 760$ cm^{-1} [ChemBook], $n = 9$, $\nu_{CN+} = 760$ cm^{-1} (from FTIR [SpectraBase]), $n = 10$, $\nu_{CN+} = 761$ cm^{-1} [106], $n = 12$, $\nu_{CN+} = 762$ cm^{-1} [ChemBook], $n = 14$, $\nu_{CN+} = 761$ cm^{-1} [106], $n = 16$, $\nu_{CN+} = 761$ cm^{-1} [106]

presence of CTAB in SERS studies of surface coatings [202, 222, 304, 342], due to the high sensitivity to this peak resulting from its close proximity when binding to a metallic surface.

By comparison the trimethylammonium group found in the choline headgroup of DOPC has a associated symmetric $\nu(C_4N^+)$ peak at 720 cm^{-1} [329]. The difference in wavenumber between the $\nu(C_4N^+)$ symmetric shifts between these two molecules stems from the presence of the electronegative negative oxygen located in the choline. This can be seen from the sensitivity of this shift to conformational changes in the headgroup. With the trans conformation yielding a peak of ~770 cm^{-1} and the gauche conformation yielding a peak of ~715 cm^{-1} [6, 22]. This is a common method to measure the population of conformations within bilayers (e.g. refs. [6, 7, 88, 120, 170, 358]). This sensitivity to conformation is suggested to originate from electrostatic interactions between the electronegative oxygen atom and positively-charged quaternary ammonium, both contained with the choline group [20, 22]. By comparison, the trimethylammonium group found on CTAB is insensitive to conformational changes seen in choline despite the close similarities between the two functional groups and consistently presents a Stokes shift of ~ 760 cm^{-1}[259]. Even though the trans conformation is the predominant conformer of DOPC found in bilayers, a small population of the choline headgroups are typically observed in the gauche conformation regardless, leading to the observation of a small peak around 770 cm^{-1} [6, 293]. Due to the close proximity of this peak to one associated with the symmetric $\nu(C_4N^+)$ CTAB peak, resulting in residual CTAB being more difficult to distinguish from the this small population of gauche conformers. However, a significantly higher SNR, than achieved here, would be required to resolve this gauche peak in these experiments.

Finally, DSPE-mPEG presents a weak band at 759 cm^{-1} associated with the ν(C–N) mode of the amide linker [182, 257]. This will overlap the $\nu(C_4N^+)$ peak of CTAB at 763 cm^{-1}. This is not a major concern given how weak this peak is, and also that DSPE-mPEG is expected to sit in the outer leaflet of the surface bilayer leading to relatively minor electric field enhancement at this bond.

Despite these potential additions at this wavenumber, there is no obvious peak that can be observed in the Raman spectrum of the DOPC – DSPE-mPEG at 768 cm^{-1}, suggesting that the majority of the CTAB has been removed from the surface of the AuNR. However the strong background signal attributed to the PEG chains of the DSPE-mPEG makes it difficult to make any further assertions beyond this. The numbers of counts at the DOPC $\nu(C_4N^+)$ is 1380 compared to 360 at 760 cm^{-1} quantitatively putting an upper limit for CTAB content at 26%. However it seems more probable, given that the presence of any peak at 760 cm^{-1} is impossible to distinguish from the background that the amount of CTAB present has been reduced to below the threshold of detection.

800–1500 cm^{-1} – Phosphate Group and Alkyl/Poly(ethylene glycol) Chains

A peak is visible in both spectra at ~959 cm^{-1} this is attributable to two degenerate asymmetric $\nu(C_4N^+)$ modes, associated with the trimethylammonium in both CTAB and DOPC. This peak position is insensitive to conformation and hence appears in the same place for all conformers of DOPC [6]. An additional asymmetric $\nu(C_4N^+)$ mode is expected to have a peak at 870 cm^{-1} and 910 cm^{-1} for DOPC and CTAB are also expected, but these are not resolvable in either spectrum [6, 75].

The rest of the observable peaks are either present in both spectra (i.e. from the alkyl chains), or only found in spectra of the phospholipids used here (e.g. phosphate and poly(ethylene glycol)). Hence they are not particularly useful as a diagnostic for the presence of CTAB. Peaks in the spectrum of CTAB – oleate

AuNRs at 1029, 1080, 1196, 1304, and 1449 cm^{-1} are all associated with the alkyl chains of CTAB. The observable peaks in the DOPC–DSPE-mPEG AuNRs at 1088, 1300, and 1445 cm^{-1} are all associated with the alkyl chains of the lipids and are close to peaks seen in the CTAB – oleate AuNR spectrum. It is probable that the ν(O−P−O) mode from the phosphate also contributes to the peak at 1080 cm^{-1}. Also, a peak at 1646 cm^{-1} associated with the ν(C=C) mode is evident and associated with the alkene bond in the chains of DOPC.

Finally, there is clearly a strong contribution from poly(ethylene glycol), which has make the background appear very uneven. Inspection of the Raman spectra of poly(ethylene glycol)s shows that these characteristically have strong bands resulting from overlapping peaks in the following regions: 770–900 cm^{-1}, 1015–1170 cm^{-1}, 1230–1330 cm^{-1}, 1410–1480 cm^{-1} [176]. These bands are marked on fig. 4.4 and the various peaks that contribute to them are summarised in table 4.3.

4.3.2 Summary

The absence of the trimethylammonium asymmetric stretching modes in the DOPC – DSPE-mPEG AuNR spectrum gives another good indication that the quantity of residual CTAB has been reduced to a very small population. It is difficult to provide absolute quantification, due to the strong background resulting from other components in our surface. All the peaks identified are consistent with the expected species of molecules present on the surface of our particles.

4.4 Zeta Potential – pH Response of Surface Functionalisations

In addition to the molecular spectroscopy performed, a pH–dependent ζ–potential study was undertaken. The electrostatic properties of the coatings of colloids can be directly measured via their ζ–potential. Different surface ligands will provide nanomaterials with varying different surface charges dependent on their surface packing density and the functional groups comprising the molecule. The charge of which are dependent on the surrounding medium pH, with different groups becoming ionised at their respective pK_a values. The ionised fraction of a given functional group can be expressed in terms of its pK_a and the bulk pH. This is expressed by the Henderson–Hasselbalch equation [122, 123], which gives the ionised fraction of anionic and cationic functional groups, X_{n-} and X_{n+} respectively, at a given pH as:

$$X_{n-} = \frac{1}{1 + 10^{\mathrm{p}K_a - \mathrm{pH}}} = \frac{[X^-]}{[XH] + [X^-]} \tag{4.1}$$

$$X_{n+} = \frac{1}{1 + 10^{\mathrm{pH} - \mathrm{p}K_a}} = \frac{[X^+]}{[X^+] + [XOH]} \tag{4.2}$$

where H and OH, are cationic and anionic counterions respectively (i.e. they do not necessaily have to be a proton or hydroxyl ion). According to Gouy–Chapman theory the ζ–potential of a given particle is related to the surface charge density, σ by an $\sinh^{-1}(\sigma)$ function [105]. Hence ζ increases with $|\sigma|$, and the change in σ due to ionisation/deionisation of functional as a result of a change in pH can be seen in the measured ζ–potential. Hence the pK_a values of individual molecules comprising the surface coating can be used to assess the species of molecules present on the surface of a particle, by observing changes in the

Molecule	Functional Group	pK_a	
CTAB	*Trimethylammonium*	n/a	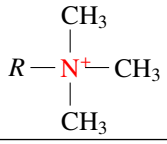
Oleic Acid	*Carboxyl*	5	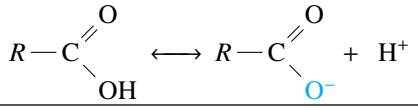
DOPC	*Phosphate*	1.86 (1)	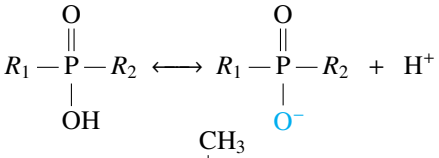
	Trimethylammonium	n/a	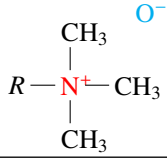
DOPG	*Phosphate*	1.89 (2.8)	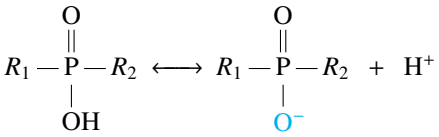
	Hydroxyl	13.7	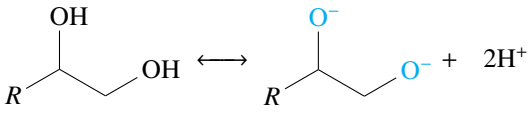
PSS	*Sulphonic acid*	-1.92	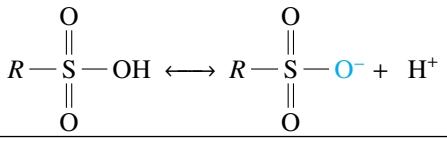
DSPE-mPEG	*Phosphate*	1.88	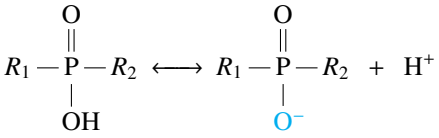
	Ethylene oxide	–	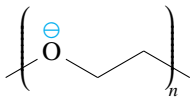

Table 4.4: Functional groups of the various molecules used to functionalise AuNRs in this section and their associated pK_a values. pK_a values were calculated using ChemAxon. The pK_a values in brackets for DOPC and DOPG are observed shifts due to inclusion in a bilayers or liposomes.

ζ–potentials as a function of medium pH. The pK_a values of the important functional groups found in the various molecules used to functionalised AuNRs in this section are given in species used in table 4.4. More importantly the presence of CTAB can be determined by measurement of a positive ζ–potential at pH values which should induce a net neutral surface charge in other species of capping agents. Alongside the DOPC – DSPE-mPEG functionalised AuNR discussed above; PSS, DOPC and DOPC – DOPG functionalised AuNRs have also been characterised by this technique.

As no single buffer can span the entire range of pH used here, a range of buffers were used (detailed in section 2.5.1). No unusual effects came about of as a result of this and the behaviours of measured ζ–potentials were consistent between buffers and with theory. All buffers used were diluted to 10 mM from the stock concentrations given in section 2.5.1 using degassed Milli–Q grade water. It is worth remembering that the stability thresholds for the magnitude of the ζ–potential specified in the same section have little

meaning for particles which are sterically stabilised or stabilised using zwitterions.

The embedding of molecules within a bilayer structure will lead to shifts in the pK_a values and a broadening of the pH response [266]. This results from the close packing of headgroups attracting counter–ions in solution creating a locally different pH compared to bulk solution [387]. For instance, positively charged functional groups will attract negatively charged ions from solution creating a local environment which is effectively lower in pH than in the bulk solution.

4.4.1 Results

CTAB

In order to provide a basis for assessing the presence of residual CTAB on the surface of the surface–modified AuNRs a single batch of AuNRs were synthesised using 100 mM CTAB (no oleate was added and the HCl concentration was also reduced by 75%). Resulting in AuNRs stabilised by CTA+ ions only.

The positively charged trimethylammonium group in CTA+ is permanently ionised in solution, hence particles stabilised with it should present a constant positive ζ–potential so long as the background ion concentration is maintained. This behaviour was witnessed for CTAB-capped AuNRs across all pH (fig. 4.5). However the actual surface charge presented by the CTAB coating was also dependent on the background concentration of CTAB, as it exists in a dynamic equilibrium with the background concentration of free CTA+ ions [296]. As this background concentration drops the packing density of CTA+ on the surface drops and the resultant ζ–potential also drops. In this experiment, the particles were washed twice by centrifugation before being resuspended in 10 mM buffer, reducing the concentration of CTAB in the bulk solution to approximately 0.1 mM, close to the limit of stability (further washing resulted in irreversible aggregation). The measured value of ζ ~ 20.5 mV, while low, reflects the depletion of the surface bound CTAB due to repeated washing. It would be expected to increase if additional CTAB were added to the colloidal dispersion (or alternatively a lower buffer concentration were used) to values in line with the higher zeta potentials reported elsewhere (e.g. refs. [11] and [410]).

CTAB – Oleate (4:1)

By comparison AuNRs prepared by the method outlined in chapter 3, using a 38 mM CTAB and 10 mM oleate growth solution (~ 4:1 molar ratio) yield a ζ–potential which changes dynamically with pH. The ζ–potential is positive at all pH values consistent with a higher surface concentrations of CTA+ than oleate-, however the presence of the negatively charged oleate ions in the surface coating has substantially suppressed the ζ–potential below the threshold for electrostatic stability in 10 mM buffer (they are stable in water for at least two years).

The pK_a of the –COOH head group of the oleate leads to a positive shift of the ζ–potential at lower pH. The estimated pK_a for a free molecule is 5.0, however the measured shift in ζ–potential indicates a pI of 4.3 suggesting a shift in the pK_a of the oleate relative to the bulk pH. This is not unexpected due to the packing of the negatively charge headgroups of oleate in amongst an excess of positively charged trimethylammonium headgroups, leading to localised repulsion of cations in the vicinity of the water/bilayer interface and an apparent pH shift of ~ 0.7 locally based on these measurements [387].

Also notable is the ratio of the ζ–potentials above (12.2 mV) and below (29.2 mV) the apparent pK_a, is actually not reflective of the ratio of surfactants used to the synthesis the AuNRs (4:1), but more closely

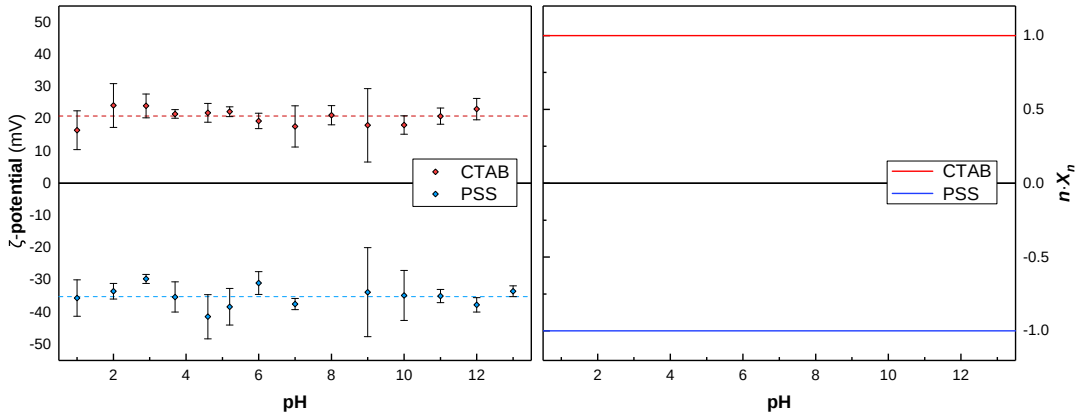

Figure 4.5: Left: Experimentally determined ζ–potentials for AuNRs coated with 100% CTAB and PSS as a function of buffer pH (10 mM). **Right:** Theoretically predicted charge for a population of CTAB and PSS monomers, where n is the ionisation number and X_n is the ionised fraction.

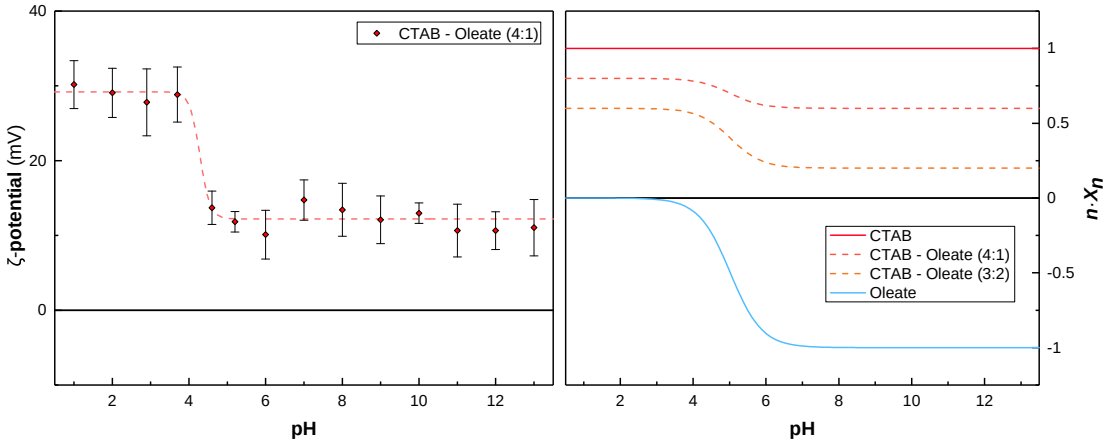

Figure 4.6: Left: Experimentally determined ζ–potentials for AuNRs synthesised in a CTAB – oleate (4:1) mixture as a function of buffer pH (10 mM). **Right:** Theoretically predicted charge for a population of CTAB and oleate monomers, where n is the ionisation number and X_n is the ionised fraction. Also presented are the predicted curves for 4:1 and 3:2 CTAB – oleate mixtures.

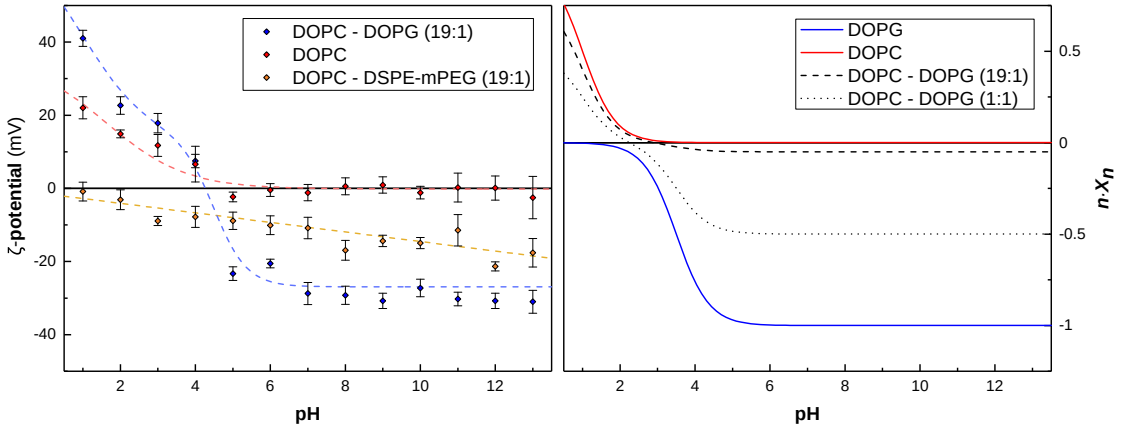

Figure 4.7: Left: Experimentally determined ζ–potentials for AuNRs functionalised using DOPC, DOPC – DOPG (19:1), and DOPC – DSPE-mPEG; as a function of buffer pH (10 mM). **Right:** Theoretically predicted charge for a population of DOPC and DOPG, where n is the ionisation number and X_n is the ionised fraction. Also presented are the predicted curves for 19:1 and 1:1 DOPC – DOPG mixtures.

resembles the curve predicted for a 3:2 molar ratio of CTAB and oleate. This implies the formed bilayer does not necessarily contain the same surfactant ratio as the original growth mixture and may instead reflect some more energetically preferable configuration of surfactants on the surface.

PSS

The primary functional group of PSS, a sulphonic acid has a pK_a of -1.92, hence it outside the range of the buffers used here and would only become protonated under the extremes of concentrated acids. Hence PSS should present a constant negative ζ–potential at all pH measured here, which is matched closely by our experimental observations fig. 4.5. Because PSS functionalisation passivates the CTAB layer, the positive charge is obscured by the PSS layer, despite still being present on the surface of the particle, it is not detectable by measurement of the AuNR ζ–potential measurements, which sensitive only to the external surface charge.

DOPC

Due to the zwitterionic character of DOPC, it is neutrally charged at physiological pH. The phosphate group has a pK_a of 1.88 when the molecule is free in solution, but this shifts to around ~pH 1 inside a DOPC bilayer [221]. Hence the pH response of the molecular charge is expected to be positive around pH 1 and decay to neutral as the pH is increased. This means that the pI for the DOPC–coated AuNRs cannot be determined from the pH range covered here because fitting accurately would require bulk pH values where all phosphate groups were completely protonated. However, the observed pH response of DOPC coated AuNRs correlates strongly with that described above. The neutral ζ–potential observed above ~pH 4 is consistent with this and suggests reduction of the residual CTAB to only trace amounts.

For comparison, other published phospholipid surfactant exchange methodologies (which utilise only a single round of sonication in phospholipid SUV solution) still present a positive charge at neutral pH, suggesting incomplete removal of the CTAB [267, 339, 398]. The work of Orendorff *et al* presented the pH dependence of the zeta potential their POPC–functionalised AuNRs, displaying a similar pH response to that seen in fig. 4.7, albeit declining to a ζ–potential of 10 mV at higher pH values, which the authors attributed to an estimated inclusion of ~10% CTAB in the surface coating [266]. Confusingly, other work have reported negative zeta–potentials for DMPC–functionalised AuNRs of -9 mV, which is difficult to explain with the functional groups that could potentially be present on the particle surface [304]. Comparatively, we observe neutral surface potential (to within ±3 mV) suggesting the additional rounds of sonication in phospholipid SUV solution deployed here are effective at removing this residual CTAB from the surface coating.

DOPC – DOPG (19:1)

The observed pH response of AuNRs functionalised in a DOPC – DOPG (19:1) lipid SUV solution is consistent with a surface coating containing two negatively charged groups with pK_as at around ~pH 1 (hard to determine reliably) and ~pH 3. This is not inconsistent with the known pK_a values for the phosphate groups of DOPC and DOPG which both fall at around pH ~1.9 when free in solution. As stated above the pK_a of DOPC is expected to shift to around pH 1 when embedded in a bilayer [221], and DOPG has been observed to have a pK_a of 2.7 embedded in liposomes [383]. Hence the observed behaviour is consistent with that expected for a DOPC – DOPG mixture on the surface. The excess negative charge of the DOPG will obscure the presence of residual CTAB in the ζ–potential measurement. It seems reasonable to assume that the residual CTAB will might be expected to be similarly low as in the pure DOPC system. The theoretically expected curves are given in fig. 4.7 alongside the combined curves for a 19:1 and a 1:1 mixture of the

two lipids. As can be seen the shape of the combined curve for a 1:1 DOPC – DOPG is considerable more consistent with the experimentally measured ζ–potential curve. This suggests, alongside the results from the mixed CTAB – oleate coatings that the ratio of different surfactant species adsorbed on the surface of a AuNP do not necessarily reflect the ratio of surfactants in the bulk solution.

DOPC – DSPE-mPEG (19:1)

Whilst the phosphate groups of DOPC and DSPE-mPEG both have pK_a values of around 1.8, they are not expected to have an apparent effect on the pH response of particles functionalised with a significant number of PEGylated phospholipids. Since ζ–potential measurements are only sensitive to the functional groups exposed at the surface of the particle, the extended PEG brush structure will effectively screen the pH response of the phosphate, choline and amide groups present on these molecules. Hence we would expect based on the protonation dynamics of PEG that the particles would present a neutral ζ–potential at all pH. This is not what is observed, instead the particles show a slightly negative ζ–potential at low pH, which grows increasingly negative with increasing pH, this behaviour has been observed elsewhere (e.g. [35, 226]). This can likely be explained by the preferential absorption of anionic species into the PEG layer, which has been observed to occur for oligo(ethylene glycol) monolayers [184].

4.4.2 Summary

The observed shifts in the ζ–potential are consistent with the known pK_a values of the molecules we have functionalised our AuNRs with. The absence of any positive charge on our DOPC–functionalised AuNRs implies that the level of CTAB on the surface of the AuNRs is being successfully reduced to trace levels during the phospholipid exchange process described above. This is also supported by the NMR and Raman spectroscopy performed above.

4.5 Stability in Biorelevant Media

The body presents a particularly challenging environment for the maintenance of colloidal stability, human plasma exhibits a relatively high salinity of around 300 mOsm·L^{-1} and contains a wide variety of biomolecules which will non-specifically bind to particles, often undermining any specific surface functionalisation bestowed on the particle. This is extremely problematic for most targeting strategies as protein corona are typically 10–100 nm in thickness [178], in excess of the size of most targeting ligands (i.e. antibodies are ~10–15 nm), leading to corona completely obscuring such molecules. Whilst such measurements have been performed for the more common AuNR coatings such as CTAB and PSS, the stability of phospholipid–coated AuNRs outside of the idealised environment of deionised water has received no attention (i.e. [50, 267, 304, 398]). Hence, it was decided to explore the stability of each of the surface functionalisations in a variety of 'biorelevant media', such as buffers, cell culture medium, serum and blood plasma.

Electrolyte			Reference Values *Human Plasma* (mM)	Dulbecco's PBS (mM)	Plasma-lyte 148 (mM)	Pseudo-plasma Buffer (mM)	RPMI 1640 (mM)	FBS (mM)
Sodium		Na^+	133 - 146	152	140	141	124.27	137
Chloride		Cl^-	95 - 105	144	98	98	100.16	103
Potassium		K^+	3.5 - 5.3	4.2	5	5	5.33	11
Calcium	*ionised*	Ca^{2+}	1 - 1.3	0.9	– –	1.3	0.42	3.4
	total	– –	2 - 2.6	– –	– –	– –	– –	– –
Phosphate		PO_4^{3-}	0.8 - 1.5	9.5	– –	1.3	5.63	1
Magnesium		Mg^{2+}	0.7 - 1	0.5	– –	1	0.42	0.1
Sulphate		SO_4^-	1	– –	– –	1	0.41	<0.0001
Ammonia		NH_4^+	0.011 - 0.051	– –	– –	– –	– –	0.5
Nitrate		NO_3^-	0.0013 - 0.013	– –	– –	– –	0.85	– –
Copper		Cu^{2+}	0.011 - 0.022	– –	– –	– –	– –	<0.0001
Zinc		Zn^{2+}	0.011 - 0.024	– –	– –	– –	– –	<0.0001
Organic acids (lactate)		$C_3H_5O_3^-$	0.5 - 2.2	– –	2	– –	– –	– –
Bicarbonate		HCO_3^-	22 - 29	– –	23	– –	– –	16.8
Carbonate		CO_3^-	23 - 30	– –	26	– –	– –	*<23?*
Acetate		$H_3CO_2^-$	2.5	– –	– –	27	23.81	0.4
Gluconate		$C_6H_{11}O_7^-$	– –	– –	– –	23	– –	– –

Table 4.5: Comparison of the various ion concentrations of the prepared buffers and media used in measuring the stability of various nanoparticle functionalisations alongside typical ranges for a healthy human adult. Human reference values taken from ref. [100] RPMI 1640 and foetal bovine serum are complex mixtures containing a large number of additional molecules, such as vitamins, amino acids and proteins, an incomplete summary of these are detailed in table 4.6.

Three buffers were selected as surrogates to test the impact of similar ion concentrations to those seen in human plasma on the stability of AuNPs. Firstly, Dulbecco's PBS (DPBS) was used as a commercially available buffer at a suitable pH and osmolarity, due to its ubiquity in the literature as a stability testing medium. DPBS has Na^+, Cl^-, K^+, Ca^{2+}, Mg^{2+} and SO_4^- concentrations within the expected reference ranges for human plasma. But it has around an eightfold excess of PO_4^{3-} ions compared to human plasma. Higher valency electrolytes such as PO_4^{3-} are significantly more detrimental to colloidal stability than monovalent electrolytes, this is expressed by the Schulze–Hardy law [1] [119, 312]. For instance, the critical coagulation concentration is typically ~100× lower for divalent counterions and ~1000× for trivalent counterions, compared with monovalent counterions [255]. Variation in concentration of phosphate will thus have a disproportionate effect of the stability of particles compared with the other common ions in blood plasma.

Secondly, Plasma–Lyte 148 (PL–148), an isotonic intravenously administered fluid replacement which is designed to resemble the electrolytic composition of human plasma was chosen as additional commercially available product with a standardised recipe. It contains sodium, chloride and potassium at normal human reference values, but also contains acetate and gluconate ions significantly well above these, they are included for medicinal purposes as alkinising agents and are metabolised to bicarbonate by muscle and peripheral tissues or renally excreted from the body [375]. It is also missing a the vast majority of electrolytes found at lower concentrations, limiting its potential as a plasma mimic somewhat.

Thirdly, a bespoke buffer was created to reflect the homeostatic concentrations of the most common electrolytes in human plasma ($C_{ion} \geq 1$ mM) dubbed 'pseudo–plasma' buffer (PP). The recipe for this is given in table 2.3. The pH of the buffer was measured to be ~pH 7.4, 1 hour after preparation.

[1] This law is normally stated as the critical coagulation concentration of an oppositely charged colloid is $\propto z^{-6}$, where z is the valency of the counterion [45]

AMINO ACIDS

Component	RPMI (mM)	FBS (mM)
Glycine	0.13	0.64
L–alanine	– –	0.92
L–arginine	1.15	0.09
L–asparagine	0.38	0.30
L–spartic acid	0.15	0.07
L–cysteine	0.21	trace
L–glutamic acid	0.14	0.68
L–glutamine	2.05	0.20
L–histidine	0.10	0.06
L–hydroxyproline	0.15	0.07
L–isoleucine	0.38	0.16
L–leucine	0.38	0.27
L–lysine	0.22	0.20
L–methionine	0.10	0.06
L–phenylalanine	0.09	0.12
L–proline	0.17	0.02
L–serine	0.29	0.29
L–threonine	0.17	0.15
L–tryptophan	0.02	trace
L–tyrosine	0.11	0.08
L–valine	0.17	0.33
Taurine	– –	0.12
Citrulline	– –	0.92
α–amino–*n*–butyric acid	– –	0.02

VITAMINS

	Component	RPMI (µM)	FBS (µM)
A	Vitamin A	– –	0.1
B1	Thiamine	30	trace
B2	Riboflavin	0.5	trace
B3	Niacinamide	8.2	trace
B4	Choline	21.4	trace
B5	D–pantothenate	0.5	trace
B6	Pyridoxine	4.9	trace
B7	Biotin	0.8	trace
–	*i*-inositol	0.19	trace
B9	Folic acid	2.2	trace
B12	Cobalamin	0.004	trace
C	Ascorbic acid	– –	trace
E	Vitamin E	– –	300

ENZYMES

Component	RPMI (U/L)	FBS (U/L)
Alkaline phosphomonoesterase	– –	255
Aspartate aminotransferase	– –	130
Creatine kinase	– –	39
γ–glutamyl transpeptidase	– –	39
Lactic dehydrogenase	– –	864

HORMONES

Component	RPMI (nM)	FBS (nM)
Bovine somatotropin	– –	1.8
Cortisone	– –	1.4
Gonadotropin	– –	0.94
Insulin	– –	0.077
Progesterone	– –	250
Prolactin	– –	0.77
Prostagladin E	– –	17
Prostagladin F	– –	34
Testosterone	– –	1.4
Thyrotropin	– –	3.3
Triiodothyronine	– –	1.8

PROTEINS

Component	RPMI (g/L)	FBS (g/L)
TOTAL	0	35.2
Albumin	– –	23
Globulin	– –	10.5
Immunoglobulin G	– –	0.184
Haemoglobin	– –	0.113
Fibronectin	– –	0.035

LIPIDS

Component	RPMI (g/L)	FBS (g/L)
Cholesterol	– –	283
Endotoxin	– –	0.000035
Triglycerides	– –	0.669
Phosphoserine	– –	0.014
Phosphoethanolamine	– –	0.0076

OTHER

Component	RPMI (nM)	FBS (nM)
α–aminoadipic acid	– –	0.095
Anserine	– –	0.080
Bilirubin	– –	6.8
Carnosine	– –	0.16
Creatine	– –	236
Cystathionine	– –	0.15
Glucose	11100	6940
Glutathione	3.3	16
Para–aminobenzoic acid	7300	trace
Phenol red	13.3	– –
Selenium Oxide, SeO_3^{2-}	– –	0.00021
Urea	– –	2660
Uric acid	– –	173

Table 4.6: Additional components present in RPMI 1640 cell culture media and commonly reported components of foetal bovine serum (the list for FBS is far from exhaustive). Values for FBS were taken from a variety of sources (refs. [23, 44, 52, 128, 206, 298, 391]). These values are averages due to the high variability between batches of FBS (unlike RPMI 1640 which has a published standardised recipe [235]).

The ion concentrations of each buffer are given in table 4.5

In addition to these electrolyte mixtures, mixtures of RPMI 1640 cell culture medium (CCM) and foetal bovine serum (FBS) were also used. CCM is commonly used in the literature as a stability–testing medium for AuNPs. It is a useful preliminary experiment to demonstrate colloidal stability throughout *in vitro* testing of NPs. Although it is somewhat limited in its similarity to the *in-vivo* environments in which theranostic AuNPs are expected to be deployed. CCM is a mixture of electrolytes, vitamins, free amino acids and nutrients (detailed in table 4.5 and table 4.6) and is intended to function as an optimal environment for the *in-vitro* growth of cells. Hence, its composition is selected to encourage indefinite proliferation of mammalian cells. It contains substantially elevated levels of PO_4^{3-} and NO_3^- compared with human plasma (PO_4^{3-} being particularly problematic to colloidal stability due to its high valency), and the bicarbonate–carbonate buffering system of the blood is entirely missing. It also contains a free amino acids profile that does not reflect that found in plasma, and elevated levels of B vitamins, glucose, and para–aminobenzoic acid. Reflecting its purpose as an artificial environment designed to nourish immortalised cells, but it is one into which these particles will be placed and hence should be considered on those grounds.

Foetal bovine serum (FBS) is a by–product of the beef industry, and is prepared from blood collected from bovine fetuses. It is a complex (and ill–defined) mixture of molecules, including electrolytes, amino acids, proteins, antibodies, enzymes and peptides. The electrolyte content is detailed in table 4.5 and other commonly identified components are given in table 4.6. Hence FBS is a close match in many regards to the composition of human blood plasma. But it presents its own problems, due to the manner by which it is collected from many individual cattle, there is a large amount of batch–to–batch variability, limiting the amount of information that can reliably be gained from a single batch. Also the method by which it is prepared changes the composition compared with that of blood plasma. Collected blood is allowed to clot at low temperature and then the clotted fraction removed by centrifugation. This leads to fibrinogen and coagulant proteins being reduced to a small fraction of their normal levels. It is also not an exact match to human sera, not only because it contains the bovine–variants of proteins, but also because it is harvested from foetuses, concentrations of growth factors are much higher and and antibody and complement protein concentrations are much lower than would be found in an adult. This is beneficial in its use as an additive to CCM for encouraging cell growth, but does make it less ideal in testing the stability of our particles. It is also notable that most studies do not report the presence of lactate in FBS. Lactate is almost certainly present in FBS at the point of collection, with presumably the presence of lactic dehydrogenase in serum leading to breakdown of lactate before its use in labs.

Regardless of the above potential issues, FBS is much closer to the *in vivo* environment in which the particles will be utilised than the simple buffers and CCM discussed above. It will also be used to enrich the media used in *in vitro* studies and hence demonstrating colloidal stability in that environment is also important. It was decided to test ratios of CCM and FBS at 100% RPMI, 90% RPMI – 10% FBS, 50% RPMI – 50% FBS, and 100% FBS, allowing some assessment of the increasing impact of serum proteins on AuNR stability.

Finally, in addition to the above media, it was decided to test AuNR stability in mouse plasma, because this would be the closest possible match to the *in vivo* models in which these particles would be tested. Plasma is different from serum as it has not been allowed to clot and hence still contains all the coagulant proteins

and fibrinogen. In order to prevent coagulation the blood was collected in a tube containing the chelation agent tripotassium ethylenediaminetetraacetic acid (K_3EDTA) and the cells removed by centrifugation. This will affect the ionic make up of the sample, K_3EDTA which will disproportionately chelate divalent cations, hence a number of electrolytes will have been removed from the plasma (i.e. Ca^{2+}, Cu^{2+}, Mg^{2+}, Zn^{2+}, Fe^{2+}) and replaced with K^+. K_3EDTA is not expected to interact with the particles given that it should be rendered chemically inert by divalent cations in the plasma. Whilst this does mean that the harvested plasma is not a perfect replicate of *in vivo* plasma, these ions make up a relatively small fraction of the electrolytes in solution and the impact of them without the presence of plasma proteins will be assessed by the 'pseudo–plasma' buffer discussed above. This collected plasma represents the closest match to the *in vivo* environment in which our NPs will operate, and would be usable over the timescale of the experiment (i.e. whole blood will clot).

4.5.1 Results

Particles were suspended at a concentration of 75 $\mu g \cdot ml^{-1}$ in 200 µl of the desired medium in a 96-well plate and the spectra of each well read at the desired time–points using a well plate–reader. This allowed a large number of samples to be processed simultaneously, reducing the time required considerably, but came at the cost of a lower SNR and occasional artefacts appearing in the data. Additionally problems were encountered, due to the inclusion of phenol red in RPMI 1640[1] with its strong absorbance peaks at 443 and 570 nm, which made baseline correction of the spectra difficult below 600 nm, and prevented normalisation of the spectra for Au^0 concentration at 400 nm. This was also true for the plasma harvested from mice which also showed strong absorbance bands below 600 nm associated with a small amount of haemoglobin and oxyhaemoglobin which entered the sample during processing. Instead, it was found that normalising to the minimum between TSPR and LSPR for each spectrum where the plasmonic contributions to the optical properties were minimised worked well as an alternative, this also meant that the effect of some of the optical artefacts at lower wavelengths in the buffer spectra could safely be ignored.

The spectra obtained are available in appendix D, and have been summarised in fig. 4.8. In number of the spectra the LSPR was observed to drop in intensity which no accompanying increases in extinction at higher wavelengths normally ascribed to aggregation. This is highly likely to be caused by AuNRs in solutions losing stability and adhering to the walls of the well-plate over the long time-scale of the experiment, leading to them effectively disappear from the measured spectra. Results are discussed for each surface functionalisation below:

CTAB – Oleate functionalised AuNRs

CTAB–functionalised particles possess an inherent instability, due to the way in which molecules dynamically exchange with the surrounding environment. Repeatedly washing of the particles by centrifugation will result in depletion of the free CTAB in the bulk solution and hence encourage the dissolution of the surface–bound CTAB, reducing the stability of these particles. Hence, two experiments with CTAB–capped AuNRs were run in parallel, one in which the CTAB – oleate stabilised particles were washed threefold and suspended in the media of interest and the other in which an additional 1 mM CTAB was added to the well. Making

[1] Phenol red free RPMI 1640 CCM is available, but it was decided that since the LSPR ($\lambda_{LSPR} > 600$ nm) was the primary means by which aggregation would be assessed, it was not worth repeating the measurement with alternative CCM.

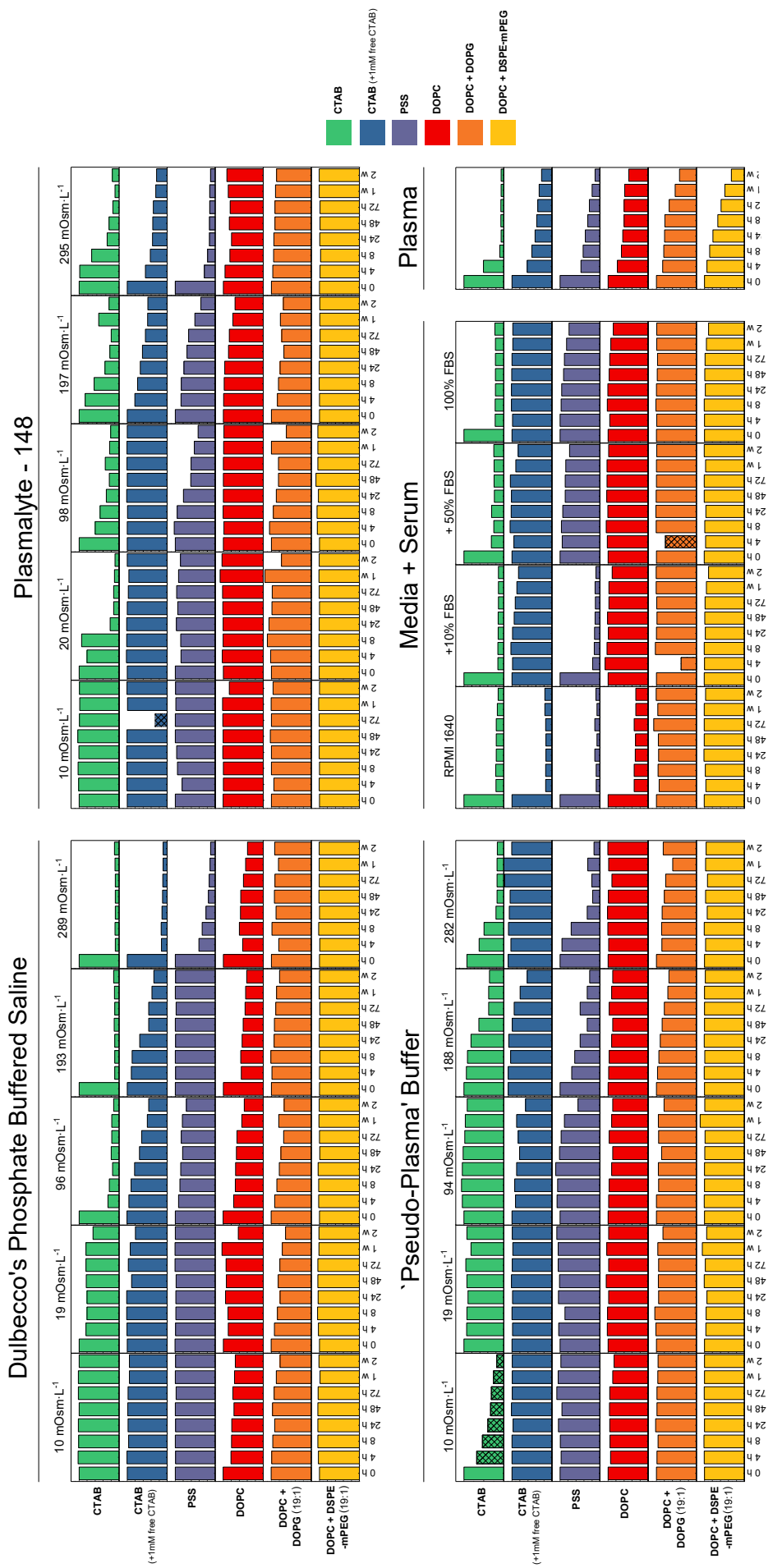

Figure 4.8: A_{LSPR} intensity normalised to $A_{\mathrm{LSPR}}(t = 0)$ as a function of time. These column plots serve as a summary of the spectra given in appendix D. Spectra were taken in three buffers; Dulbecco's phosphate–buffered saline, Plasma–lyte 148, and 'pseudo–plasma' buffer. They were also taken in mixtures of RPMI 1640 cell culture media and foetal bovine serum, at 100% RPMI, 90% RPMI – 10% FBS, 50% RPMI – 50% FBS and 100% FBS. And finally also in mouse plasma. Spectra were taken at 0, 4, 8, 24, 48, 72 hours and at 1 and 2 weeks after resuspension in media, hence the x–axis is not linear. It should be noted that the CTAB–AuNR spectra (no additional free CTAB) in serum containing media where obscured by a strong scattering signal, probably from large aggregates, making the normalisation unreliable. The LSPR is still visible in those spectra, but difficult to deconvolute from the background (see appendix D.3) Hatched bars indicate spectra which were not reliably collected by the spectrometer.

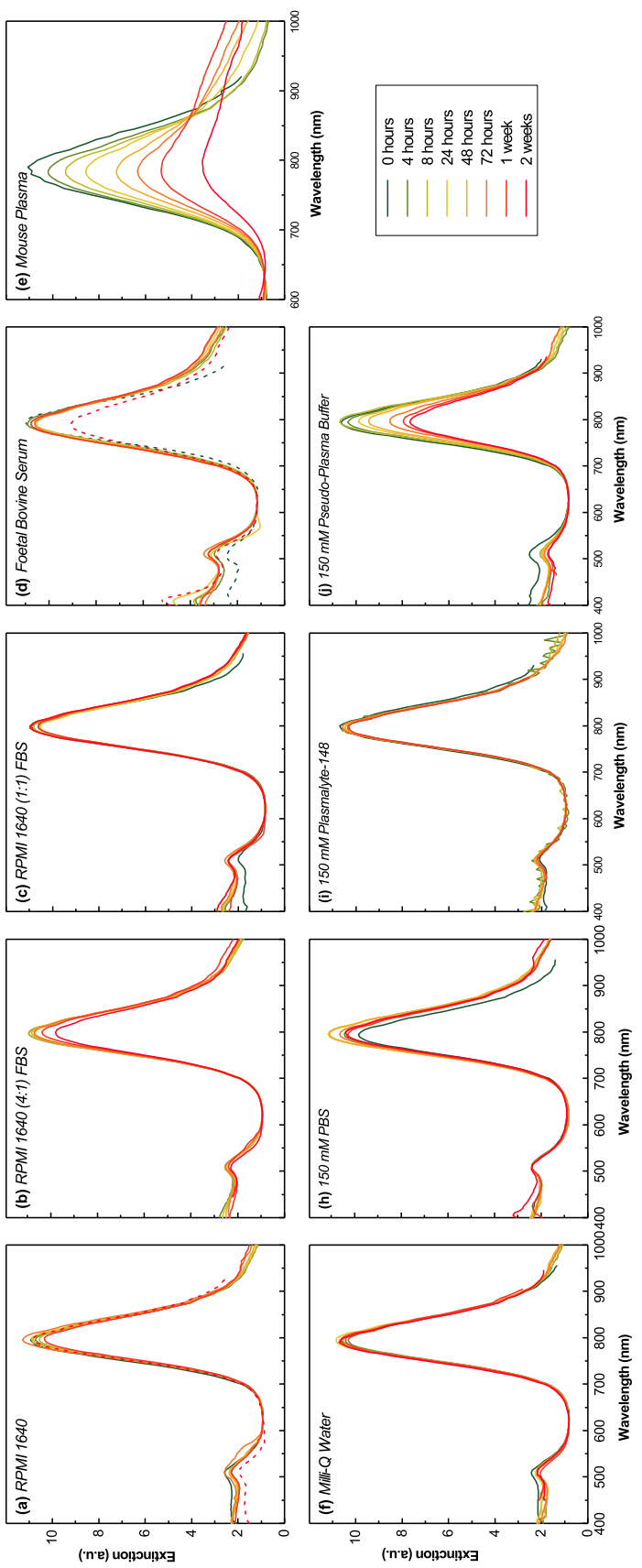

Figure 4.9: Stability of DOPC – DSPE-mPEG (19:1) coated AuNRs assessed by the preservation of their plasmonic properties as a function of time. AuNRs were stored in a variety of buffers and biorelevant media: **(a)** RPMI 1640 cell culture medium, **(b)** RPMI 1640 containing 10% Foetal Bovine Serum (FBS), **(c)** RPMI 1640 containing 50% FBS,**(d)** FBS, **(e)** Blood plasma harvested from a BALB/c nude mouse, **(f)** Milli-Q water, **(g)** 151 mM Dulbecco's phosphate buffered saline, **(h)** 151 mM Plasmalyte-148, and **(i)** 151 mM plasma mimicking buffer. Spectra have been background subtracted and normalised to 610 nm (normalisation to 400 nm was prevented due to components of some of the various media such as residual haemoglobin and phenol red have absorbance in this region). The spectra below 600 nm for AuNRs incubated in plasma were unusable due to the presence of haemoglobin obscuring the spectral features of the AuNRs.

it possible to distinguish between aggregation induced by degradation of the CTAB bilayer and charge screening due to ions in solution.

The effects of this are easily visible in the results; the presence of 1 mM free CTAB increased the stability of the particles in solution in higher osmolarities in all cases. Particles without additional CTAB were unstable in 96, 20, and 188 mOsm·L^{-1} in DPBS, PL148 and PP[1] buffers respectively. The addition of 1 mM free CTAB improved stability at higher concentrations of DPBS although aggregation was still visible. In PL148 and PP buffers the particles were stable at increased concentrations of 98 and 282 mOsm·L^{-1} respectively. Both sets of experiments showed worst stability in PO_4^{-3} rich environments such as DPBS and RPMI 1640 CCM, which is expected given the interaction between the trivalent negative charge of the PO_4^{-3} and the positive charge of the N^+–$(CH_3)_3$ headgroup of CTAB.

Both sets of CTAB–capped AuNRs were unstable in 100% RPMI CCM. However, the addition of serum stabilises the particles in the presence of CTAB, suggesting proteins in the serum were providing stability to the particles through the formation of a corona. These particles also showed better stability in mouse plasma, presumably also resulting from corona formation. They still aggregated over the course of 24 hours though. The well containing plasma without additional CTAB became visibly cloudy, suggesting the formation of large aggregates which scattered light strongly. This additional signal meant that the normalisation performed on the other spectra became unreliable, the TSPR and LSPR are visible in these spectra, but much weaker than this scattering signal. The formation of these large aggregates would imply some interaction between molecules in the media and the less stable CTAB–AuNRs, which is otherwise prevented by maintaining a higher surface charge in the presence of 1 mM CTAB.

The results for the triply washed samples containing an additional 1 mM CTAB in PBS, pure RPMI, and RPMI + 10% FBS are consistent with those reported elsewhere for singly–washed CTAB–AuNRs [137]. Demonstrating the clear requirement to maintain a high background concentration of CTAB to maintain colloidal stability.

Poly(styrene sulfonate) functionalised AuNRs

PSS–AuNRs was observed to aggregate at 289, 98, and 94 mOsm·L^{-1} in DPBS, PL148, and PP, respectively. Faster and more complete aggregation was observed above these concentrations. The variation in the maximum concentration is difficult to explain, being negatively charged the stability of PSS–stabilised NPs should be much less affected by the presence of PO_4^{-3} due to it being a co–ion[2]. It is also not consistent with the presence of small concentration the divalent counterions in Ca^{2+} and Mg^{2+} in DPBS and PP.

PSS–AuNRs were also unstable in RPMI 1640 culture medium. This has been observed elsewhere, where the presence of serum proteins was required to maintain stability [289]. The particles here were not stable in 10% serum–enriched RPMI 1640 (which have been observed to be stable in elsewhere (i.e. [289, 393])). However, increasing the serum content further did convey stability and PSS–functionalised AuNRs show good stability in 50% and 100% serum, suggesting corona formation can stabilise the particles, consistent with these other results.

[1] The case of 10 mOsm·L^{-1} PP buffer has been deemed to be an artefact. The drop–off in LSPR peak intensity is paired with a blueshift in peak position, a trend that is more consistent with directional oxidative etching of the AuNRs [294]. Given that the same trend is not seen for higher concentrations of the buffer, it seems more likely that this results from an optical artefact, due to the presence of something strongly refractive in the well such as a bubble. Hence this result has been ignored in further discussion.

[2] The effect on the critical coagulation concentration of co–ions is given by the inverse Schulze–Hardy law, which states that it is proportional to z^{-1}, where z is the valency of the co–ion [45].

The particles aggregate at a faster rate than CTAB–coated particles in mouse plasma. Over the course of the experiment the LSPR decreased to the point of being virtually undetectable, accompanied by an increase in the extinction at higher wavelengths consistent with the formations of aggregates.

DOPC functionalised AuNRs

DOPC showed relatively poor stability in DPBS, relative to PL-148 and PP, and is also have poor stability in RPMI 1640 CCM suggesting that the higher concentrations of PO_4^{-3} has a disproportionate impact on the stability of DOPC functionalised AuNRs. There was little–to–no reduction in LSPR intensity of DOPC–functionalised AuNRs in PL–148 or PP.

Whilst the DOPC–AuNRs were not stable in RPMI 1640, enriching with serum stabilises the NPs, suggesting either the formation of a corona or the reduction in the PO_4^{-3} concentration stabilised the particles. It is more likely primarily driven by corona formation, given that a 10% reduction in RPMI concentration led to near complete stability, but both effects are likely to be occurring to some extent. DOPC–AuNRs were stable in the presence of serum.

As with all other functionalisations the particles showed worse stability in mouse plasma, compared with pure FBS. As is visible in the drop in LSPR intensity and growth in extinction at higher wavelengths. The LSPR intensity dropped to around 60% of its initial intensity, so they performed marginally worse than the other phospholipid coated AuNRs.

DOPC – DOPG (19:1) functionalised AuNRs

The DOPC – DOPG AuNRs were relatively stable in all buffers tested. A small drop off in LSPR intensity was seen in some cases, although it did not correlate with ionic strength. They were also stable in all combinations of media and FBS and will almost certainly be forming a corona in the presence of serum, due to charge interactions between the PSS and serum proteins.

Some aggregation in plasma was visible over the course of the experiment, but they retained the around 80% of their absorbance peak over the course of the first 24 hours, making them suitable NIR–absorbent for *in vivo* use over this period.

DOPC – DSPE-mPEG functionalised AuNRs

The spectra associated with the DOPC – DSPE-mPEG AuNRs in each media are given in fig. 4.9. The spectra in buffers are given at the highest concentrations tested.

No aggregation was visible in the spectra of DOPC – DSPE-mPEG in any of the buffers, in media or in serum. The optical properties were consistent across all concentrations and time points.

Again, as with the other phospholipid–functionalised AuNRs some aggregation was displayed in mouse plasma however and it is fairly consistent with the results seen for the other phospholipid coated AuNRs. The intensity of the LSPR is around 80% of its initial value after 24 hours, which is still high enough to utilise for photo–thermal therapy, suggesting they are stable enough for *in vivo* use.

4.5.2 Discussion

All varieties of phospholipid–functionalised AuNRs showed higher stability than the CTAB– and PSS–AuNRs. The DOPC functionalised AuNRs faired worse in DPBS and RPMI media, but worked similarly well in all other cases, suggesting they should be suited to *in vivo* use. The DOPC – DOPG and DOPC – DSPE–mPEG AuNRs showed similar stability in FBS and mouse plasma, with the DOPC – DSPE–mPEG showing marginally better stability in some of the buffers, likely resulting from the additional steric stabilisation. All three of these show potential for *in vivo* use.

The measured stability of CTAB – oleate AuNRs in the presence of 1 mM free CTAB is somewhat redundant in the context of their use in theranostics, given the high toxicity of free CTAB. However it does provide some insight into maintaining their stability in higher salinity conditions. PSS AuNRs showed worse stability than CTAB – oleate functionalised AuNRs under a number of conditions, which is somewhat unanticipated, as it generally reported that PSS functionalisation is used provides additional stability alongside higher biocompatibility [134, 318]. Given the large number of publications surrounding theranostic applications of PSS–AuNRs, they will continue to be used in this study as a reference point for comparison as biocompatible surface functionalisation.

All coatings performed considerably worse in mouse plasma compared with FBS, this probably results from a non–specific interaction between the AuNRs and the fibrinogen/coagulant proteins that are removed during the processing of FBS. If it is the presence of fibrinogen and coagulant proteins that are root cause of this increased instability, it could have important implications for the applications of nanoparticles in *in vivo* applications. In order to definitely establish this though further experiments are needed observing nanoparticles in a range of sera, plasma, and more simple protein suspensions.

In an ideal world, these stability measurements would be accompanied by additional characterisation of corona formation during incubation in media, serum and blood plasma. This would involve the monitoring the change in size and surface charge the particles after incubation via techniques such as dynamic light scattering, electron microscopy, fluorescence correlation spectroscopy and measurement of the ζ–potential. Characterisation of the population of proteins on the particles surface via methods such analytical ultra-centrifugation, isothermal titration calorimetry, liquid chromatography – mass spectroscopy and molecular spectroscopy (i.e. FTIR, Raman or NMR). However, resources are finite and time is limited, and these experiments were deemed outside the feasible scope of this project.

4.6 Conclusion

In this chapter, we have demonstrated that the displacement of CTAB with a variety of phospholipids can be achieved through repeated rounds of sonication and cleaning through centrifugation. This repeated process appears to be more effective at removing CTAB from the surface of AuNRs than other published methods. We have shown this through characterisation of the surface through NMR spectroscopy, surface–enhanced Raman spectroscopy and pH–dependent ζ–potential measurements, in all cases we were unable to identify the presence of CTAB on the surface of the phospholipid–functionalised AuNRs. The ζ–potential measurements in particular do not show any residual positive charge from CTAB at pH values where we would expect the AuNRs to be otherwise neutral.

We have also shown they display superior colloidal stability compared with alternative surface coatings, such as CTAB and PSS, in the presence of wide range of 'biorelevant' media, such as buffers, cell culture media, serum and blood plasma. We have elected to focus on DOPC – DSPE-mPEG AuNRs going forward on the basis that the additional steric stabilisation should be of benefit. Hence, in the next chapter we proceeded to assess the potential of these as theranostic agents, by measuring their photothermal properties, biocompatibility, cellular uptake and biodistribution in mice.

Chapter 5

Theranostic Application of Gold Nanoparticles

5.1 Motivation

In this chapter the potential of the particles synthesised in chapter 3 and modified with phospholipids in chapter 4 for use in theranostics will be explored. Whilst their stability in a variety of biologically relevant media was explored in section 4.5, a large number of other questions remain around their biocompatibility and suitability for use as photothermal conversion agents. Here we investigate their inherent toxicity to human colorectal cell lines and their interactions with these cells, as well as whether they induce lysis. We also characterise the ability of these particles to generate heat under NIR illumination, their usefulness as photoacoustic contrast agents, and the ability of these particles to induce cell death through photothermal heating. Finally, we assess their biocompatibility *in vivo* and measure the biodistribution of our particles after intravenous injection, with and without a conjugated targeting affimer.

5.2 Gold Nanorods in this Chapter

As discussed section 1.4.1 (and also shown in fig. 1.11), the optimum wavelength range for *in vivo* light penetration is 650–850 nm, with the optimum contrast in multispectral optoacoustic tomography (MSOT) being achieved between 800 and 850 nm. Hence it was decided that to utilise particles with an LSPR maximum in this region. A 1 L batch of AuNRs were synthesised in a growth solution containing 48 mM CTAB and 13.5 mM sodium oleate, yielding AuNRs with an LSPR maximum of 811 nm (fig. 5.1(d)). TEM measurements gave the average dimensions of these AuNRs as (57 ± 7) nm in length with an average diameter of (13.1 ± 1.2) nm (fig. 5.1(a)–(c)&(e)). These were then functionalised with DOPC – DSPE-mPEG (19:1), which led to the LSPR blueshifting to 801 nm (fig. 5.1(d)). These particles were used for all experiments in this chapter unless otherwise stated.

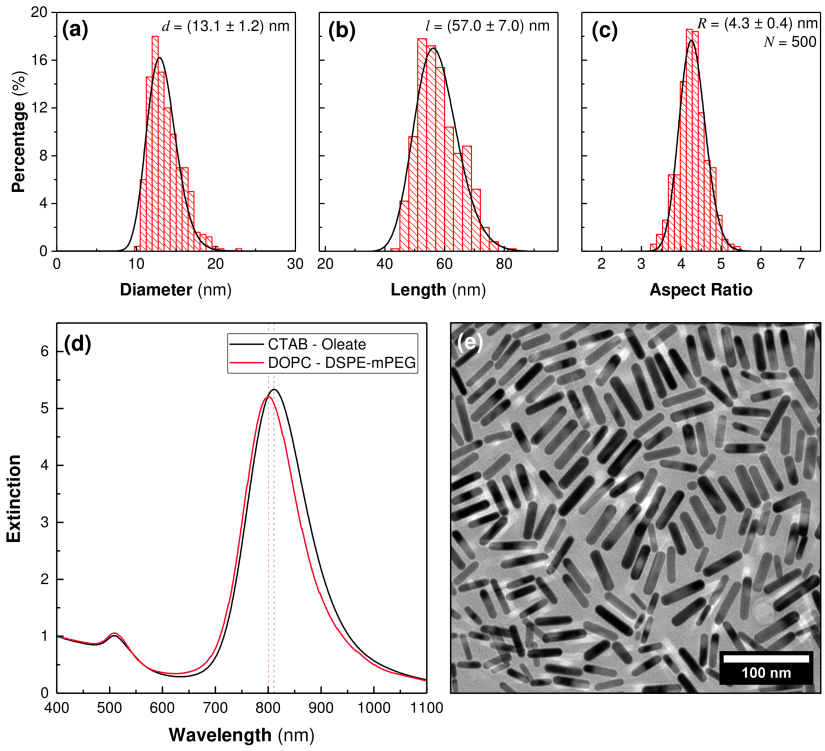

Figure 5.1: Characterisation of the AuNRs used in this chapter. **(a)–(c)** Distribution of diameters, lengths and aspect ratios of AuNRs based on measurements from 500 AuNRs. Dimensions are given as the median size ± the measured standard deviation. **(d)** UV–vis spectra before and after functionalisation with DOPC – DSPE-mPEG (19:1). **(e)** TEM image of a (425 × 425) nm region of AuNRs representative of the sample.

5.3 Biocompatibility

5.3.1 Selection of Cell Lines

For the purposes of targeting these AuNRs it was decided to use human carcinoembryogenic antigen (CEA) as the target protein. In healthy individuals, CEA is typically only found at high levels of expression during foetal development in the gastrointestinal (GI) tract (and also the liver to a much lesser extent) [360]. It was first identified as a specific marker of colorectal cancer in 1965 [107], and has since become recognized as one of the most reliable biomarkers for monitoring the treatment of colorectal cancers [378]. It is over expressed in 90% of GI cancers, 70% of lung cancers, and 50% of breast cancers [108], and hence can be used as a highly specific marker for use in targeting cancerous tumours.

The targeting molecule of interest was a cysteine terminated CEA–specific affimer, provided by the Millner group[1], which has been shown to be effective in targeting CEA–positive tumours in mice with silica NPs [163, 346]. This could be conjugated to the surface of our AuNRs through simple maleimide–thiol linker chemistry, through the replacement of DSPE-mPEG with DSPE-PEG-Maleimide in our phospholipid surface coatings [125].

Two cell lines were selected based on reports in the literature, LS174T, a human colorectal adenocarcinoma (Dukes' type B) and SW620, a human colorectal adenocarcinoma (derived from a metastasis) (Dukes' type B). CEA has been widely reported in the literature to be over expressed by LS174T [114, 136, 319, 345, 346]. By comparison SW620 has been reported to only produce minimal levels

[1] School of Biological Sciences, University of Leeds

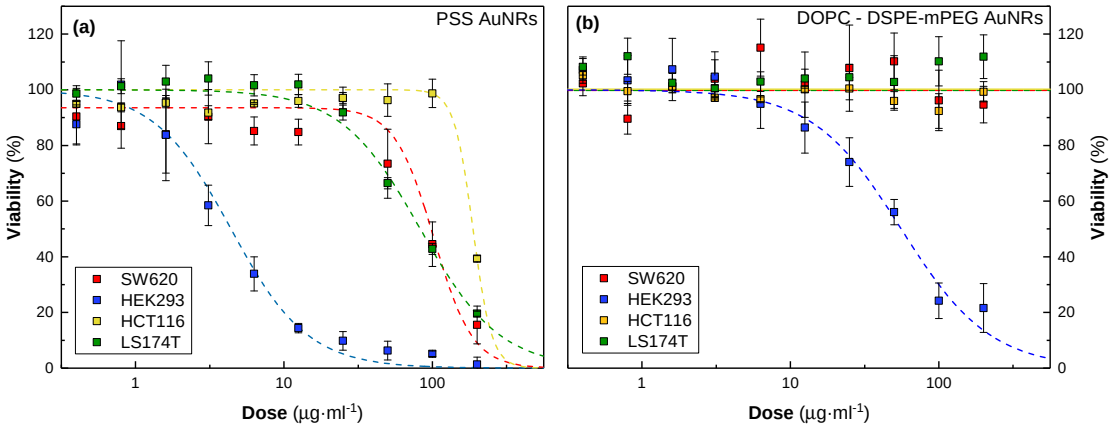

Figure 5.2: *In vitro* cell viabilities of SW620, HEK293, HCT116 and LS174T cells after 24 hours incubation with AuNRs. Cells incubated with increasing concentrations of **(a)** PSS–AuNRs and **(b)** DOPC – DSPE-mPEG (19:1) coated AuNRs. Results are expressed as a percentage of the control plates (0 $\mu g \cdot ml^{-1}$)) and is the mean result from three plates at different passage numbers. Results are fitted with a Hill-type dose–response curve.

[136, 285, 319]. This was confirmed experimentally by our collaborators in the Leeds Institute for Medical Research by flow cytometry and immunofluorescence staining (data not shown). Hence going forward LS174T was selected as our CEA–positive cell line and SW620 as our negative control.

5.3.2 *In Vitro* Toxicity

Based on the cell–lines identified in the previous subsection; the cytotoxicity of the DOPC – DSPE-mPEG functionalised AuNRs was assessed on four cell lines; three CEA–negative (SW620 colorectal adenocarcinoma, HEK293 embryonic kidney, HCT116 colorectal adenocarcinoma) and one CEA–positive (LS174T colorectal adenocarcinoma).

The toxicities for phospholipid–functionalised AuNRs in the literature are limited to two studies, the first in HeLa cells using phosphatidylcholine–functionalised AuNRs up to concentrations of 2.9 $\mu g \cdot ml^{-1}$ and reported 20% cell death (although this is likely due to high residual levels of CTAB) [339]. The second using DMPC–functionalised AuNRs measured cell viabilities up to 20 $\mu g \cdot ml^{-1}$ in MCF–7 and HMEC–1 cells, with no drop off in viability [304]. Neither of these are particularly high doses and the IC_{50} was not reported in either case. Hence the upper limit to the cytotoxicity of these particles, whilst expected to be significantly lower than CTAB–functionalised AuNRs, remains an open question. An extremely high upper concentration of 200 $\mu g \cdot ml^{-1}$ was decided upon hoping that the IC_{50} could be determined. Viabilities were compared with those seen for PSS–functionalised AuNRs, due to their ubiquity in the literature and the relative ease of preparation. PSS–coated NPs typically present IC_{50} values in *in vitro* cell studies between 1 and 100 $\mu g \cdot ml^{-1}$ [196, 278, 289, 393], the values are highly variable between cell lines, hence assays had to be performed for each potential cell–line under consideration to provide a direct comparison.

The results of the cell viability assays are presented in fig. 5.2. In all cases, the DOPC – DSPE-mPEG–coated AuNRs showed higher viabilities than their PSS–coated equivalents. For three cell lines, SW620, HCT116 and LS174T, the IC_{50} could not be determined as ~100% cell viability was seen even at the highest dose. HEK293 cells showed some toxicity, reaching 50% viability at (55 ± 1) $\mu g \cdot ml^{-1}$, by comparison when

treated with PSS–AuNRs this dose was found to be (4 ± 1) $\mu g \cdot ml^{-1}$. The IC_{50} for the SW620, HCT116 and LS174T cells treated with PSS–AuNRs were (102 ± 1), (186 ± 1), and (81 ± 1) $\mu g \cdot ml^{-1}$ respectively.

Hence these particles appear to be highly biocompatible and are safe for use at the concentrations we expect to achieve *in vivo*.

5.3.3 Cellular Uptake

One potential concern that remained after these assays was that the higher viabilities may arise through a lack–of–uptake by the cells. If the particles were not interacting with the cells at all and sitting inertly in the surrounding media then we would expect higher viabilities through this alone. Qualitative concentration–dependent studies of the uptake by colorectal cells. This was undertaken twofold firstly, by optical microscopy using darkfield and differential interference contrast (DIC) techniques (fig. 5.3) and secondly through electron microscopy imaging of sections taken through the cells. Due to time restraints, only a single cell–line was investigated, SW620, it seems reasonable to assume similar interactions in all cell lines.

Cells were incubated in media containing AuNRs at concentrations between 0 and 200 $\mu g \cdot ml^{-1}$ for 24 hours (i.e. spanning the range of concentrations and incubation period used in the viability assays above). And the cell fixed and embedded in mounting medium. The resultant darkfield and DIC images are show in fig. 5.3. Not much uptake can be seen at 0.32 $\mu g \cdot ml^{-1}$ and below. At 1.6 $\mu g \cdot ml^{-1}$ a small number of green spots can be seen inside the cells in the darkfield image. At the higher concentration increasing amounts of these bright spots can be seen inside the cells. The amount of bright objects inside the cells correlates strongly with the particle concentration (this method is **not** quantitative however). The positions of these also correlate with what appear to be small 'ball–like' objects in the DIC images. Hence, these signals have been attributed to uptake of particles by the cells. Curiously, at 200 $\mu g \cdot ml^{-1}$, huge numbers of AuNRs seem to be being up taken by the cells, with no noticeable impact on the functioning of the cells visible in the viability assays above. This would seem to suggest that these coatings are inherently biocompatible and support the conclusions from chapter 4 that the CTAB concentration in the particles has been reduced to only trace levels.

However, some problems are evident from these figures. We know from the darkfield experiments in chapter 3 that the colour of scattered light from these AuNRs is red (fig. 3.11). The spots visible at 1.6 and 8 $\mu g \cdot ml^{-1}$ are green and at higher concentrations a variety of colours are visible. These colours are more consistent with that expected for AuNR aggregates due to plasmonic coupling between many particles. Based on the observed stability in serum–enriched CCM in section 4.5, this aggregation is unlikely to be occurring outside of the cells and intracellular aggregation is the most likely cause of this. This is extremely problematic to their potential use in photothermal therapy as it renders the optical properties of these particles useless for this purpose.

To complement this, it was decided to use electron microscopy to investigate what the state of the AuNRs in the intracellular environment. Pellets of the SW620 cells incubated with AuNRs for 4 hours were prepared for imaging, by fixing, embedding in resin, and microtoming. Two example images are given in fig. 5.4, showing AuNRs that had been up–taken into cells. No AuNRs were observed in isolation and in the lower figure a relatively large cluster was observed. Only a limited number of images of the AuNRs inside cells were able to be acquired in the time available, so the conclusions that can be drawn from these images are

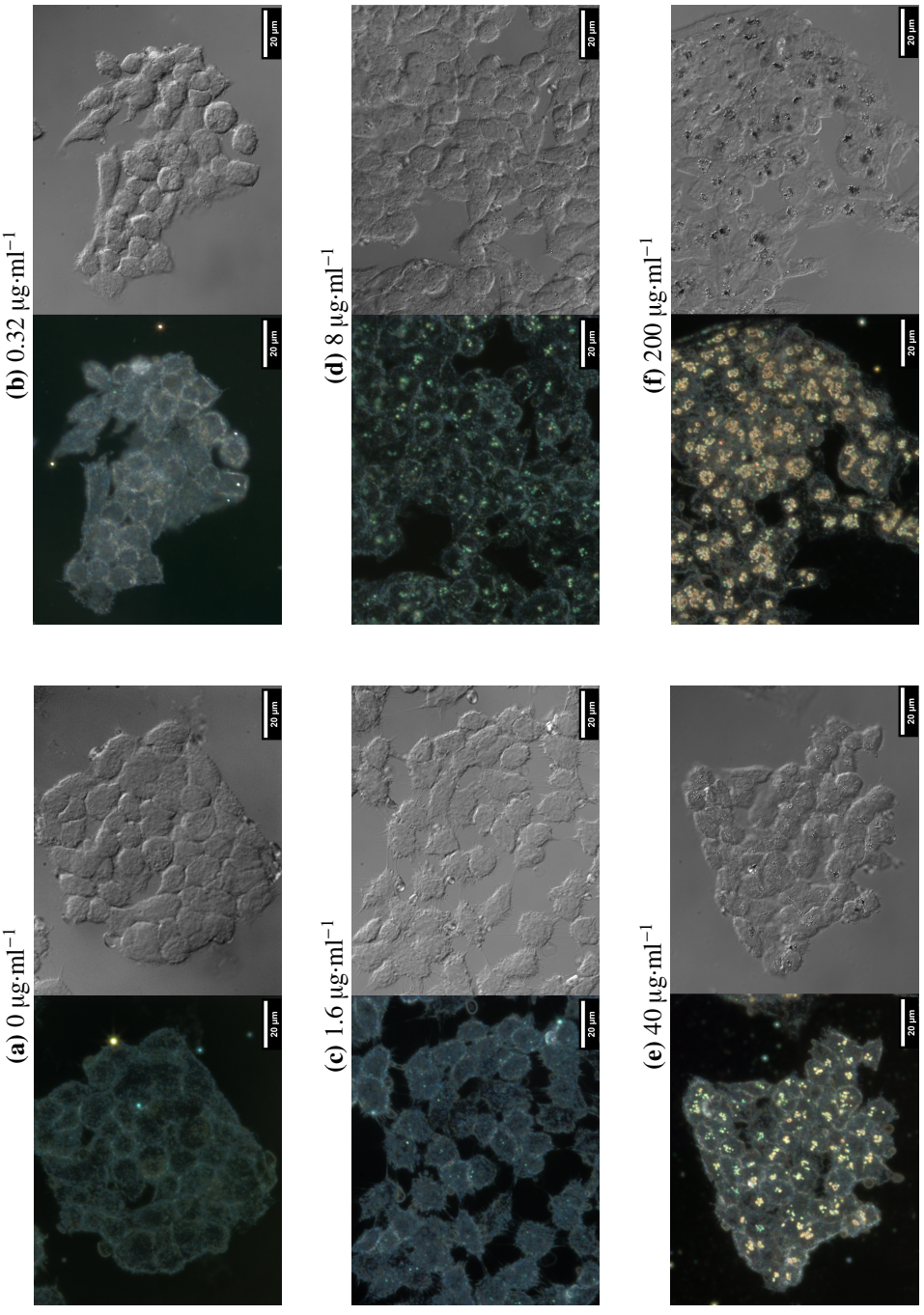

Figure 5.3: Darkfield and DIC images of SW620 cells incubated with DOPC – DSPE-mPEG (19:1) functionalised AuNRs at different concentrations for 6 hours. **(a)** 0 µg·ml^{-1} (control), **(b)** 0.32 µg·ml^{-1}; **(c)** 1.6 µg·ml^{-1}, **(d)** 8 µg·ml^{-1}; **(e)** 40 µg·ml^{-1}, and **(f)** 200 µg·ml^{-1}. Cells are fixed with paraformaldehyde and embedded in mounting medium.

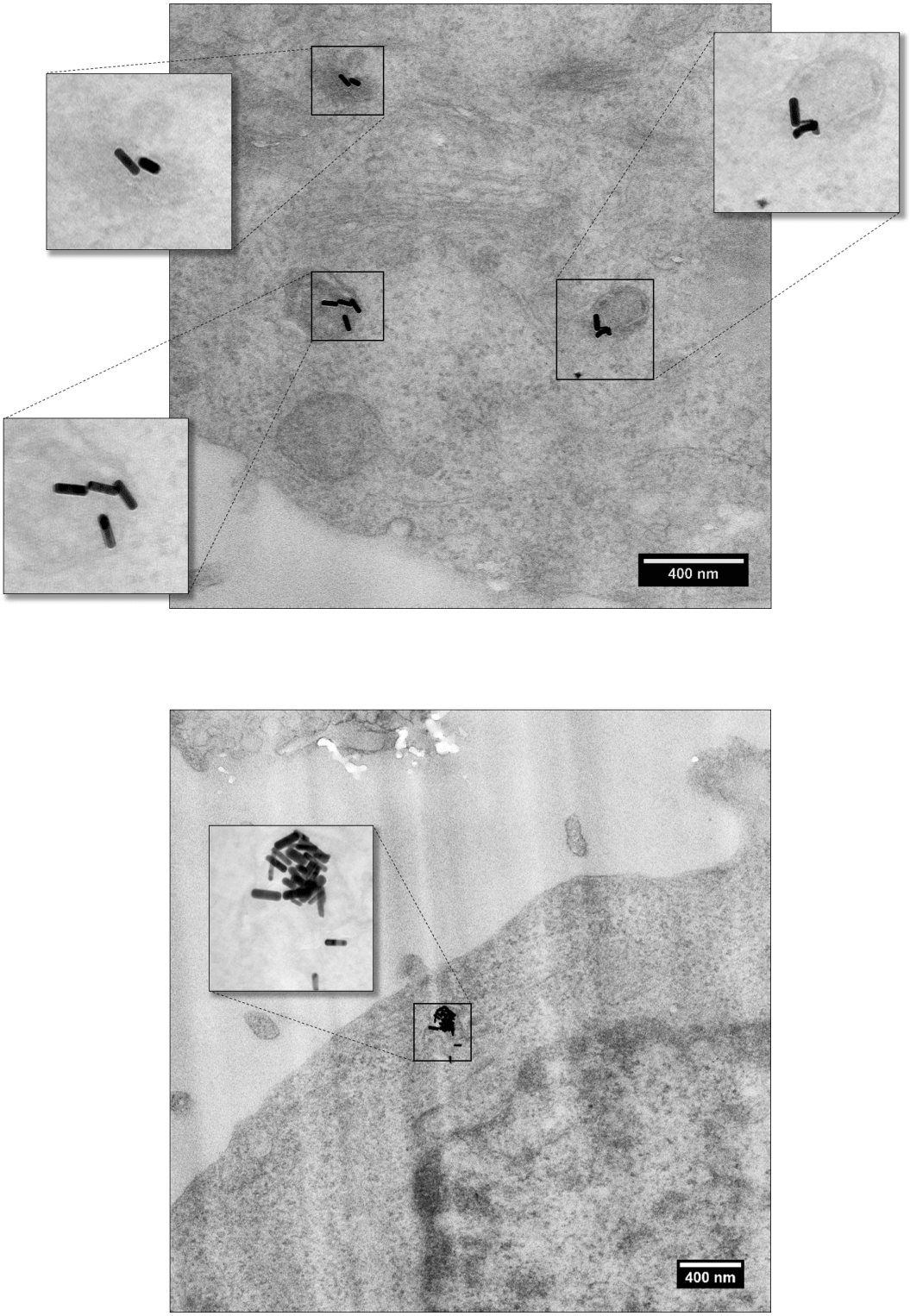

Figure 5.4: TEM micrographs of cell sections containing endocytosed AuNRs. Cells were incubated with DOPC – DSPE-mPEG AuNRs for four hours, before fixing, embedding in resin, and sectioning. Cells were stained with osmium tetroxide and uranyl acetate for contrast.

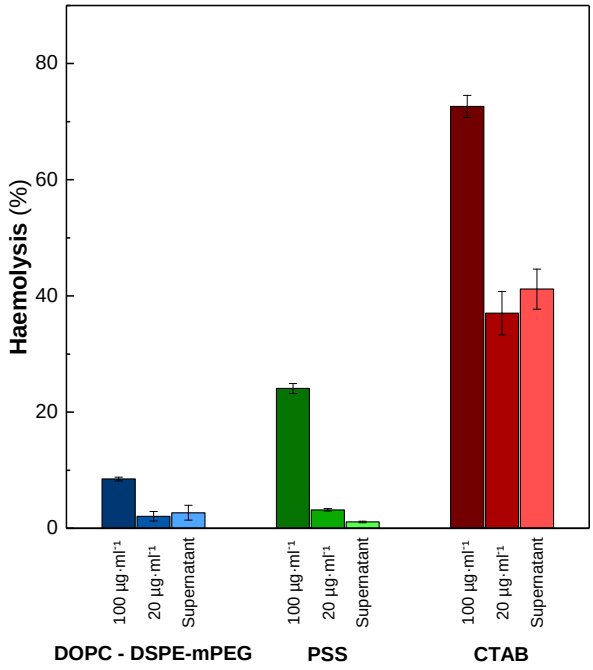

Figure 5.5: Measured haemolysis fractions for DOPC – DSPE-mPEG (19:1), PSS and CTAB – oleate functionalised AuNRs at 100 µg·ml^{-1} and 20 µg·ml^{-1}. The lysis values for the supernatant extracted from 100 µg·ml^{-1} AuNRs is also presented.

limited, but these images would seem to support the case that intracellular aggregation is being observed. Based on the staining of the cells it would appear that these particles are also contained within endosomes, suggesting uptake through endocytosis, which is consistent with what is expected for NPs of this size.

5.3.4 Haemolysis

Another concern relating to the use of nanoparticles *in vivo* is that of haemolysis, the rupture or destruction of red blood cells. Free CTAB being a positively charged amphiphile can disrupt the negatively charged membrane of red blood cells (or any other cell) inducing haemolysis [191]. This membrane disruption is one of the primary mechanisms by which CTAB is toxic. Hence a sensible prerequisite of *in vivo* testing of AuNRs of any novel surface functionalisation is that of haemolysis testing. Particles were tested at 100 µg·ml^{-1} and 20 µg·ml^{-1}. The presence of free CTAB is a primary concern, hence the supernatant of the 100 µg·ml^{-1} concentrations of each functionalisation were also tested. If these came back at similar values to the 100 µg·ml^{-1} AuNR samples, the supernatant itself could be concluded to be the cause of any observed haemolysis (this was not observed to be the case for the PSS and DOPC – DSPE-mPEG AuNRs).

It was found that the absorbance from the transverse mode prevented accurate calculation of the lysis fraction at 540 nm, the wavelength typically used for these assays. instead the Soret band at 420 nm was used. This solution has also been implemented for other AuNP haemolysis assays elsewhere in the literature (i.e. ref. [191]).

The haemolysis assay showed lysis fractions below 10 % for all DOPC – DSPE-mPEG AuNR concentrations. The PSS AuNRs showed higher lysis values, but were relatively low. Where as the CTAB functionalised AuNRs showed very high lysis values above 75% at 100 µg·ml^{-1}, and 40% for the 20 µg·ml^{-1} case, as well as the supernatant. Hence functionalisation with PSS and phospholipids has significantly improved the *in vivo* toxicity of the AuNRs, with the phospholipid–functionalised AuNRs performing better at higher doses. This is consistent with the cytotoxicity data collected above.

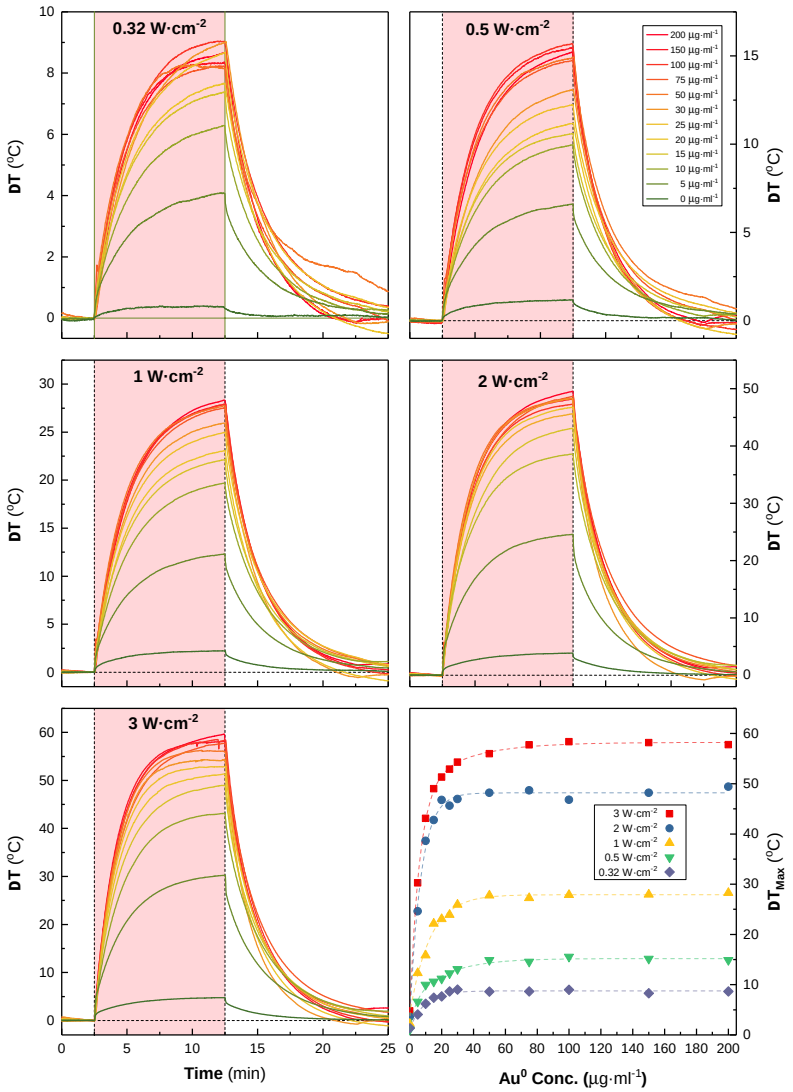

Figure 5.6: **(a) – (e)** Temperature profiles of 200 µl AuNR solutions (5 to 200 µg·ml^{-1}) heated at by CW laser irradiation at the LSPR (811 nm) for 10 min at a variety of intensities: **(a)** 0.32 W·cm^{-2}, **(b)** 0.5 W·cm^{-2}, **(c)** 1 W·cm^{-2}, **(d)** 2 W·cm^{-2}, **(e)** 3 W·cm^{-2}. The legend in **(b)** applies to figures **(a) – (e)**. **(f)** Max temperature as a function of Au^0 concentration. The maximum temperature achievable plateaus as the nanoparticles effectively absorb all light incident on the sample at concentrations above ~50 µg·ml^{-1}.

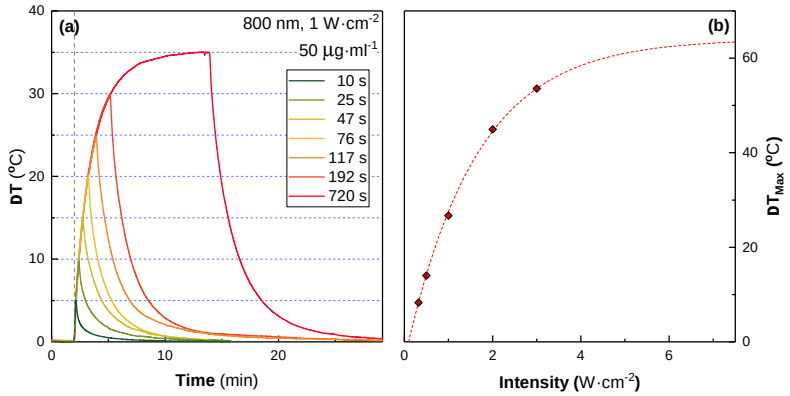

Figure 5.7: **(a)** Heating profile of a sample heated to increasingly high temperatures in 5°C increments. The time required to achieve this are given in the legend; the time required increases asymptotically as ΔT approaches 35.3°C. **(b)** ΔT_{max} at 200 µg·ml^{-1} as a function of laser intensity. The data is fitted with an exponential association curve. Increasing heat losses to the environment at higher ΔT result in the curve saturating at ~64°C. All measurements were taken at a background temperature of 37°C

5.4 Photothermal Heating with AuNRs

To confirm that the prepared phospholipid–functionalised AuNRs could generate suitable temperatures to induce cell death, preparatory studies measuring the temperature increase of the AuNRs under continuous–wave illumination were performed. Measurements were carried out on a bespoke experimental rig assembled with the express purpose of monitoring the effects of photothermal heat generation by plasmonic nanoparticles on cells. Samples were prepared on a 96–well plate in 200 μL aliquots and temperatures measured by directly placing a thermocouple into the well. Neighbouring wells to those containing samples were left empty to provide better thermal insulation, and minimise the rate of heat flow out of the illuminated well (and simultaneously prevent indirect heating of other sample–containing wells). All measurements were taken at a background temperature of 37°C.

Figure 5.6(a)–(e) shows the temperature response of colloidal AuNR solutions ranging in concentration between 0 and 200 $\mu g \cdot ml^{-1}$ at light intensities between 0.32 $W \cdot cm^{-2}$ and 3 $W \cdot cm^{-2}$. The maximum temperature observed at each laser intensity as a function of concentration is summarised in fig. 5.6(f).

Illustrated in fig. 1.12 are the effects of increased temperatures on human tissue, it can be seen that an increase in temperature of +10°C is required in order to achieve cell death over short exposure times. Higher temperatures are far more effective at achieving cell death with +23°C providing energy to induce instantaneous protein coagulation resulting in incredibly rapid cell death.

Hence, by comparison an increase in temperature of +9°C is achievable at 0.32 $W \cdot cm^{-2}$ at concentrations of above 50 $\mu g \cdot ml^{-1}$, which close to the lower threshold for inducing cell death. 0.32 $W \cdot cm^{-2}$ is significant because the maximum permissible exposure (MPE) at 811 nm with a CW source, hence in an ideal world it would not be exceeded. However, 50 $\mu g \cdot ml^{-1}$ is a concentration that could not be realistically achieved *in vivo* without resorting to intratumoural injections. Beyond this the heating in this set-up is occurring in an idealised set–up, it is not limited by the high attenuation of human tissue (i.e. this is the temperature increase we could achieve at the skin surface). Under these conditions a +9°C increase is not large enough, regardless of the high concentration required to achieve it.

If the MPE is ignored, on the justification that the small amount of potential collateral damage that could occur due to the beam is a worthwhile price for the potential therapeutic benefits of the treatment, the higher beam powers do offer temperature increases which look significantly more promising. For instance at 1 $W \cdot cm^{-2}$, a +10°C can be achieved at 5 $\mu g \cdot ml^{-1}$ and a +23°C increase at 20 $\mu g \cdot ml^{-1}$. At 2 $W \cdot cm^{-2}$, +23°C is achievable at 5 $\mu g \cdot ml^{-1}$. At these higher powers the temperature increases even at relatively low concentrations are high enough that they would be therapeutically relevant. The fact that we have to exceed the MPE to achieve these however is problematic. However, considering the large collateral damage that is associated with with treatment via current generation chemotherapeutic agents, a cost–benefit argument would be relatively easy to present to justify using such beam powers. The potential damage to tissue at these powers is not particularly severe compared with the potential benefits of cancer therapy. Alternatively, other laser sources could be utilised such as nanosecond pulsed lasers which use much lower total fluences to generate highly–localised high–temperature transient heating around the nanoparticle. Although these have not been explored here due to time constraints, but are of considerable interest.

The heat profiles of each curve can reliably be recreated, and heating to desired max temperature will consistently produce a curve which matches the shape of the initial shape of the heating response (fig. 5.7(a)).

The time required to achieve a particle temperature increases asymptotically as the temperature increase approaches the saturation value.

Finally, the limitations of the experimental set–up can be seen. Heat losses to the environment become increasingly dominant at higher values of ΔT, leading to a maximum realisable value of ΔT. Plotting the maximum temperature achieved at the highest concentrations of AuNRs as function of laser intensity reveals that the highest value of ΔT we can achieve is ~64°C (fig. 5.7(b)). Increasing ΔT beyond this would require better thermal isolation of the illuminated site, although this would not offer any significant insight into the therapeutic potential our AuNRs.

We can also compare our observed heating rates with those predicted in section 1.3.2, where an estimate of the initial heating rate (i.e. with minimal losses to the environment) of 2.4 °C·s^{-1} was calculated based on FEM simulations of the extinction cross-section of a AuNR with an LSPR of 800 nm under 1 W·cm^{-1} illumination. The equivalent case here (~75 µg·, 1 W·cm^{-1}) has an initial heating rate of 0.8 °C·s^{-1}. The calculations are likely overestimating, because they (a) assume a perfectly monodisperse sample (i.e. all AuNRs are perfectly matched to the excitation wavelength) and (b) the FEM simulations fail to account for plasmonic damping effects such as electron–surface scattering. The numbers are relatively close however, suggesting that inclusion of these factors would likely bring them into closer agreement.

5.4.1 Thermal Stability Under CW Illumination

A commonly raised concern about the potential of AuNRs as therapeutic agents is that of thermal stability. This is not an unjustified concern, however the nature of problem is seems to be misunderstood in the literature. For instance a number of publications have offered the 'low thermal stability' of nanorods as a reason to utilise other novel NIR–absorbing nanomaterials, whilst using a continuous–wave lasers to demonstrate the 'higher' stability of such materials (for example refs. [27] and [49]). This seems to stem from a misunderstanding of the nature of the heating generated by continuous wave lasers versus that of nanosecond–pulse lasers. The maximum local temperature increase achieved under continuous–wave heating is significantly lower than that achieved under pulsed illumination.

Calculated solutions the heating of single nanorods under typical continuous wave and nanosecond pulsed illumination conditions are presented in fig. 1.10. Continuous–wave illumination will result in bulk heating and can achieve macroscopic increases in temperature of several 10°C, but it is very difficult to achieve temperatures that will cause rapid reshaping of AuNRs. By comparison, individual AuNRs are expected to instantaneously achieve temperatures well in excess of 300°C under a typical pulse from a nanosecond–pulsed laser (see fig. 1.10 & ref. [279]). This is not in excess of the melting point of Au, but will provide sufficient energy to atoms to enable significant migration of atoms from the AuNR tips towards the centre of the rod, lowering the aspect ratio [341]. Hence, a relatively short train of pulses is capable of reducing the maximum LSPR wavelength below that of the illumination source, significantly reducing photothermal efficiency.

Both regimes present opportunities, the higher temperatures achievable with nanosecond–pulsed lasers, offer much more efficient photothermal killing, the high temperatures will instantaneously denature proteins, and can potentially induce cavitation, providing mechanical stress, which is even more effective at damaging cells. But this comes with the potential downside of photothermal reshaping and the higher cost of Nd:YAG

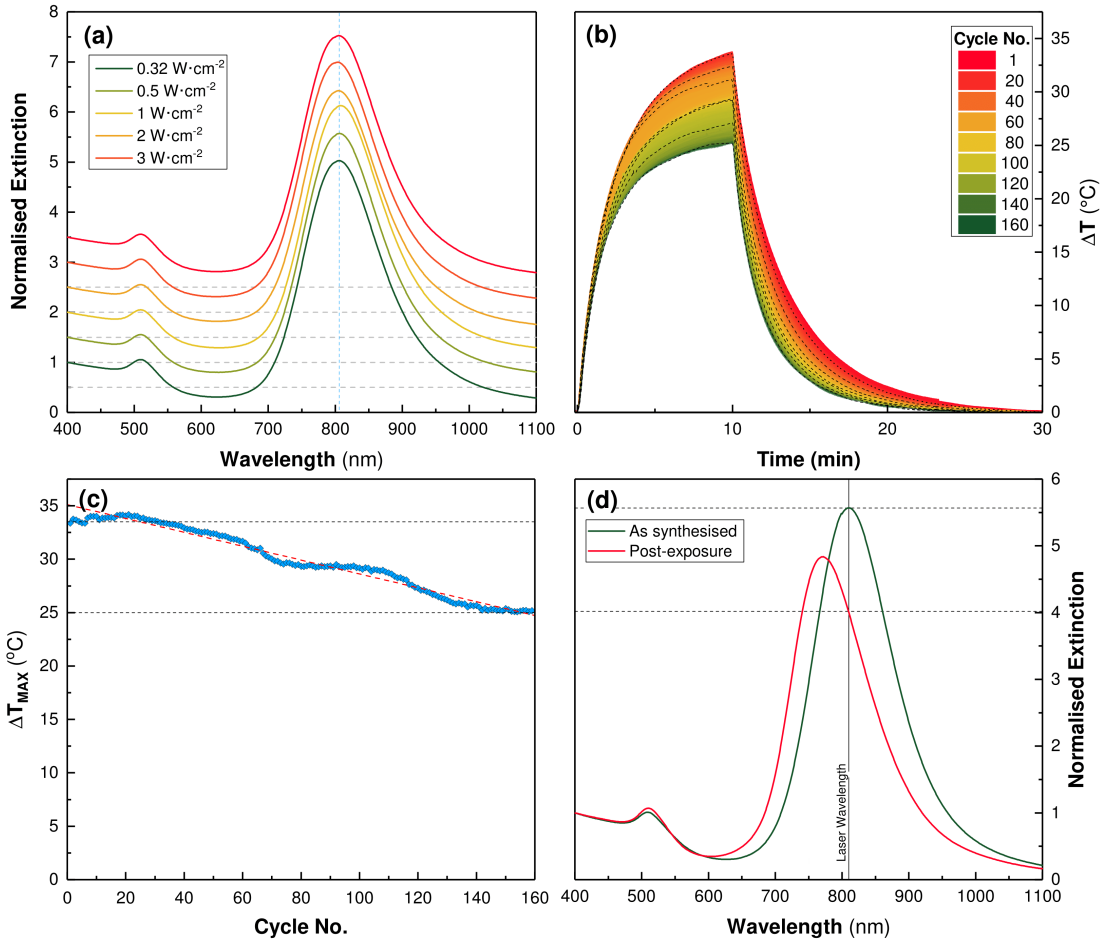

Figure 5.8: **(a)** Heating curves of 200 µL 75 µg·mL AuNR solution illuminated at its LSPR maximum (801 nm) in repeated cycles. Cycles consisted of 10 minute of laser exposure at 1 W·cm^{-2}, followed by 20 minutes of cooling (no laser exposure). 30 minutes sections corresponding to each heating cycle have been overlaid. Dashed lines mark every 20 cycles. **(b)** The maximum temperature achieved as a function of cycle number, it can be seen to decrease roughly linearly with time. **(c)** UV-vis spectrum before and after laser exposure, the extinction at the laser illumination wavelength for each spectrum have been marked.

laser systems. At typical fluences continuous–wave lasers do not face this issue, but they require significantly longer periods of exposure and high concentrations of AuNRs to achieve temperatures likely the induce the death of surrounding cells. Non–tunable continuous wave sources are significantly cheaper that the nanosecond–pulsed systems typically used in these applications. At higher fluences (12 W·cm^{-2}), it has been reported that CW illumination can induce significant thermal reshaping [121].

No discernible change in the optical properties of the AuNRs was observed during the experiments performed in fig. 5.6, the resultant spectra from the 75 µg·ml^{-1} after illumination at each laser intensity are given in fig. 5.8(a). To further test the stability of our particles under repeated CW photothermal heating the LSPR resonance and measuring the maximum temperature increase over time. A 200 µL solution was sealed airtight inside a single well of a 96–well plate at 37°C and then heated in cycles of 10 minutes at 1 W·cm^{-2} laser exposure followed by 20 minutes unilluminated. To demonstrate that degradation of the optical properties under CW illumination is not a concern, this was tested to excess and allowed to run over the course of 3.5 days (~160 cycles). The resultant temperature responses have been compiled in fig. 5.8(b). Over the course of this time period a reduction in ΔT_{max} was visible, reducing from ΔT_{max} = 35°C to ΔT_{max} = 25 °C (fig. 5.8(c)). This this drop was achieved over a cumulative total illumination time of 26 h 40 m,

well in excess of what would be used in treatment. This represents an average drop of 0.06°C per cycle, which is negligible. Inspection of the spectra of the AuNRs before and after these photothermal heating cycles showed a drop in the LSPR intensity and blueshift in the peak position (fig. 5.8(c)). There was a drop in absorbance at the laser wavelength of ~29% (consistent with the drop in ΔT_{max} of ~26%). The change in the shape of the spectrum is consistent with that seen for reshaping of AuNRs when heated in solution due to surface migration of atoms [247, 341, 411], as compared to the highly selective reshaping of AuNRs resonant close to the laser wavelength seen under high intensity pulsed systems [110, 174].

Hence it seems that these particles show good thermal stability under CW illumination and this should not be considered a concern going forward. Their stability under pulsed illumination is another matter and is discussed further in the next section.

5.5 Photoacoustics

AuNRs represent some of the most promising agents for use in photoacoustics, the combination of large absorbance crosssections (which are tunable and spectrally narrow) as well as their extremely high photothermal conversion efficiency, meaning that they are well suited as targets which produce a large signal and can be spectrally deconvoluted with relative ease. The theory behind signal generation is well understood and the existing challenges surrounding their use lie largely in problems surrounding maintaining their stability *in vivo* and the thermal stability of AuNRs under the high peak powers seen during nanosecond–pulsed illumination [382].

With regards to the thermal stability of AuNRs, in many ways AuNRs are victims of their own success, the very properties which make them appealing; the large absorbance crosssections and high efficiencies of heat generation, leads to the generation of temperatures high enough to induce thermal reshaping. Smaller diameter AuNRs (similar in dimensions to the ones used here) with their higher surface–to–volume ratios and lower heat generation per NP have been reported to be less likely to undergo thermal reshaping than larger AuNRs [51, 173]. The only reported study on the thermal stability of phospholipid–functionalised AuNRs, observed minimal reshaping of phosphatidylcholine–capped AuNRs of similar dimensions to those utilised here under 10 Hz pulsed nanosecond illumination at 127 mJ·cm^{-2} over the course of several minutes [127]. Hence whilst this is a commonly reported problem, it was not clear whether this would be an issue that would affect our particles.

As an initial proof of concept, AuNRs were synthesised with LSPR maxima approximately 100 nm apart (630 nm, 750 nm, 847 nm and 935 nm) across the tunable range of the laser source (680 – 950 nm) and their photoacoustic response measured as a function of illumination wavelength. The samples were placed in an agar phantom to replicate the expected illumination condition *in vivo* and measured using a pre–clinical MSOT imaging system. The photoacoustic (PA) response is expected to scale linearly with the absorbance of the sample (eq. (1.24)), hence the measured PA response should correlate strongly with the absorbance spectrum of the sample. However the sensitivity of the system to individual absorbers components is limited by the surrounding components. In particular the absorbance of water increases substantially between 850 and 980 nm, hence samples which display similar increasing absorbance in this region are difficult to deconvolute from the water signal. There is a large amount of water in the system, the phantom is suspended in a water bath (enabling acoustic transmission), the agar phantom is self is ~96% water by weight and the

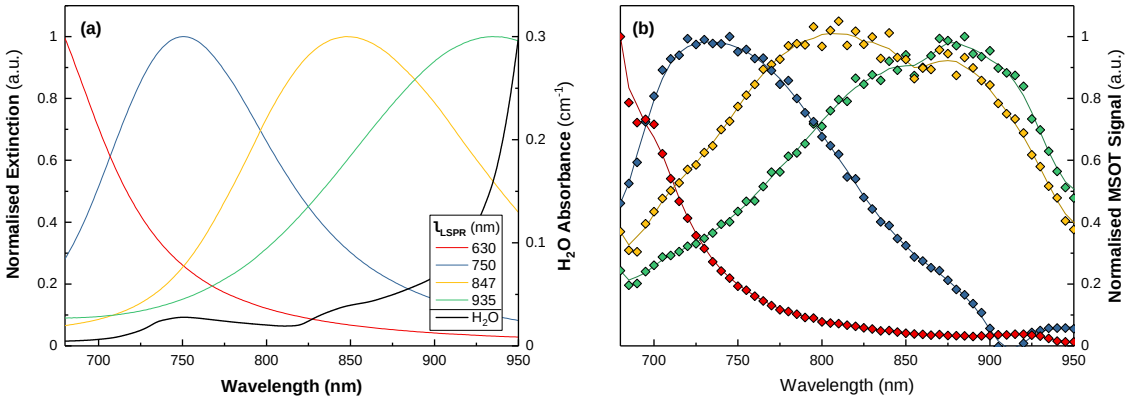

Figure 5.9: (a) UV–vis extinction spectra of AuNRs with a resonances at 630 nm, 750 nm, 850 nm and 935 nm. Samples were diluted to have an absorbance of 5 at their LSPR maximum. AuNR spectra are normalised to their maximum extinction in the range 680–950 nm. Also plotted is the absorbance spectra of H_2O (right axis), showing the increasing absorbance from 850 nm to 950 nm. Absorbance values for water taken from ref. [270]. **(b)** Photoacoustic spectra, as determined from MSOT images reconstructed using a back projection algorithm. PA intensity values were calculated by averaging the intensity of the top 5% of pixels in the region of interest (3 mm circle placed over the position of the sample). Spectra were corrected by subtracting the PA response of the water control from that of the AuNR suspensions and normalised to the maximum PA intensity in the range 680–950 nm. The PA spectra show good qualitative similarity to the UV–vis spectra below 850 nm. At higher wavelengths the increasing absorbance of water (and hence that in the surrounding water bath) reduces the intensity of light reaching the sample and hence suppresses the PA signal, leading the spectra above 850 nm to become increasingly unreliable.

AuNRs themselves are suspended in water. This all contributes to a large increases in light attenuation before it reaches the sample (reducing the intensity of the PA signal), and creates a much stronger background PA signal. Hence samples which display an absorbance below 850 nm are optimal for use within these phantoms.

In vivo there are additional absorbance signals which need to be considered such as haemoglobin (Hb), oxyhaemoglobin (HbO_2), melanin and fat. At typical *in vivo* concentrations these components combined these have a minimum absorbance in the visible–NIR at ~800 nm (see fig. 1.11). Hence PA contrast agents which absorb here can be more easily deconvoluted from Hb, HbO_2 and H_2O, and thus typically present the best contrast in reconstructions.

The UV-vis and recorded PA spectra are presented in fig. 5.11(a)&(b). It can be seen that all four spectra correlate relatively strongly below 850 nm, consistent with what is stated above. Above 900 nm it becomes apparent that the spectra have become more unreliable, as it becomes increasingly difficult to distinguish between the sample and background H_2O signal. This is particularly apparent in the λ_{LSPR} = 935 nm spectrum, which presents an apparent maximum closer to 890–900 nm in its PA spectrum. Regardless of this, it is relatively easily to distinguish between the spectra of each set of AuNRs and clearly demonstrates that these particles are suitable PA conversion agents.

To optimise the AuNRs for use *in vivo*, it was decided to work as close to 800 nm as possible. Hence, the AuNRs described above in section 5.2 were used going forward (λ_{LSPR} = 801 nm after phospholipid exchange). In order to find the required AuNR concentrations to reliably image them *in vivo*, AuNR phantoms were measured at a variety of concentrations between 0.32 $\mu g \cdot ml^{-1}$ and 1000 $\mu g \cdot ml^{-1}$. Five spectral runs were taken on the samples at a single position in the phantom. The reconstructed PA intensity maps recorded by the MSOT scanner are given in fig. 5.10 and the spectra reconstructed from these scans are given in

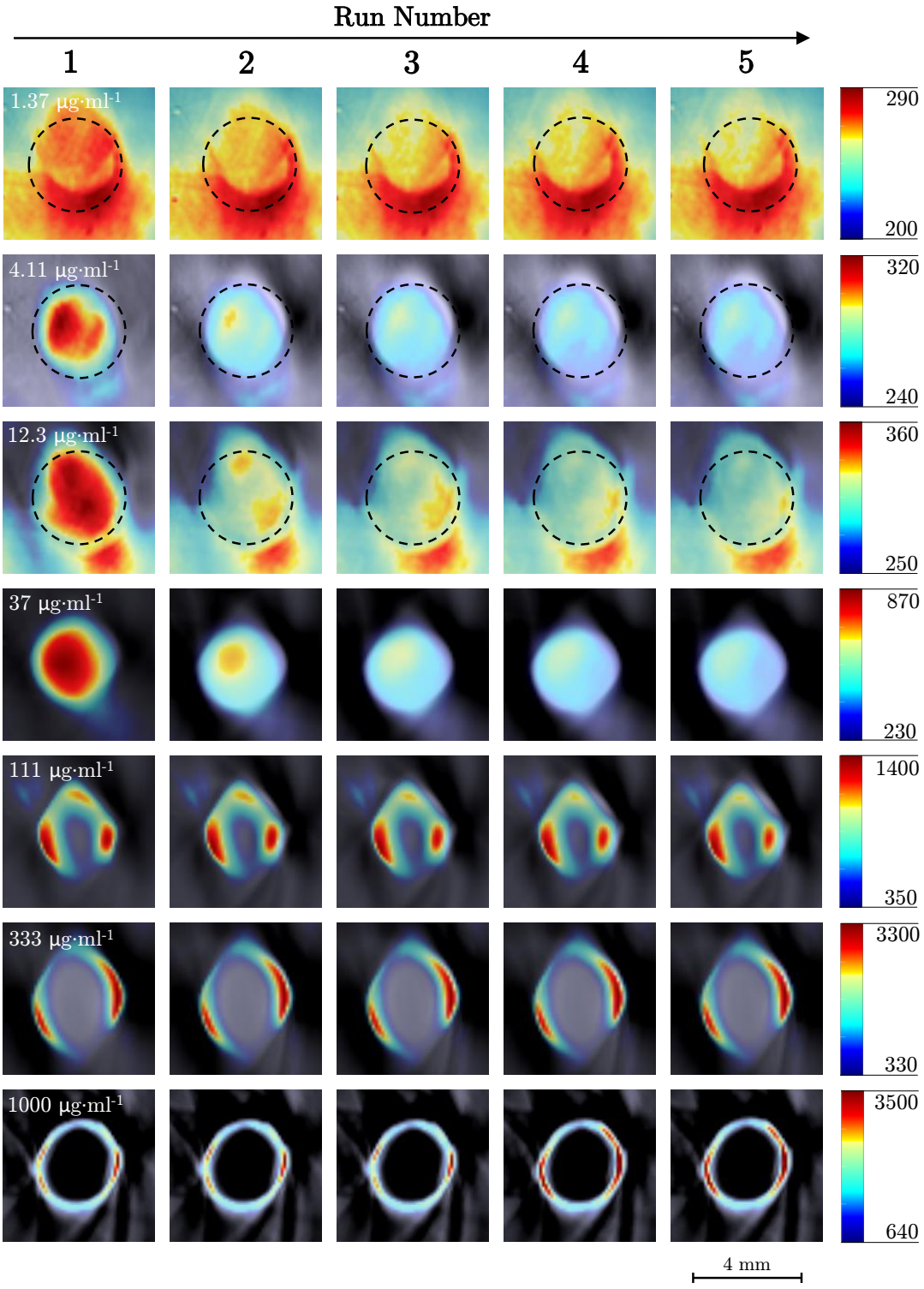

Figure 5.10: MSOT intensity maps of a single plane through an agar phantom containing a variety of AuNR concentrations. Images were reconstructed using a linear reconstruction algorithm which calculated the spatial distribution of the AuNR solution based on an extinction spectrum measured using a UV-vis spectrometer. The reconstructions have been cropped to the region of interest around the AuNR solution; an example of a non–cropped image is give in fig. 2.7. Each row consists of a single measurement, with 5 repeats measured in series (displayed left to right). The linear regression algorithm struggles to reconstruction the sample distribution at lower concentrations, which is evident from the signal visible in the background of the 1.37, 4.11, and 12.33 µg·ml^{-1} images. For concentrations of 111 µg·ml^{-1} and above, it is evident that light is no longer penetrating the interior of the sample, leading to a ring of single from the surface particles which are effectively screening the interior AuNRs. There is also a noticeable drop off in intensity after the first measurement for all concentrations below 37 µg·ml^{-1} indicating that the spectral properties of the probe have changed (i.e the AuNRs have thermally reshaped).

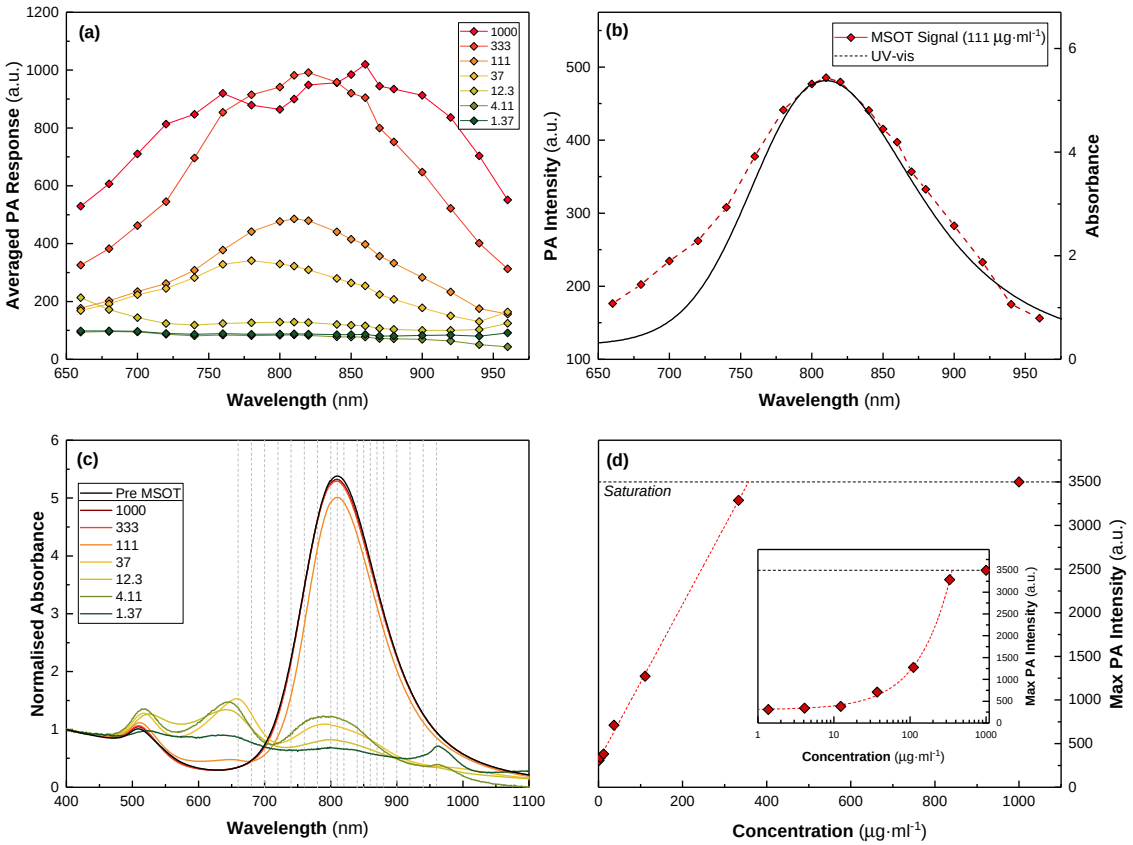

Figure 5.11: **(a)** Photoacoustic spectra, as determined from MSOT images reconstructed using a back projection algorithm. PA intensity values were calculated by averaging the intensity of the top 5% of pixels the region of interest (3 mm circle placed over the position of the sample). The values shown are those obtained during the first of the five runs show in fig. 5.10. **(b)** Comparison of the photoacoustic spectra obtained for the 37 µg·ml^{-1} concentration and the UV-vis of the sample prior to laser exposure. **(c)** UV–vis spectra of samples before and after being exposed to the laser source inside the MSOT scanner for the images give in fig. 5.10. Lower concentration samples clearly undergo thermal reshaping. Gray lines indicate the wavelengths used to measure the photoacoustic response of the particles. **(d)** The maximum pixel intensity measured by the MSOT as a function of AuNR concentration. Samples were prepared by serial dilution from 1000 µg·ml^{-1}. Fitted with a linear function below ~360 µg·ml^{-1} (with an assumed maximum achievable PA intensity value of 3500 a.u.). Inset is the same data plotted using a logarithmic x–axis.

fig. 5.11(a). In the spectra it can be see for the 333 and 1000 µg·ml^{-1} samples, the intensity of the PA response has begun to become increasingly saturated, leading to the top of the spectral response of the particles to become flattened. This saturation could be attributed to either complete absorption of all incident light by the sample, or the reaching the peak negative pressure of the transducers in the system. The former seems more likely based on the reconstructions seen in fig. 5.10, which show minimal signal generation inside the the phantom, suggesting complete absorption of the light at the surface of the phantom.

The spectral response of the 111 µg·ml^{-1} phantom correlates very strongly with the UV–vis spectrum fig. 5.11(b), however below this the correlation becomes increasingly weak. The spectra of the 37 µg·ml^{-1} phantom has a blue–shifted peak, this is presumed to result from thermal reshaping. The wavelength of the laser source was swept from 660 to 960 nm, hence reshaping could occur below the LSPR maximum, reducing the PA intensity at the original LSPR once the laser had been tuned to it, leading to a reduced signal and a apparent blueshift in the maximum PA intensity.

Below 37 µg·ml^{-1} it was not possible to clearly distinguish the spectrum of the AuNRs, this also attributed to thermal reshaping at lower wavelengths. This is supported by UV–vis spectra taken of the samples after

measurement on the MSOT imaging system (fig. 5.11(c)), which show significant reduction in the absorbance of the particles over the wavelength range of the laser exposure. There is also a noticeable increase in the absorbance between 600 and 660 nm consistent with the observed reshaping behaviour of AuNRs under high intensity pulsed lasers [110, 174, 207, 208]

Some reshaping can be inferred from the 111 $\mu g \cdot ml^{-1}$ spectrum, by the increased absorbance below 680 nm and reduced intensity of the LSPR maximum. These features are not present in the spectra of concentrations above this, and there was no reduction in the strength of the PA signal in later scans, leads to the conclusion that they do not appear to undergo significant reshaping. It is unclear whether this results from any reshaped AuNRs making up a very small proportion of the total population of AuNRs or the higher concentrations somehow providing a shielding effect. The potential benefits of this are quite limited, given that such particle concentrations cannot be achieved *in vivo* without intratumoural injections.

The reshaping can be seen more clearly through inspection of the reconstructed images of the AuNR PA signal distribution shown in fig. 5.9, in it can be seen that the AuNR signal intensity drops dramatically after the second spectral scan for concentrations below 37 $\mu g \cdot ml^{-1}$. Reconstructions are generated based on spectral data for the AuNRs obtained by UV–vis prior to the measurement, which enables the response of the particles to be deconvoluted from the background signal. However the change in spectral properties caused by thermal reshaping is preventing the reconstruction algorithm from being able to identify their presence, meaning the spatial distribution cannot be reliably reconstructed. Equally the signal from the 1.37 $\mu g \cdot ml^{-1}$ phantom was so weak that it could not reliably be reconstructed, leading to the system presenting a near meaningless intensity profile.

At higher concentrations, light cannot penetrate the centre of the sample leading to the reconstructed image resembling a ring. The width of this ring decreases with increasing concentration as the penetration depth of incident light is further reduced. Hence any heating is confined to relatively narrow shell around the outside of the sample, which could potentially leave only a relatively small fraction of the sample to thermally reshape. If this is occurring it is not evident in the post–MSOT UV-vis spectrum though.

It was planned that further studies of the AuNRs in the MSOT imaging system would be performed, however technical issues with the system prevented further measurements, including its use for *in vivo* measurements, alongside time restrictions. It was also planned that these additional measurements would be supported by TEM images of the particles post–exposure, but these were prevented by the same technical difficulties and hence this dataset does not exist.

The PA signal intensity is expected to scale linearly with concentration up to a saturation value at which all light incident on the sample is absorbed. The short duration of the laser pulses here and the small length scales involved in heating, means that macroscopic heat flow out of the system can be assumed to be negligible[1]. Hence, the concentration dependence of the heat–generation–per–pulse (and hence PA signal intensity) is described by a linear function up to some saturation value fig. 5.11, unlike the exponential association function used to describe the CW heating above (fig. 5.7(f)).

The fact that these particles reshape under pulsed illumination presents another major hurdle, which will remain unaddressed by this thesis due to time restraints. As stated earlier this problem was not unanticipated, and has been widely recognized in the literature [51, 341, 351], although it was unclear whether it would

[1] The width of the generated pulse is defined by the stress relaxation time and is typically ~1 μs (see section 1.4.3), hence the thermal diffusion length can be calculated as $d_{th} = 2\sqrt{\alpha t}$ ~0.7 μm. Hence macroscopic transfer of heat generated by the particles to the environment during pulse generation will be negligible.

be the case for the particles used here. The fluences observed inside phantoms are also likely to be higher than those achieved *in vivo*, where tissue is likely be more attenuating, as the phantoms only replicate the scattering seen in tissue, but not the absorbance. Hence, these AuNRs may still be usable *in vivo*.

The solution to preventing reshaping that has gained most traction is the use of silica coating to prevent thermal reshaping of AuNPs during PA imaging or photothermal therapy utilising pulsed lasers [31, 53, 59, 60, 157, 216, 382]. If the silica layer is made thick enough it also offers the potential benefit of preventing plasmonic coupling between particles that have undergone aggregation [62]. This represents a potential avenue for future work as these phospholipid coatings will readily bind to the silica surfaces, enabling any benefits of them to still be realised.

5.6 *In vitro* Photothermal Studies

The bespoke rig used in section 5.4 for solution heating was deployed here to measure the effects of laser ablation on colorectal cells prepared in a 96–well plate. No temperature monitoring was performed during these assays, as introducing a thermocouple into the media would undermine the sterility of the plate. A thermal imaging camera was an alternative option, but 96–well plates are not transparent at the wavelengths that such cameras use. Hence, any temperatures recorded by such devices are the external temperature of the plate, not temperature of the well itself, hence the information garnered is not particularly useful other than confirming heating is occurring (which can be fairly reliably assumed).

As an initial experiment was performed to demonstrate that laser exposure at 801 nm (the LSPR maxima of the AuNRs to be used) was not detrimental to the cells. SW620 cells were plated in 96–well plates and exposed to light at maximum achievable laser intensity from our laser source, for times between 0 and 10 minutes. The intensity was 3.85 W·cm^{-2}, which is 12 times higher than the MPE. Each exposure time was repeated across six wells and the viability measured by the CCK–8 assay was expressed as a percentage of that of the control.

No drop in viability was seen at any exposure time (fig. 5.12 hence the background effect of irradiating the cells at this laser intensity or below were deemed to have no effect on cells *in vitro*. The expected heating should come entirely from RPMI 1640 CCM, the most absorbing component of which at 801 nm is water. Figure 5.6 shows that we only expect a temperature increase of ~4°C in the absence of AuNRs at this intensity, which is consistent with the observed lack of cell death.

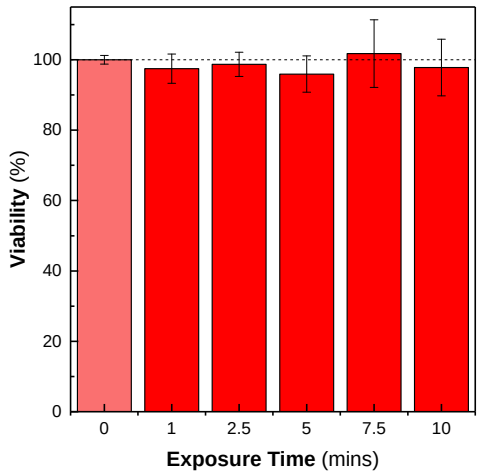

Figure 5.12: Viability of SW620 exposed to 3.85 W·cm^{-2} CW laser light at 801 nm (maximum output power). Experiments were performed in the absence of AuNRs to demonstrate no negative effects on cell viability due to laser exposure. The background temperature was maintained at 37°C during laser exposure.

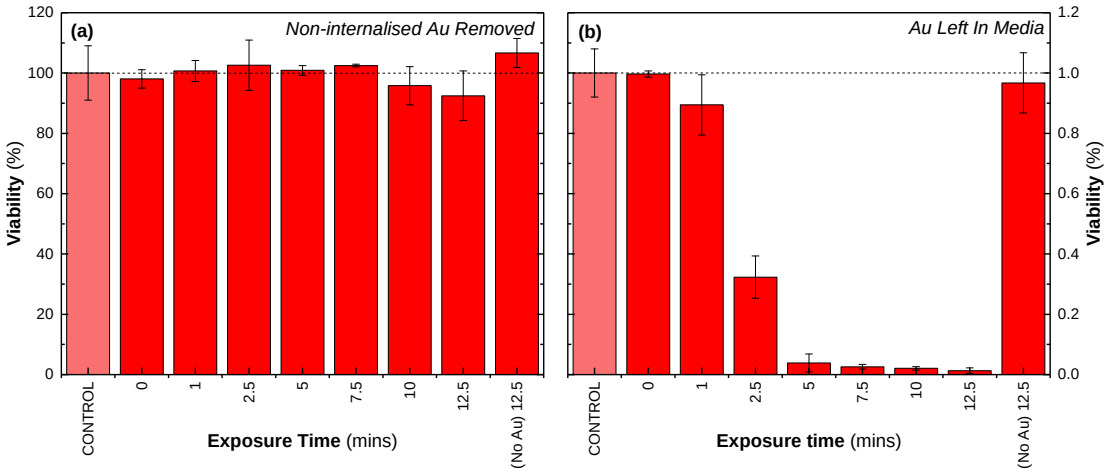

Figure 5.13: Viabilities of SW620 cells exposed to 1 W·cm^{-2} CW laser light. Cells were incubated with 40 μg·ml^{-1} for 4 hours before illumination. **(a)** shows cell viabilities if the media is replaced with fresh RPMI 1640 CCM and **(b)** shows cell viabilities with the original AuNR–enriched media still present (i.e. non–internalised AuNRs are still in solution). Both figures are calculated from the results of separate assays repeated in triplicate. All viabilities are expressed as a percentage of the control (i.e. cells that received no Au and no laser exposure).

5.6.1 Cells Incubated With AuNRs

It was decided to proceed to testing photothermal ablation of cells using of AuNRs. Cells were incubated with AuNRs for four hours prior to illumination. In order to slightly more closely match the uptake conditions we expect *in vivo*. The media was removed, the cells washed with PBS and the media replaced after four hours of incubation prior to the laser exposure, removing free AuNRs in solution, and relying only on the particles that had been endocytosised by the cells.

At the MPE (0.32 W·cm^{-2}) no cell death was observed (results not shown). It was thus decided to repeat the experiment at an increased laser intensity of 1 W·cm^{-2}, the resultant assay is shown in fig. 5.13(a). Again, no cell death was observed for any exposure time.

As an initial demonstration that the heat generation from AuNRs at this concentration and laser intensity could induce cell death. The entire experiment was repeated without replacing the media prior to laser exposure. The results of this assay are shown in fig. 5.13(b). A reduction in viability to 80 % is seen after 1 minute of exposure and is reduced to with error of 0% after 5 minutes. The lack of cell death seen above therefore does not seem to emanating from aggregation in solution induced as a result of an unforeseen interaction by the cells.

Two probable explanations for the issues seen have been postulated:

1. Cells are not being incubated long enough for significant AuNR uptake to occur.
2. The particles are undergoing intracellular aggregation (loss of optical properties).

To eliminate incubation time as a cause, another photothermal viability assay was run, this time varying the incubation time after the addition of AuNR enriched media. The laser power was also increased to 2 W·cm^{-2} to increase the chances of observing cell death. The results of this assay are presented in fig. 5.14. Again all viabilities are within error of (or above) 100%, based on the darkfield images presented in fig. 5.3, it can reasonably be concluded that limited uptake is not the problem causing the lack of observed cell death. Ideally this data would be supported by a more quantitative measurement of AuNR uptake, such as ICP–MS

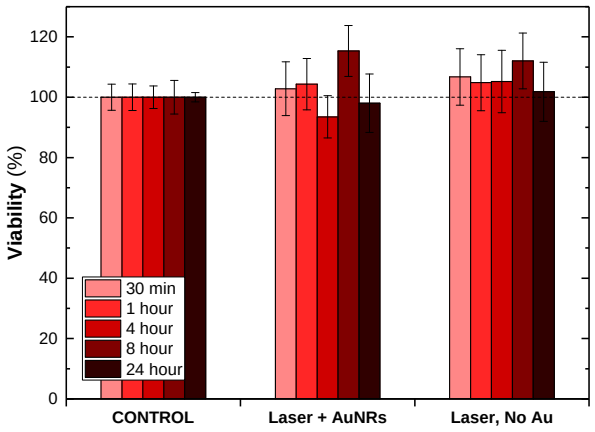

Figure 5.14: Viabilities of SW620 cells exposed to 2 W·cm^{-2} CW laser light for 5 minutes. Cells were incubated with 40 µg·ml^{-1} for varying amounts of time. Cell viabilities are expressed as a percentage of the control wells. All wells were repeated in triplicate. Only the results from a single well plate are presented.

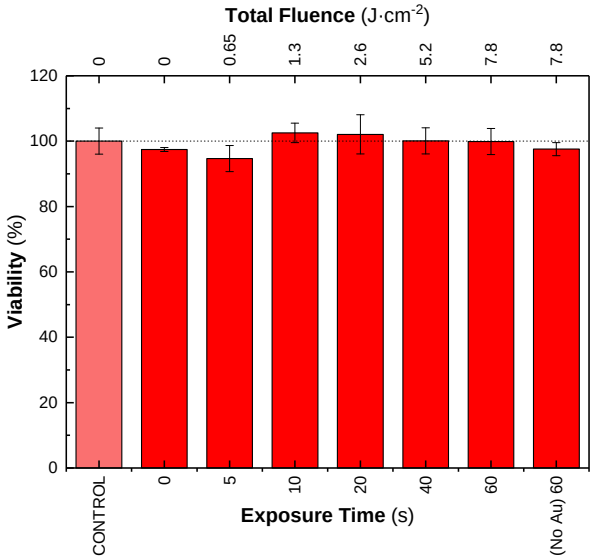

Figure 5.15: Photothermal viability assay of SW620 cells treated using a Nd:YAG nanosecond–pulsed laser. Cells were incubated with 40 µg·ml^{-1} for 4 hours prior to the AuNR–containing media being removed, the cells washed with DPBS and supplied with fresh non-AuNR containing media. The cells were then exposed to the laser tuned to 800 nm, with a pulse fluence of 13 mJ·cm^{-2} and repetition of 10 Hz for between 0 and 60 seconds. Cell viabilities were expressed as a percentage of the control. Only the results from a single well plate are presented.

which have been performed elsewhere (i.e. ref [262]), but this was not feasible within the limited time frame available at the end of this project.

As discussed in section 5.3.3, the green colour of the AuNRs located within cells is suggestive of intracellular aggregation, this is the most likely cause of the lack of cell death. It would seem that particles are entering the cell through endocytosis, aggregating into clusters within cytosomes, resulting in the complete loss of the longitudinal LSPR required to generate heat from our NIR laser source. In a final attempt to induce cell death through photothermal ablation, an alternative nanosecond–pulsed Nd:YAG OPO laser located within the McLaughlan group lab[1] was utilised. As has already been discussed, these lasers enable much higher temperatures to be achieved in a volume highly localised to the AuNRs. Hence, such lasers should be able to induce cell death if the AuNRs are absorbent in the NIR.

[1] School of Electronic and Electrical Engineering, University of Leeds

The assays in fig. 5.13(a) were repeated with the new laser source. A pulse fluence of 13 mJ·cm^{-2} was selected as this has been shown to induce cell death in other viability assays on this system [174, 393]. Cells were incubated with AuNRs at 40 µg·ml^{-1} for 4 hours, before removal of the media, washing with DPBS and addition of fresh AuNR–free media. Samples were exposed to the laser between 0 and 60 seconds (up to 600 pulses and 7.8 J·cm^2 total fluence). No decreases in viability was observed as a result of any length of exposure, suggesting that AuNRs up taken by the cells are no longer absorbent in the NIR.

These results are pretty devastating for the potential of AuNRs functionalised with DOPC – DSPE-mPEG (19:1) alone to be used a photothermal agents. It is not as if the particles incapable of generating the heat required to kill cells as is evident from fig. 5.14(b), and it is also apparent the particles are being up taken by the cells based on the darkfield images in fig. 5.3 and the EM images in fig. 5.4. Hence the most reasonable explanation is that of intracellular aggregation, which seems to be largely unavoidable with the current particles. A new strategy will be required in order to make such phospholipid coatings a viable option, such as pre–coating with silica to prevent plasmonic coupling if intracellular aggregation was to occur.

5.7 Murine Models

Murine models were used to assess the *in vivo* toxicity, and the efficacy of targeting our AuNRs to CEA. 16 nude BALB/c mice, 5 females and 11 males, were prepared with subcutaneous tumours of LS174T colorectal adenocarcinoma (positive CEA–expression). The murine experiments were completed as two separate experiments, the five females in the first experiment and 11 males in the second. The mice were assigned groups based on the whether the particles were functionalised with affimer or not and the time point at which they would be sacrificed. These have been summarised in the following table:

Administered AuNRs	**Mouse Gender**	**Time Point**			
		24 h	48 h	72 h	9 d
Untargeted	F	2	1	–	2
	M	–	2	–	–
Targeted	F	–	–	–	–
	M	3	3	3	–

It was originally planned that there would be three time points in total at 24 h, 48 h and 9 d. However the planned experiments were postponed after the laser inside the MSOT scanner suffered a mechanical fault, in order for an attempt to repair it to be made. It was not possible to repair the MSOT scanner during this delay. But it did mean that the 9 d time point fell outside of the expiry date of the project license. This meant 3 of the mice were sacrificed prematurely relative to the planned schedule of experiments, at 72 h. Whilst not ideal, this has not affected our ability to draw conclusions from the *ex vivo* distribution data we collected.

The MSOT scanner had major technical faults immediately prior to both *in vivo* experiments. Because the mice had been prepared with subcutaneous tumours in preparation for these experiments, it was not possible to delay in time for repairs to be carried out on the scanner. Hence no *in–vivo* imaging of the mice after DOPC – DSPE-mPEG AuNRs administration was performed and the only information on biodistribution

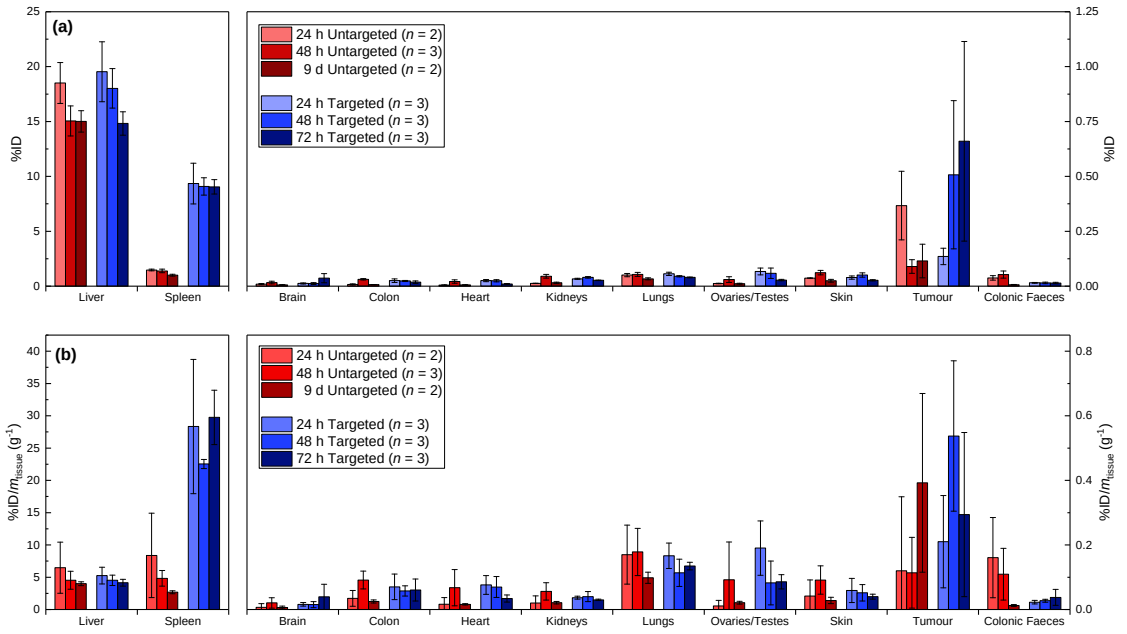

Figure 5.16: *Ex vivo* biodistribution of phospholipid–functionalised AuNRs as determined by ICP–MS. **(a)** as percentage of the injected dose, and **(b)** as a percentage of injected dose per gram of tissue/sample.

was obtained *ex vivo* after the mice were sacrificed.

Targeted AuNRs

Targeted particles were prepared by replacing the 5% DSPE-mPEG in the phospholipid mixture used to displace the CTAB with DSPE-PEG-Mal and preparing the particles in the same manner as previously discussed. The maleimide in DSPE-PEG-Mal allowed conjugation of thiolated targeting agents. In this case we used a cysteine terminated CEA–specific affimer, which had been shown to be effective in targeting silica NPs *in vivo* [163, 346]. The DOPC – DSPE-PEG-Mal (19:1) AuNRs were washed once more, and then mixed with a solution containing 18 mM CEA affimer + 23 mM TCEP, such that there was 3.3× excess of affimer relative to the number of expected maleimide sites (calculated to be approximately 90 per AuNR). The mixture was left under gentle stirring for 2 hours, before cleaning by centrifugation and sterilisation using a syringe filter.

In vivo Biocompatibility

Mice were administered with 2 mg of AuNRs suspended in 200 µl PBS at 0 h via tail vein injection, and observed intermittently over the following 9 d/72 h. All mice survived post–injection to the planned time point at which they would be sacrificed. There were no noticeable detrimental effects to their health during this period, and no noticeable differences between the mice injected with targeted and untargeted AuNRs. This further supports the conclusion that these particles demonstrate good biocompatibility based on the *in vitro* experiments performed above.

5.7.1 *Ex vivo* Biodistribution

In order to assess the biodistribution of the particles *ex vivo* analysis of the organs was undertaken by ICP–MS. The following organs were harvested in their entirety; the brain, colon, heart, kidneys, liver, lungs,

sex organs, spleen. In addition the tumour was harvested and samples of the skin and colonic faeces were also taken. It was expected that the tissues which would show the highest uptake were the liver, spleen and tumour. As a result of them being cleared by the mononuclear phagocyte system (MPS), with AuNRs being filtered out by the liver and spleen, and ultimately cleared from the body via faeces. Each of the samples was lyophilised, and digested in *aqua regia* to liberate any gold into solution. The samples were then centrifuged to remove undigested particulate matter and processed by ICP–MS to determine the Au concentration in solution.

The results of this study are presented in fig. 5.16, and are given as a fraction of the injected dose (%ID) of AuNRs and as %ID per gram of tissue/sample processed. The error on some of the %ID per gram values are quite large, due to the low masses of some of the recovered samples, often close to the sensitivity of the scales use to measure them ($\Delta m = \pm 1$ mg), this is particularly true for some of the tumour masses.

It can be seen that the majority of the sample is ending up in the liver and spleen, with 15 – 30% being observed there. There were differences between the mice administered with targeted and untargeted AuNRs. In the untargeted case, the total amount of AuNRs in the liver was much higher than the spleen, but the overall concentration (%ID per gram) was fairly similar. This distribution is consistent with reported biodistribution values for PEGylated particles more generally [5, 102, 251, 299]. The introduction of a targeting ligand increased the uptake into the spleen significantly, when expressed in %ID per gram it can be seen that the concentration of gold in the spleen is around 5–6× higher than that seen in the liver. It is not clear what drives this increased uptake, the mice in this study were immuno–compromised, and hence could not produce the T–cells required to drive uptake of foreign tissues into the spleen. There is little in the literature to suggest that CEA would be expected to be at elevated levels within the spleen, and other studies targeting CEA with nanoparticles did not report significant uptake in to the spleen (i.e. [163, 346] although neither study provided quantitative biodistribution measurements). It is not clear what is driving this increase in spleenic uptake, and further studies would be required to properly explore it.

More worryingly, the concentrations of these particles in the liver and spleen are not changing significantly with time. The untargeted AuNRs are still present in the liver at similar concentrations after 9 days. The same is true for the concentrations of targeted AuNRs in the liver after 72 h. This also paired with the observation of relatively low quantities of Au in the colonic faeces, suggesting a very low rate of clearance. This is extremely problematic, as it indicates that the body is not clearing these particles after they are collected by the MPS system. This is also consistent with time dependent studies of the clearance of PEGylated particles, which have found similarly high levels of PEGylated particles in the liver and spleen 15 months after administration of the original AuNPs [11]. In the vast majority of cases, there are no reported cases of long–term toxicity emerging from this continued presence. It does however remain an open question whether the persistence of such particles *in vivo* should be tolerated as part of any treatment

No residual Au is seen in any of the other organs, the %ID measured for the brain, colon, heart, kidneys, lungs, sex organs and skin are all close to the detection limit of the ICP–MS. This is expected, but also good as it indicates that these coatings are not being unexpectedly retained by any of the other major organs.

Tumour Up Take

Figure 5.16 shows only a marginal increase in uptake, when the targeted AuNRs are administered, with the average %ID falling below 0.7% at all times points. However inspection of the individual data for each

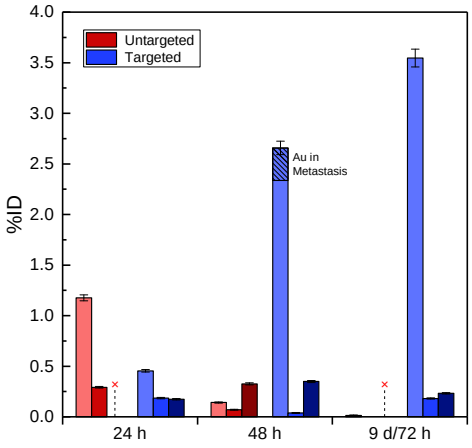

Figure 5.17: Observed %ID values for each tumour measured using ICP–MS. Each bar is data from the subcutaneous tumour(s) of a separate mouse. In a single case a metastasized tumour site was found, this has been stacked above the main tumour bar. A red × indicates the 'absence' of a data point (i.e. the dataset was $n = 2$). Errors are instrumental.

tumour shows a high degree of variability between the mice. Plotted in fig. 5.17 are the measured %ID values for each tumour. It can be seen that the majority of tumours measured showed %ID < 0.5%, indicating low uptake similar to the other non–liver and non–spleen samples.

There are notably two tumours which showed increased uptake of targeted AuNRs into the the tumours at 48 h and 72 h (%ID ~ 0.5%) by comparison with the other tumours (typically %ID ~ 0.1%). In two instances the amount of targeted AuNRs located in the tumour was considerably increased with % ID = 2.7% and 3.5%. These are both well above the 0.7% median value for %ID for the delivery of targeted nanoparticles to tumours identified by Wilhelm *et al.* in 2016 [379], although it is below the highest uptakes observed by them at ~10.5%.

In the 48 h case, the tumour had metastasized, suggesting that the tumour was vascularised. Because we did not have access to real–time MSOT imaging the mice, we were no able to ascertain which tumours were vascularised, through imaging of the biodistribution of Hb and HbO_2. Tentatively, based on this, it might be speculated that that tumour vascularisation is a prerequisite of successfully deploying a targeting strategy. This offers a potential future line of inquiry, and the use of *in vivo* MSOT might help elucidate this with its ability to image both haemoglobin and oxyhaemoglobin (although unfortunately we were unable to perform these measurement in tandem with the ICP–MS quantification).

It's also worth remarking on that fact that in the combined data (fig. 5.16), the 24 h time–point showed higher uptake for the mice administered with untargeted AuNRs. It can be seen from the data in fig. 5.17 that this originates from a unusually high uptake from a single mouse, combined with the low number of repeats at this time-point (n=2). It seems probable that this individual result is an outlier, although there is little basis to completely exclude it, and other explanation such as the enhanced permeability and retention effect could be offered plausibly (although it would fail to explain why it never appeared in any of the other untargeted cases).

5.7.2 *In vivo* Biodistribution of PSS–AuNRs

As mentioned repeatedly, it was planned that the above *ex vivo* studies would be supported by *in vivo* MSOT imaging, but this was prevented by technical issues with the scanners and the time limitations surrounding the experiments. However, earlier work has looked the mapping the *in–vivo* biodistribution of the control PSS–AuNRs. These measurements were taken prior to the decision to functionalise the AuNRs with an affimer (and hence change the the control particles to AuNRs functionalised with no DSPE-PEG-Mal). These

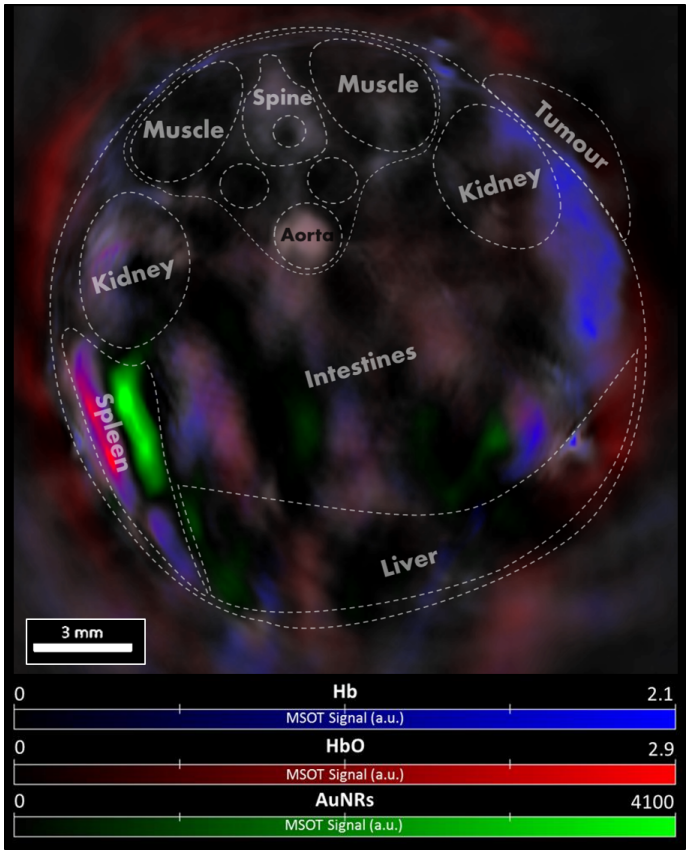

Figure 5.18: Reconstructed photoacoustic intensity map measured using a MSOT scanner of c/BALB nude mouse injected with PSS–functionalised AuNRs and prepared with a subcutaneous tumour. The image was taken 24 hours after injection of 100 µg of AuNRs. The observed cross–section is taken through a plane containing the tumour, kidneys, liver, and spleen. The AuNR signal is predominantly found in the spleen/liver, with little–to–no uptake into the tumour. The outlines of organs have been added as a guide based on the positions seen in a cryo–slice of a mouse given in the MSOT software, hence they are not definitively correct, but represent a best guess.

experiments were performed over a year earlier with PSS–AuNRs synthesised with a LSPR maximum of 900 nm. The mice were also administered with a lower dose of 100 µg AuNRs in 100 µL PBS based on the lower observed cytotoxicity for these particles (fig. 5.2(a)).

This data has some relevance in that it showed a very similar *in vivo* biodistribution to what we would expect based on the DOPC – DSPE-mPEG AuNR *ex vivo* distribution data shown in fig. 5.16. An example MSOT image 24 hours after injection is shown in fig. 5.18. It has been annotated with 'suggested' positions of the organs, based on organ distributions seen in mouse cryo–slices shown with the reconstruction software and the structures seen within the image itself. However these should not be treated as the definitive positions of the organs, there is a lot of variation between individuals and the reconstructed images are fairly ambiguous, making organ identification difficult. What can be seen is that the majority of AuNRs have ended up the spleen (or liver) in the lower–left part of the image.

The results also suggest that aggregation may not as larger issue *in vivo*, compared with the problems seen *in vitro*. A strong, spectrally deconvolutable, MSOT signal was still detectable after 24 hours, which is highly indicative that the AuNRs had not aggregated and undergone plasmonic coupling. It is worth remembering that when tested PSS–AuNRs showed poor stability relative to the DOPC – DSPE-mPEG AuNRs under all conditions (fig. 4.8). Which might suggest that the DOPC – DSPE-mPEG would maintain stability to similar extent in the *in vivo*. When stored in 100% FBS, PSS–AuNRs showed good stability, presumably through the formation of a corona. So this *in vivo* stability is not necessarily such a surprise.

Unfortunately, the lack of MSOT images of the DOPC – DSPE-mPEG AuNRs *in vivo* means that the usefulness of these comparisons are fairly limited, and we know very little about the state of them *in vivo*, other than where they has accumulated at the time of sacrifice. Although there is some basis to believe they might maintain their plasmonic properties *in vivo*, but further work would be required to determine this.

5.8 Conclusion

These surface coatings show excellent biocompatibility both *in vitro* and *in vivo*. They also demonstrate the ability to generate a good level of heat under CW illumination and are able to maintain thermal stability over multiple 'treatment cycles'. However images of the particles after uptake by cells suggests they are undergoing intracellular aggregation, destroying their plasmonic properties and rendering them inert as a photothermal treatment modality. This conclusion is supported by the failed attempts at *in vitro* photothermal treatment using only the AuNRs ingested by cells, whereas AuNRs free in the culture medium could easily induce cell death.

The thermal stability of the AuNRs under pulsed illumination is also a problem. Whilst these shown initial strong contrast under PA imaging, they rapidly underwent thermal reshaping preventing there further use. The lack of thermal stability under these systems is particularly problematic, as it will prevent them being used as an imaging modality.

The obvious solution to these issues is silica coating, providing a stabilising silica layer in excess of 10 nm should prevent plasmonic coupling during aggregation and prevent the particles from reshaping under typical nanosecond pulses. This would simultaneously solve the issues surrounding the inability to thermally ablate cells *in vitro* and make them much more robust photoacoustic contrast agents. Silica coated AuNRs could easily be modified with phospholipids, allowing them to achieve a wide range of surface properties through control of the lipid composition. The phospholipid coatings still offer potential benefits, but they will need to used in addition to other surface functionalisation techniques.

The *in vivo* distribution of our particles is very similar to that seen for other nanoparticles, with large uptake into the spleen and liver. The conjugation of a targeting ligand unexpectedly increased uptake into the spleen. There was increased uptake into the tumour in two cases, suggesting that the targeting strategy may have potential, although significant questions remain about the reliability of it as a technique. These experiments would need to be supported by additional experiments, including real–time *in vivo* imaging to better understand what is occurring.

Chapter 6

Conclusion and Future Work

The aim of this project was to develop gold nanomaterials for use in the photothermal treatment of cancer. This work was split into three key areas; developing methods to synthesise suitable particles for use in the treatment of cancer, investigation of suitable surface functionalisations for use in this application and exploration of the potential of these particles as theranostic agents through *in vivo* and *in vitro* experiments. This chapter summarises the results of each chapter and discusses the future work which would extend and improve upon the results obtained in this thesis.

In Chapter 3, focus was given to the synthesis of AuNRs. The role of oleate as a co–surfactant in the seedless synthesis of AuNRs was investigated. It was shown that through variation of the concentrations of oleate and CTAB in the growth solution provided good and reproducible control over the morphology of synthesised AuNRs. This is important as control over the morphology of AuNRs is crucial to controlling their optical properties and hence optimising them for use as photothermal conversion agents. It was also demonstrated that the presence of oleate in seedless synthesis presented the additional benefits of significantly improving the shape yield and monodispersity compared to traditional seedless syntheses performed using only CTAB. This is also beneficial to their application as photothermal conversion agents as the more intense and narrower LSPR band leads more efficient heat generation from the population of AuNRs as a whole. This synthesis was scaled up to 2 L with no appreciable drop in the quality of the end–product, potentially making industrial scale syntheses more possible.

Experiments were also run characterizing the effects of varying other parameters in the synthesis in the presence of oleate. Additionally, initial experiments were performed looking at the dynamic changes in the spectrum of the particles during the synthesis as a function of oleate concentration. It was observed that increasing oleate concentration dramatically slowed the growth kinetics, suggesting that oleate plays a role regulating the rate at which gold is reduced onto the forming nanoparticle surface in this synthesis.

This protocol as offers a facile method synthesise high quality AuNR samples with good control over the particle morphology.

In Chapter 4, the development of phospholipid based surface coatings for AuNRs was explored. A protocol was developed to ensure the thorough removal of CTAB, improving the biocompatibility and stability of the particles. The removal of CTAB was demonstrated through a combination of NMR, SERS

and pH–dependent zeta potential measurements. The level of CTAB was reduced to such an extent it was not detectable by any of these techniques, suggesting reduction to trace amounts. These coatings offer a straightforward method to replace the CTAB coating at low cost with highly tunable surface properties (in this chapter particles were stabilised with anionic, zwitterionic and steric phospholipids), which can easily be decorated with other components through the inclusion of specialist lipids decorated with functional groups such as maleimide.

The stability of these particles was also investigated and compared to that of CTAB and PSS functionalised AuNRs. The phospholipid coated particles shown superior stability to these alternative coatings in a variety of biologically relevant media selected to replicate conditions within the body. This suggests that particles once functionalised in this manner can be used reliably in a wide variety of environments.

In Chapter 5, initial experiments looking to use these particles in medical contexts were performed. Foremost it was shown that particles functionalised in this manner show very low cytoxicities, compared with PSS coated AuNRs. This is despite a large number of AuNRs being internalised by the cells (as demonstrated using darkfield and EM). There was little to no observed lysis in the presence of the phospholipid functionalised AuNRs and no toxic effects seen in any of the *in vivo* tests. Combined these results suggest that these particles are biocompatible and thus represent a facile method to achieve the detoxification of AuNRs. It also gives credence to the conclusion from Chapter 4 that the CTAB used in the synthesis of these particles has been successfully displaced.

They also were shown to generate the expected levels of heat for AuNRs of this size upon illumination with NIR light and were relatively stable under extended CW laser exposure. The AuNRs initially showed good contrast when measured using a preclinical MSOT scanner, but evidently underwent thermal reshaping under the nanosecond pulses of the laser source used in this system, preventing their further use as contrast agents.

Attempts at killing cells *in vitro* under CW laser exposure showed mixed results. Cells illuminated in cell culture medium containing AuNRs died very quickly under NIR illumination, demonstrating the potential efficacy of PPTT using these AuNRs. However when relying only on AuNR that were internalised by cells, little–to–no cell death was observed. This was true for illumination with continuous wave lasers and nanosecond pulsed lasers. It seems highly probable that the particles that are internalised by cells are undergoing intracellular aggregation, this view is supported by the darkfield and electron microscopy images of AuNRs within cells.

Finally, the AuNRs were tested *in vivo* in murine models prepared with subcutaneous LS174T tumours. The particles showed no toxic effects in any of the mice. Unfortunately, no *in vivo* imaging was possible during these experiments. However, the final biodistribution was determined *ex vivo* via elemental analysis, showing significant uptake into the liver with minimal uptake into the tumour. This is consistent with clearance via the MPS system. Additional AuNRs conjugated with an affimer targeted to CEA, showed a similar biodistribution to the untargeted particles, albeit with significantly increased uptake in to the spleen. Two of the nine tumours treated with targeted AuNRs showed significantly increased uptake, with minimal uptake into the others. Additional experiments are needed before interpretation can be drawn on this data.

Combined this data shows potential for phospholipid functionalised AuNRs as theranostics agents, with their low toxicity, good heat generation and good initial contrast in PAI. But it also highlights problems

that will need to addressed before they can be realised as a cancer treatment strategy. Primarily, these are intracellular aggregation and thermal reshaping. There remain open questions about the efficacy of the targeting strategy deployed here. The strategies with which these are intended to be addressed are discussed in the next section.

6.1 Future Work

Some of the work in Chapter 3 remains unfinished, primarily that of the kinetic spectra taken during the growth. Work is ongoing to collect more of these in order to elucidate the impact of both surfactants on the growth. Currently all of the collected spectra were taken at a single concentration of CTAB, whilst varying the oleate concentration alone. In order to distinguish whether the changes that have been observed result from purely changing the concentration of surfactant in the solution (rather than just the oleate concentration); more measurements are needed also varying the concentration of CTAB. This should help provide more information on the actual effects on the growth kinetics that we are witnessing. Ideally these measurements will be supported by TEM of the particles at various points during the growth. It is possible to halt the growth of AuNRs instantaneously through the injection of strong solution of thiolated polystyrene [273] enabling a snapshot of the particles at single point during the growth to be achieved. This should allow the building up of an understanding of the mechanism by which the presence of oleate effects the growth, which could potentially enable further improvements in the synthesis of AuNRs.

Additional experiments taking this synthetic protocol forward are planned, attempting to implement it under continuous flow conditions. This should enable the volume of particles that can be synthesised to be scaled up considerably. The ease with which we can tune the optical properties of our AuNRs means that such methods can utilise the relative concentrations of NaOL and CTAB as direct inputs with which to control the morphology of AuNRs, providing a simple, industrially applicable method for the bulk production of AuNRs.

The issues with intracellular aggregation and thermal reshaping do seem to have an obvious solution, silica coating. This has been repeatedly demonstrated as an effective strategy against thermal reshaping [31, 53, 59, 60, 157, 216, 382]. Whilst it does not prevent intracellular aggregation it can act to mitigate the problematic parts of it, by separating the AuNR cores and preventing plasmonic coupling [62]. This does not negate the potential advantages of phospholipid coatings, as they offer a simple method to easily tune the surface properties of silica–coated AuNRs. Phospholipids will readily form a bilayer on silica and hence such particles can be imbued with the same surface functionality. This should significantly improve the efficacy of photothermal treatment with these AuNRs and improve their stability during photoacoustic imaging.

It would also be a good idea to test the other lipid compositions tested in Chapter 4 in *in vitro* and *in vivo* conditions to demonstrate the versatility of this method. It is highly probable that these would present similarly low toxicities, and as such would be a facile method of fine–tuning the surface properties of AuNRs.

It was always intended that the *in vivo* targeting work would be accompanied by *in vitro* studies of the targeting. However events conspired to prevent this from happening. The following experiments should be performed to demonstrate the validity of the targeting strategies. The CEA–negative (SW620) and

CEA–positive (LS174T) should be prepared with concentrations of both targeted and non-targeted AuNRs and then a time dependent study of the uptake be performed. There are three core methods by which the difference in uptake can be assessed. Firstly, darkfield imaging of the cells fixed at different time points will give a qualitative assessment of the particle uptake into each cell line. Secondly, this can be accompanied by EM imaging of the cells fixed at the same time–points can provide information on the relative changes in the particles positions within the cells. Finally, elemental analysis can be performed on pellets of the cells incubated under the same conditions will provide a quantitative assessment of the average mass of Au per cell. These combined would allow a good understanding of the efficacy and nature of targeting in each cell line.

Additionally, it would be beneficial to obtain the missing *in vivo* imaging that was prevented by mechanical failure of the preclinical MSOT scanner. This would provide addition insights into the dynamic biodistribution immediately after administration of the AuNRs. It is also possible to conjugate a thiolated fluorophore to the AuNR through the same protocol as the targeting ligand was attached. This would provide a method to image the distribution of AuNRs within tissue sections, enabling a qualitative understanding of the distribution of the AuNRs within individual organs.

Taken together these improvements would both provide of greater understanding of how these particles behave both *in vitro* and *in vivo*, and would also simultaneously significantly improve the efficacy of these particles as theranostic agents.

Appendix A

Particle Sizes

Particle sizes obtained from analysis of TEM images.

Shape yields were based on counting all particles in a each EM image analysed and expressing the AuNR number as percentage of total number of particles observed.

28.4 mM CTAB, 17.5 mM NaOL – 99.7% AuNRs, LSPR = 746 nm, *N* = 294

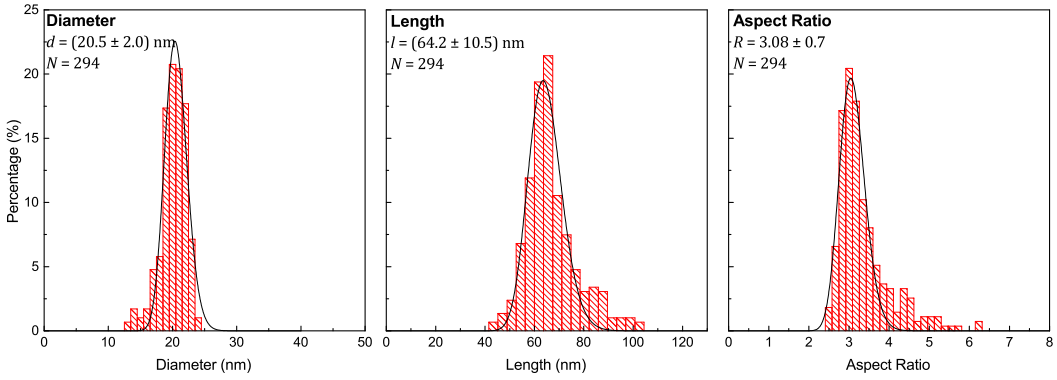

38 mM CTAB, 11 mM NaOL – 98% AuNRs, LSPR = 864 nm, *N*=301

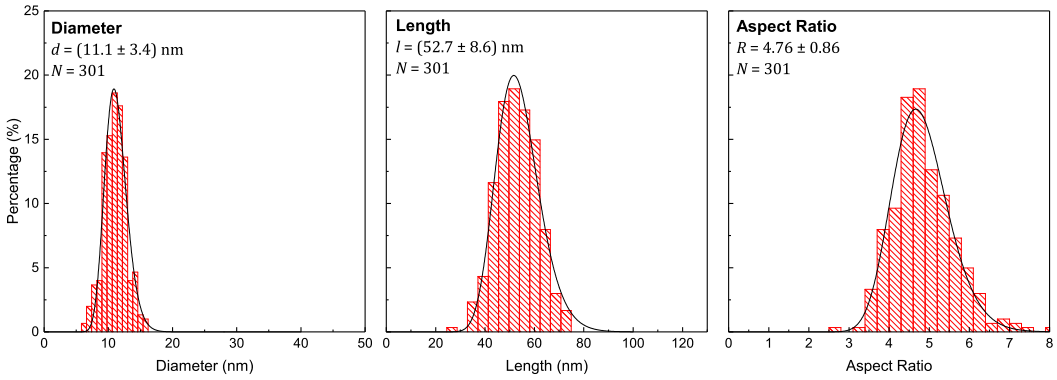

38 mM CTAB, 17.5 mM NaOL – 99.0% AuNRs, LSPR = 773 nm, N = 302

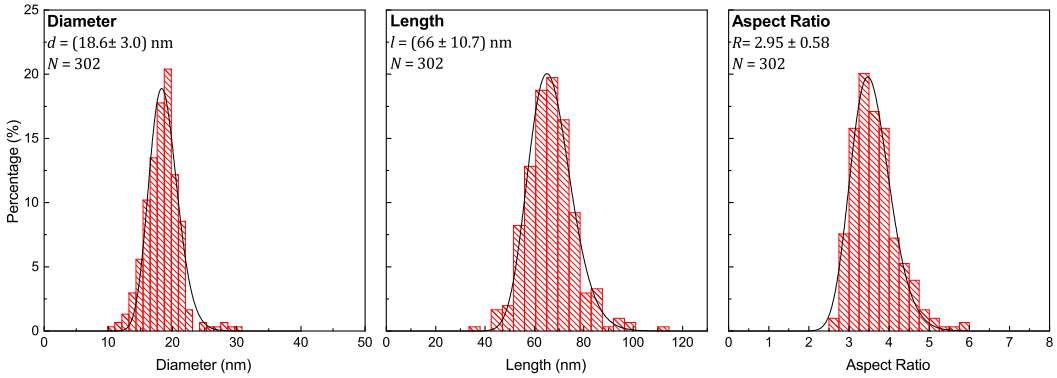

38 mM CTAB, 20.2 mM NaOL – 97.7%, LSPR = 650 nm, N = 340

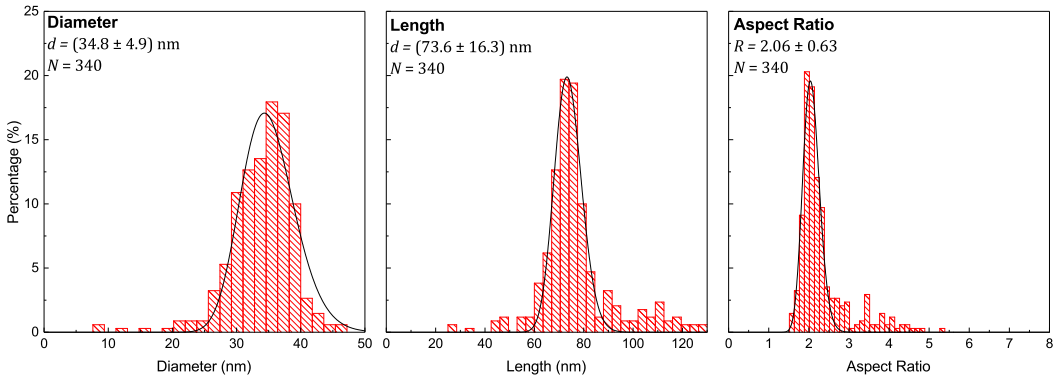

38 mM CTAB, 22.5 mM NaOL – 99.8% AuNRs, LSPR = 730 nm, N = 399

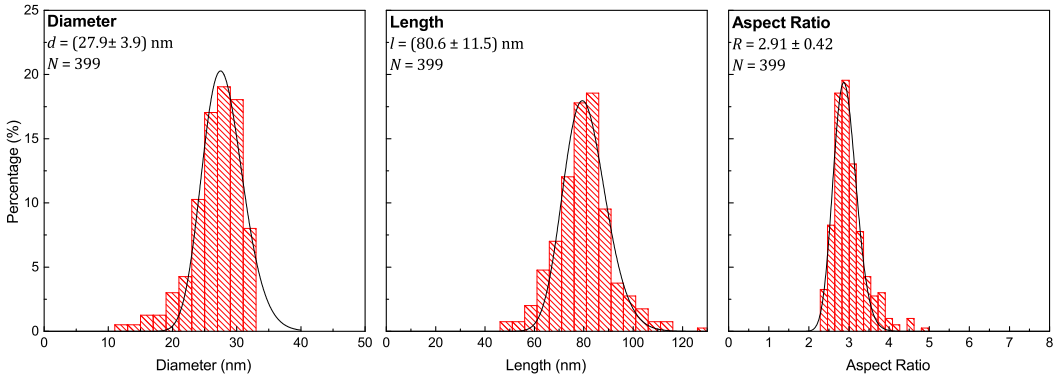

48 mM CTAB, 11 mM NaOL – 97% AuNRs, LSPR = 883 nm, N = 258

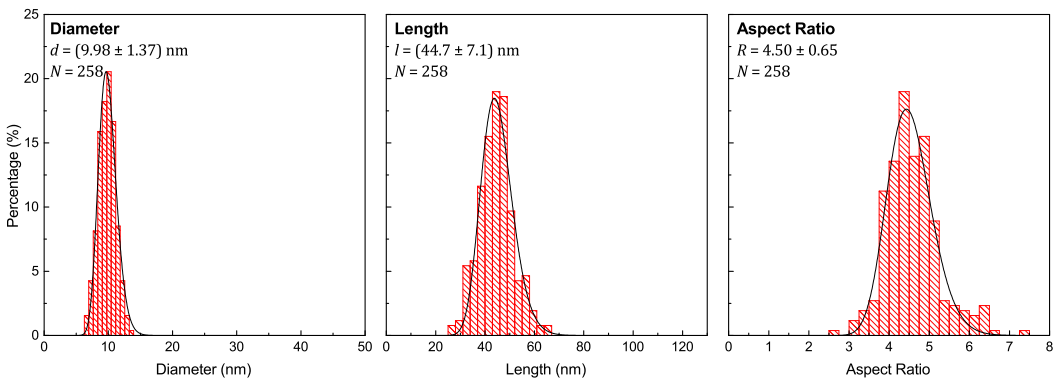

48 mM CTAB, 12.5 mM NaOL – 99.97% AuNRs, LSPR = 848 nm, N = 266

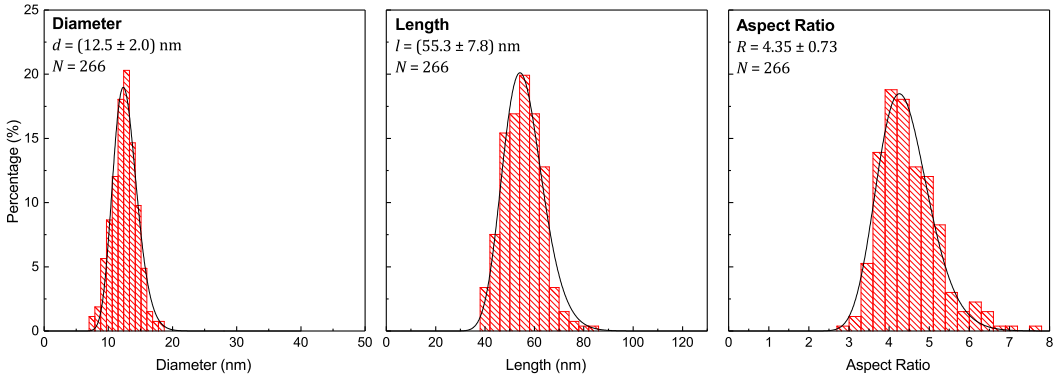

48 mM CTAB, 15 mM NaOL – 99.1% AuNRs, LSPR = 869 nm, N = 362

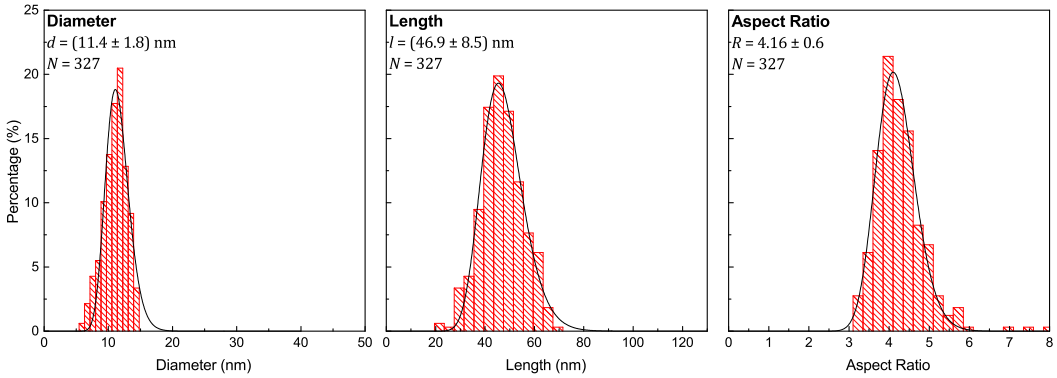

48 mM CTAB, 17.5 mM NaOL – 99.7% AuNRs, LSPR = 728 nm, N = 346

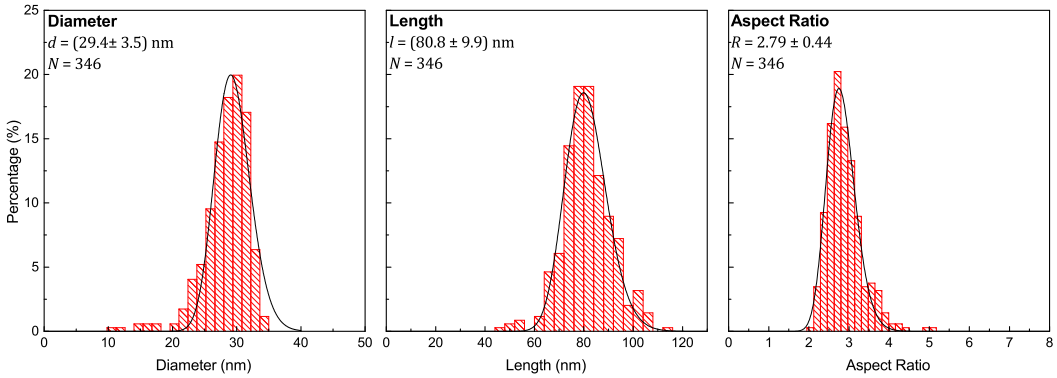

48 mM CTAB, 20.2 mM NaOL – 99.7% AuNRs, LSPR = 730 nm, N = 596

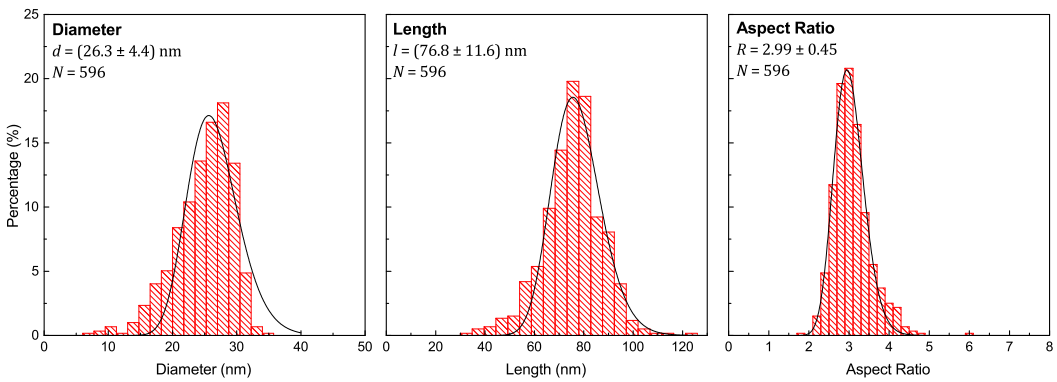

48 mM CTAB, 22.5 mM NaOL – 99.6% AuNRs, LSPR = 737 nm, N = 301

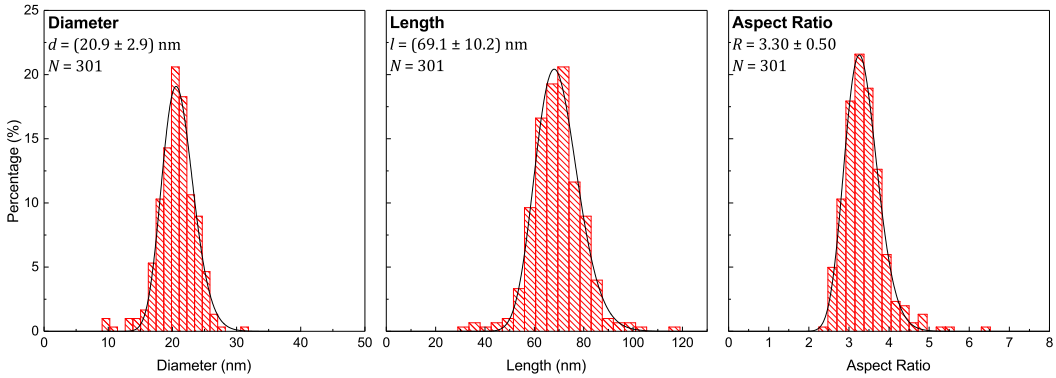

48 mM CTAB, 25 mM NaOL – 98.0% AuNRs, LSPR = 724 nm, N = 355

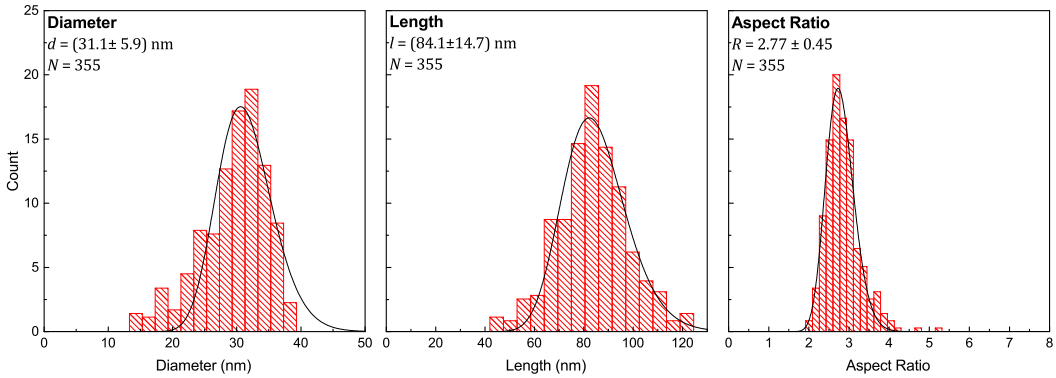

60 mM CTAB, 11 mM NaOL – 71.6% AuNRs, LSPR = 895 nm, N = 351

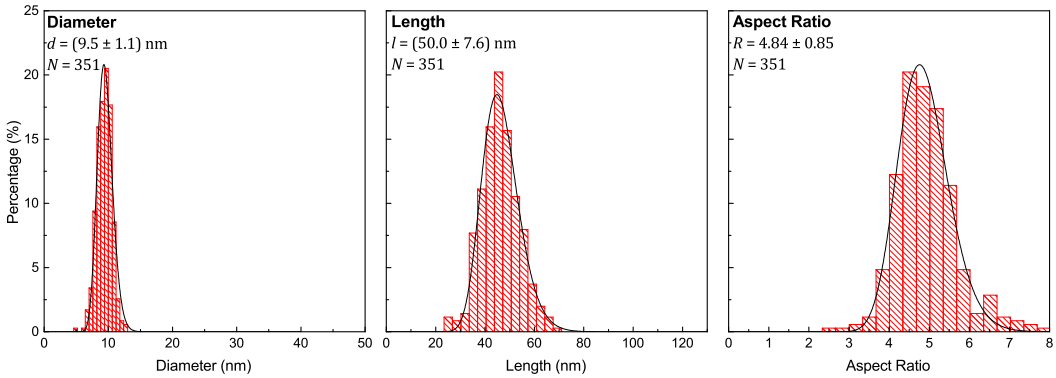

60 mM CTAB, 17.5 mM NaOL – 100% AuNRs, LSPR = 739 nm, N = 306

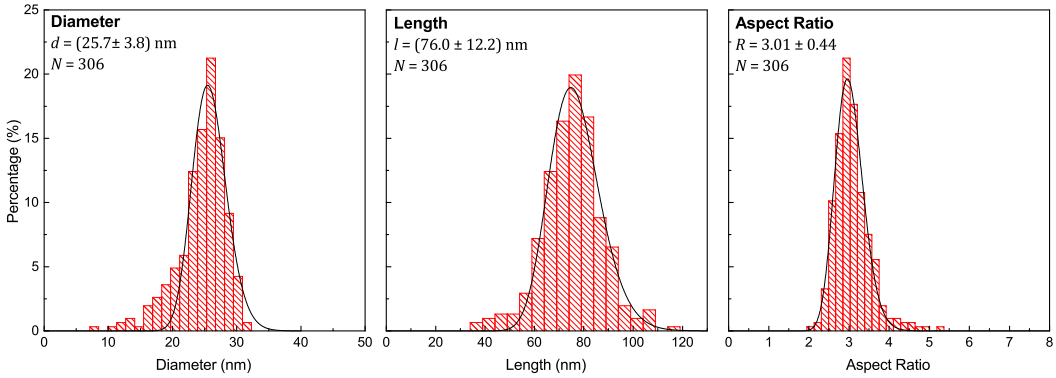

60 mM CTAB, 20.2 mM NaOL – 99.0% AuNRs, LSPR = 727 nm, N = 258

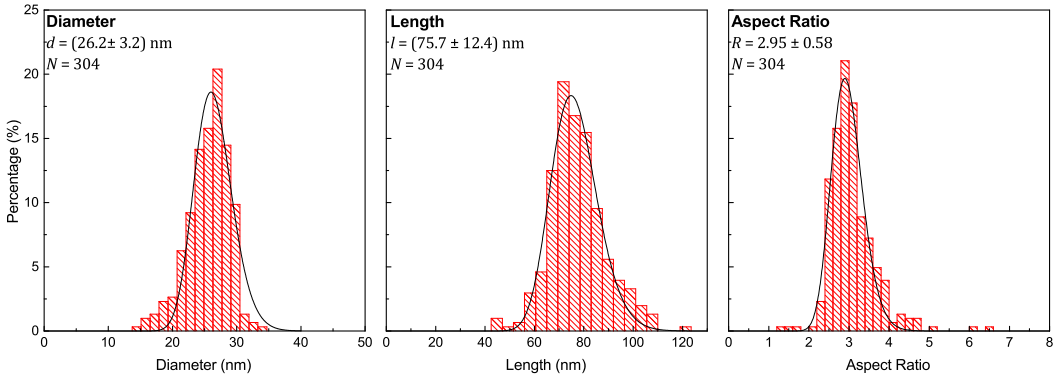

72 mM CTAB, 17.5 mM NaOL – 97.5% AuNRs, LSPR = 829 nm, N = 271

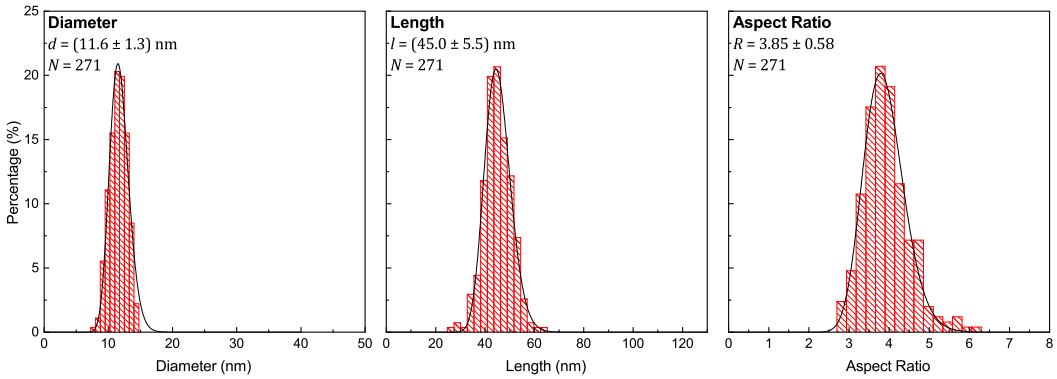

Appendix B

Kinetic UV–vis Measurements of AuNR Synthesis

Presented here is the analysis of all current kinetic spectra, as discussed in in section 3.5. For each figure, **(a)** contain the kinetic UV-vis spectra. **(b)** contains the LSPR extinction and FWHM . **(c)** contaoins the LSPR peak wavelength as a function of time. **(d)** contains the extinction at 400 nm and the corresponding concentration of Au^0; inset into this panel is the derivative of the Au^0 concentration giving the rate of Au^0 reduction. The dashed vertical lines in (b)–(d) are the times of peak reduction (blue) and the time of maximum LSPR wavelength (red). In the instances where these two times coincided the line is black.

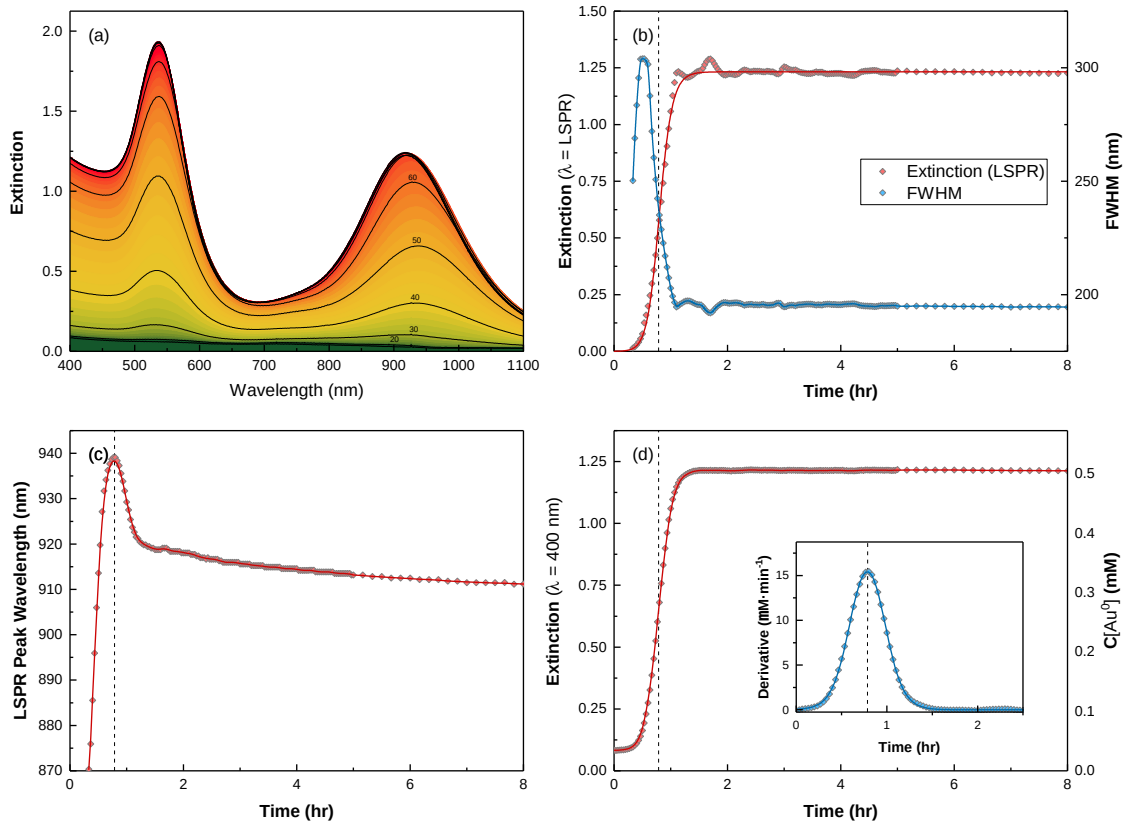

48 mM CTAB, 7.5 mM NaOL

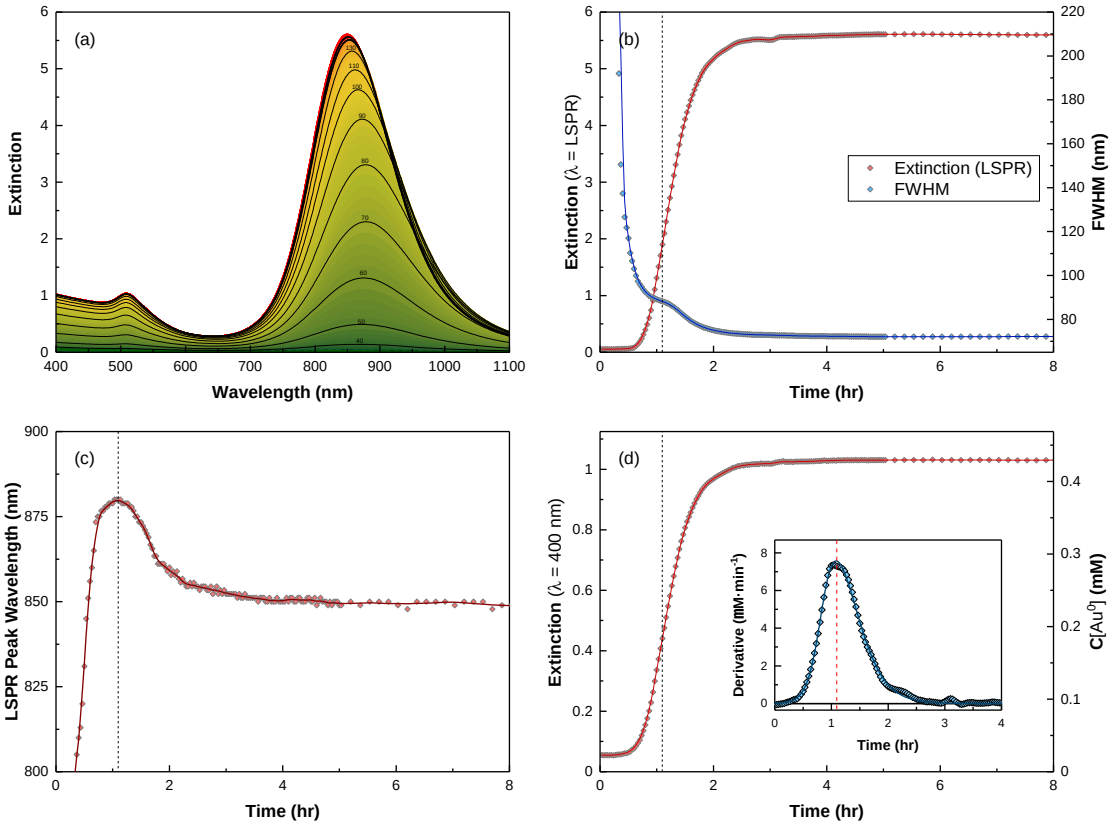

48 mM CTAB, 12.5 mM NaOL

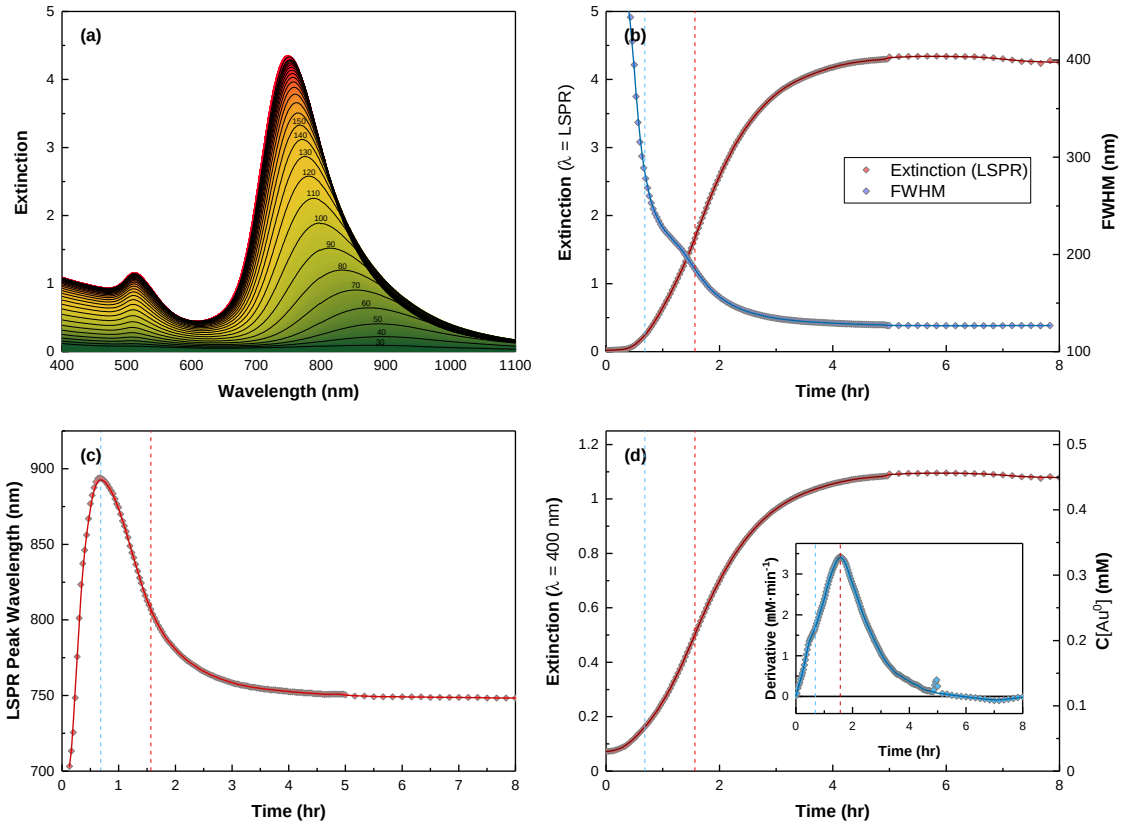

48 mM CTAB, 17.5 mM NaOL

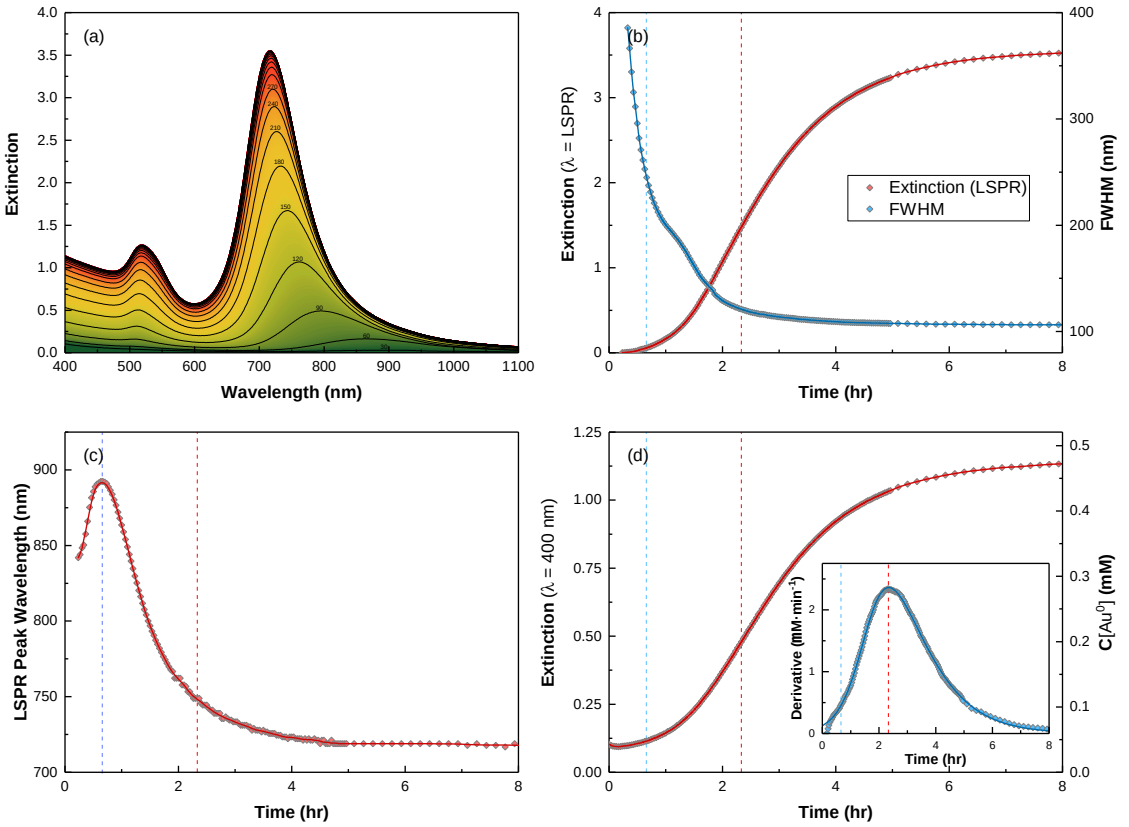

48 mM CTAB, 20 mM NaOL

The synthesis solution containing 48 mM CTAB, 25 mM NaOL presented an issue. The growth solution became was cloudy upon preparation indicating the formation of structures that scattered light strongly such as vesicles or bubbles. In the spectra presented **(a)** the formation of plasmonic peaks is apparent, but an additional spectrum, which evolves with time is present also limiting the usefulness of the kinetic spectra. The spectrum of the final product after washing via centrifugation is given as the thick black in this panel, without the scatter spectrum resulting from the growth solution. We cannot reliably extract the LSPR peak extinction and FWHM values from these spectra. In panel **(b)** an attempt at correcting the extinction value at 400 nm has been made. The correction was made by subtracting the extinction value at 1100 nm (where there is minimal plasmonic and no interband contribution) multiplied through by a scaling factor, to give a final extinction value of ~ 1.2 at 400 nm. The recovered values broadly fit in with the trends seen in fig. 3.13, but should still be treated with skepticism. Panel **(c)** presents the position of the peak LSPR wavelength as a function of time.

B. Kinetic UV–vis Measurements of AuNR Synthesis

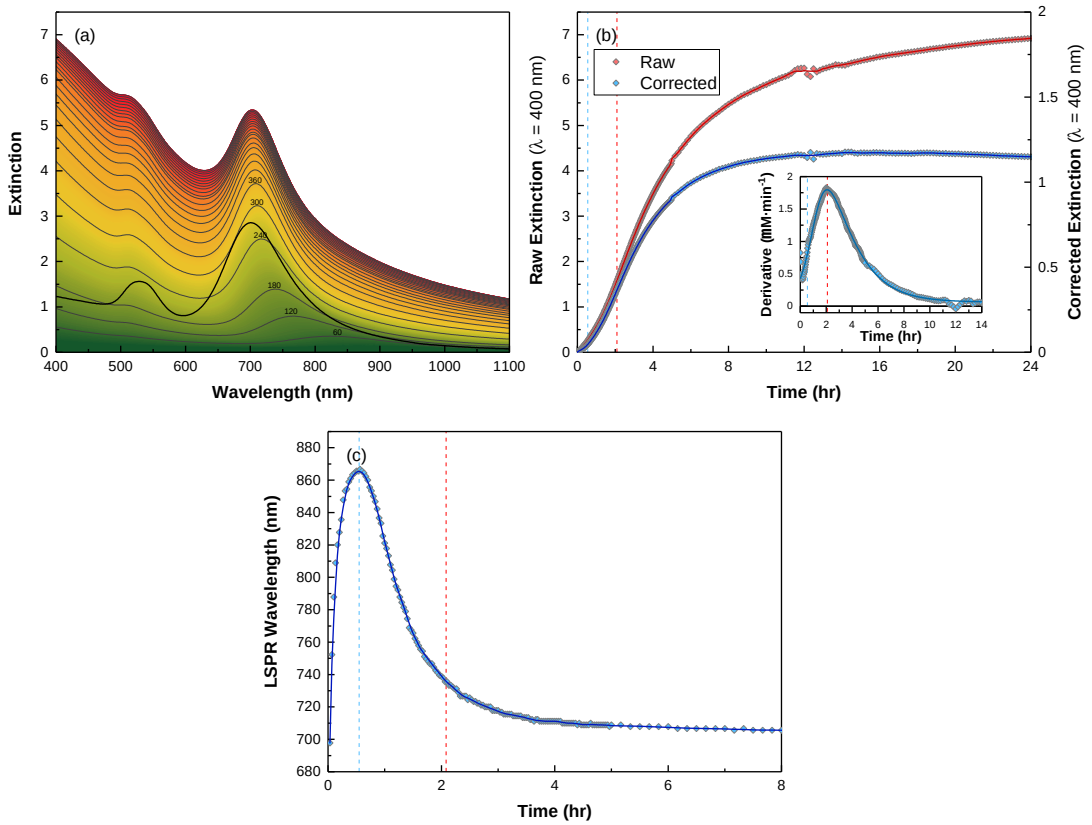

48 mM CTAB, 25 mM NaOL

Appendix C

Nuclear Magnetic Spectroscopy

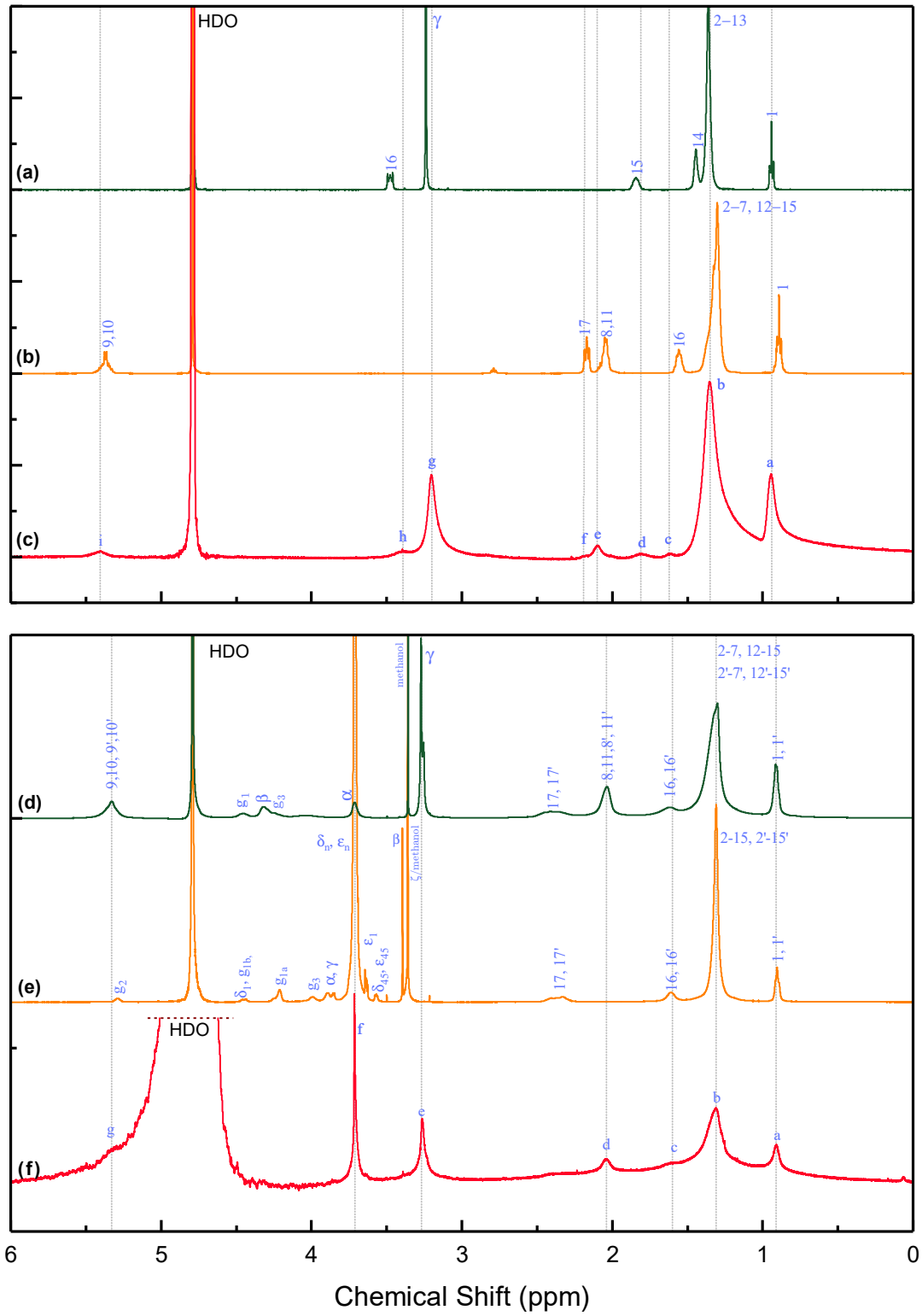

^{1}H NMR spectra for **(a)** 10 mM CTAB, **(b)** 10 mM oleate, **(c)** ~25 nM CTAB – oleate (4:1) functionalised AuNRs; **(d)** 10 mM DOPC, **(e)** 10 mM DSPE-mPEG and **(f)** ~25 nM DOPC – DSPE-mPEG (19:1) functionalised AuNRs. Chemical shifts labels are given in fig. 4.2 and tables 4.1 and 4.2. Line overlapping the peaks associated with the AuNR spectra have been extended across all associated spectra as a visual aid. All spectra were taken in D_2O, details of sample preparation and acquisition settings for each spectrum are given in section 2.5.3

Appendix D

Stability in Biorelevant Media

D.1 Aqueous

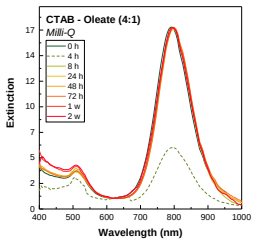

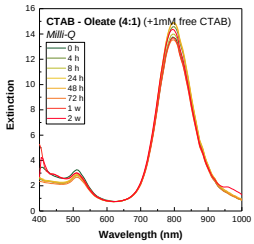

[PSS data missing]

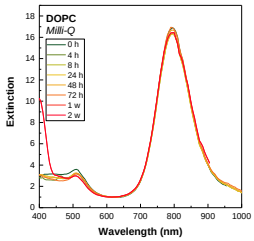

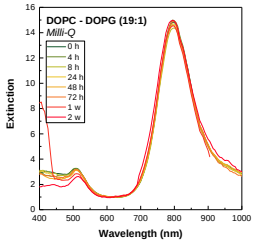

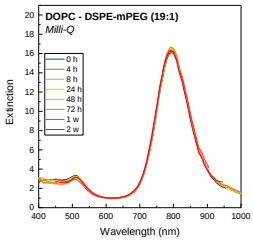

D.2 Buffers

D.2.1 Dulbecco's Phosphate–Buffered Saline

CTAB – Oleate (4:1)

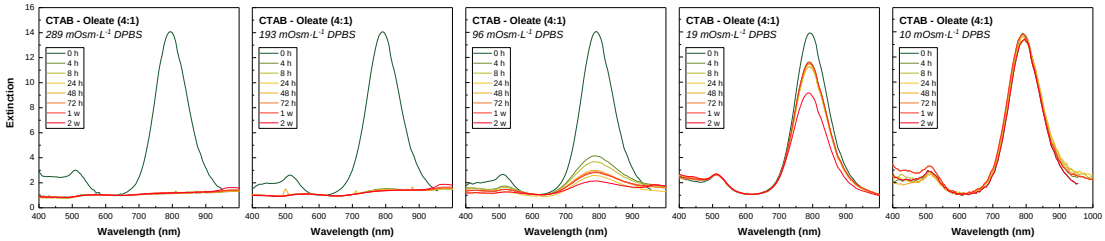

CTAB – Oleate (4:1) + 1 mM free CTAB in solution.

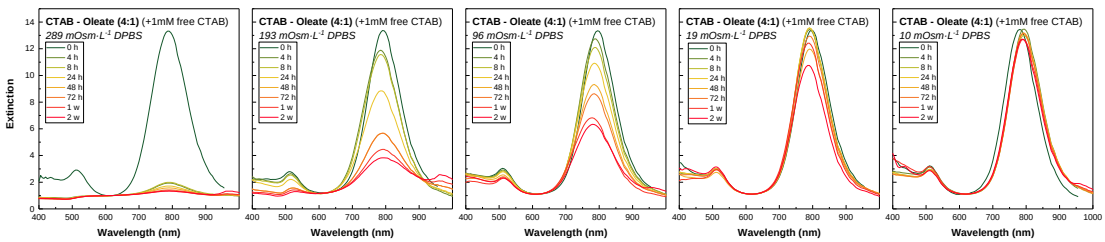

PSS

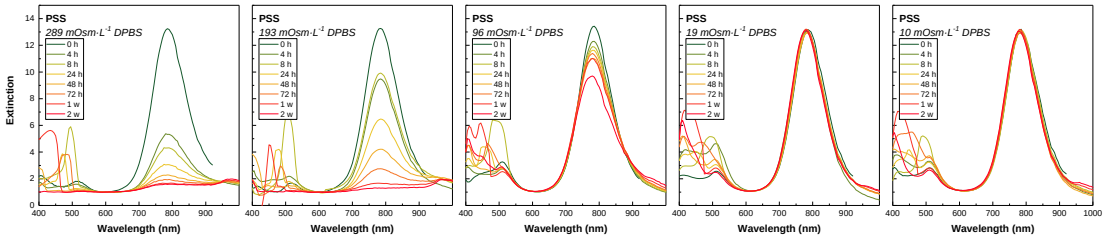

DOPC

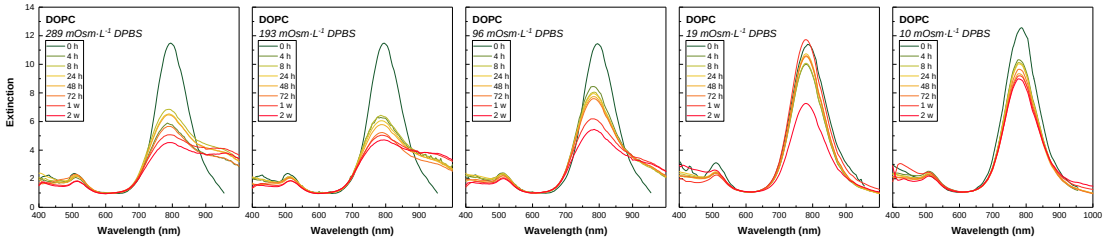

DOPC – DOPG (19:1)

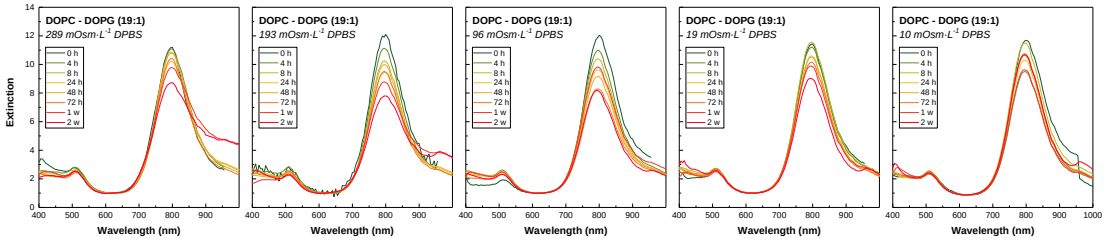

DOPC – DSPE-mPEG (19:1)

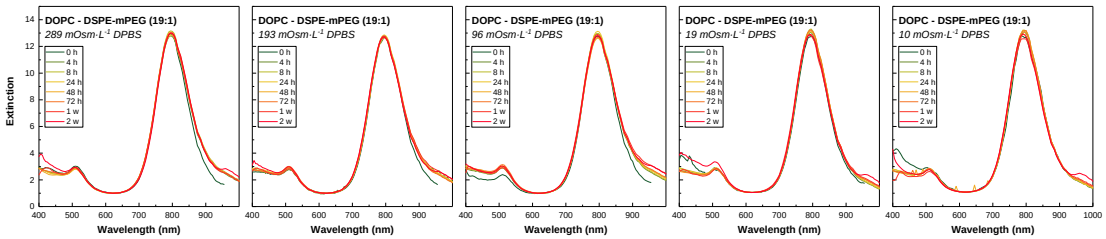

D.2.2 Plasmalyte–148

CTAB – Oleate (4:1)

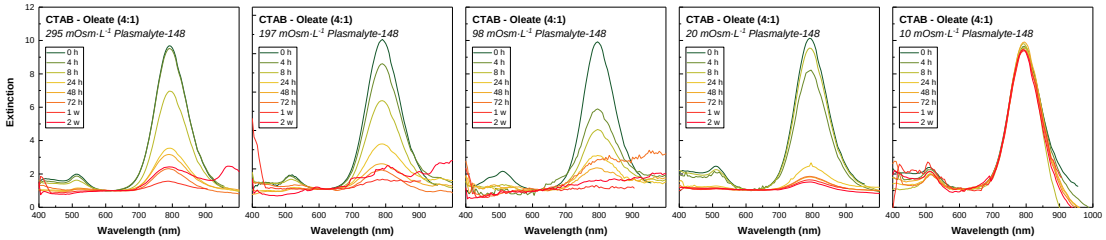

CTAB – Oleate (4:1) + 1 mM free CTAB in solution.

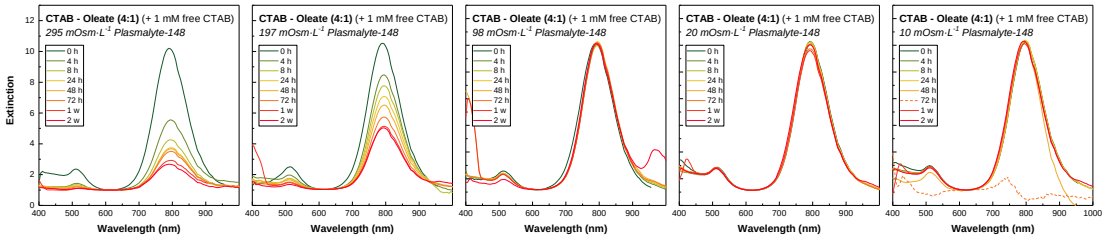

PSS

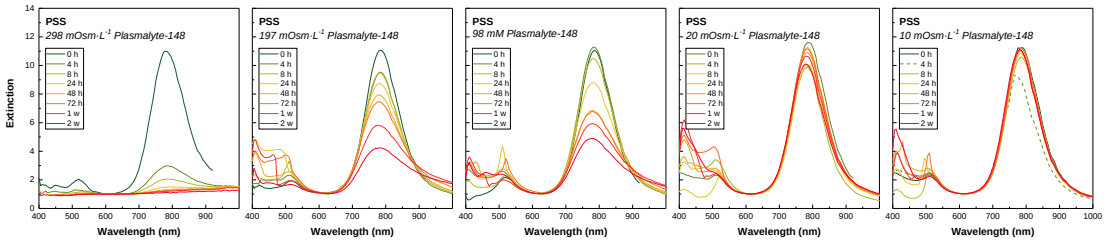

DOPC

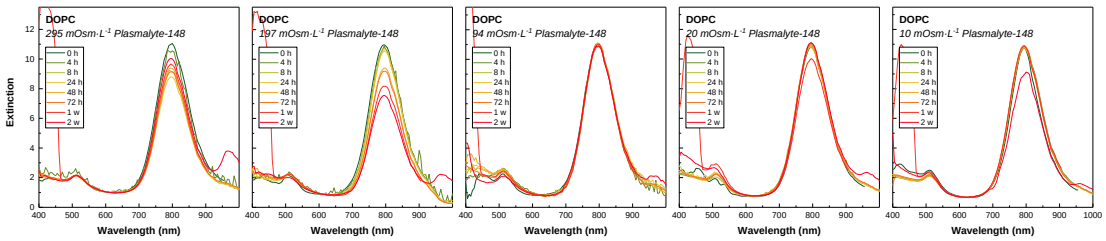

DOPC – DOPG (19:1)

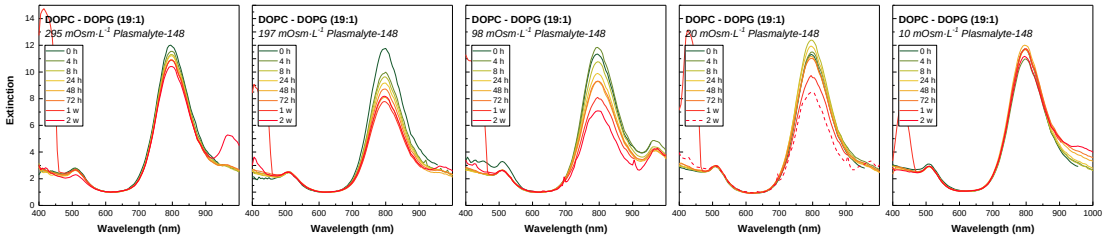

DOPC – DSPE-mPEG (19:1)

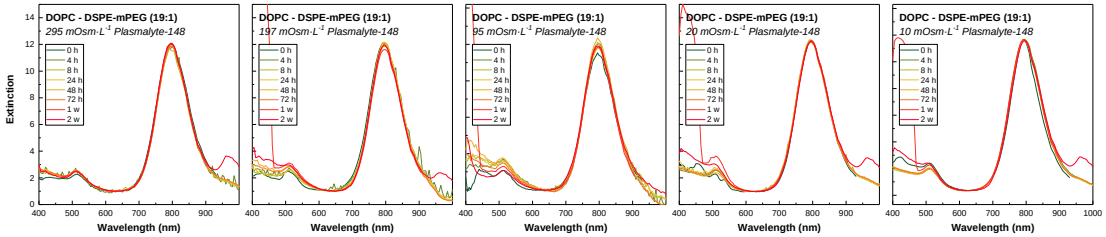

D.2.3 'Pseudo–Plasma' Buffer

CTAB – Oleate (4:1)

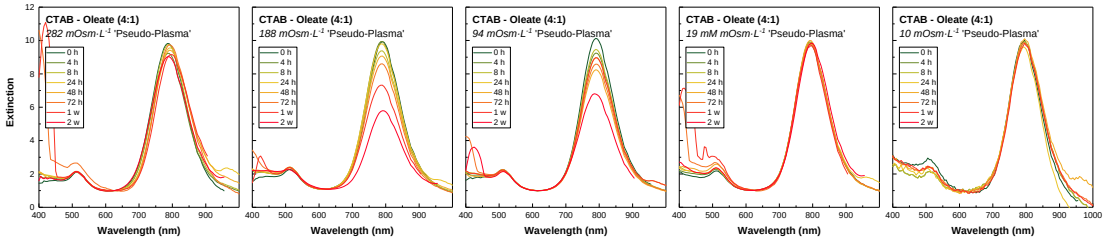

CTAB – Oleate (4:1) + 1 mM free CTAB in solution.

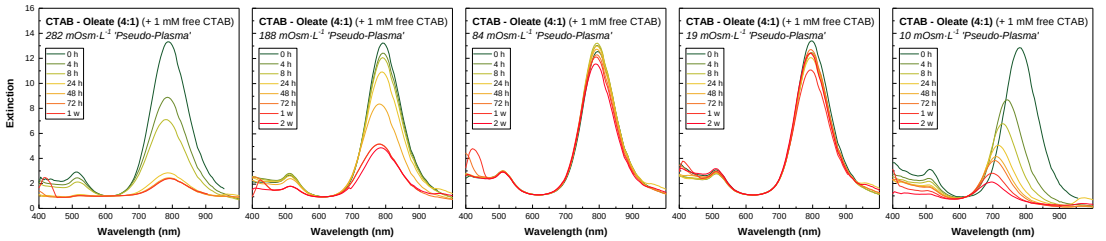

PSS

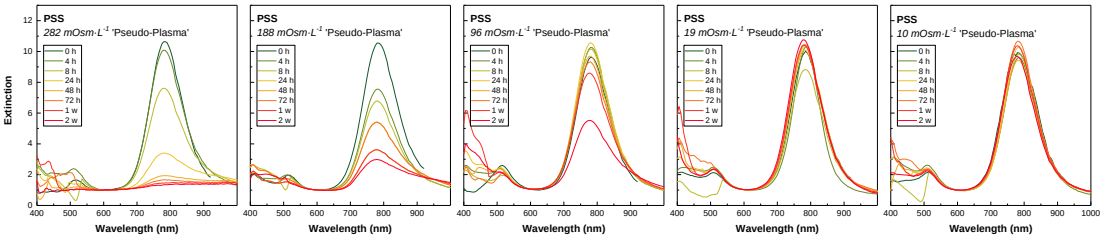

DOPC

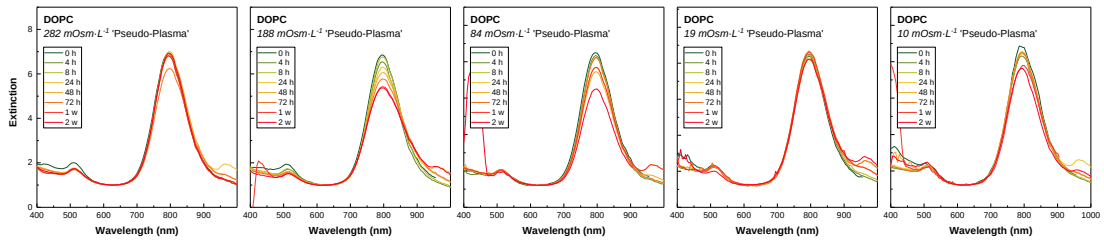

DOPC – DOPG (19:1)

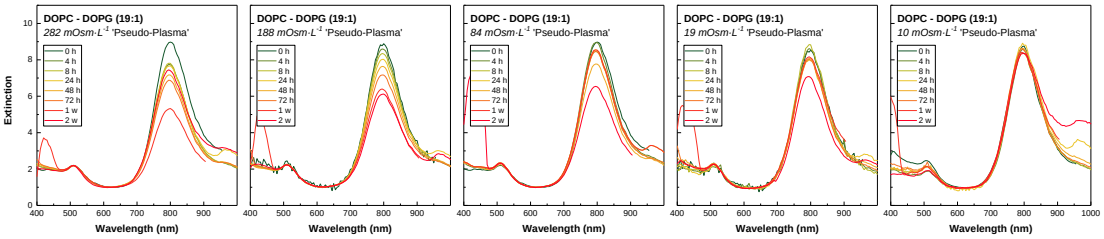

DOPC – DSPE-mPEG (19:1)

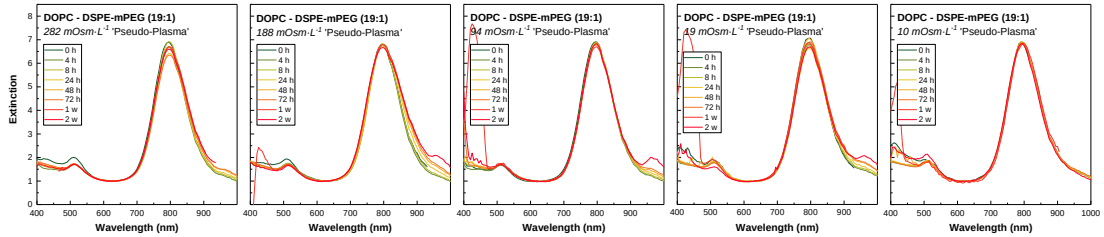

D.3 Media and Serum

CTAB – Oleate (4:1)

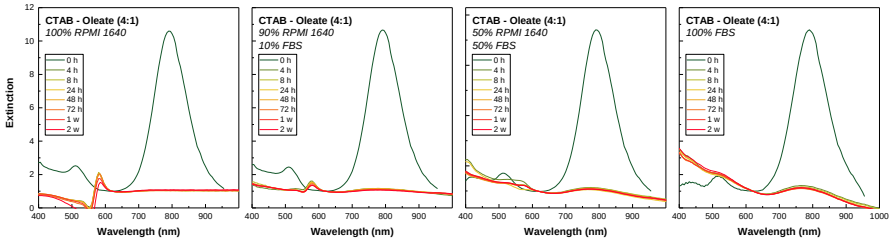

CTAB – Oleate (4:1) + 1 mM free CTAB in solution.

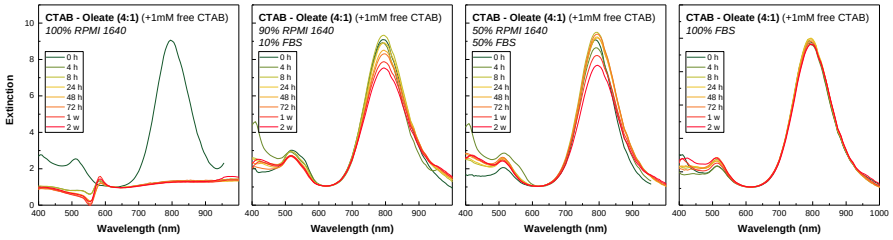

PSS

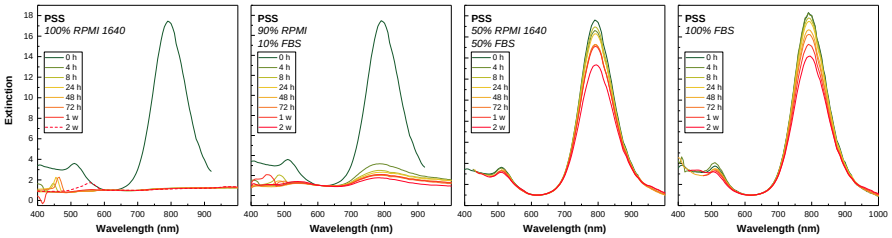

DOPC

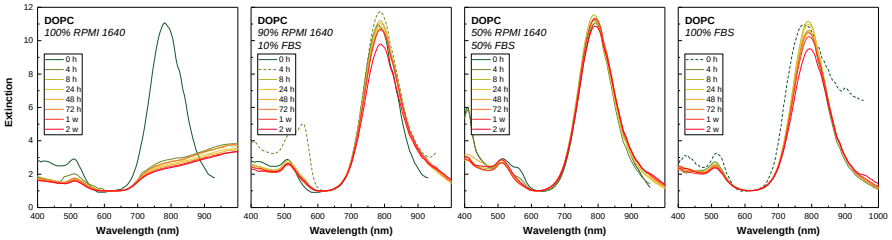

DOPC – DOPG (19:1)

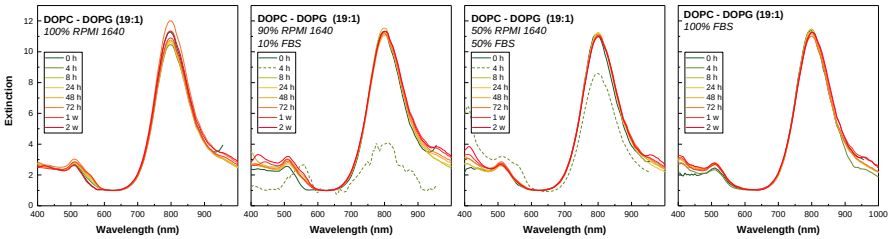

DOPC – DSPE-mPEG (19:1)

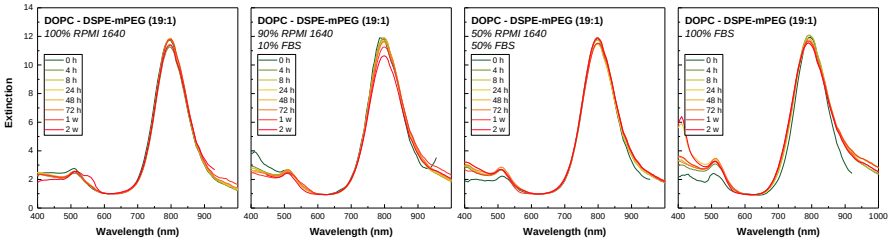

D.4 Plasma

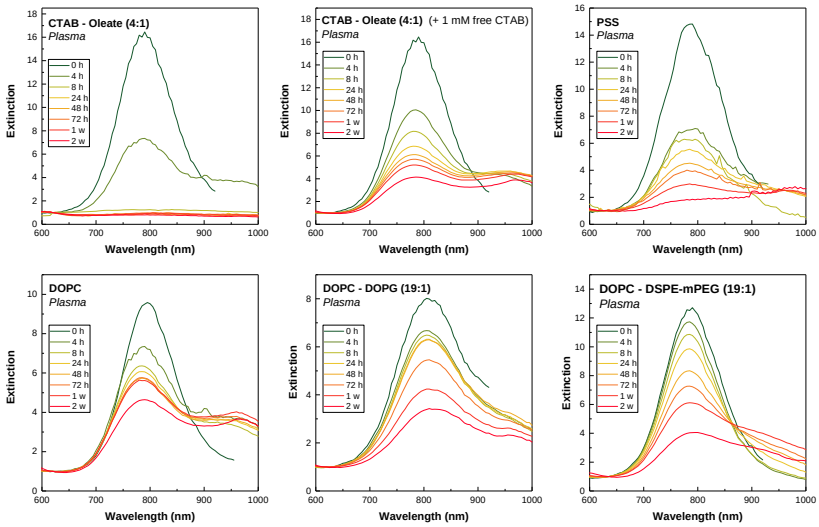

References

[1] ANSI Z136.1 American national standard for safe use of lasers. Standard, American Laser Institute, Orlando, FL, 2014.

[2] Aaron, J., Travis, K., Harrison, N., and Sokolov, K. Dynamic imaging of molecular assemblies in live cells based on nanoparticle plasmon resonance coupling. *Nano Letts. 9* (2009), 3612.

[3] Aden, A. L., and Kerker, M. Scattering of electromagnetic waves from two concentric spheres. *J. App. Phys. 22* (1951), 1242.

[4] Adjei, I. M., Sharma, B., and Labhasetwar, V. Nanoparticles: Cellular uptake and cytotoxicity. In *Nanomaterial: Impacts on cell biology and medicine*, D. G. Capco and Y. Chen, Eds. Springer, Dordrecht, Netherlands, 2014, p. 73.

[5] Akiyama, Y., Mori, T., Katayama, T., and Niidome, T. The effects of PEG grafting level and injection dose on gold nanorod biodistribution in the tumor–bearing mice. *J. Control. Release 139* (2009), 81.

[6] Akutsu, H. Direct determination by Raman scattering of the conformation of the choline group in phospholipid bilayers. *Biochemistry 20* (1981), 7359.

[7] Akutsu, H., and Nagamori, T. Conformational analysis of the polar head group in phosphatidylcholine bilayers: A structural change induced by cations. *Biochemistry 30* (1991), 4510.

[8] Albanese, A., and Chan, W. C. W. Effect of gold nanoparticle aggregation on cell uptake and toxicity. *ACS Nano 5* (2011), 5478.

[9] Alberts, B., Johnson, A., Lewis, J., Raff, M., Roberts, K., and Walter, P. *Molecular Biology of the Cell. 4th edition.* Garland Science, New York, 2002.

[10] Aldewachi, H., Chalati, T., Woodroofe, M. N., Bricklebank, N., Sharrack, B., and Gardiner, P. Gold nanoparticle–based colorimetric biosensors. *Nanoscale 10* (2018), 18.

[11] Ali, M. R. K., Rahman, M. A., Wu, Y., Han, T., Peng, X., Mackey, M., Wang, D., Shin, H. J., Chen, Z. G., Xiao, H., Wu, R., Tang, Y., Shin, D. M., and El-Sayed, M. A. Efficacy, long–term toxicity, and mechanistic studies of gold nanorods photothermal therapy of cancer in xenograft mice. *Proc. Nat. Acad. Sci. 114* (2017), E3110.

[12] Ali, M. R. K., Snyder, B., and El-Sayed, M. A. Synthesis and optical properties of small Au nanorods using a seedless growth technique. *Langmuir 28* (2012), 9807.

[13] Alkilany, A. M., Nagaria, P. K., Hexel, C., Shaw, T. J., Murphy, C. J., and Wyatt, M. D. Cellular uptake and cytotoxicity of gold nanorods: Molecular origin of cytotoxicity and surface effects. *Small 5* (2009), 701.

[14] Allen, T. J., and Beard, P. C. Pulsed near–infrared laser diode excitation system for biomedical photoacoustic imaging. *Optics Letts. 31* (2006), 3462.

[15] Allen, T. J., and Beard, P. C. Dual wavelength laser diode excitation source for 2D photoacoustic imaging. *Proc. SPIE 6437* (2007), 1.

[16] Allen, T. J., Cox, B. T., and Beard, P. C. Generating photoacoustic signals using high-peak power pulsed laser diodes. *Proc. SPIE 5696* (2005), 233.

[17] Amendola, V., Pilot, R., Frasconi, M., Maragó, O. M., and Iatí, M. A. Surface plasmon resonance in gold nanoparticles: a review. *Journal of Physics: Condensed Matter 29* (2017), 203002.

[18] AN120906 The diffusion barrier technique for accurate and reproducible protein mobility measurement. Application note, Malvern Instruments Ltd, Malvern, UK, 2017.

[19] AN140930 Zeta potential measurements of high conductivity colloidal samples. Application note, Malvern Instruments Ltd, Malvern, UK, 2014.

[20] Ashworth, C. R., Matthews, R. P., Welton, T., and Hunt, P. A. Doubly ionic hydrogen bond interactions within the choline chloride-urea deep eutectic solvent. *Phys. Chem. Chem. Phys. 18* (2016), 18146.

[21] ASTM E2865–12(2018) Standard guide for measurement of electrophoretic mobility and zeta potential of nanosized biological materials. Standard, ASTM International, West Conshohocken, PA, 2018.

[22] Bae, J., and Hong, S. B. Conformation of intrazeolitic choline ions and the framework topology of zeolite hosts. *Chem. Sci. 9* (2018), 7787.

[23] Baetz, A. L., Hubbert, W. T., and Graham, C. K. Developmental changes of free amino acids in bovine fetal fluids with gestational age and the interrelationships between the amino acid concentrations in the fluid compartments. *J. Reprod. Fert. 44* (1975), 437.

[24] Baier, G., Costa, C., Zeller, A., Baumann, D., Sayer, C., Araujo, P. H. H., Mailänder, V., Musyanovych, A., and Landfester, K. BSA adsorption on differently charged polystyrene nanoparticles using isothermal titration calorimetry and the influence on cellular uptake. *Macromol. Biosci. 11* (2011), 628.

[25] Bakshi, M. S. How surfactants control crystal growth of nanomaterials. *Cryst. Growth Des. 16* (2016), 1104.

[26] Bao, C., Beziere, N., del Pino, P., Pelaz, B., Estrada, G., Tian, F., Ntziachristos, V., de la Fuente, J. M., and Cui, D. Gold nanoprisms as optoacoustic signal nanoamplifiers for *in–vivo* bioimaging of gastrointestinal cancers. *Small 9* (2013), 68.

[27] Bao, Z., Liu, X., Liu, Y., Liu, H., and K., Z. Near–infrared light–responsive inorganic nanomaterials for photothermal therapy. *Asian J. Pharm. 11* (2016), 349.

[28] Bard, A., and Faulkner, L. *Electrochemical Methods: Fundamentals and Applications*. John Wiley and Sons, New York, 1980.

[29] Barnard, A. S. Direct comparison of kinetic and thermodynamic influences on gold nanomorphology. *Acc. Chem. Res. 45* (2012), 1688.

[30] Bartczak, D., and Kanaras, A. G. Preparation of peptide–functionalized gold nanoparticles using one pot EDC/sulfo–NHS coupling. *Langmuir 27* (2011), 10119.

[31] Bayer, C. L., Chen, Y. S., Kim, S., Mallidi, S., Sokolov, K., and Emelianov, S. Multiplex photoacoustic molecular imaging using targeted silica–coated gold nanorods. *Biomed. Opt. Express 2* (2011), 1828.

[32] Bell, A. G. Upon the production and reproduction of sound by light. *Am. J. Sci. 9* (1880), 404.

[33] Bell, A. G. Production of sound by radiant energy. *The Manufacturer and Builder 13* (1881), 156.

[34] Ben-Jaber, S., Peveler, W. J., Quesada-Cabrera, R., Cortés, E., Sotelo-Vazquez, C. Abdul-Karim, N., Maier, S. A., and Parkin, I. P. Photo–induced enhanced Raman spectroscopy for universal ultra–trace detection of explosives, pollutants and biomolecules. 12189.

[35] Bloemen, M., Brullot, W., Luong, T. T., Geukens, N., Gils, A., and Verbiest, T. Improved functionalization of oleic acid-coated iron oxide nanoparticles for biomedical applications. *J. Nanoparticle Res. 14* (2012), 1100.

[36] Bohren, C. F., and Huffman, D. R. *Absorption and Scattering of Light by Small Particles*. Wiley Interscience, New York, 1983.

[37] Boisselier, E., Salmon, L., Ruiz, J., and Astruc, D. How to very efficiently functionalize gold nanoparticles by "click" chemistry. *Chem. Commun. 44* (2008), 5788.

[38] Bowen, T. Radiation-induced thermoacoustic soft tissue imaging. *IEEE Trans. Sonics and Ultrasonics* (1981), 817.

[39] Boysen, E., and Boysend, N. *Nanotechnology for Dummies. 2nd Edition.* Wiley, Hoboken, NJ, 2005.

[40] Brennan, J. L., Hatzakis, N. S., Tshikhudo, T., Dirvianskyte, N., Razumas, V., Patkar, S., Vind, J., Svendsen, A., Nolte, R. J. M., Rowan, A. E., and Brust, M. Bionanoconjugation via click chemistry: The creation of functional hybrids of lipases and gold nanoparticles. *Bioconjugate Chem. 17* (2006), 1373.

[41] Brenner, B. M., Bohrer, M. P., Baylis, C., and Deen, W. M. Determinants of glomerular permselectivity: Insights derived from observations *in vivo*. *Kidney Int. 12* (1977), 229.

[42] Brust, M., Walker, M., Bethell, D., Schiffrin, D., and Whyman, R. Synthesis of thiol-derivatised gold nanoparticles in a two-phase liquid-liquid system. *J. Chem. Soc. Chem. Comms.* (1994), 801.

[43] Bullen, C., Zijlstra, P., Bakker, E., Gu, M., and Raston, C. Chemical kinetics of gold nanorod growth in aqueous CTAB solutions. *Cryst. Growth Des. 11* (2011), 3375.

[44] Bump, E. A., and Reed, D. J. A unique property of fetal bovine serum: High levels of protein–glutathione mixed disulfides. *In Vitro 13* (1977), 115.

[45] Cao, T., Szilagyi, I., Oncsik, T., Borkovec, M., and Trefalt, G. Aggregation of colloidal particles in the presence of multivalent co–ions: The inverse Schulze–Hardy rule. *Langmuir 31* (2015), 6610.

[46] Carchini, G., Almora-Barrios, N., Revilla-López, G., Bellarosa, L., García-Muelas, R., García-Melchor, M., Pogodin, S., Błoński, P., and López, N. How theoretical simulations can address the structure and activity of nanoparticles. *Topics in Catalysis 56* (2013), 1262.

[47] Carneiro, M. F. H., and Barbosa, F. Gold nanoparticles: A critical review of therapeutic applications and toxicological aspects. *J. Toxicol. Environ. Health B 19* (2016), 129.

[48] Casas, J., Venkataramasubramani, M., Wang, Y., and TangL. Replacement of cetyltrimethylammoniumbromide bilayer on gold nanorod by alkanethiol crosslinker for enhanced plasmon resonance sensitivity. *Biosens. Bioelectron. 49* (2013), 525.

[49] Cassano, D., Santi, M., DAutilia, F., Mapanao, A. K., Luin, S., and Voliani, V. Photothermal effect by NIR–responsive excretable ultrasmall–in–nano architectures. *Mater. Horiz. 6* (2019), 531.

[50] Castellana, E. T., Gamez, R., and Russell, D. H. Label–free biosensing with lipid–functionalized gold nanorods. *J. Am. Chem. Soc. 133* (2011), 4182.

[51] Cavigli, L., de Angelis, M., Ratto, F., Matteini, P., Rossi, F., Centi, S., Fusi, F., and Pini, R. Size affects the stability of the photoacoustic conversion of gold nanorods. *J. Phys. Chem. C 118* (2014), 16140.

[52] Cheever, M., Master, A., and Versteegen, R. A method for differentiating fetal bovine serum from newborn calf serum. *BioProcess J. 16* (2017), 1.

[53] Chen, L. C., Wei, C. W., Souris, J. S., Cheng, S. H., Chen, C. T., Yang, C., Li, P. C., and Lo, L. W. Enhanced photoacoustic stability of gold nanorods by silica matrix confinement. *J. Biomed. Opt. 15* (2010), 016010.

[54] Chen, W., Ayala-Orozco, C., Biswal, N. C., Perez-Torres, C., Bartels, M., Bardhan, R., Stinnet, G., Liu, X. D., Ji, B., Deorukhkar, A., Brown, L. V., Guha, S., Pautler, R. G., Krishnan, S., Halas, N. J., and Joshi, A. Targeting pancreatic cancer with magneto–fluorescent theranostic gold nanoshells. *Nanomedicine 9* (2014), 1209.

[55] Chen, W. H., Yang, C. X., Qiu, W. X., Luo, G. F., Jia, H. Z., Lei, Q., Wang, X. Y., Liu, G., Zhuo, R. X., and Zhang, X. Z. Multifunctional theranostic nanoplatform for cancer combined therapy based on gold nanorods. *Adv. Healthcare Mater. 4* (2015), 2247.

[56] Chen, W. R., Adams, R. L., Bartels, K. E., and Nordquist, R. E. Chromophore-enhanced *in vivo* tumor cell destruction using an 808-nm diode laser. *Cancer Letts. 94* (1995), 125.

[57] Chen, W. R., Adams, R. L., Carubelli, R., and Nordquist, R. E. Laser–photosensitizer assisted immunotherapy: a novel modality for cancer treatment. *Cancer Letts. 115* (1997), 25.

[58] Chen, W. R., Adams, R. L., Higgins, A. K., Bartels, K. E., and Nordquist, R. E. Photothermal effects on murine mammary tumors using indocyanine green and an 808-nm diode laser: An *in–vivo* efficacy study. *Cancer Letts. 98* (1996), 169.

[59] Chen, Y. S., Frey, W., Kim, S., Homan, K., Kruizinga, P., Sokolov, K., and Emelianov, S. Y. Enhanced thermal stability of silica–coated gold nanorods for photoacoustic imaging and image–guided therapy. *Opt. Express 18* (2010), 8867.

[60] Chen, Y. S., Kruizinga, P., Joshi, P. P., Kim, S. Homan, K., Sokolov, K., Frey, W., and Emelianov, S. Y. On stability of molecular therapeutic agents for noninvasive photoacoustic and ultrasound image-guided photothermal therapy. In *Proceedings Vol. 7564, Photons Plus Ultrasound: Imaging and Sensing 2010* (2010), p. 75641Q.

[61] Choi, W. I., Kim, J. Y., Kang, C., Byeon, C. C., Kim, Y. H., and Tae, G. Tumor regression *in vivo* by photothermal therapy based on gold–nanorod–loaded, functional nanocarriers. *ACS Nano 5* (2011), 1995–2003.

[62] Comenge, J., Fragueiro, O., Sharkey, J., Taylor, A., Held, M., Burton, N. C., Park, B. K., Wilm, B., Murray, P., Brust, M., and Lévy, R. Preventing plasmon coupling between gold nanorods improves the sensitivity of photoacoustic detection of labeled stem cells *in vivo*. *ACS nano 10* (2016), 7106.

[63] Cox, B., and Beard, P. Modeling photoacoustic propagation in tissue using *k*-space techniques. In *Photoacoustic Imaging and Spectroscopy*, L. Wang, Ed. CRC Press, Boca Raton, FL, 2009, p. 10.

[64] Creighton, J., Blatchford, C., and Albrecht, M. Plasma resonance enhancement of Raman scattering by pyridine adsorbed on silver or gold sol particles of size comparable to the excitation wavelength. *J. Chem. Soc. Faraday Trans. 2 75* (1979), 790.

[65] Crippa, P. R., Cristofoletti, V., and Romeo, N. A band model for melanin deducted from optical absorption and photoconductivity experiments. *Biochim. Biophys. Acta 538* (1978), 164.

[66] Cubeddu, R., Pifferi, A., Taroni, P., Torricelli, A., and Valentini, G. A solid tissue phantom for photon migration studies. *Phys. Med. Biol. 42* (1997), 1971.

[67] Czamara, K., Majzner, K., Pacia, M. Z., Kochan, K., Kaczor, A., and Baranska, M. Raman spectroscopy of lipids: A review. *J. Raman Spectrosc. 46* (2015), 4.

[68] Danhier, F. To exploit the tumor microenvironment: Since the EPR effect fails in the clinic, what is the future of nanomedicine? *J. Controlled Release 244* (2016), 108.

[69] Davidson, A. M. *High resolution characterisation of gold nanoparticle coronae by differential centrifugal sedimentation*. PhD thesis, University of Liverpool, 2018. University of Liverpool [PhD Thesis].

[70] Davidson, A. M., Brust, M., Cooper, D. L., and Volk, M. Sensitive analysis of protein adsorption to colloidal gold by differential centrifugal sedimentation. *Anal. Chem. 89* (2017), 6807.

[71] De Gelder, J. *Raman spectroscopy as a tool for studying bacterial cell compounds*. PhD thesis, Ghent University, 2008. Ghent University [PhD Thesis].

[72] De Gelder, J., De Gussem, K., Vandenabeele, P., and Moens, L. Reference database of Raman spectra of biological molecules. *J. Raman Spectrosc. 38* (2007), 1133.

[73] de Jong, W. H., Hagens, W. I., Krystek, P., Burger, M. C., Sips, A. J. A. M., and Geertsma, R. E. Particle size–dependent organ distribution of gold nanoparticles after intravenous administration. *Biomaterials 29* (2008), 1912.

[74] Debye, P., and Hückel, E. Zur Theorie der Elektrolyte. II. Grenzgesetz für die elektrische Leitfähigkeit [German] (On the theory of electrolytes. II. Limiting law for electric conductivity). *Phys. Z. 24* (1923), 305.

[75] Dendramis, A. L., Schwinn, E. W., and Sperline, R. P. A surface-enhanced Raman scattering study of CTAB adsorption on copper. *Surf. Sci. 134* (1983), 675.

[76] DeVoe, H. Optical properties of molecular aggregates. I. Classical model of electronic absorption and refraction. *J. Chem. Phys. 41* (1964), 393.

[77] DeVoe, H. Optical properties of molecular aggregates. II. Classical theory of the refraction, absorption, and optical activity of solutions and crystals. *J. Chem. Phys. 43* (1965), 3199.

[78] Docter, D., Westmeier, D., Markiewicz, M., Stolte, S., Knauer, S. K., and Stauber, R. H. The nanoparticle biomolecule corona: Lessons learned – challenge accepted? *Chem. Soc. Rev. 44* (2015), 6094.

[79] Draine, B. T., and Flatau, P. J. Discrete–dipole approximation for scattering calculations. *J. Opt. Soc. Am. A 11* (1994), 1491.

[80] Drude, P. Zur Elektronentheorie der Metalle [German] (On the electronic theory of metals). *Ann. Phys. 306* (1900), 566.

[81] Duff, D. G., Baiker, A., and Edwards, P. P. A new hydrosol of gold clusters. *J. Chem. Soc. Chem. Commun. 1* (1993), 96.

[82] Edgar, J. A., McDonagh, A. M., and Cortie, M. B. Formation of gold nanorods by a stochastic"popcorn" mechanism. *ACS Nano 6* (2012), 1116.

[83] Eghtedari, M., Oraevsky, A., Copland, J. A., Kotov, N. A., Conjusteau, A., and Motamedi, M. High sensitivity of *in vivo* detection of gold nanorods using a laser optoacoustic imaging system. *Nano Letts. 7* (2007), 1914.

[84] Ekici, O., Harrison, R. K., Durr, N. J., Eversole, D. S., Lee, M., and Ben-Yakar, A. Thermal analysis of gold nanorods heated with femtosecond laser pulses. *J. Phys. D: Appl. Phys. 41* (2008), 185501.

[85] El Kadi, N., Martins, F., Clausse, D., and Schulz, P. C. Critical micelle concentrations of aqueous hexadecytrimethylammonium bromide-sodium oleate mixtures. *Colloid Polym. Sci 281* (2003), 353.

[86] Esumi, K., Matsuhisa, K., and Torigoe, K. Preparation of rodlike gold particles by UV irradiation using cationic micelles as a template. *Langmuir 11* (1995), 3285.

[87] Faraday, M. The Bakerian lecture: Experimental relations of gold (and other metals) to light. *Phil. Trans. 147* (1857), 145.

[88] Fasanella, A., Cosentino, K., Beneduci, A., Chidichimo, G., Cazzanelli, E., Barberi, R. C., and Castriota, M. Thermal structural evolutions of DMPC–water biomimetic systems investigated by Raman Spectroscopy. *Biochim. Biophys. Acta 1860* (2018), 1258.

[89] Fievet, F., Lagier, J. P., Blin, B., Beaudoin, B., and Figlarz, M. Homogeneous and heterogeneous nucleations in the polyol process for the preparation of micron and submicron size metal particles. *Solid State Ionics 32* (1989), 198.

[90] Fievet, F., Lagier, J. P., and Figlarz, M. Preparing monodisperse metal powders in micrometer and submicrometer sizes by the polyol process. *MRS Bull. 14* (1989), 2934.

[91] Fleming, D. A., and Williams, M. E. Size-controlled synthesis of gold nanoparticles via high-temperature reduction. *Langmuir 20* (2004), 3021–3023.

[92] Folch, J., Lees, M., and Stanley, G. A simple method for the isolation and purification of total lipides from animal tissues. *J. Biol. Chem 226* (1957), 497.

[93] for National Statistics, O. Deaths registered in England and Wales (series DR): 2017, 2018.

[94] Foss, C. A., Hornyak, G. L., Stockert, J., and Martin, C. Optical properties of composite membranes containing arrays of nanoscopic gold cylinders. *J. Phys. Chem. 96* (1992), 7497.

[95] Foucault, R., Birke, R. L., and Lombardi, J. R. SERS of surfactants in monolayer and multibilayer forms on an electrified Ag surface. *Langmuir 19* (2003), 8818.

[96] Fratoddi, I., Venditti, I.and Cametti, C., and Russo, M. V. How toxic are gold nanoparticles? The state–of–the–art. *Nano Res. 8* (2015), 1771.

[97] Frens, G. Particle size and sol stability in metal colloids. *Kolloid-Zeitschrift und Zeitschrift für Polymere 250* (1972), 736.

[98] Frens, G. Controlled nucleation for the regulation of the particle size in monodisperse gold suspensions. *Nature 241*, 105 (1973), 20.

[99] Frölich, H. *Theory of Dielectrics*. Oxford University Press, London, 1958.

[100] Fuggle, S. CLINICAL BIOCHEMISTRY REFERENCE RANGES HANDBOOK, 2019.

[101] Gans, R. Über die Form Ultramikroskopischer Goldteilchen [German] (On the form of ultramicroscopic gold particles). *Ann. Phys. 342* (1912), 881.

[102] Gao, H., Liu, J., Yang, C., Cheng, T., Chu, L., Xu, H., Meng, A., Fan, S., Shi, L., and Liu, J. The impact of PEGylation patterns on the *in vivo* biodistribution of mixed shell micelles. *Int. J. Nanomedicine 8* (2013), 4229.

[103] Gao, J., Bender, C. M., and Murphy, C. J. Dependence of the gold nanorod aspect ratio on the nature of the directing surfactant in aqueous solution. *Langmuir 19* (2003), 9065.

[104] Garg, N., Scholl, C., Mohanty, A., and Jin, R. The role of bromide ions in seeding growth of Au nanorods. *Langmuir 26* (2010), 10271.

[105] Ge, Z., and Wang, Y. Estimation of nanodiamond surface charge density from zeta potential and molecular dynamics simulations. *J. Phys. Chem. B 121* (2016), 3394.

[106] Gökce, H., and Bahçeli, S. The molecular structures, vibrational spectroscopies (FT–IR and Raman) and quantum chemical calculations of *n*–alkyltrimethylammonium bromides. *Optics and Spectroscopy 115* (2013), 632.

[107] Gold, P., and Freedman, S. O. Specific carcinoenmbryonic antigens of the human digestive system. *J. Exp. Med. 122* (1965), 467.

[108] Gold, P., Shuster, J., and Freedman, S. O. Carcinoembryonic antigen (CEA) in clinical medicine. Historical perspectives, pitfalls and projections. *Cancer 42* (1978), 1399.

[109] Gole, A., and Murphy, C. J. Polyelectrolyte–coated gold nanorods: Synthesis, characterization and immobilization. *Chem. Mater. 17* (2005), 1325.

[110] González-Rubio, G., Díaz-Núñez, P., Rivera, A., Prada, A., Tardajos, G., González-Izquierdo, J., Bañares, L., Llombart, P., Macdowell, L. G., Alcolea Palafox, M., Liz-Marzán, L. M., Peña-Rodríguez, O., and Guerrero-Martínez, A. Femtosecond laser reshaping yields gold nanorods with ultranarrow surface plasmon resonances. *Science 358* (2017), 640.

[111] Goodrich, G. P., Bao, L., Gill-Sharp, K. L., Sang, K. L., Wang, J. C., and Payne, J. D. Photothermal therapy in a murine colon cancer model using near–infrared absorbing gold nanorods. *J. Biomed. Opt. 15* (2010), 018001.

[112] Gorelikov, I., and Matsuura, N. Single–step coating of mesoporous silica on cetyltrimethyl ammonium bromide–capped nanoparticles. *Nano Letts. 8* (2008), 369.

[113] Govorov, A. O., and Richardson, H. H. Generating heat with metal nanoparticles. *Nano Today 2* (2007), 30.

[114] Guadagni, F., Witt, P. L., Robbins, P. F., Schlom, J., and Greiner, J. W. Regulation of carcinoembryonic antigen expression in different human colorectal tumor cells by interferon–γ. *Cancer Research 50*, 19 (1990), 6248.

[115] Gunduz, N., Ceylan, H., Guler, M. O., and Tekinay, A. B. Intracellular accumulation of gold nanoparticles leads to inhibition of macropinocytosis to reduce the endoplasmic reticulum stress. *Sci. Rep. 7* (2017), 40493.

[116] Hakimian, F., Ghourchian, H., Hashemi, A., Arastoo, M., and Behnam Rad, M. Ultrasensitive optical biosensor for detection of miRNA–155 using positively charged Au nanoparticles. *Sci. Rep. 8* (2018), 2943.

[117] Hale, G. M., and Querry, M. R. Optical constants of water in the 200–nm to 200–m wavelength region. *Appl. Optics 12* (1973), 555.

[118] Hao, J., Lu, R., Wang, H., and Dong, S. NMR and ESR Studies on the microenvironmental properties of sodium perfluorooctanoate and cetyltrimethylammonium bromide mixed micellar solutions. *J. Dispersion Sci. Technol 18* (1997).

[119] Hardy, W. B., and Neville, F. H. A preliminary investigation of the conditions which determine the stability of irreversible hydrosols. *Proc. R. Soc. London 66* (1900), 110.

[120] Harrand, M. Polarized Raman spectra of oriented dipalmitoylphosphatidylcholine (DPPC). I. Scattering activities of skeletal stretching and methylene vibrations of hydrocarbon chains. *J. Chem. Phys. 79* (1984), 5639.

[121] Harris-Birtill, D., Singh, M., Zhou, Y., Shah, A., Ruenraroengsak, P., Gallina, M. E., Hanna, G. B., Cass, A. E. G., Porter, A., Bamber, J., and Elson, D. S. Gold nanorod reshaping *in vitro* and *in vivo* using a continuous wave laser. *PLoS ONE 12* (10 2017), 1.

[122] Hasselbalch, K. A. Die Berechnung der Wasserstoffzahl des Blutes aus der freien und gebundenen Kohlensäure desselben, und die Sauerstoffbindung des Blutes als Funktion der Wasserstoffzahl [German] (The calculation of blood pH from free and bound carbonic acid, and blood oxygen binding as a function of pH). *Biochem. Z. 78* (1916), 112.

[123] Henderson, L. J. Concerning the relationship between the strength of acids and their capacity to preserve neutrality. *Am. J. Physiol. 21* (1908), 173.

[124] Henry, D. C. The Cataphoresis of Suspended Particles. Part I. The Equation of Cataphoresis. *Proc. Royal Soc. A 133* (1931), 106.

[125] Hermanson, G. T. *Bioconjugate Techniques, 3rd Edition*. Academic Press, London, UK, 2013.

[126] Holmlin, R. E., Chen, X., Chapman, R. G., Takayama, S., and Whitesides, G. M. Zwitterionic SAMs that resist nonspecific adsorption of protein from aqueous buffer. *Langmuir 17* (2001), 2841.

[127] Horiguchi, Y., Honda, K., Kato, Y., Nakashima, N., and Niidome, Y. Photothermal reshaping of gold nanorods depends on the passivating layers of the nanorod surfaces. *Langmuir 24* (2008), 12026.

[128] Hosios, A. M., Hecht, V. C., Danai, L. V., Johnson, M. O., Rathmell, J. C., Steinhauser, M. L., Manalis, S. R., and Vander-Heiden, M. G. Amino acids rather than glucose account for the majority of cell mass in proliferating mammalian cells. *Dev. Cell 36* (2016), 540.

[129] Hotchkiss, J. W., Lowe, A. B., and Boyes, S. G. Surface modification of gold nanorods with polymers synthesized by reversible addition–fragmentation chain transfer polymerization. *Chem. Mater. 19* (2007), 6.

[130] Hotchkiss, J. W., Mohr, B. G. R., and Boyes, S. G. Gold nanorods surface modified with poly(acrylic acid) as a template for the synthesis of metallic nanoparticles. *J. Nanopart. Res. 12* (2010), 915.

[131] Tong, W. and Walsh, M. J. and Mulvaney, P. and Etheridge, J. and Funston, A. M. Control of symmetry breaking size and aspect ratio in gold nanorods: Underlying role of silver nitrate. *J. Phys. Chem. C 121* (2017), 3549.

[132] Hu, Q., Nielsen, M. H., Freeman, C. L., Hamm, L. M., Tao, J., Lee, J. R. I., Han, T. Y. J., Becker, U., Harding, J. H., Dove, P., and De Yoreo, J. The thermodynamics of calcite nucleation at organic interfaces: Classical vs. non–classical pathways. *Faraday Discuss. 159* (2012), 509–523.

[133] Hu, W., Mao, A., Wong, P., Larsen, A., Yazaki, P., Wong, J. Y. C., and Shively, J. E. Characterization of 1,2-Distearoyl-sn-glycero-3-phosphoethanolamineN-[Methoxy(polyethylene glycerol)-2000] and its complex

with doxorubicin using nuclear magnetic resonance spectroscopy and molecular dynamics. *Bioconjugate Chem. 28*, 6 (2017), 1777.

[134] Hu, X., and Gao, X. Multilayer coating of gold nanorods for combined stability and biocompatibility. *Phys. Chem. Chem. Phys. 13* (2011), 10028.

[135] Hu, Z., Wang, X., Wang, W., Zhang, Z., Gao, H., and Mao, Y. Raman spectroscopy for detecting supported planar lipid bilayers composed of ganglioside–GM1/sphingomyelin/cholesterol in the presence of amyloid–β. *Phys. Chem. Chem. Phys. 17* (2015), 22711.

[136] Huang, E. Y., Chang, J. C., Chen, H. H., Hsu, C. Y., Hsu, H. C., and Wu, K. L. Carcinoembryonic antigen as a marker of radioresistance in colorectal cancer: a potential role of macrophages. *BMC Cancer 18* (2018), 321.

[137] Huang, H. C., Barua, S., Kay, D. B., and Rege, K. Simultaneous enhancement of photothermal stability and gene delivery efficacy of gold nanorods using polyelectrolytes. *ACS Nano 3* (2009), 2941.

[138] Huang, H. C., Rege, K., and Heys, J. J. Spatiotemporal temperature distribution and cancer cell death in response to extracellular hyperthermia induced by gold nanorods. *ACS Nano 4* (2010), 28920.

[139] Huang, J., Jackson, K. S., and Murphy, C. J. Polyelectrolyte wrapping layers control rates of photothermal molecular release from gold nanorods. *Nano Letters 12* (2012), 2982–2987.

[140] Huang, Q., Zou, Y., Zhong, S., Yang, X., Li, J., Huang, W., Zhu, H., Cheng, C., Ding, M., Zhu, L. G., and Shi, Q. Silica–coated gold nanorods with high photothermal efficiency and biocompatibility as a contrast agent for *in vitro* terahertz imaging. *J. Biomed. Nanotechnol. 15* (2019), 910.

[141] Huang, X., El-Sayed, I. H., Qian, W., and El-Sayed, M. A. Cancer cell imaging and photothermal therapy in the near-infrared region by using gold nanorods. *J. Am. Chem. Soc. 128* (2006), 2115.

[142] Hubert, F., Testard, F., and Spalla, O. Cetyltrimethylammonium bromide silver bromide complex as the capping agent of gold nanorods. *Langmuir 24*, 17 (2008), 9219–9222.

[143] Jackson, S. R., McBride, J. R., Rosenthal, S. J., and Wright, D. W. Wheres the silver? Imaging trace silver coverage on the surface of gold nanorods. *J. Am. Chem. Soc. 136* (2014), 5261.

[144] Jain, P. K., and El-Sayed, M. A. Plasmonic coupling in noble metal nanostructures. *Chem. Phys. Letts. 487* (2010), 153.

[145] Jain, P. K., Lee, K. S., El-Sayed, I. H., and El-Sayed, M. A. Calculated absorption and scattering properties of gold nanoparticles of different size, shape, and composition: applications in biological imaging and biomedicine. *J. Phys. Chem. B 110* (2006), 7238.

[146] Jana, N. R. Gram–scale synthesis of soluble, near–monodisperse gold nanorods and other anisotropic nanoparticles. *Small 1* (2005), 875.

[147] Jana, N. R., Gearheart, L., and Murphy, C. J. Wet chemical synthesis of high aspect ratio cylindrical gold nanorods. *J. Phys. Chem. B 105*, 19 (2001), 4065.

[148] Jana, N. R., Gearheart, L., and Murphy, C. J. Seed–mediated growth approach for shape–controlled synthesis of spheroidal and rod-like gold nanoparticles using a surfactant template. *Adv. Mater. 13* (2001), 1389.

[149] Jaque, D., Maestro, L., del Rosal, B., Haro-Gonzalez, P., Benayas, A., Plaza, J., Martín Rodríguez, E., and García Solé, J. Nanoparticles for photothermal therapies. *Nanoscale 6* (2014), 9494.

[150] Jaswon, M. A. Integral equation methods in potential theory. I. *Proc. R. Soc. Lond. A 275* (1963), 23.

[151] Javadian, S., Ruhi, V., Heydari, A., Shahir, A., Yousefi, A., and Akbari, J. Self–assembled CTAB nanostructures in aqueous/ionic liquid systems: effects of hydrogen bonding. *Ind. Eng. Chem. Res. 52* (2013), 4517.

[152] Jessl, S., Tebbe, M., Guerrini, L., Fery, A., Alvarez-Puebla, R. A., and Pazos-Perez, N. Silver–assisted synthesis of gold nanorods: the relation between silver additive and iodide impurities. *Small 14* (2018), 1703879.

[153] Joa, S., and Pemberton, J. A surface enhanced Raman scattering investigation of interfacial structure at silver electrodes in electrolyte solutions of the isomers of butanol. *Langmuir 8* (1992), 2301.

[154] Johnson, C. J., Dujardin, E., Davis, S. A., Murphy, C. J., and Mann, S. Growth and form of gold nanorods prepared by seed–mediated, surfactant-directed synthesis. *J. Mater. Chem. 12* (2002), 1765.

[155] Johnson, N. J. J., Oakden, W., Stanisz, G. J., Scott Prosser, R., and van Veggel, F. C. J. M. Size–tunable, ultrasmall $NaGdF_4$ nanoparticles: Insights into their T_1 MRI contrast enhancement. *Chem. Mater. 23*, 16 (2011), 3714.

[156] Johnson, P. B., and Christy, R. W. Optical constants of the noble metals. *Phys. Rev. B. 6* (1972), 4370.

[157] Jokerst, J. V., Thangaraj, M., Kempen, P. J., Sinclair, R., and Gambhir, S. S. Photoacoustic imaging of mesenchymal stem cells in living mice via silica–coated gold nanorods. *ACS Nano 6* (2012), 5920.

[158] Jones, S. T., Taylor, R. W., Esteban, R., Abo-Hamed, E. K., Bomans, P. H. H., Sommerdijk, N. A. J. M., Aizpurua, J., Baumberg, J. J., and Scherman, O. A. Gold nanorods with sub–nanometer separation using cucurbit[n]uril for SERS applications. *Small 10* (2014), 4298.

[159] Kalepu, S., and Nekkanti, V. Insoluble drug delivery strategies: Review of recent advances and business prospects. *Acta Pharm. Sin. B 5* (2015), 442.

[160] Kalyanasundaram, K., and Thomas, J. The conformational state of surfactants in the solid state and in micellar form. A laser-excited Raman scattering study. *J.Phys. Chem. 80* (1976), 1462.

[161] Karabutov, A. A., Savateeva, E. V., and Oraevsky, A. A. Optoacoustic supercontrast for early cancer detection. *Proc. SPIE 4256* (2001), 179.

[162] Kennedy, W. J., Izor, S., Anderson, B. D., Frank, G., Varshney, V., and Ehlert, G. J. Thermal reshaping dynamics of gold nanorods: Influence of size, shape, and local environment. *ACS Appl. Mater. Interfaces 10* (2018), 43865.

[163] Khaled, Y. S., Shamsuddin, S., Tiernan, J., McPherson, M., Hughes, T., Millner, P., and Jayne, D. G. Theranostic CEA–affimer functionalised silica nanoparticles allow specific *in vitro* fluorescent imaging of colorectal cancer cells. *Eur. J. Surg. Oncol. 44* (2018), S1.

[164] Khan, Z., Singh, T., Hussain, J., and Hashmi, A. Au(III)-CTAB reduction by ascorbic acid: Preparation and characterization of gold nanoparticles. *Colloids Surf. B 104* (2013), 11.

[165] Khlebtsov, B. N., Khanadeev, V., Ye, J., Sukhorukov, G. B., and Khlebtsov, N. G. Overgrowth of gold nanorods by using a binary surfactant mixture. *Langmuir 30* (2014), 1696.

[166] Khlebtsov, N., and Dykman, L. Biodistribution and toxicity of engineered gold nanoparticles: A review of *in vitro* and *in vivo* studies. *Chem. Soc. Rev. 40* (2011), 1647.

[167] Khlebtsov, N. G. Determination of size and concentration of gold nanoparticles from extinction spectra. *Anal. Chem. 80*, 17 (2008), 6620.

[168] Kim, D. S., Kim, Y. T., Hong, S. B., Kim, J., Heo, N. S., Lee, M. K., Lee, S. J., Kim, B. I., Kim, I. S., Huh, Y. S., and Choi, B. G. Development of lateral flow assay based on size–controlled gold nanoparticles for detection of hepatitis B surface antigen. *Sensors 16* (2016), 2154.

[169] Kim, S., Chen, Y. S., Luke, G., and Emelianov, S. Y. *in vivo* three–dimensional spectroscopic photoacoustic imaging for monitoring nanoparticle delivery. *Biomed. Opt. Express 2* (2011), 2540.

[170] Kint, S., Wermer, P. H., and Scherer, J. R. Raman spectra of hydrated phospholipid bilayers. 2. Water and head-group interactions. *J. Phys. Chem. 96* (1992), 446.

[171] Kneipp, K., Wang, Y., Kneipp, H., Perelman, L., Itzkan, I., Dasari, R., and Feld, M. S. Single molecule detection using surface–enhanced Raman scattering (SERS). *Phys. Rev. Lett. 78* (1997), 1667.

[172] Knight, W. D. Nuclear magnetic resonance shift in metals. *Phys. Rev. 76* (1949), 1259.

[173] Knights, O. B., and McLaughlan, J. R. Gold nanorods for light–based lung cancer theranostics. *Int. J. Mol. Sci. 19* (2018), 3318.

[174] Knights, O. B., Ye, S., Ingram, N., Freear, S., and McLaughlan, J. R. Optimising gold nanorods for photoacoustic imaging *in vitro*. *Nanoscale Adv. 1* (2019), 1472.

[175] Koch, M., Suhr, C., Roth, B., and Meinhardt-Wollweber, M. Iterative morphological and mollifier–based baseline correction for Raman spectra. *J. Raman Spectrosc. 48* (2017), 336.

[176] Koenig, J. L., and Angood, A. C. Raman spectra of poly(ethylene glycols) in solution. *J. Polym. Sci., Part A2: Polym. Phys. 8* (1970), 1787.

[177] Koglin, E., Tarazona, A., Kreisig, S., and Schwuger, M. *in–situ* investigations of coadsorbed cationic surfactants on charged surfaces: a sers microprobe study. *Colloids Surf. A 123* (1997), 523.

[178] Kokkinopoulou, M., Simon, J., Landfester, K., Mailänder, V., and Lieberwirth, I. Visualization of the protein corona: Towards a biomolecular understanding of nanoparticle–cell–interactions. *Nanoscale 9*, 25 (2017), 8858.

[179] Kooby, D. A., Carew, J. F., Halterman, M. W., Mack, J. E., Bertino, J. R., Blumgart, L. H., Federoff, H. J., and Fong, Y. Oncolytic viral therapy for human colorectal cancer and liver metastases using a multi-mutated herpes simplex virus type–1 (G207). *FASEB J. 13* (1999), 1325–1334.

[180] Koshy, P., Aswal, V. K., Venkatesh, M., and Hassan, P. A. Unusual scaling in the rheology of branched wormlike micelles formed by cetyltrimethylammonium bromide and sodium oleate. *J. Phys. Chem. B 115* (2011), 10817.

[181] Kou, L., Sun, J., Zhai, Y., and He, Z. The endocytosis and intracellular fate of nanomedicines: Implication for rational design. *Asian J. Pharm. Sci. 8* (2013), 1.

[182] Krafft, C., Neudert, L., Simat, T., and Salzer, R. Near infrared Raman spectra of human brain lipids. *Spectrochim. Acta, Part A 61* (2005), 1529.

[183] Kreke, P. J., Magid, L. J., and Gee, J. C. ^{1}H and ^{13}C NMR studies of mixed counterion, cetyltrimethylammonium bromide/cetyltrimethylammonium dichlorobenzoate, surfactant solutions: The intercalation of aromatic counterions. *Langmuir 12*, 3 (1996), 699.

[184] Kreuzer, H. J., Wang, R. L. C., and Grunze, M. Hydroxide ion adsorption on self-assembled monolayers. *J. Am. Chem. Soc. 125*, 27 (2003), 8384.

[185] Krpetić, v., Nativo, P., Sée, V., Prior, I. A., Brust, M., and Volk, M. Inflicting controlled nonthermal damage to subcellular structures by laser–activated gold nanoparticles. *Nano Letts 10* (2010), 4549.

[186] Krug, H. F. Nanosafety research – Are we on the right track? *Ang. Chem. Int. Ed. 53* (2014), 12304.

[187] Kruger, R. A., Liu, P., Fang, Y., and Robert, A. C. Photoacoustic ultrasound (PAUS)–reconstruction tomography. *Med. Phys. 22* (1995), 1605.

[188] Kumari, A., and Yadav, S. K. Cellular interactions of therapeutically delivered nanoparticles. *Expert Opin. Drug Deliv. 8* (2011), 141.

[189] Lai, J., Zhang, L., Niu, W., Qi, W., Zhao, J., Liu, Z., Zhang, W., and Xu, G. One–pot synthesis of gold nanorods using binary surfactant systems with improved monodispersity, dimensional tunability and plasmon resonance scattering properties. *Nanotechnology 25* (2014), 125601.

[190] Lal, S., Clare, S. E., and Halas, N. J. Nanoshell–enabled photothermal cancer therapy: Impending clinical impact. *Acc. Chem. Res. 41* (2008), 1842.

[191] Lau, I. P., Chen, H., Wang, J., Ong, H. C., Leung, K. C. F., Ho, H. P., and Kong, S. K. *in vitro* effect of ctab– and peg–coated gold nanorods on the induction of eryptosis/erythroptosis in human erythrocytes. *Nanotoxicology 6* (2012), 847.

[192] Laufer, J., Delpy, D., Elwell, C., and Beard, P. C. Quantitative spatially resolved measurement of tissue chromophore concentrations using photoacoustic spectroscopy: Application to the measurement of blood oxygenation and haemoglobin concentration. *Phys. Med. Biol. 52* (2007), 141.

[193] Laufer, J., Elwell, C., Delpy, D., and Beard, P. C. In vitro measurements of absolute blood oxygen saturation using pulsed near-infrared photoacoustic spectroscopy: accuracy and resolution. *Phys. Med. Biol. 50* (2005), 4409.

[194] Lee, C., and Bain, C. D. Raman spectra of planar supported lipid bilayers. *Biochim. Biophys. Acta 1711*, 1 (2005), 59.

[195] Lee, S., Anderson, L. J. E., Payne, C. M., and Hafner, J. H. Structural transition in the surfactant layer that surrounds gold nanorods as observed by analytical surface–enhanced Raman spectroscopy. *Langmuir 27* (2011), 14748.

[196] Leonov, A. P., Zheng, J., Clogston, J. D., Stern, S. T., Patri, A., and Wei, A. Detoxification of gold nanorods by treatment with polystyrenesulfonate. *ACS Nano 2* (2008), 2481.

[197] Li, M. L., Wang, J. C., Schwartz, J. A., Gill-Sharp, K. L., Stoica, G., and Wang, L. V. *in vivo* photoacoustic microscopy of nanoshell extravasation from solid tumor vasculature. *J. Biomed. Opt. 14* (2009), 010507.

[198] Li, P., Wu, Y., Li, D., Su, X., Luo, C., Wang, Y., Hu, J., Li, G., Jiang, H., and Zhang, W. Seed–mediated synthesis of tunable–aspect–ratio gold nanorods for near–infrared photoacoustic imaging. *Nano. Res. Letts. 13* (2018), 313.

[199] Li, P. C., Huang, S. W., Wei, C. W., Chiou, Y. C., Chen, C. D., and Wang, C. R. C. Photoacoustic flow measurements by use of laser–induced shape transitions of gold nanorods. *Opt. Lett. 30* (2005), 3341.

[200] Li, P. C., Wei, C. W., Liao, C. K., Chen, C. D., Pao, K., Wang, C. R., Wu, Y. N., and Shieh, D. B. Multiple targeting in photoacoustic imaging using bioconjugated gold nanorods. *Photons Plus Ultrasound: Imaging and Sensing 2006: The Seventh Conference on Biomedical Thermoacoustics, Optoacoustics, and Acousto–optics 6086* (2006), 60860M.

[201] Li, W., and Chen, X. Gold nanoparticles for photoacoustic imaging. *Nanomedicine 10* (2015), 299.

[202] Li, Y., Cu, J. Z., Zhi, L., Xu, H., Pan, M. W., Zhong, G. J., and Li, Z. M. Multiple stage crystallization of gamma phase poly(vinylidene fluoride) induced by ion–dipole interaction as revealed by time–resolved FTIR and two-dimensional correlation analysis. *Polymer 55* (2014), 4765.

[203] Li, Z., Huang, P., Zhang, X., Lin, J., Yang, S., Liu, B., Gao, F., Xi, P., Ren, Q., and Cui, D. RGD–conjugated dendrimer–modified gold nanorods for *in vivo* tumor targeting and photothermal therapy. *Mol. Pharmaceutics 7* (2009), 94.

[204] Li, Z., Tang, S., Wang, B., Li, Y., Huang, H., Wang, H., Li, P., Li, C., Chu, P. K., and Yu, X. F. Metabolizable small gold nanorods: Size-dependent cytotoxicity, cell uptake and *in–vivo* biodistribution. *ACS Biomater. Sci. Eng. 2* (2016), 789.

[205] Lind, A. C., and Greenberg, J. M. Electromagnetic scattering by obliquely oriented cylinders. *J. Appl. Phys. 37* (1966), 3195.

[206] Lindl, T. *Zell- und Gewebekultur*, 5th edition ed. Spektrum Akademischer Verlagan, Heidelberg, 2002.

[207] Link, S., Burda, C., Nikoobakht, B., and El-Sayed, M. A. Laser–induced shape changes of colloidal gold nanorods using femtosecond and nanosecond laser pulses. *J. Phys. Chem. B 104* (2000), 6152–6163.

[208] Link, S., Wang, Z. L., and El-Sayed, M. A. How does a gold nanorod melt? *J. Phys. Chem. B 104* (2000), 7867.

[209] Liopo, A., Wang, S., Derry, P. J., Oraevsky, A. A., and Zubarev, E. R. Seedless synthesis of gold nanorods using dopamine as a reducing agent. *RSC Adv. 5* (2015), 91587.

[210] Lippert, J. L., Gorczyca, L. E., and Meiklejohn, G. A laser Raman spectroscopic investigation of phospholipid and protein configurations in hemoglobin–free erythrocyte ghosts. *Biochim. Biophys. Acta, Biomembr. 382* (1975), 51.

[211] Lohse, S. E., Burrows, N. D., Scarabelli, L., Liz-Marzán, L. M., and Murphy, C. J. Anisotropic noble metal nanocrystal growth: the role of halides. *Chem. Mater. 26* (2013), 34.

[212] Loo, C., Lowery, A., Halas, N. J., West, J., and Drezek, R. Immunotargeted nanoshells for integrated cancer imaging and therapy. *Nano Letts. 5* (2005), 709.

[213] Lorentz, H. A. Over het Verband tusschen de Voortplantlngssnelheid van het Licht en de Dichtheid en Samenstelling der Middenstoffen [Dutch] (Concerning the relation between the velocity of light propagation and the composition of media). *Verh. Kon. Akad. Wet. Amsterdam, Afd. Natuurkd. 18* (1878), 39.

[214] Luft, J. H. Improvements in epoxy resin embedding methods. *J. Cell Biol. 9* (1961), 409–414.

[215] Luk, K. H., Hulse, R. M., and Phillips, T. L. Hyperthermia in cancer therapy. *West. J. Med. 132* (1980), 179.

[216] Luke, G. P., Bashyam, A., Homan, K. A., Makhija, S., Chen, Y. S., and Emelianov, S. Y. Silica–coated gold nanoplates as stable photoacoustic contrast agents for sentinel lymph node imaging. *Nanotechnology 24* (2013), 455101.

[217] Maier, S. A. *Plasmonics: Fundamentals and Applications*. Springer, New York, NY, 2007.

[218] Manke, A. Mechanisms of nanoparticle–induced oxidative stress and toxicity. *BioMed Res. Int. 2013* (2014), 942916.

[219] Marbella, L. E., and Millstone, J. E. NMR techniques for noble metal nanoparticles. *Chem. Mater. 27* (2015), 2721.

[220] Marks, L. D., and Peng, L. Nanoparticle shape, thermodynamics and kinetics. *J. Phys. Condens. Matter 28* (2016), 053001.

[221] Marsh, D. *Handbook of Lipid Bilayers*. CRC Press, Boca Raton, 2013.

[222] Matthews, J. R., Payne, C. M., and Hafner, J. H. Analysis of phospholipid bilayers on gold nanorods by plasmon resonance sensing and surface-enhanced Raman scattering. *Langmuir 31* (2015), 9893–9900.

[223] Meena, S. K., Celiksoy, S., Schäfer, P., Henkel, A., Snnichsen, C., and Sulpizi, M. The role of halide ions in the anisotropic growth of gold nanoparticles: A microscopic, atomistic perspective. *Phys. Chem. Chem. Phys. 18* (2016), 13246.

[224] Meena, S. K., and Sulpizi, M. Understanding the microscopic origin of gold nanoparticle anisotropic growth from molecular dynamics simulations. *Langmuir 29* (2013), 14954–14961.

[225] Melancon, M. P., Lu, W., Yang, Z., Zhang, R., Cheng, Z., Elliot, A. M., Stafford, J., Olson, T., Zhang, J. Z., and Li, C. *in vitro* and *in vivo* targeting of hollow gold nanoshells directed at epidermal growth factor receptor for photothermal ablation therapy. *Mol. Cancer Ther. 7* (2008), 1730.

[226] Meng, F., Engbers, G. H. M., and Feijen, J. Polyethylene glycolgrafted polystyrene particles. *J. Biomed. Mater. Res. B 70A* (2004), 49.

[227] Mico, V., Charalambous, A., Peyman, S. A., Abou-Saleh, R., Markham, A. F., Coletta, P. L., and Evans, S. D. Evaluation of lipid–stabilised tripropionin nanodroplets as a delivery route for combretastatin A4. *Int. J. Pharmaceut. 526* (2017), 547.

[228] Mie, G. Beiträge zur Optik trüber Medien, Speziell Kolloidaler Metallösungen [German] (Contributions to the optics of turbid media: Colloidal metal solutions). *Ann. Phys. 330* (1908), 377.

[229] Miraglia, D. B., Rodríguez, J. L. M., Minardi, R. M., and Schulz, P. C. Critical micelle concentration and HLB of the sodium oleate–hexadecyltrimethylammonium bromide mixed system. *Journal of Surfactants and Detergents 14* (2010), 401.

[230] Miraglia, D. B., Schulz, E. N., Rodríguez, J. L. M., Schulz, P. C., and Salinas, D. Effect of the concentration and composition on the size and shape of micelles of sodium oleate–cetyltrimethylammonium bromide mixtures. *J. Colloid Interface Sci 351* (2010), 197.

[231] Miranda, O. R., Dollahon, N. R., and Ahmadi, T. S. Critical concentrations and role of ascorbic acid (vitamin C) in the crystallization of gold nanorods within hexadecyltrimethyl ammonium bromide (CTAB)/tetraoctyl ammonium bromide (TOAB) micelles. *Cryst. Growth Des. 6* (2006), 2747.

[232] Mirska, D., Schirmer, K., Funari, S. S., Langner, A., Dobner, B., and Brezesinski, B. Biophysical and biochemical properties of a binary lipid mixture for DNA transfection. *Colloids Surf. B 40* (2005), 51.

[233] Mondal, B., Ramlal, S., Lavu, P. S., N, B., and Kingston, J. Highly sensitive colorimetric biosensor for staphylococcal enterotoxin B by a label–free aptamer and gold nanoparticles. *Front. Microbiol. 9* (2018), 179.

[234] Mondes, V., Antonsson, E., Plenge, J., Raschpichler, C., Halfpap, I., Menski, A., Graf, C., Kling, M. F., and Rühl, E. Plasmonic electric near-field enhancement in self-organized gold nanoparticles in macroscopic arrays. *App. Phys. B 122* (2016), 155.

[235] Moore, G. E., Gerner, R. E., and Franklin, H. A. Culture of normal human leukocytes. *JAMA 199* (1967), 519.

[236] MRK1651-02 The diffusion barrier technique: Practical aspects and data interpretation. Application note, Malvern Instruments Ltd, Malvern, UK, 2012.

[237] MRK1960 Measuring protein isoelectric point using the Zetasizer Nano ZSP. Application note, Malvern Instruments Ltd, Malvern, UK, 2013.

[238] Murphy, C. J., Sau, T. K., Gole, A. M., Orendorff, C. J., Gao, J., Gou, L., Hunyadi, S. E., and Li, T. Anisotropic metal nanoparticles:Synthesis, assembly, and optical applications. *J. Phys. Chem. B 109* (2005), 13857.

[239] Myroshnychenko, V., Rodríguez-Fernández, J., Pastoriza-Santos, I., Funston, A. M., Novo, C., Mulvaney, P., Liz-Marzán, L. M., and García de Abajo, F. J. Modelling the optical response of gold nanoparticles. *Chem. Soc. Rev. 37* (2008), 1792.

[240] Nakata, A., Nomoto, T., Toyota, T., and Fujinami, M. Tip–enhanced Raman spectroscopy of lipid bilayers in water with an alumina– and silver–coated tungsten tip. *Anal. Sci. 29* (2013), 865.

[241] Nasilowski, M., Mahler, B., Lhuillier, E., Ithurria, S., and Dubertret, B. Two-dimensional colloidal nanocrystals. *Chemical Reviews 116*, 18 (2015), 10934.

[242] Nativo, P., Prior, I. A., and Brust, M. Uptake and intracellular fate of surface–modified gold nanoparticles. *ACS nano 2* (2008), 1639–1644.

[243] Nel, A., Mädler, L., Velegol, D., Xia, T., Hoek, E. M. V., Somasundaran, P., Klaessig, F., Castranova, V., and Thompson, M. Understanding biophysicochemical interactions at the nano–bio interface. *Nat. Mater. 8* (2009), 543.

[244] Nernst, W. Zur kinetik der Lösung befindlichen Körper I. Theorie der Diffusion [German] (On the kinetics of the bodies in solution I. Theory of diffusion). *Z. Physik Chem 2* (1888), 613.

[245] Nernst, W. Zur Theorie der umkehrbarer galvanisher Elemente [German] (The theory of reversible galvanic elements). *Sitzungsber. Preuss. Akad. Wiss 1* (1889), 83.

[246] Nernst, W. Die elektromotorische Wirksamkeit der Jonen [German] (The electromotive activity of ions). *Z. Physik Chem 4* (1889), 129.

[247] Ng, K. C., and Cheng, W. Fine–tuning longitudinal plasmon resonances of nanorods by thermal reshaping in aqueous media. *Nanotechnology 23* (2012), 105602.

[248] Nguyen, T. N. H., Nguyen, T. L. T., Luong, T. T. T., Nguyen, C. M. T., and Nguyen, T. P. P. Synthesis of gold nanorods with a longitudinal surface plasmon resonance peak of around 1250 nm. *Adv. Nat. Sci: Nanosci. Nanotechnol. 7* (2016), 015006.

[249] Nichols, J. W., and Bae, Y. H. EPR: Evidence and fallacy. *J. Controlled Release 190* (2014), 451.

[250] Nie, S., and Emory, S. R. Probing single molecules and single nanoparticles by surface–enhanced Raman scattering. *Science 275* (1997), 1102.

[251] Niidome, T., Yamagata, M., Okamoto, Y., Akiyama, Y., Takahashi, H., Kawano, T., Katayama, Y., and Niidome, Y. PEG–modified gold nanorods with a stealth character for *in–vivo* applications. *J. Control. Release 114* (2006), 343.

[252] Niidome, Y., Nakamura, Y., Honda, K., Akiyama, Y., Nishioka, K., Kawasaki, H., and Nakashima, N. Characterization of silver ions adsorbed on gold nanorods: Surface analysis by using surface-assisted laser desorption/ionization time–of–flight mass spectrometry. *Chem. Commun. 13* (2009), 1754.

[253] Nikoobakht, B., , and El-Sayed, M. Preparation and growth mechanism of gold nanorods (NRs) using seed–mediated growth method. *Chem. Mater. 15* (2003), 1957.

[254] Nikoobakht, B., and El-Sayed, M. A. Evidence for bilayer assembly of cationic surfactants on the surface of gold nanorods. *Langmuir 17* (2001), 6368.

[255] Nitzsche, R., and Connah, M. The use of the Malvern Zetasizer for the measurement of Zeta Potential. Manual, Malvern Instruments Ltd, Malvern, UK, 2012.

[256] Nyborg, W. L. Solutions of the bio-heat transfer equation. *Phys. Med. Biol 33*, 7 (1988), 785.

[257] Nyquist, R. A. *Interpreting infrared, Raman, and nuclear magnetic resonance spectra. Volume 1*. Academic Press, San Diego, CA, 2001.

[258] Nyquist, R. A. *Interpreting infrared, Raman, and nuclear magnetic resonance spectra. Volume 2*. Academic Press, San Diego, CA, 2001.

[259] Ohno, K., Tonegawa, A., Yoshida, H., and Matsuura, H. Spectroscopic evidence for an intramolecular C−H···N hydrogen bond: Infrared and Raman spectroscopy and *ab initio* molecular orbital calculations of N,N–dimethylpropylamine and propyltrimethylammonium bromide. *J. Mol. Struct 435* (1997), 219.

[260] Oldenburg, S. J., Averitt, R. D., Westcott, S. L., and Halas, N. J. Nanoengineering of optical resonances. *Chem. Phys. Letts. 288* (1998), 243.

[261] O'Neal, D. P., Hirsch, L. R., Halas, N. J., Payne, J. D., and West, J. L. Photo–thermal tumor ablation in mice using near infrared–absorbing nanoparticles. *Cancer Letts. 209* (2004), 171.

[262] Ong, Z. Y., Chen, S., Nabavi, E., Regoutz, A., Payne, D. J., Elson, D. S., Dexter, D. T., Dunlop, I. E., and Porter, A. E. Multibranched gold nanoparticles with intrinsic LAT–1 targeting capabilities for selective photothermal therapy of breast cancer. *ACS Appl. Mater. Interfaces 9* (2017), 39259.

[263] Opilik, L., Bauer, T., Schmid, T., Stadler, J., and Zenobi, R. Nanoscale chemical imaging of segregated lipid domains using tip–enhanced Raman spectroscopy. *Phys. Chem. Chem. Phys. 13* (2011), 9978.

[264] Oraevsky, A. A., Jacques, S. L., Esenaliev, R. O., and Tittel, F. K. Laser–based optoacoustic imaging in biological tissues. *Proc. SPIE 2134A* (1994).

[265] Oraevsky, A. A., Karabutov, A. A., and Savateeva, E. V. Enhancement of optoacoustic tissue contrast with absorbing nanoparticles. *Proc. SPIE 4434* (2001), 60.

[266] Orendorff, C. J., Alam, T. M., Sasaki, D. Y., Bunker, B. C., and Voigt, J. A. Phospholipid–gold nanorod composites. *ACS Nano*, 4 (2009), 971.

[267] Orendorff, C. J., and Murphy, C. J. Quantitation of metal content in the silver–assisted growth of gold nanorods. *J. Phys. Chem. B 110* (2006), 3990.

[268] Palla-Papavlu, A., Shaw-Stewart, J., Dinca, V., Savopol, T., Kovacs, E., Lippert, T., Wokaun, A., and Dinescu, M. Liposome micropatterning based on laser–induced forward transfer. *Appl. Phys. A 102* (2011), 651.

[269] Pallares, R. M., Su, X., Lim, S. H., and Thanh, N. T. K. Fine-tuning of gold nanorod dimensions and plasmonic properties using the Hofmeister effects. *J. Mater. Chem. C 4* (2016), 53.

[270] Palmer, K. F., and Williams, D. Optical properties of water in the near infrared. *J. Opt. Soc. Am. 64* (1974), 1107.

[271] Palpant, B. Photothermal properties of gold nanoparticles. In *Gold Nanoparticles for Physics, Chemistry and Biology*, C. Louis and O. Pluchery, Eds. Imperial College Press, 2012, ch. 4, p. 75.

[272] Park, J. W., and Shumaker-Parry, J. S. Structural study of citrate layers on gold nanoparticles: role of intermolecular interactions in stabilizing nanoparticles. *J. Am. Chem. Soc. 136* (2014), 19071.

[273] Park, K., Drummy, L. F., Wadams, R. C., Koerner, H., Nepal, D., Fabris, L., and Vaia, R. A. Growth mechanism of gold nanorods. *Chem. Mater. 25* (2013), 555.

[274] Peng, X., Manna, L., Yang, W., Wickham, J., Scher, E., Kadavanich, A., and Alivisatos, A. P. Shape control of CdSe nanocrystals. *Nature 404* (2000), 59.

[275] Pérez-Juste, J., Liz-Marzán, L., Carnie, S., Chan, D. Y. C., and Mulvaney, P. Electric–field–directed growth of gold nanorods in aqueous surfactant solutions. *Adv. Funct. Mater. 14* (2004), 571.

[276] Petrova, H., Perez Juste, J., Pastoriza-Santos, I., Hartland, G. V., Liz-Marzán, L. M., and Mulvaney, P. On the temperature stability of gold nanorods: comparison between thermal and ultrafast laser–induced heating. *Phys. Chem. Chem. Phys. 8* (2006), 814.

[277] Pierrat, S., Zins, I., Breivogel, A., and Sönnichsen, C. Self–assembly of small gold colloids with functionalized gold nanorods. *Nano Letts 7* (2007), 259.

[278] Pissuwan, D., Kumagai, Y., and Smith, N. I. Effect of surface–modified gold nanorods on the inflammatory cytokine response in macrophage cells. *Part. Part. Syst. Char. 30* (2013), 427.

[279] Pitsillides, C. M., Joe, E. K., Wei, X., Anderson, R. R., and Lin, C. P. Selective cell targeting with light–absorbing microparticles and nanoparticles. *Biophys. J. 84* (2003), 4023.

[280] Polito, A. B., Maurer-Gardner, E. I., and Hussain, S. M. Surface chemistry manipulation of gold nanorods preserves optical properties for bio-imaging applications. *J. Nanopart. Res. 17* (2015), 485.

[281] Prescott, S. W., and Mulvaney, P. Gold nanorod extinction spectra. *J. Appl. Phys. 99* (2006), 123504.

[282] Qian, X., H., P. X., O., A. D., Yin-Goen, Q., Chen, G. Z., Shim, D. M., Yang, L., Young, A. N., Wang, M. D., and Nie, S. *in–vivo* tumor targeting and spectroscopic detection with surface–enhanced raman nanoparticle tags. *Nat. Biotech. 26* (2008), 83.

[283] Qin, Z., Wang, Y., Randrianalisoa, J., Raeesi, V., Chan, W. C. W., Lipiński, W., and Bischof, J. C. Quantitative comparison of photothermal heat generation between gold nanospheres and nanorods. *Sci. Rep. 6* (2016), 29836.

[284] Qu, M., Mehrmohammadi, M., Truby, R., Graf, I., Homan, K., and Emelianov, S. Contrast–enhanced magneto–photo–acoustic imaging *in vivo* using dual–contrast nanoparticles. *Photoacoustics 2* (2014), 55.

[285] Quarles, J. M., Morris, N. G., and Leibovitz, A. Carcinoembryonic antigen production by human colorectal adenocarcinoma cells in matrix–perfusion culture. *In Vitro 16*, 2 (1980), 113.

[286] Quarta, A., Ragusa, A., Deka, S., Tortiglione, C., Tino, A., Cingolani, R., and Pellegrino, T. Bioconjugation of rod–shaped fluorescent nanocrystals for efficient targeted cell labeling. *Langmuir 25* (2009), 12614.

[287] R., K., Cheyssac, P., Aouaj, A., Lereah, Y., Deutscher, G., Ben-David, T., Penisson, J. M., and Bourret, A. Surface melting enhanced by curvature effects. *Surface Science 303* (1994), 231.

[288] Rashidi-Huyeh, M., and Palpant, B. Thermal response of nanocomposite materials under pulsed laser excitation. *J. Appl. Phys. 96* (2004), 4475.

[289] Rayavarapu, R. G., Petersen, W., Hartsuiker, L., Chin, P., Janssen, H., van Leeuwen, F. W. B., Otto, C., Manohar, S., and van Leeuwen, T. G. *in vitro* toxicity studies of polymer–coated gold nanorods. *Nanotechnology 21* (2010), 145101.

[290] Richardson, H. H., Hickman, Z. N., Govorov, A. O., Thomas, A. C., Zhang, W., and Kordesch, M. E. Thermooptical properties of gold nanoparticles embedded in ice: characterization of heat generation and melting. *Nano Letts. 6* (2006), 783.

[291] Riddick, T. M. *Control of Colloid Stability through Zeta Potential: With a Closing Chapter on its Relationship to Cardiovascular Disease*. Livingston Publishing Company, Livingston, MT, 1968.

[292] Roach, L., Ye, S., Moorcroft, S., Critchley, K., Coletta, P., and Evans, S. Morphological control of seedlessly–synthesized gold nanorods using binary surfactants. *Nanotechnology 29* (2018), 135601.

[293] Robinson, A. J., Richards, W. G., Thomas, P. J., and Hann, M. M. Head group and chain behavior in biological membranes: A molecular dynamics computer simulation. *Biophys. J 67* (1994), 2345.

[294] Rodríguez-Fernández, J., Pérez-Juste, J., Mulvaney, P., and Liz-Márzan, L. M. Spatially–directed oxidation of gold nanoparticles by Au(III)–CTAB complexes. *J. Phys. Chem. B 109* (2005), 14257.

[295] Rosencwaig, A. *Photoacoustics and Photoacoustic Spectroscopy*. John Wiley and Sons, 1980.

[296] Rostro-Kohanloo, B. C., Bickford, L. R., Payne, C. M., Day, E. S., Anderson, L. J. E., Zhong, M., Lee, S., Mayer, K. M., Zal, T., Adam, L., Dinney, C. P. N., Drezek, R. A., West, J. L., and Hafner, J. H. The stabilization and targeting of surfactant–synthesized gold nanorods. *Nanotechnology 20* (2009), 434005.

[297] Ruff, J., Hassan, N., Morales-Zavala, F., Steitz, J., Araya, E., Kogan, M. J., and Simon, U. CLPFFD–PEG functionalized NIR–absorbing hollow gold nanospheres and gold nanorods inhibit β–amyloid aggregation. *J. Mater. Chem. B 6* (2018), 2432.

[298] Ryan, W. L., and Cardin, C. Amino acids and ammonia of fetal calf serum during storage. *Proc. Soc. Exp. Biol. Med. 123* (1966), 27.

[299] S., S. J., Xu, Q., Kim, N., Hanes, L., and Ensign, L. M. PEGylation as a strategy for improving nanoparticle–based drug and gene delivery. *Adv. Drug Delivery Rev. 99* (2016), 28.

[300] Sadauskas, E., Danscher, G., Stoltenberg, M., Vogel, U., Larsen, A., and Wallin, H. Protracted elimination of gold nanoparticles from mouse liver. *Nanomed. Nanotechnol. Biol. and Med. 5* (2009), 162.

[301] Sagitova, E. A., Prokhorov, K. A., Nikolaeva, G. Y., Baimova, A. V., Pashinin, P. P., Yarysheva, A. Y., and Mendeleev, D. I. Raman analysis of polyethylene glycols and polyethylene oxides. *J. Phys. Conf. Ser. 999* (2018), 012002.

[302] Salavatov, N. A., Dement'eva, O. V., Mikhailichenko, A. I., and Rudoy, V. M. Some aspects of seedless synthesis of gold nanorods. *Colloid J. 80* (2018), 541.

[303] Sánchez-Iglesias, A., Winckelmans, N., Altantzis, T., Bals, S., Grzelczak, M., and Liz-Marzán, L. M. High–yield seeded growth of monodisperse pentatwinned gold nanoparticles through thermally induced seed twinning. *J. Am. Chem. Society 139* (2016), 107.

[304] Santhosh, P. B., Thomas, N., Sudhakar, S., Chadha, A., and Mani, E. Phospholipid stabilized gold nanorods: Towards improved colloidal stability and biocompatibility. *Phys. Chem. Chem. Phys. 19* (2017), 18494.

[305] Sarna, T., and Sealy, R. C. Photoinduced oxygen consumption in melanin systems. Action spectra and quantum yields for eumelanin and synthetic melanin. *Photochem. Photobiol 39* (1984), 69.

[306] Sau, T. K., and Murphy, C. J. Seeded high yield synthesis of short Au nanorods in aqueous solution. *Langmuir 20* (2004), 6414.

[307] Scarabelli, L., Grzelczak, M., and Liz-Marzán, L. M. Tuning gold nanorod synthesis through prereduction with salicylic acid. *Chem. Mater. 25* (2013), 4232.

[308] Scarabelli, L., Sánchez-Iglesias, A., Pérez-Juste, J., and Liz-Marzán, L. M. A tips and tricks practical guide to the synthesis of gold nanorods. *J. Phys. Chem. Letts. 6* (2015), 4270.

[309] Schnacter, D. The source of toxicity in CTAB and CTAB–stabilized gold nanorods, 2013. Graduate School, New Brunswick [PhD Thesis].

[310] Schulz, F., Friedrich, W., Hoppe, K., Vossmeyer, T., Weller, H., and Lange, H. Effective PEGylation of gold nanorods. *Nanoscale 8* (2016), 7296.

[311] Schulz, F., Homolka, T., Bastús, N. G., Puntes, V., Weller, H., and Vossmeyer, T. Little adjustments significantly improve the Turkevich synthesis of gold nanoparticles. *Langmuir 30* (2014), 10779.

[312] Schulze, H. Schwefelarsen in wässriger Lösung [German] (Sulfur arsenic in aqueous solution). *J. Prakt. Chem. 25* (1882), 431.

[313] Settanni, G., Zhou, J., Suo, T., Schöttler, S., Landfester, K., Schmid, F., and Mailänder, V. Protein corona composition of poly(ethylene glycol)- and poly(phosphoester)-coated nanoparticles correlates strongly with the amino acid composition of the protein surface. *Nanoscale 9* (2017), 2138.

[314] Shah, A., Alles, E., Box, C., Eccles, S., Robinson, S., de Souza, N., and Bamber, J. Non–invasive molecular profiling of cancer using photoacoustic imaging of functionalized gold nanorods. *Proc. SPIE 8943* (2014), 10.

[315] Shard, A. G., Wright, L., and Minelli, C. Robust and accurate measurements of gold nanoparticle concentrations using UV-visible spectrophotometry. *Biointerphases 13* (2018), 61002.

[316] Sharma, V., Park, K., and Srinivasarao, M. Colloidal dispersion of gold nanorods: Historical background, optical properties, seed-mediated synthesis, shape separation and self-assembly. *Mater. Sci. Eng. R Rep 65* (2009), 1.

[317] Shawky, S. M., Awad, A. M., Allam, W., Alkordi, M. H., and El-Khamisy, S. F. Gold aggregating gold: A novel nanoparticle biosensor approach for the direct quantification of hepatitis C virus RNA in clinical samples. *Biosens. Bioelectron. 92* (2017), 349.

[318] Shi, Z., Ren, W., Gong, A., Zhao, X., Zou, Y., Brown, E. M. B., Chen, X., and Wu, A. Stability enhanced polyelectrolyte–coated gold nanorod-photosensitizer complexes for high/low power density photodynamic therapy. *Biomaterials 35* (2014), 7058.

[319] Shi, Z. R., Tsao, D., and Kim, Y. S. Subcellular distribution, synthesis, and release of carcinoembryonic antigen in cultured human colon adenocarcinoma cell lines. *Cancer Res. 43*, 9 (1983), 4045.

[320] Shibaev, A. V., Makarov, A. V., Kuklin, A. I., Iliopoulos, I., and Philippova, O. E. Role of charge of micellar worms in modulating structure and rheological properties of their mixtures with nonionic polymer. *Macromolecules 51* (2018), 213.

[321] Siedentopf, H., and Zsigmondy, R. Uber Sichtbarmachung und Größenbestimmung ultramikoskopischer Teilchen, mit besonderer Anwendung auf Goldrubingläser [German] (About the visualization and sizing of ultramicroscopic particles, with particular application to gold ruby glasses). *Ann. Phys. 315* (1902), 1.

[322] Sigle, D. O., Kasera, S., Herrmann, L. O., Palma, A., de Nijs, B., Benz, F., Mahajan, S., Baumberg, J. J., and Scherman, O. A. Observing single molecules complexing with cucurbit [7] uril through nanogap surface–enhanced Raman spectroscopy. *J. Phys. Chem. Letts. 7* (2016), 704–710.

[323] Smith, A. M., Mancini, M. C., and Nie, S. Second window for *in vivo* imaging. *Nat. Nano. 4* (2009), 710.

[324] Smitha, S. L., Gopchandran, K. G., Ravindran, T. R., and Prasad, V. S. Gold nanorods with finely tunable longitudinal surface plasmon resonance as SERS substrates. *Nanotechnology 22* (2011), 265705.

[325] Socrates, G. *Infrared and Raman Characteristic Group Frequencies, Third Edition*. John Wiley & Sons, Chicester, London, 2004.

[326] Sonavane, G., Tomoda, K., and Makino, K. Biodistribution of colloidal gold nanoparticles after intravenous administration: Effect of particle size. *Colloids Surf. B 66* (2008), 274.

[327] Song, J., Yang, X., Jacobson, O., Huang, P., Sun, X., Lin, L., Yan, X., Niu, G., Ma, Q., and Chen, X. Ultrasmall gold nanorod vesicles with enhanced tumor accumulation and fast excretion from the body for cancer therapy. *Adv. Mater. 27* (2015), 1.

[328] Song, Z., Shi, J., Zhang, Z., Qi, Z., Han, S., and Cao, S. Mesoporous silica–coated gold nanorods with a thermally responsive polymeric cap for near–infrared–activated drug delivery. *J. Mater. Sci. 53* (2018), 7165.

[329] Spiker, R. C., and Levin, I. W. Raman spectra and vibrational assignments for dipalmitoyl phosphatidylcholine and structurally related molecules. *Biochim. Biophys. Acta 388* (1975), 361.

[330] Stevens, M. M., Honerkamp-Smith, A. R., and Keller, S. L. Solubility limits of cholesterol, lanosterol, ergosterol, stigmasterol, and β–sitosterol in electroformed lipid vesicles. *Soft Matter 6* (2010), 5882.

[331] Sui, Z. M., Chen, X., Wang, L. Y., Xu, L. M., Zhuang, W. C., Chai, Y. C., and Yang, C. J. Capping effect of CTAB on positively charged Ag nanoparticles. *Physica E 33* (2006), 308.

[332] Sun, Y., Gates, B., Mayers, B., and Xia, Y. Crystalline silver nanowires by soft solution processing. *Nano Letts 2* (2002), 165.

[333] Sun, Y., and Xia, Y. Large–scale synthesis of uniform silver nanowires through a soft, self–seeding, polyol process. *Adv. Mater. 14* (2002), 833.

[334] Sun, Y., Yin, Y., Mayers, B., Herricks, T., and Xia, Y. Uniform silver nanowires synthesis by reducing $AgNO_3$ with ethylene glycol in the presence of seeds and poly (vinyl pyrrolidone). *Chem. Mater. 14* (2002), 4736.

[335] Swan, J. W., and Furst, E. W. A simpler expression for Henrys function describing the electrophoretic mobility of spherical colloids. *J. Colloid and Int. Sci. 388* (2012), 92.

[336] Symm, G. T. Integral equation methods in potential theory. II. *Proc. R. Soc. Lond. A 275*, 1360 (1963), 33.

[337] Takahashi, H., Niidome, T., Nariai, A., Niidome, Y., and Yamada, S. Photothermal reshaping of gold nanorods prevents further cell death. *Nanotechnology 17* (2006), 4431.

[338] Takahashi, H., Niidome, T., Nariai, A., Niidome, Y., and Yamada, S. Gold nanorod-sensitized cell death: Microscopic observation of single living cells irradiated by pulsed near-infrared laser light in the presence of gold nanorods. *Chem. Letts. 35* (2006), 500.

[339] Takahashi, H., Niidome, Y., Niidome, T., Kaneko, K., Kawasaki, H., and Yamada, S. Modification of gold nanorods using phosphatidylcholine to reduce cytotoxicity. *Langmuir 22* (2005), 2.

[340] Takatani, S., and Graham, M. D. Theoretical analysis of diffuse reflectance from a two–layer tissue model. *IEEE Trans. Biomed. Eng. 26* (1979), 656.

[341] Taylor, A. B., Siddiquee, A. M., and Chon, J. W. M. Below melting point photothermal reshaping of single gold nanorods driven by surface diffusion. *ACS Nano 8* (2014), 12071.

[342] Tebbe, M., Kuttner, C., Männel, M., Fery, A., and Chanana, M. Colloidally stable and surfactant–free protein–coated gold nanorods in biological media. *ACS applied materials & interfaces 7* (2015), 5984.

[343] Tenzer, S., Docter, D., Kuharev, J., Musyanovych, A., Fetz, V., Hecht, R., Schlenk, F., Fischer, D., Kiouptsi, K., Reinhardt, C., Landfester, K., Schild, H., Maskos, M., K., K. S., and Stauber, R. H. Rapid formation of plasma protein corona critically affects nanoparticle pathophysiology. *Nature nanotechnology 8* (2013), 772.

[344] Teraphongphom, N. T., Kong, C. S., Warram, J., and Rosenthal, E. Specimen mapping in head and neck cancer using fluorescence imaging: Specimen mapping in HNC. *Laryngoscope Investig. Otolaryngol. 2* (2017), 1.

[345] Thomas, S. N., Zhu, F., Schnaar, R. L., Alves, C. S., and Konstantopoulos, K. Carcinoembryonic antigen and CD44 variant isoforms cooperate to mediate colon carcinoma cell adhesion to E- and L-selectin in shear flow. *J. Bio. Chem. 283* (2008), 15647.

[346] Tiernan, J. P., Ingram, N., Marston, G., Perry, S. L., Rushworth, J. V., Coletta, P. L., Millner, P. A., Jayne, D. G., and Hughes, T. A. CEA–targeted nanoparticles allow specific *in vivo* fluorescent imaging of colorectal cancer models. *Nanomedicine 10* (2015), 1223.

[347] TN101104 Measuring the zeta potential of high conductivity samples using the Zetasizer Nano. Application note, Malvern Instruments Ltd, Malvern, UK, 2017.

[348] Tong, L., Zhao, Y., Huff, T. B., Hansen, M. N., Wei, A., and Cheng, J. X. Gold nanorods mediate tumor cell death by compromising membrane integrity. *Adv. Mater. 19* (2007), 3136.

[349] Turkevich, J., Stevenson, P. C., and Hillier, J. A study of the nucleation and growth processes in the synthesis of colloidal gold. *Farad. Discuss. 11* (1951), 55.

[350] UK, C. R. Advancing care, advancing years: Improving cancer treatment and care for an aging population, 2018.

[351] Ungureanu, C., Kroes, R., Petersen, W., Groothuis, T. A. M., Ungureanu, F., Janssen, H., van Leeuwen, F. W. B., Kooyman, R. P. H., Manohar, S., and van Leeuwen, T. G. Light interactions with gold nanorods and cells: Implications for photothermal nanotherapeutics. *Nano Letts. 11* (2011), 1887.

[352] van Haute, D., and Berlin, J. M. Challenges in realizing selectivity for nanoparticle biodistribution and clearance: Lessons from gold nanoparticles. *Ther. Deliv. 8* (2017), 763.

[353] van Veen, R. L. P., Sterenborg, H. J. C. M., Pifferi, A., Torricelli, A., and Cubeddu, R. Determination of VIS–NIR absorption coefficients of mammalian fat, with time– and spatially resolved diffuse reflectance and transmission spectroscopy. In *Biomedical Topical Meeting* (2004), p. SF4.

[354] Vasir, J., and Labhasetwar, V. Targeted drug delivery in cancer therapy. *Technol. Cancer Res. Treat. 4* (2005), 363–374.

[355] Vigderman, L., Manna, P., and Zubarev, E. R. Quantitative replacement of cetyltrimethylammonium bromide by cationic thiol ligands on the surface of gold nanorods and their extremely large pptake by cancer cells. *Angew. Chem. 124* (2012), 660–665.

[356] Vijayakumar, S., and Ganesan, S. *in vitro* cytotoxicity assay on gold nanoparticles with different stabilizing agents. *J. Nanomater. 2012* (2012), 14.

[357] Vines, J. B., Yoon, J. H., Ryu, N. E., Lim, D. J., and Park, H. Gold nanoparticles for photothermal cancer therapy. *Front. Chem. 7* (2019), 167.

[358] Živanović, V., Kochovski, Z., Arenz, C., Lu, Y., and Kneipp, J. SERS and Cryo-EM directly reveal different liposome structures during interaction with gold nanoparticles. *J. Phys. Chem. Letts. 9* (2018), 6767.

[359] Wadams, R. C., Fabris, L., Vaia, R. A., and Park, K. Time–dependent susceptibility of the growth of gold nanorods to the addition of a cosurfactant. *Chem. Mater. 25* (2013), 4772.

[360] Wagener, C., Hain, F., Födisch, H. J., and Breuer, H. Localisation of carcinoembryonic antigen in embryonic and fetal human tissues. *Histochemistry 78* (1983), 1.

[361] Wall, M. A., Harmsen, S., Pal, S., Zhang, L., Arianna, G., Lombardi, J. R., Drain, C. M., and Kircher, M. F. Surfactant–free shape control of gold nanoparticles enabled by unified theoretical framework of nanocrystal synthesis. *Adv. Mater. 29* (2017), 1605622.

[362] Walsh, M. J., Tong, W., Katz-Boon, H., Mulvaney, P., Etheridge, J., and Funston, A. M. A mechanism for symmetry breaking and shape control in single-crystal gold nanorods. *Acc. Chem. Res 50* (2017), 2925.

[363] Wang, J., Bai, R., Yang, R., Liu, J., Tang, J., Liu, Y., Li, J., Chai, Z., and Chen, C. Size– and surface chemistry–dependent pharmacokinetics and tumor accumulation of engineered gold nanoparticles after intravenous administration. *Metallomics 7* (2015), 516.

[364] Wang, J., Huang, H., Zhang, D., Chen, M., Zhang, Y., Yu, X., Zhou, L., and Wang, Q. Synthesis of gold/rare-earth-vanadate core/shell nanorods for integrating plasmon resonance and fluorescence. *Nano Research 8* (2015), 2548.

[365] Wang, J., Wang, H., Yan, L., Hu, Z., Wu, X., and Li, F. Dual targeted and pH–responsive gold nanorods with improved chemotherapy and photothermal ablation for synergistic cancer treatment. *RSC Adv. 9* (2019), 5270.

[366] Wang, P. K., Ansermet, J. P., Rudaz, S., Wang, Z., Shore, S., Slichter, C. P., and Sinfelt, J. H. NMR studies of simple molecules on metal surfaces. *Science 234*, 4772 (1986).

[367] Wang, W., Li, J., Lan, S., Rong, L., Liu, Y., Sheng, Y., Zhang, H., and Yang, B. Seedless synthesis of gold nanorods using resveratrol as a reductant. *Nanotechnology 27* (2016), 165601.

[368] Wang, Y., He, J., Liu, C., Chong, W. H., and Chen, H. Thermodynamics versus kinetics in nanosynthesis. *Ang. Chem. Int. Ed. 54* (2015), 2022.

[369] Wang, Y., Xie, X., Wang, X., Ku, G., Gill, K. L., O'Neal, D. P., Stoica, G., and Wang, L. V. Photoacoustic tomography of a nanoshell contrast agent in the *in–vivo* rat brain. *Nano Letts. 4* (2004), 1689.

[370] Wang, Z. L. Transmission electron microscopy of shape-controlled nanocrystals and their assemblies. *J. Phys. Chem. B 103* (2000), 1153.

[371] Wang, Z. L., Petroski, J. M., Green, T. C., and El-Sayed, M. A. Shape transformation and surface melting of cubic and tetrahedral platinum nanocrystals. *J. Phys. Chem. B 102* (1998), 6145.

[372] Weber, J., Beard, P. C., and Bohndiek, S. E. Contrast agents for molecular photoacoustic imaging. *Nat Meth 13* (2016), 639.

[373] Wedding, U., Honecker, F., Bokemeyer, C., Pientka, L., and Höffken, K. Tolerance to chemotherapy in elderly patients with cancer. *Cancer Control 14* (2007), 44–56.

[374] Wei, Q., Jin, J., and Shen, J. J. pH controlled synthesis of high aspect–ratio gold nanorods. *J. Nanosci. Nanotechnol. 8* (2008), 5708.

[375] Weinberg, L., Collins, N., van Mourik, K., Tan, C., and Bellomo, R. Plasma–Lyte 148: A clinical review. *World J. Crit. Care Med. 5* (2016), 235.

[376] Weissleder, R. Progress continues in the development of smaller, more penetrable probes for biological imaging. *Nat. Biotech. 19* (2001), 316.

[377] Werlein, A., Peters, A., Ngoune, R., Winkler, K., and Pütz, G. Interference of phosphatidylcholines with *in vitro* cell proliferation no flock without black sheep. *Biochim. Biophys. Acta, Biomembr. 1848*, 7 (2015), 1599.

[378] Wick, M. R., and Mills, S. E. Benign and borderline tumors of the lungs and pleura. In *Practical Pulmonary Pathology: A Diagnostic Approach (3rd Edition)*, L. K.O. and M. Wick, Eds. Elsevier, 2018, p. 665.

[379] Wilhelm, S., Tavares, A. J., Dai, Q., Ohta, S., Audet, J., Dvorak, H. F., and Chan, W. C. W. Analysis of nanoparticle delivery to tumours. *Nat. Rev. Mater. 1* (2016), 16014.

[380] Wu, Y., Ali, M. R. K., Dong, B., Han, T., Chen, K., Chen, J., Tang, Y., Fang, N., Wang, F., and El-Sayed, M. A. Gold nanorod photothermal therapy alters cell junctions and actin network in inhibiting cancer cell collective migration. *ACS Nano 12* (2018), 9279.

[381] Xiong, Y., Cai, H., Wiley, B. J., Wang, J., Kim, M. J., and Xia, Y. Synthesis and mechanistic study of palladium nanobars and nanorods. *J. Am. Chem. Soc. 129* (2007), 3665.

[382] Xu, C., Chen, F., Valdovinos, H. F., Jiang, D., Goel, S., Yu, B., Sun, H., Barnhart, T. E., Moon, J. J., and Cai, W. Bacteria–like mesoporous silica-coated gold nanorods for positron emission tomography and photoacoustic imaging–guided chemo–photothermal combined therapy. *Biomaterials 165* (2018), 56.

[383] Xu, L., Öjemyr, L. N., Bergstrand, J., Brzezinski, P., and Widengren, J. Protonation dynamics on lipid nanodiscs: Influence of the membrane surface area and external buffers. *Biophys. J. 110* (2016), 1993.

[384] Xu, N., Bai, B., Tan, Q., and Jin, G. Accurate geometric characterization of gold nanorod ensemble by an inverse extinction/scattering spectroscopic method. *Opt. Express 21*, 18 (2013), 21639.

[385] Xu, Y., Zhao, Y., Chen, L., Wang, X., Sun, J., Wu, H., Bao, F., Fan, J., and Zhang, Q. Large–scale, low–cost synthesis of monodispersed gold nanorods using a gemini surfactant. *Nanoscale 7* (2015), 6790.

[386] Xu, Z. C., Shen, C. M., Xiao, C. W., Yang, T. Z., Chen, S. T., Li, H. L., and Gao, H. J. Fabrication of gold nanorod self-assemblies from rod and sphere mixtures via shape self-selective behavior. *Chem. Phys. Lett. 432* (2006), 222.

[387] Yamaguchi, S., Bhattacharyya, K., and Tahara, T. Acid–base equilibrium at an aqueous interface: pH spectrometry by heterodyne–detected electronic sum frequency generation. *J. Phys. Chem. C 115* (2011), 4168.

[388] Yamauchi, H., Ito, S., Yoshida, K., Itoh, T., Tsuboi, Y., Kitamura, N., and Miyasaka, H. Temperature near gold nanoparticles under photoexcitation: Evaluation using a fluorescence correlation technique. *J. Phys. Chem. C 117*, 16 (2013), 8388.

[389] Yang, X., Skrabalak, S. E., Li, Z. Y., Xia, Y., and Wang, L. V. Photoacoustic tomography of a rat cerebral cortex *in vivo* with Au nanocages as an optical contrast agent. *Nano Letts. 7* (2007), 3798.

[390] Yang, Y., Liu, J., Fu, Z. W., and Qin, D. Galvanic replacement-free deposition of Au on Ag for core–shell nanocubes with enhanced chemical stability and SERS activity. *J. Am. Chem. Soc. 136* (2014), 8153.

[391] Yang, Z., and Xiong, H. R. Culture conditions and types of growth media for mammalian cells. In *Biomedical Tissue Culture*, L. Ceccherini-Nelli and B. Matteoli, Eds. InTechOpen, London, UK, 2012, p. 3.

[392] Yavuz, M. S., Cheng, Y., Chen, J., Cobley, C. M., Zhang, Q., Rycenga, M., Xie, J., Kim, C., Song, K. H., Schwartz, A. G., Wang, L. V., and Xia, Y. Gold nanocages covered by smart polymers for controlled release with near-infrared light. *Nat. Mater. 8* (2009), 935.

[393] Ye, S., Marston, G., McLaughlan, J. R., Sigle, D. O., Ingram, N., Freear, S., Baumberg, J. J., Bushby, R. J., Markham, A. F., Critchley, K., Coletta, P. L., and Evans, S. D. Engineering gold nanotubes with controlled length and near–infrared absorption for theranostic applications. *Adv. Funct. Mater. 25* (2015), 2117.

[394] Ye, T., Dai, Z., Mei, F., Zhang, X., Zhou, Y., Xu, J., Wu, W., Xiao, X., and Jiang, C. Synthesis and optical properties of gold nanorods with controllable morphology. *J. Phys. Condens. Matter. 28* (2016), 434002.

[395] Ye, X., Jin, L., Caglayan, H., Chen, J., Xing, G., Zheng, C., Doan-Nguyen, V., Kang, Y., Engheta, N., Kagan, C. R., and Murray, C. B. Improved size-tunable synthesis of monodisperse gold nanorods through the use of aromatic additives. *ACS Nano 6* (2012), 2804.

[396] Ye, X., Zheng, C., Chen, J., Gao, Y., and Murray, C. B. Using binary surfactant mixtures to simultaneously improve the dimensional tunability and monodispersity in the seeded growth of gold nanorods. *Nano Letts. 13* (2013), 765.

[397] Yee, K. Numerical solution of initial boundary value problems involving Maxwell's equations in isotropic media. *IEEE Trans. Antennas Propag. 14* (1966), 302.

[398] Yoo, J. H., Han, H. S., Lee, C., Yoo, K. P., and Kang, T. Surface–enhanced Raman scattering–based detection of molecules in an aqueous solution via lipid–modified gold nanorods. *J. Nanosci. Nanotechnol. 13* (2013), 7239.

[399] Yoon, S., Lee, B., Yun, J., Han, J. G., Lee, J. S., and Lee, J. H. Systematic study of interdependent relationship on gold nanorod synthesis assisted by electron microscopy image analysis. *Nanoscale 9* (2017), 7114.

[400] Yu, Chang, S., Lee, C., and Wang, C. R. C. Gold nanorods: Electrochemical synthesis and optical properties. *J. Phys. Chem. B 101* (1997), 6661.

[401] Yu, R., Liz-Marzán, L. M., and García de Abajo, F. J. Universal analytical modeling of plasmonic nanoparticles. *Chem. Soc. Rev. 46* (2017), 6710.

[402] Zeiss, C. Ultramikroskopie für Kolloide [German] (Ultramicroscopy for colloids). *Mikro. 229* (1907).

[403] Zeiss, C. Über ein neues Ultramikroskop [German] (On a new ultramicroscope). *Phys. Z. 14* (1913), 975.

[404] Zeng, J., Zheng, Y., Rycenga, M., Tao, J., Li, Z. Y., Zhang, Q., Zhu, Y., and Xia, Y. Controlling the shapes of silver nanocrystals with different capping agents. *J. Am. Chem. Soc. 132*, 25 (2010), 8552.

[405] Zhang, Q., Jing, H., Li, G. G., Lin, Y., Blom, D. A., and Wang, H. Intertwining roles of silver ions, surfactants, and reducing agents in gold nanorod overgrowth: Pathway switch between silver underpotential deposition and gold–silver codeposition. *Chem. Mater. 28* (2016), 2728.

[406] Zhang, W. Probing the behaviors of gold nanorods in metastatic breast cancer cells based on UV-vis-NIR absorption spectroscopy. *PLoS ONE 7* (2012), e31957.

[407] Zhang, Z., and Lin, M. Fast loading of PEG–SH on CTAB–protected gold nanorods. *RSC Adv. 4* (2014), 17760.

[408] Zhao, J., and Stenzel, M. H. Entry of nanoparticles into cells: The importance of nanoparticle properties. *Polym. Chem. 9* (2018), 259.

[409] Zhou, H. S., Honma, I., Komiyama, H., and Haus, J. W. Controlled synthesis and quantum–size effect in gold-coated nanoparticles. *Phys. Rev. B 50* (1994), 12052.

[410] Zijlstra, P., van Stee, M., Verhart, N., Gu, Z., and Orrit, M. Rotational diffusion and alignment of short gold nanorods in an external electric field. *Phys. Chem. Chem. Phys. 14* (2012), 4584.

[411] Zou, Z., Zhang, Q., Zhao, Q., Peng, F., Wang, H., Yu, H., and Yang, J. Thermal stability of gold nanorods in an aqueous solution. *Colloids Surf. A 372* (2010), 177.

[412] Zsigmondy, R. Uber wässrige Lösungen metallischen Goldes [German] (On aqueous solutions of metallic gold). *Justus Liebig's Ann. Chem. 301* (1898), 29.